UCSF
UC San Francisco Electronic Theses and Dissertations

Title

Toxicological applications of cell and animal models for in vivo nuclear magnetic resonance spectroscopy

Permalink

https://escholarship.org/uc/item/1k78601n

Author

Macdonald, Jeffrey Marshall

Publication Date

1995

Peer reviewed|Thesis/dissertation

eScholarship.org Powered by the California Digital Library
University of California

TOXICOLOGICAL APPLICATIONS OF CELL AND ANIMAL MODELS FOR *IN VIVO*

NUCLEAR MAGNETIC RESONANCE SPECTROSCOPY

by

Jeffrey Marshall Macdonald

DISSERTATION

Submitted in partial satisfaction of the requirements for the degree of

DOCTOR OF PHILOSOPHY

in

PHARMACEUTICAL CHEMISTRY

in the

GRADUATE DIVISION

of the

UNIVERSITY OF CALIFORNIA

San Francisco

Date **University Librarian**

Degree Conferred: . . . . . .

Dedicated to Haley Patricia Macdonald, my daughter.

ACKNOWLEDGEMENTS

I am grateful to Dr. Thomas L. James for his mentorship, belief in my skills (persistence is more credible), and the many calm, cool, collected, and level-headed discussions (ranging from career goals to bad dreams) during my doctoral experience. I thank Dr. Lawrence Litt for the support since my arrival at UCSF: providing my first employment at UCSF, chairing my orals examination, and reviewing this dissertation. I thank my Academic Adviser, Dr. Susan P. Hawkes, for her support and guidance in academics, research (cell culture technology), my oral examination, and the insightful comments on my dissertation. I am lucky to have been chosen by such fine scholars, in terms of intellect and integrity, to guide me through some seemingly impossible hurdles.

I am eternally grateful to my wife for her solid support (the all-nighters to finish the dissertation), understanding, and love (the best of all) during the most difficult challenge of my life. I am fortunate to have parents, Patricia Anne and Ivan LeRoy Macdonald, who instilled self-respect and the realization of my full potential, and brothers that contributed to my doctoral success: Terry and Rhoda who taught me my best writing skills (blame them Tom, Larry, and Sue), Tim counciling me on my science career, and Mike for psychotherapy. I thank Glen and Pat Myers for their support ever since I met their daughter in 1984.

I extend a special thank you to Dr. Olga Schmidlin for my education in mammalian physiology, without her support this dissertation would have never been completed. I thank Setec Inc. for the bioreactor technology and Dennis Tajiri for the biotechnology expertise. I thank Dr.'s John Kurhanewizc for my three-year apprenticeship in *in vivo* NMR, Lee-Hong Chang for the spirited tutoring in *in vivo* NMR and primal scream, Mary Espanol for the consistent "hot tips" in a broad range of fields, Mark Grillo for generously donating his hepatocyte isolation knowledge to our productive collaboration, and Sharon Fleming for her collaboration in generating the

intestinal cell data in (Chapter 3). Thanks Veenstra, Benjamen, Mason, Eckert, "Redman", and Berl for the support. I thank the various scientists that have flowed through the UCSF Biomedical Magnetic Resonance Facility for helpful advise during my tenure at UCSF. I thank the UCSF Research Evaluation Allocation Committee for funding the research on strategies for monitoring glutathione by *in vivo* NMR (Chapter 5). I especially thank the UC Toxic Substances and Research and Teaching Program for funding the research presented in Chapters 4, 6, and 7.

TOXICOLOGICAL APPLICATIONS OF CELL AND ANIMAL MODLES FOR *IN VIVO* NUCLEAR MAGNETIC RESONANCE SPECTROSCOPY

by

Jeffrey M. Macdonald

ABSTRACT

The goal of this study was to develop NMR-compatible cell and animal models for toxicology using novel biotechnology and NMR hardware. Three NMR-compatible cell models and one animal hepatic model are described. The cell models are based on suspension, encapsulation, and membrane-type bioreactor technology and are demonstrated with isolated rat intestinal mucosal cells, a human prostatic adenocarcinoma cultured cell-line (DU 145), and isolated rat hepatocytes, respectively. The animal model permits determination of kinetic, biochemical, and physiological processes in intact rat liver. Together the cell and animal models permit the toxicological investigation of dose-response, cell composition, and endocrine, immune, inter-organ and physico-chemical interactions .

We conclude that for toxicological NMR study of cells, one should use the airlift bioreactor for prokaryotes, unicellular plants, parasites, and non-anchorage dependent mammalian cells, but this design creates sufficient mortality to anchorage-dependent mammalian cells and renders non-interpretable data. The tricentric™ membrane-type bioreactor should be used with anchorage-dependent mammalian cells; the diffusion distance, the global density versus spectroscopic signal-to-noise, and extracellular matrix will need to be optimized for each cell-type.

The animal hepatic model permitted the non-invasive monitoring of pH, ^{31}P, and ^{13}C metabolites in rat liver by a novel implantable triple-tuned NMR surface coil during intravenous administration of 2-^{13}C-glycine. Major ^{13}C-labeled metabolites were serine, glutathione and γ-glugly. Glutathione and γ-glugly coresonated *in vivo*, but γ-glugly was determined to be more rapidly synthesized. Serine was doubly-labeled which was

dose dependent. ^{13}C NMR spectroscopic analysis of the urine time course revealed that by 3 hrs, the major ^{13}C-labeled metabolites are glycine, creatinine, with possible labeling of glycine conjugates and oxalate; significant amounts of urea were excreted. Plasma samples revealed that 2-^{13}C-glycine was the predominant ^{13}C-labeled metabolite. The effect of an intraperitoneal bolus injection of dibromoethane (80 mg/kg) revealed that γ-glugly/glutathione decreased by 80% at 1.5 hrs after the bolus injection The glycine signal also decreased and was due to increased utilization caused by *de novo* purine, protein, and other still unknown biosyntheses. The ^{31}P NMR spectra revealed that at 1.5 hrs there was a decrease of pH, but no discernable change in ATP levels.

The combination of the novel cell and animal models and NMR analysis of tissue extract and body fluids provides a powerful range of techniques for investigation of mechanism(s) of toxic action.

Thomas L. James

TABLE OF CONTENTS

Page

OVERVIEW

Chapter 1: Overview of NMR Applicability to Problems in Toxicology..... 1

PART I: CELL MODELS

Chapter 2: Review of Available NMR-Compatible Cell Models..... 22

Chapter 3: Novel Application of Previously Developed NMR-Compatible Cell Models..... 25

Chapter 4: Comparison of Two Novel NMR-Compatible Bioreactor Prototypes for Multinuclear NMR Spectroscopy and MRI of Perfused Isolated Rat Hepatocytes..... 44

PART II: ANIMAL MODEL FOR XENOBIOTIC STRESS IN LIVER

Chapter 5: Review of Toxicological and *In Vivo* NMR Studies of Liver..... 85

Chapter 6: In Vivo Monitoring of Hepatic Glycine and High-Energy Phosphorus Metabolism in Anesthetized Rats by ^{13}C and ^{31}P NMR..... 94

Chapter 7: The Effect of Cystine Dimethyl Ester and Dibromoethane on Glutathione and Glycine Metabolism, Bioenergetics, and Intra-cellular pH by *In Vivo* ^{13}C and ^{31}P NMR Spectroscopy..... 135

Chapter 8: Concluding Remarks: The Necessity to Integrate Cell and Animal Models and Extract NMR Data..... 165

UCSF LIBRARY

LIST OF TABLES

Page

Table 1: Comparison of ^{31}P metabolite levels under three different experimental conditions: (1) 25 mM glucose and confluency (n=5), (2) 25 mM glucose and log phase (n=3), and (3) 5.5 mM glucose and log phase (n=3); in Chapter 3. 36

LIST OF FIGURES

Page

CHAPTER 1

Figure 1: Pathways to irreversible cell death in acute toxicity. 6

Figure 2: One-pulse ^{1}H NMR spectra of liver *in vivo* (A) and extract (B). 11

Figure 3: One-pulse ^{31}P NMR spectra of liver *in vivo* (A) and extract (B). 14

Figure 4: One-pulse ^{13}C *i*NMR spectrua with decoupling during acquisition of liver *in vivo* (A) and extract (B). 16

Figure 5: Transaxial MRI of rat abdominal region. 18

CHAPTER 2

CHAPTER 3

Figure 1: One-pulse ^{31}P spectra (81 MHz) of nude mouse xenograft of DU 145 (A) and perfused DU 145 cells (B) grown in 5.5 mM glucose and harvested at log phase of growth. 30

Figure 2: Bar graph comparing ^{31}P metabolites of nude mouse xenograft and perfused DU 145 cells . 31

Figure 3: One-pulse ^{31}P spectra (81 MHz) of DU 145 cells grown in 25 mM glucose, harvested at confluency (A); 25 mM glucose, harvested at log phase (B); 5.5 mM glucose, harvested at log phase (C). 35

Figure 4: Airlift bioreactor used for the *in vivo* ^{13}C NMR studies of isolated rat intestinal cells. 38

Figure 5: *In vivo* ^{13}C NMR spectra of suspended rat intestinal cells 20 (A), 60 (B), and 120 (C) min after administration of 2-^{13}C-glucose. 41

Figure 6: A graph of the *in vivo* ^{13}C NMR spectra shown in Figure 5. 42

CHAPTER 4

Figure 1: Drawing of a liver ascinus showing the three zones (A) and a cross section of a tricentric™ bioreactor fiber pair (B). 51

Figure 2: A schematic of the bioreactor, NMR coils, and plastic stand. 56

Figure 3: Schematic of the bioreactor loop. 57

Figure 4: One-pulse ^{13}C spectra of 150 mM glutathione with decoupling during acquisition in a 5 mm NMR tube (A), in the annular space of the bioreactor (B), and obtained with a spin-echo sequence in the annular space of the bioreactor (C). 64

Figure 5: A transaxial T_1 (A) and T_2-weighted (B) MRI. 65

Figure 6: T_2 -weighted transaxial MRI of bioreactor #1. 67

Figure 7: Transaxial T2-weighted MRIs of the bioreactor with and without flow and cells (A-C). D and E are enlargements of A-C. 69

Figure 8: T_2-weighted transaxial images of bioreactor #1 (A) and #2 (B). 70

Figure 9: The effect of P_i in the buffer on hepatocyte viability. 71

Figure 10: One-pulse ^{31}P spectra of *in vivo* liver (A), hepatocytes perfused in bioreactor #1 (B), after isolation (C), and the PCA extract of hepatocytes in B (D). 73

Figure 11: ^{31}P spectra of hepatocytes perfused in bioreactor #2 (A) and the PCA extract (B). 75

Figure 12: β-ATP/P_i timecourse from isolated rat hepatocytes perfused in bioreactor #1 and #2. 76

CHAPTER 5

Figure 1: Major metabolic pathways for 1,2 dibromoethane (x=Br). 87

Figure 2: One-pulse ^{1}H NMR spectra of 300 mM GSH (A) and with ^{14}N decoupling (B). 91

Figure 3: One-pulse ^{1}H NMR spectra of pure formamide (A) and with ^{14}N decoupling (B). 93

CHAPTER 6

Figure 1: A diagram depicting the fate of glycine. 96

Figure 2: The many biochemical pathways, inter-organ cycles, and relation to other amino acids of glycine. 98

Figure 3: Schematic representation of (A) the coaxial dual-slotted photo-etched surface coil and plastic stand, and (B) the surface coil implant in a rat. 104

Figure 4: The central portion of a ^{13}C NMR spectra of rat liver extract (A), and *in vivo* obtained at baseline (B) and at 230 min (C). 105

Figure 5: A portion of the ^{13}C spectrum of a liver extract obtained at pH 3.00 (A) and 7.40 (B). 106

Figure 6: Kinetics of 2-^{13}C-glycine and ^{13}C-GSH/γ-glugly in rat liver 107

over 210 min of 2-^{13}C-glycine intravenous infusion.

Figure 7: Liver extracts of rat given a 4.4 mM/kg i.p. injection of ^{13}C glycine dissected at 1, 2, 4 and 6 hours. 109

Figure 8: The {^{13}C}-^{1}H NMR POCE pulse sequence used to obtain the difference spectrum (C). 110

Figure 9: ^{13}C spectra of plasma deproteinized (A) and normal (B) obtained 2 hrs after the start of 2-^{13}C-glycine infusion. 112

Figure 10: A portion (10-33 ppm) of the ^{13}C spectrum from the extract of the liver shown in Figure 4A (A), and a control rat liver extract (B). 114

Figure 11: A portion (68-98 ppm) of the ^{13}C spectrum from the extract of the liver shown in Figure 4A (A), and a control rat liver extract (B). 115

Figure 12: A portion (68-98 ppm) of the ^{13}C spectrum from the extract of the liver shown in Figure 4A (A), and a control rat liver extract (B). 117

Figure 13: ^{13}C spectra of urine taken from the control after 1 (A), 2 (B), 3 (C), and 4 (D) hours of ^{13}C-glycine infusion. 119

Figure 14: An *in vivo* ^{31}P NMR spectrum of rat liver 65-100 min after start of intravenous 2-^{13}C-glycine infusion. 120

Figure 15: The structure of ^{13}C-labeled metabolites of 2-^{13}C-glycine found in tissue extracts and urine. 122

Figure 16: Points of control for decreasing g-glugly accumulation. 126

Figure 17: Aspartates role in the urea cycle and effect of glycine infusion. 131

Figure 18: Schematic illustrating the two pools of glutamine. 132

CHAPTER 7

Figure 1: The mechanism of OTC, CDME, and glycine intracellular transport and GSH formation. 136

Figure 2: *In vivo* ^{13}C NMR spectra of rat liver using protocol #1 (A), #2 (B), #3 (D) and #4 (C). 142

Figure 3: PCA extracts of the livers shown in Figure 2 with protocol #1 (A), #2 (B), #3 (D), and #4 (C). 143

Figure 4: Kinetics of the protocol #1 and #4.
144

Figure 5: A portion of the ^{13}C NMR spectra (45-125 ppm) obtained from PCA extracts of the liver shown in Figure 3 with protocol #4 (A), #2 (B), and #1 (C). 146

Figure 6: A portion of the of the ^{13}C NMR spectra (10-42 ppm) obtained from PCA extracts of the liver shown in Figure 3 with protocol #4 (A), #2 (B), and #1 (C). 147

Figure 7: Kinetics of the protocol #1 and #2. 149

Figure 8: A portion of the of the ^{13}C NMR spectra (20-76 pmm) obtained from PCA extracts of the liver shown in Figure 3 with protocol #1 (A), #2 (B), and control rat (C). 150

Figure 9: The *in vivo* ^{13}C spectra showing the timecourse of the effect of DBE. 152

Figure 10: Kinetics of the effect of DBE. 153

Figure 11: The *in vivo* ^{13}C spectra prior to liver dissection (A), the extract (B), and the precipitate formed when the extract was titrated from pH 7.4 to 5.0 (C). 154

Figure 12: The urine obtained from 3-4.5 hr of glycine infusion for protocol #5 (A) and # 4 (B), and the PCA extract of the kidney from the *in vivo* experiment shown in Figure 2 with protocol #4 (C). 156

Figure 13: The *in vivo* ^{31}P spectra of rat liver administered protocol # 4. 157

Figure 14: The *in vivo* ^{31}P spectra of rat liver administered protocol # 5. 158

OVERVIEW

CHAPTER 1

Overview of NMR Applicability to Problems in Toxicology

HISTORICAL PERSPECTIVE AND DEFINITIONS

Toxicology: Toxicology is the branch of science studying poisons. A poison is any agent capable of producing injury to biological systems, and can be chemical [endogenous or xenobiotic (e.g., any foreign chemical)] or physical (irritation, temperature, sound, and humidity). By this definition, anything can be a poison depending on the dose, so toxicology studies have focused on poisons that are toxic at relatively low doses and are easily dosed, such as chemicals. The biological system can be parasitic, viral, bacterial (i.e., antibiotics), invertebrate (i.e., insecticides), and vertebrate (i.e., anti-cancer drugs, antivermine). Therefore, toxicology is a broad multidisciplinary science that includes all kingdoms of the phylogenetic tree, and environmental, biological, chemical and physical sciences. Specifically, biochemical toxicology is the study of the effects of poisons and their mechanism(s) of toxic action on biological systems.

The earliest *Homo Sapiens* were well aware of the toxic effects of animal venoms and poisonous plants, as written in the Egyptian Ebers Papyrus, our earliest medical record dated ca 1500 BC. This document contains over 800 pharmaceutic recipes, some of which include the following poisons: hemlock, lead, copper, and antimony; aconita, an arrow poison of ancient China; opium, used as a poison and antidote; and plants containing the alkaloids, digitalis and belladonna.

The Greeks and Romans quite commonly used plant, animal and mineral poisons. Ancient Greek capital punishment included suicidal death by ingesting hemlock. Socrates (470 to 399 BC) was sentenced to death by eating hemlock and described the sensations of numbness and tunnel-vision to his student prior to his death. The Roman empire was plagued by poison-related political assassinations. For example, Agrippina killed Claudius using arsenic in order to make Nero emperor of Rome (Amdur et al., 1991).

Ergotomine, a toxic alkaloid produced by a fungus that grows on poorly stored rye, is hallucinogenic at low doses and was attributed to witchcraft in the Dark and Middle Ages (Barger, 1931). During the Middle Ages, poisoning was practiced by families, such as the Borgias, and some clergy for monitory gain and promotion. The practice of poisoning was actually commercialized by Catherine Deshayes in France, where she was eventually executed for her many poisonings, including over 2,000 infants.

However, it was not until the Sixteenth Century that the scientific study of toxicology was begun by Paracelsus (1493-1541) who developed the concepts of the toxic agent, dose-response to a toxicant, the distinction between therapeutic and toxic dose, and the necessity for experimentation. The father of modern toxicology was Mattieu Joseph Bonaventura Orfila (1787-1853) who, at the University of Paris, identified toxicology as a separate science and introduced forensic toxicology as a means to identify poisons for legal evidence in murder cases.

Modern biochemical toxicology has evolved with society and technology. For example, the advent of pesticides, industrial and municipal wastes, food additives, and other modern-day pollutants required the determination of their health risks to society. Radiotracer and chromatography technology has permitted picomolar detection of toxicants and elucidation of mechanisms of toxic action by determining kinetics, biodistribution, and biotransformation of toxicants. Enzyme assay and biotechnology

have helped elucidate the effects of toxicants on protein and mRNA levels, function, and composition. In conjunction, these technologies have helped form theories of toxic injury, but these theories have never been tested non-invasively within the living tissue, because technology to monitor metabolism non-invasively in living tissue has not been available. *In vivo* nuclear magnetic resonance (NMR) is a relatively recent technology that permits the non-invasive monitoring of metabolism in any tissue of interest but it is not yet an accepted technology in toxicology research.

IN VIVO NUCLEAR MAGNETIC RESONANCE SPECTROSCOPY AND MAGNETIC RESONANCE IMAGING

In vivo NMR spectroscopy is used to study the biochemistry of living systems. The NMR phenomenom was first demonstrated by Bloch and Purcell in 1945. They found that the nucleus of any isotopic element with a quantum number not equal to zero when placed in a magnetic field will have a precessional frequency (ω_0) that is proportional to the static magnetic field ($\mathbf{B_0}$). This relationship is given by the Larmor equation:

$$\omega_0 = \gamma \mathbf{B_0}$$

where γ is the gyromagnetic ratio, a constant dependent on the nucleus of interest. This nuclear precessional frequency is in the range of millions of precessions per second, or megahertz (MHz), which is the radiofrequency range. The best example of precessional frequency that we can visualize is a spinning top. As a top winds down we can see it wobble about its center axis with a ω_0, in Hz (sec^{-1}), that is proportional to its spinning velocity (v_s). The earth is another example: viewing the earth from the sun as our frame of reference, we note that the earth's axis lists 23.45° due to the torque caused by the moon, and its v_s is one day. In addition, from earth we would watch the north star, *polaris*, move from within 1° of the north axis to 47° in 12,960 years and back to its

original position in another 12,960 years. Therefore, the earth rotates about its axis every 25,920 years, or a ω_0 of 1.2×10^{-18} MHz (Eisenberg and Lerner, 1981).

Bloch and Purcell found that the NMR phenomenon occurs when the exact frequency as the precessional frequency (ω_0) is administered perpendicular to the B_0 field, creating a second field ($\mathbf{B_1}$). The B_1 field is generated by a radiofrequency (rf) transmitter. NMR-observable nuclei of atoms absorb this rf energy and resonate. When B_1 is turned off, the nuclei emit their magnetic energy, which is picked up by the same rf transmitter, now acting as a receiver, and this energy induces an electromotive force in the receiver as described by Faraday's law. The resulting voltage is manipulated to obtain the ω_0 of the nuclei.

In 1974, *in vivo* NMR spectroscopy was born after it was demonstrated that high resolution ^{31}P NMR spectra of frog sartorius muscle were maintained in good physiological condition in the spectrometer (Hoult et al., 1974). Since the mid-1970's, NMR has evolved into one of the most powerful tools for non-invasive monitoring of biochemical concentration and flux, pH, enzyme kinetics, oxidation state, metal ion binding, compartmentation and molecular mobility (Gadian, 1989; James, 1975). In the late 1970's, the conventional NMR spectrometer was modified by the addition of gradient coils to become the first magnetic resonance imager (MRI). MRI is essentially an ^1H NMR spectroscopic map with image intensity equal to the peak height of ^1H_2O. MRI has revolutionized diagnostic radiology in the last 15 years, permitting high resolution images of soft tissue that were never thought possible. *In vivo* NMR spectroscopic and MRI research have primarily been used by the biomedical field, where methods for diagnosis and determination of the mechanism of disease have revolutionized this field.

Several groups have conducted MRI and NMR spectroscopic studies of the liver (Cohen, 1991). These studies have ranged from the investigation of normal biochemistry to biochemical consequences of toxicants. To date, few studies have used *in vivo* NMR spectroscopy to investigate toxicological mechanisms and theories for irreversible cell

death due to xenobiotic exposure. The reason for this is partially because *in vivo* NMR is a relatively new method that has just recently been introduced to the field of toxicology (Hazle et al., 1989). In addition, the primary goal of most research areas in toxicology, such as forensic, analytical and environmental, is to obtain the smallest detection limit possible for detecting potent toxicants, and *in vivo* NMR has a relatively poor detection limit, in the mM range, as compared with other analytical techniques.

Biochemical toxicology is composed of toxicokinetics (study of the kinetics of toxicants in biological systems) and toxicodynamics (study of the effects of toxicants in biological systems). Toxicodynamics has become increasingly important in biochemical toxicology (Amdur et al., 1991) because public safety relies on and industry is regulated by accurate xenobiotic toxicity thresholds. In the last decade, especially, the public, industry, and scientists have demanded better biomarkers of toxicity for toxicodynamic determine the mechanism(s) of toxic action permitting more accurate risk assessment.

In vivo NMR spectroscopy and MRI have not yet been widely accepted in biochemical toxicology, but are powerful tools for determining toxicodynamics. Although present toxicodynamic studies are designed to non-invasively monitor biomarkers of toxicity directly within organs of interest, they have relied on analysis of proteins or radiotracer metabolites in body fluids to indirectly study the organ of interest. To obtain information directly from the tissue using methods presently available in toxicodynamics, biopsies or complete destruction of the tissue is necessary. The non-invasive modality of *in vivo* NMR spectroscopy and MRI, and their inherent ability to monitor all compounds containing NMR-observable nuclei better capabilities to observe and determe novel toxic phenomena by serendipity than present toxicology techniques.

BIOCHEMICAL TOXICOLOGY: STATE OF THE ART

Depending on the toxicant, there are several pathways for acute and chronic cell toxicity. Figure 1 illustrates pathways for alkylating agents, redox cyclers, uncouplers of oxidative phosphorylation, or receptor-specific acute toxicity. Cellular necrosis follows from severe environmental trauma and is biochemically and morphologically distinguished from apoptosis, or normal gene-directed cell death, by loss of energy [or adenosine 5' triphosphate (ATP)] generation and cell swelling (Alison and Sarraf, 1994). Alkylating agents, such as 1,2 dibromoethane, deplete antioxidant stores and then cause the loss of ATP production by alkylation of important enzymes in the mitochondria or

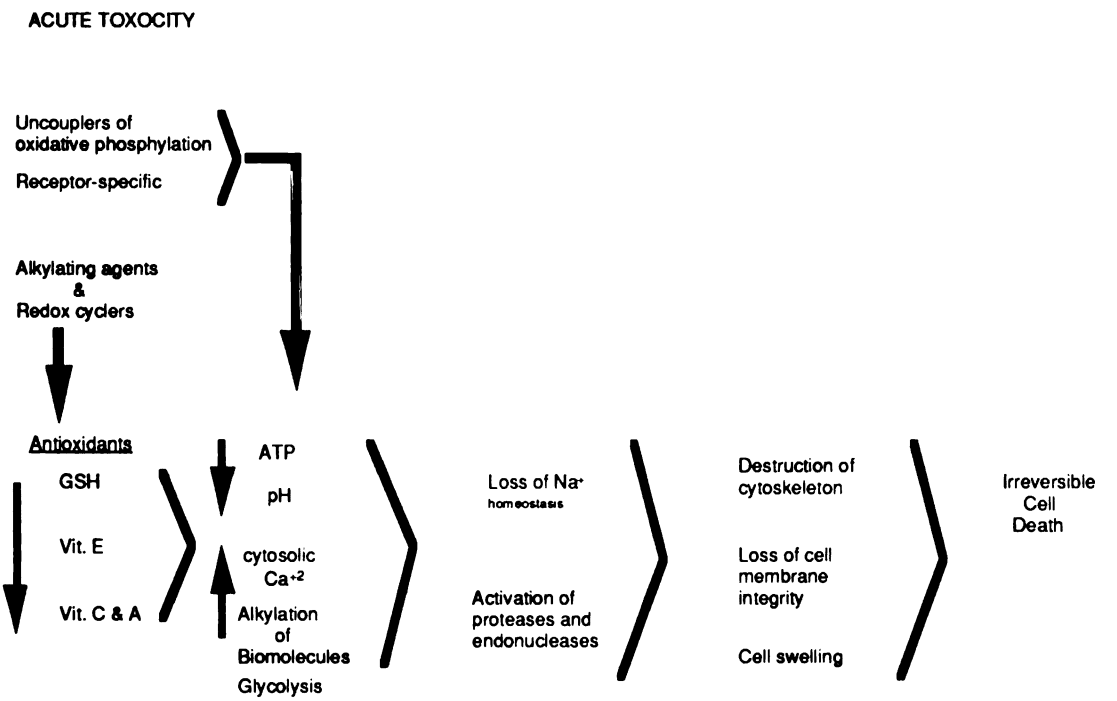

Figure 1: Pathways to irreversible cell death in acute toxicity. Alkylating agents and redox cyclers directly decrease antioxidants whereas receptor-specific toxicants and uncouplers of oxidative phosphorylation have other targets (see text).

cytosol, thus destroying their function, and displace Ca^{+2} from intracellular thiol storage sites (Reed, 1990a). As oxidative metabolism decreases, anaerobic glycolysis increases to keep pace with ATP demand, and lactate accumulates causing pH to decrease. As intracellular Ca^{+2} concentration increases, proteases and endonucleases are activated causing cell digestion. In addition, continued loss of ATP stops the ion pumps which causes the loss of maintaining cellular osmolarity leading to loss of cell membrane integrity, destruction of cytoskeleton, and cell swelling or blebbing. Even with very large blebs or bubbles in the cell membrane, cells can be revived. However, at some critical point the cell membrane integrity is lost and macromolecules leak out. The result is cell death. Redox cyclers, such as acetaminophen, cause oxidative stress which depletes antioxidants and causes lipid peroxidation, eventually causing loss of energy generation, whereas, uncouplers of oxidative phosphorylation work directly by inhibiting mitochondrial energy generation (Fig. 1). For alkylating agents, redox cyclers, and uncouplers of oxidative phosphorylation, the decrease in ATP could be distinguished from the decrease in pH if one had the temporal resolution and the methodology to simultaneously monitor these biochemical biomarkers of xenobiotic stress.

Toxicants with specific targets, such as receptors or even mitochondrial oxidative phosphorylation, are generally more toxic than toxicants with non-specific targets, such as alkylating agents or redox cyclers. Receptor-specific toxicants have varied initial actions, but all eventually inhibit ATP generation, and the same irreversible cell death sequence shown in Figure 1 is followed. For example, cyanide binds to hemoglobin causing anoxia, while pertussis toxin binds to a G-coupled protein causing an increase in intracellular Ca^{+2} and activation of proteases and endonucleases. Both toxicants at this stage then inhibit ATP generation and follow the sequence in Figure 1 to irreversible cell death. This response is similar to an ischemic response which interferes with the generation of energy by loss of blood flow. Antioxidants are the first line of defense with

glutathione (GSH) being the most abundant and important in quenching reactive intermediates, such as hydroperoxides (Reed, 1990b).

GSH is a tripeptide (γ-L-glutamyl-L-cysteinyl-glycine), and the most abundant antioxidant found in virtually all cells. It functions in metabolism, transport, immune response, and cellular protection (Dolphin et al., 1989; Tateishi and Sakamoto, 1983). Intracellular steady-state GSH concentrations depend on rate of synthesis, cell efflux, redox cycling of GSH, and conjugation of electrophilic compounds via GSH-S-tranferase (Dolphin et al., 1989; Reed, 1990b). Presently, the primary means of non-invasive monitoring of GSH changes is by enzymatic or chemical analysis of blood plasma or radiotracer studies (Andersen, 1985; Chasseaud, 1988; Hayes et al., 1987). These studies suffer from the inability to (1) directly monitor and correlate proximal and temporal GSH changes within the same individual, and (2) correlate *in vivo* enzyme function with *in vitro* activity. Although there have been many *in vivo* NMR spectroscopy studies performed on the liver (Cohen, 1991), none have attempted to measure GSH levels *in vivo*. All studies performed to date that have successfully monitored GSH have used erythrocytes, or cells immersed in D_2O for ^1H NMR (Rabenstein and Keire, 1989) or perfused in culture medium for ^{13}C NMR (Gamcsik and Colvin, 1991).

As mentioned above, biochemical toxicology has evolved from the need to determine the *in vivo* target or receptor of toxicants and identification of toxic metabolites, to understanding of their mechanism(s) of toxic action. Toxicants often have multiple paths to irreversible cell death that is dose and organ specific (Amdur et al., 1991). Presently, there are few non-invasive techniques available that can adequately ascertain toxic injury at the cellular or tissue level. Although body fluid analysis has been successful for toxicokinetics and can monitor biomarkers of toxic injury, it does not generate organ-specific information. Needle biopsy or dissection of tissues with subsequent extract analysis gives conclusive information regarding biochemical metabolite and toxicant levels. However, these studies require a large number of animals,

UCSF LIBRARY

which often generate large standard deviations at the various time points obtained during the time course of dosing experiments. Differences between replicate samples can be due to environmental and genetic differences between individuals, sample preparation inaccuracies, and/or differences in biochemical metabolite homeostasis at the time of animal sacrifice (Higashi et al., 1989; Hodgson and Guthrie, 1984). In fact, biochemical homeostatic information within a single individual is unattainable by conventional toxicologic techniques (Higashi et al., 1989). In particular, oxidatively labile metabolites, such as GSH, and acid/base-labile high energy phosphate metabolites are extremely prone to analytical degradation during the time required for tissue excision and sample preparation.

There are few methods available for the non-invasive measurement of intracellular pH in whole animals and *in vivo* NMR spectroscopy is the only method that is entirely non-invasive (Gillies et al., 1982). Since *in vivo* NMR spectra contain information on all relatively small metabolites containing NMR-observable nuclei, such as ^{31}P, ^{1}H, and ^{13}C, serendipitous discovery of unknown mechanisms of toxic injury can be revealed.

There is a great need for development of non-invasive methodologies for toxicological study of intact animals (Monk and Lau, 1988; Reed, 1990b). Multinuclear *in vivo* NMR spectroscopy permits the monitoring of every biomarker, except antioxidants, listed in Figure 1: ATP, pH and indicators of cell death by ^{31}P NMR; sodium homeostasis by ^{23}Na NMR; calcium homeostasis by ^{19}F NMR; and glycolysis by ^{13}C NMR. Interestingly, GSH has not yet been monitored by *in vivo* NMR spectroscopy in spite of its large tissue concentration, which can be as high as 8 mM in liver (Meister, 1989).

IN VIVO NMR SPECTROSCOPY: CURRENT STATE OF THE ART

Since the liver is the primary organ for detoxification in the body and thus of major concern for toxicologists, a review of the literature of *in vivo* NMR spectroscopy of liver is presented here. NMR spectroscopy is an alternative technique to analysis of tissue extracts and body fluid, and can non-invasively monitor metabolic fluxes in response to xenobiotic or environmental stress. The dynamics of many endogenous metabolites can be followed in real time simultaneously since all compounds with NMR-observable nuclei (i.e., ^{1}H, ^{31}P, ^{13}C) appear as peaks in the spectrum as long as their concentrations are greater than 1 mM. The axis of a NMR spectrum, known as the chemical shift (δ), is in parts per million (ppm). The chemical shift dispersion is defined as the range of the chemical shift attained by a particular NMR-observable nuclei. The spectrum is typically referenced to an arbitrary peak within the spectrum. For example, an *in vivo* ^{1}H spectrum is commonly referenced to the water peak which is known to have a signal 4.7 ppm from the primary standard tetramethylsilane (TMS), and has a chemical dispersion of 10 ppm, while ^{13}C is generally referenced to an external standard, or to the methylene of lipids, at 30 ppm (relative to TMS) and has a chemical shift dispersion of 210 ppm.

^{1}H NMR spectroscopy has the second highest sensitivity among the NMR-observable nuclei; ^{3}H is the most sensitive. There are few *in vivo* ^{1}H NMR spectroscopy studies of liver metabolism because of the poor resolution caused by its small chemical shift dispersion, respiratory and involuntary movement, and short T_2 caused by paramagnetic compounds, leading to broad signals. Relative to other NMR-observable nuclei, spin-lattice (T_1) and spin-spin (T_2) relaxation measurements of *in vivo* water protons have been more common (Hazle et al., 1989). Figure 2A is an *in vivo* ^{1}H NMR spectrum of the liver which has a linewidth of 80 Hz at one half the peak height of water. The additional peak labeled glycogen in Figure 2A does not appear in the perchloric acid

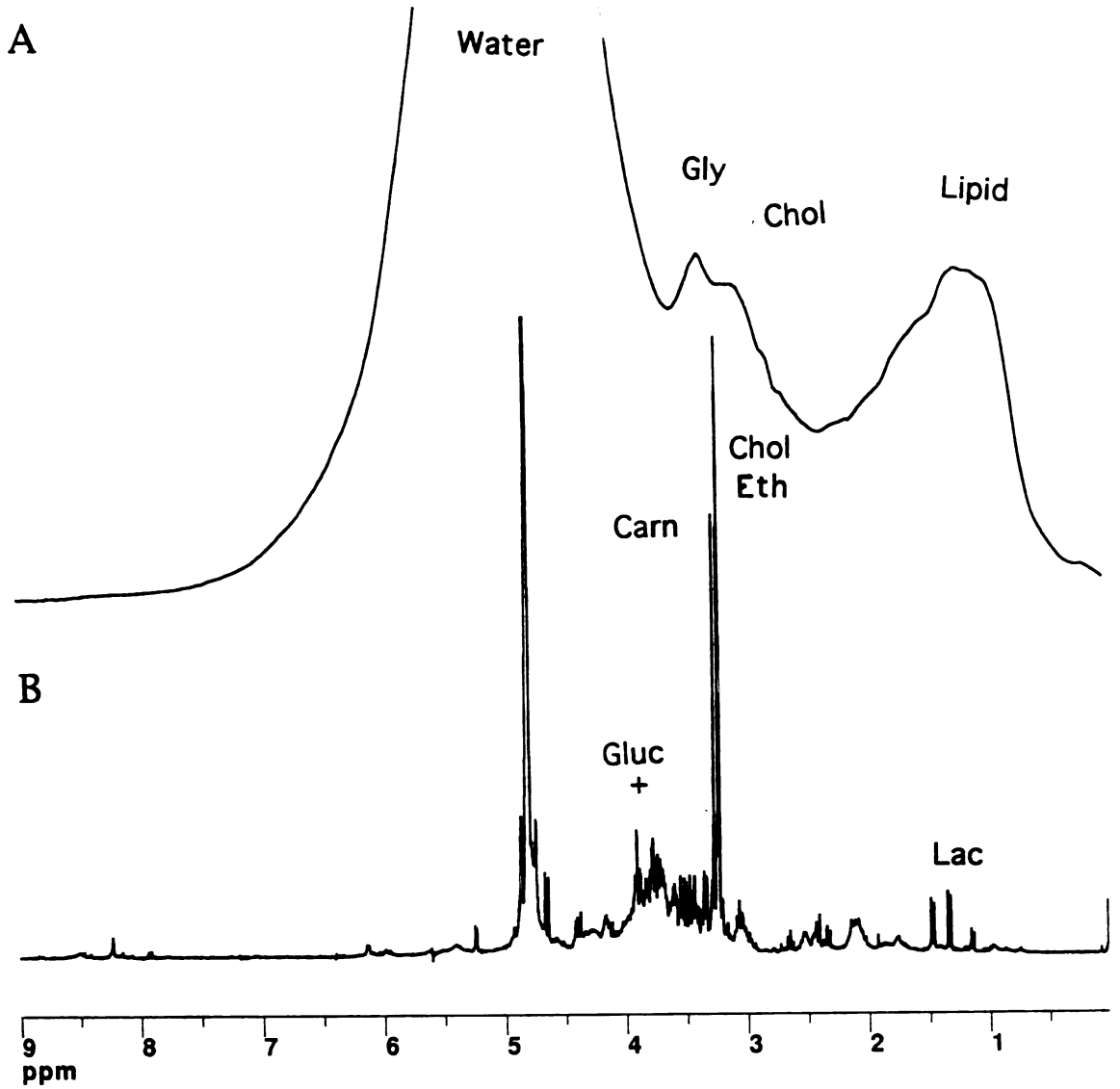

Figure 2: A one-pulse ^{1}H *in vivo* NMR spectrum of rat liver obtained at 4.7 T (A) and PCA rat liver extract obtained at 300 MHz (B). The parameters for A and B, respectively, are: acquisitions=10 and 40; TR=5.5 s and 1.5 s; SW=3024 and 3024 Hz; and CB=4K and 16K. Abbreviations are as follows: Gly, glycogen; Chol, trimethyl of choline; ETH, ethanolamine; Carn, trimethyl of carnitine; Gluc+, glucose and other metabolites; Lac, lactate.

(PCA) liver extract (Fig. 2B). This peak was incorrectly identified as GSH (Soher et al., 1993) and has been proposed to be glycogen (R. G. Shulman, 1993; verbal communication after presentation of Soher et al., 1993).

Many endogenous signals of high concentration, especially from the methyl, methylene and methine protons, appear between 0.5 and 4.5 ppm. The PCA liver extract in Figure 2B reveals that mostly choline and some ethanolamine dominate the signal between 2.0 and 4.0 ppm, while lipid signals dominate the region near 1.0 ppm (Fig. 2A). Choline and carnitine have trimethyl groups and therefore contribute 3-fold greater signal per mole to this region than monomethyl compounds with molar equivalence . Therefore, due to the lack of adequate *in vivo* resolution and the dominant trimethyl and water signal between 2.0 and 5.0 ppm, ^{1}H NMR spectroscopy of the liver is presently not feasible for compounds resonating at concentrations of less than 10 mM in this region. Spectroscopic editing, lipid suppresion, and localization permit ^{1}H metabolites to be monitored in perfused liver between 0 and 2.0 ppm (Jue et al., 1985). Recent ^{1}H chemical shift imaging (CSI) studies of human liver have resulted in linewidths of 15 Hz at 1.5 Tesla permitting spectral resolution of relatively concentrated liver metabolites resonating between water and choline (Soher et al., 1993). CSI is a mixture of MRI and NMR spectroscopy, using an external coil and magnetic gradients to obtain NMR spectra from various regions of interest.

We conclude that ^{1}H NMR spectroscopy of the liver will not be feasible *in vivo* for compounds with concentrations less than 10 mM. This is due to poor natural linewidths, which are generally 60-100 Hz at half height on the ^1H_2O resonance at a magnetic field strength of 4.7 Tesla, and an enormous signal due to trimethyl protons of choline and carnitine. For organs other than liver, one can routinely obtain 20-30 Hz linewidth on the water resonance at 4.7 Tesla, and toxicological study of lower concentration metabolites are feasible, particularly when using more advanced pulse-editing techniques.

In vivo ^{31}P NMR spectroscopy of the liver has been performed in mice, rats, rabbits, and humans since 1980. These liver studies monitor pH and phosphate metabolites and have focused on the normal biochemistry, such as ^{31}P metabolite visibility, effect of hormones and excess nutrients (Ackerman et al., 1980; Eriksson et al., 1994; Iles et al., 1980; Jue et al., 1987; Koretsky et al., 1983; Malloy et al., 1986; Masson and Quistoff, 1992; Okuda et al., 1987; Radda, 1986; Thiaudiere et al., 1993; Walsh et al., 1993), the effect of hypoxia (Desmoulin et al., 1987; Schmidt et al., 1986), neoplasia (Morikawa et al., 1992; Murphy et al., 1992) and ethanol use (Brauer and Ling, 1991; Cunningham et al., 1986; Helzberg et al., 1987; Masson et al., 1992). The ^{31}P NMR determination of intracellular pH is possible because the chemical shift of phosphates are pH-sensitive, and with the appropriate chemical shift reference, one can obtain the correct intracellular pH (Seo et al., 1983).

The *in vivo* ^{31}P NMR spectrum of rat liver is composed of three peaks for nucleotide triphosphate (NTP) and one peak for nicotinamide diphosphate (NAD/NADH), phosphodiesters (PDE), phosphomonoesters (PME), and inorganic phosphate (P_i) (Fig. 3A). These ^{31}P metabolites are indicators of bioenergetics (ATP), phospholipid metabolism (PDE and PME), and cell death (high P_i). Individual metabolites cannot be resolved in the PME and PDE regions of the *in vivo* spectrum due to spectroscopic imperfections and presence of paramagnetics, such as iron. However, tissue obtained at the end of NMR experiments can be extracted for subsequent metabolite identification and quantification by NMR, chromatographic or other analytical methods. The ^{31}P NMR high resolution spectrum (300 MHz) of a PCA extract of the rat liver allows identification of the individual peaks contained under the PME and PDE regions (Fig. 3B).

In vivo ^{31}P CSI of liver is sensitive enough to be performed with an external coil (Menon et al., 1995). However, *in vivo* ^{13}C CSI is too insensitive; in fact, ^{13}C is 64-fold and 4-fold less sensitive than ^{1}H and ^{31}P NMR spectroscopy, respectively, for the same

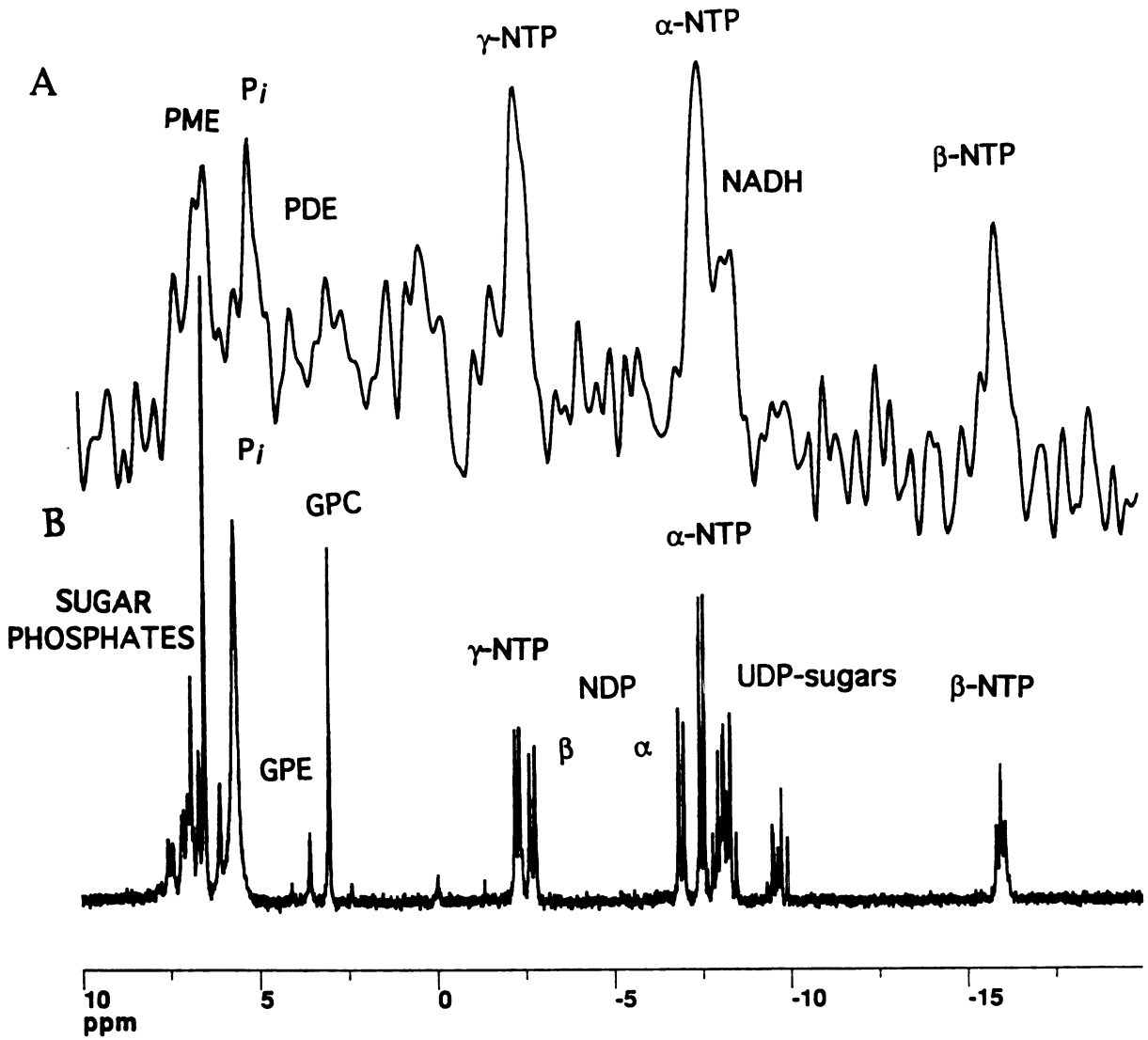

Figure 3: A ^{31}P NMR spectrum of rat liver using one-pulse *in vivo* NMR at 4.7 T (A) and PCA rat liver extract obtained at 300 MHz (B). The abbreviations are as follows: PME, phosphomomoesters; P_i, phosphate; PDE, phosphodiester; NTP, nucleoside triphosphate; NDP, nucleoside diphosphate; NADH, nicotinamide adenenine diphosphate; GPC glycerophosphocholine; GPE, glycerophosphoethanolamine; UDP, uridine diphospho.

number of nuclei (James, 1975). Additionally, the large chemical shift dispersion causes Gibbs artifact where part of the spectrum emanates from a different region of interest, such as a thoracic muscle, thereby interfering with the liver ^{13}C NMR spectrum. To resolve any sensitivity problems, *in vivo* ^{13}C NMR studies generally use implanted surface coils (Pahl-Wostl and Seelig, 1987) and, if a particular metabolite is to be monitored, ^{13}C-labels are infused. The natural-abundance of ^{13}C is 1.1 % (James, 1975). But ^{13}C abundance can theoretically be enhanced to 100%, thus selectively increasing the ^{13}C signal emanating from tissue to attain a sensitivity as high as ^{1}H and ^{31}P as stated above.

Nuclear manipulations such as decoupling, nuclear Overhauser enhancement (nOe), and polarization transfer can enhance ^{13}C sensitivity. Decoupling and nOe will enhance the ^{13}C signal two- and three-fold, respectively (James, 1975). however, energy deposition during a nOe experiment will heat the liver, particularly if an implanted surface coil is used. Polarization transfer will enhance signal nearly four-fold with a power deposition similar to decoupling. A recent sequence, B_1 insensitive nuclear enhancement by polarization transfer (BINEPT), has permitted use of ^{13}C NMR spectroscopy with a surface coil (Merlke et al., 1992), although, it has not been demonstrated on internal organs. Although BINEPT shows future promise and was unsuccessfully attempted in our study, we have employed *in vivo* ^{13}C NMR with an implanted surface coil, decoupling during acquisition, and infusion of ^{13}C-labeled compounds.

In vivo ^{13}C NMR spectroscopy of the liver has been the most successful for determining metabolism and biochemical mechanisms of pathology. For example, use of ^{13}C-labeled compounds has permitted monitoring of metabolic pathways such as gluconeogenesis, the tricarboxcylic acid cycle and related anaplerotic reactions, fatty acid metabolism and ketogenesis, glycogen synthesis and degradation, and triglyceride and phospholipid metabolism (Cohen, 1991; London, 1988a; Seelig and Burlina, 1992),

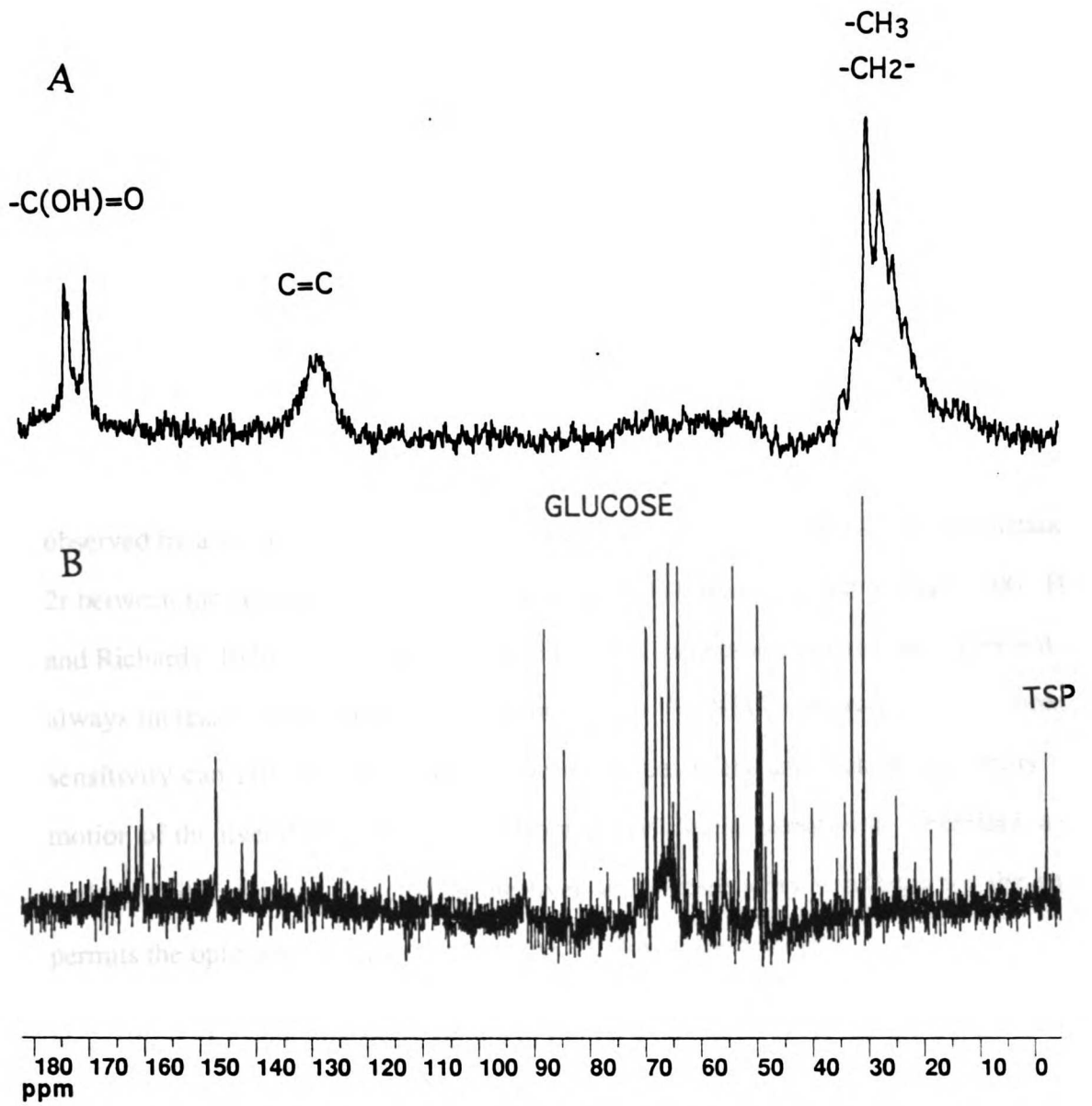

Figure 4: A ^{13}C *i*NMR spectrum of rat liver using one-pulse with decoupling during acquisition *in vivo* at 4.7 T (A) and PCA rat liver extract obtained at 300 MHz (B). Coupled 1-13C-formate resonates at 174 ppm. The -CH=CH- id from unsaturated lipids and the peaks centered at 30 ppm are primarily due to lipids. For A and B, respectively, SW=6666 Hz and 10,000 Hz; TR=2 s and 15 s; CB=4K and 16K. The *in vivo* spectrum took 10 min to acquire.

as well as the effect on primary metabolism of xenobiotics such as ethanol and streptozotocin (Cohen, 1987a). Figure 4A is an *in vivo* ^{13}C NMR spectrum of rat liver illustrating the large chemical shift dispersion of 210 ppm and the high resolution of individual peaks. Figure 4B shows the spectrum of the PCA extract of the liver illustrating that glucose which is present at a concentration of about 5 mM is the primary water soluble metabolite and that fats and proteins comprise the majority of the *in vivo* signal.

Figure 5 is an MRI of a rat illustrating the anatomy and the distance between the external surface coil and the liver. The abdominal muscle and skin of the rat creates separation between the liver and the surface coil, affecting its sensitivity. The signal observed by a surface coil with radius, r, decreases as a function of r^3 and, at a distance of 2r between the coil and the liver, there is no signal (Fukushima and Roeder, 1981; Hoult and Richards, 1976). Therefore, coil implantation, as opposed to external placement, will always increase signal sensitivity, and for *in vivo* ^{13}C NMR spectroscopy this enhanced sensitivity can provide the difference between feasibility and lack of feasibility. The motion of the liver due to respiration also decreases signal sensitivity. Therefore, a rigid surface coil implanted directly on the liver and a respiratory ventilator for the animal permits the optimum sensitivity for *in vivo* ^{13}C NMR spectroscopy.

In vivo ^{31}P and ^{13}C NMR spectroscopy, in conjunction, can monitor all the critical biomarkers of xenobiotic stress shown in Figure 1, although GSH has not yet been monitored as mentioned previously. However, *in vivo* NMR has complexities associated with a living system such as uncontrolled endocrine, immune, inter-organ transport of metabolites, inter-cellular interactions, and physico-chemical parameters. The influence of these parameters is significant when stress is applied. NMR-compatible cell models have evolved to control for these factors. In general, *in vivo* NMR-compatible animal and cell models have not been successfully integrated to complement each other. The reason for this is that the development of NMR-compatible cell models has required a major

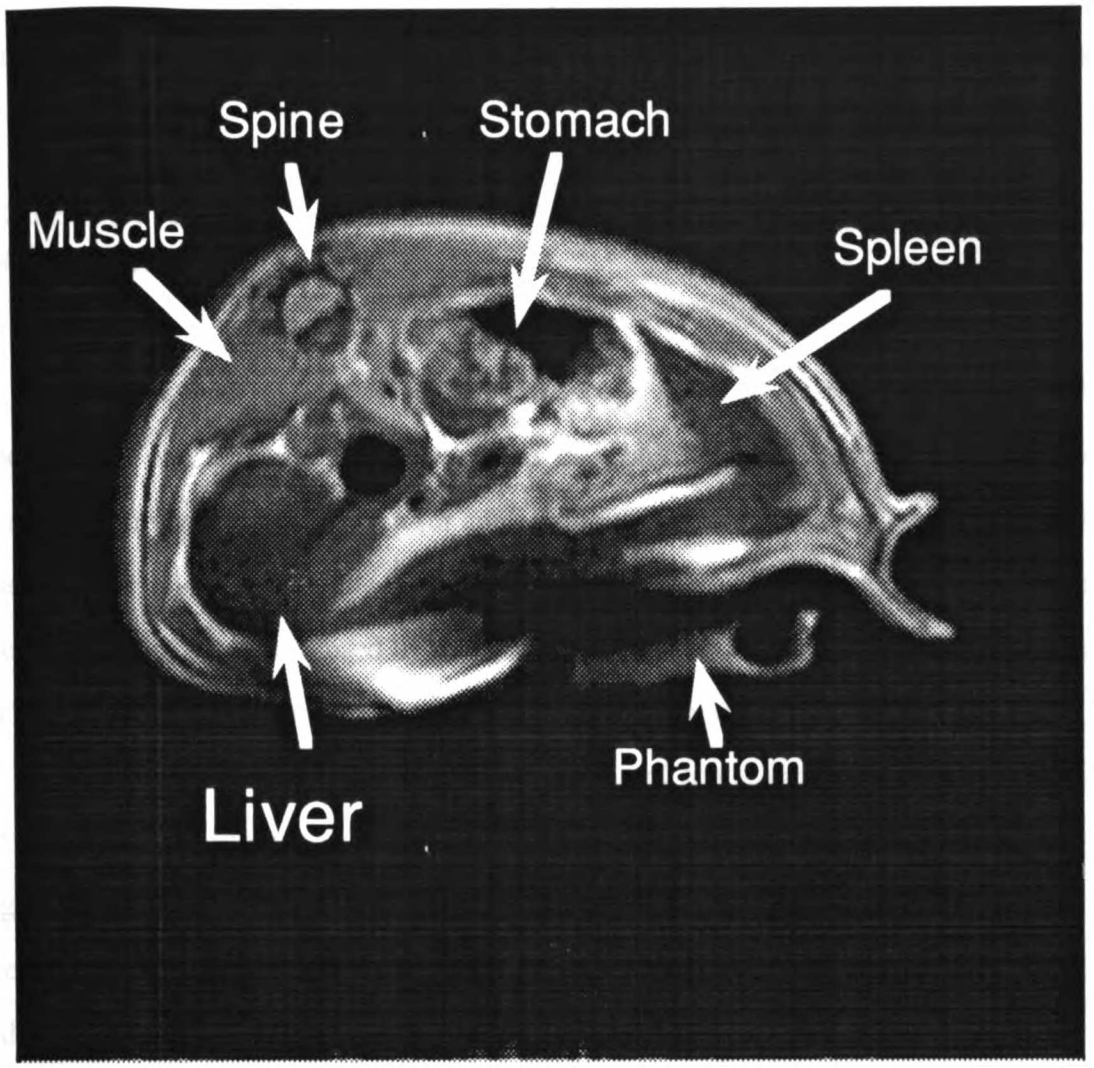

UCSF LIBRARY

Figure 5: Transaxial MRI of rat abdominal region. The phantom is a piece of 5mm NMR tube filled with water and is lying next to the edge of the surface coil. TE = 58; TE=3s; Na = 1.

time commitment, and generally NMR groups are not large or comprehensive enough to achieve collaborations between physiologists, cell biologists and NMR spectroscopists.

NECESSITY OF CELL MODELS FOR INTERPRETATION OF DATA FROM ANIMAL MODELS

Multinuclear *in vivo* NMR spectroscopy is a powerful tool for studying mechanisms of toxic injury but needs the integration of cell, animal, and metabolite identification via tissue extraction for application to biochemical toxicology. This section discusses problems associated with the use of *in vivo* NMR animal models and interpretation of the data caused by insufficient control of immune, endocrine, inter-organ cycling of metabolites, intercellular interactions, and physico-chemical parameters.

One problem associated with interpretation of NMR data from animal systems is the occurence of edema, or tissue swelling following xenobiotic stress. When injury begins to affect cell membrane integrity and arachidonic acid, or other cytokines, are released into the extracellular space (Fig. 1), white blood cells are attracted to the region, and edema ensues. The tissue swells and causes most of it to move away from the sensitive volume of the surface coil. A surface coil continues to monitor the same region, but now that region may contain only half of the original cells from the tissue of interest, the other half is composed of infiltrated lymphocytes and extracellular fluid. Lymphocytes and extracellular fluid may have different biochemical compositions and functions from the tissue of interest. Therefore, the biochemical changes that occur during xenobiotic stress, the purpose of the *in vivo* experiment, are typically obscured by the immune response. No existing *in vivo* NMR technique controls for the immune response. For example, CSI has set voxel sizes similar to the sensitive volume of a surface coil. Presently, the only way to control for the immune response is to perform *in*

vivo NMR studies of excised tissue or cells contained within a volume coil and introduces artefacts of its own.

Problems associated with the endocrine response are best illustrated by loss of glycogen during surgery and vasoconstriction caused by the hormones glucagon and adrenaline, respectively. For example, the first natural-abundance *in vivo* ^{13}C NMR studies of liver glycogen found that upon surgery glycogen disappears because glucagon is secreted by the pancreas due to the trauma of surgery (Alger et al., 1984). Glycogen degradation is stopped by introducing β-adrenergic blockers, such as propranolol. Adrenaline, which is a vasoconstrictor, increases blood pressure but decreases blood flow to the liver. Adrenaline may be released from the adrenal glands during xenobiotic stress diminishing oxygen delivery, leading to an increase in glycolysis and subsequently decreasing pH. One could incorrectly attribute these effects to the xenobiotic mechanism of toxic action as shown in Figure 1.

Inter-organ cycling of metabolites can affect the interpretation of the kinetics of ^{13}C-labeled metabolites. The kidney/liver salvage/storage cycle and Cori cycle can generate substrates which do not originate in the liver but are stored there. For example, amino acids are recycled between the liver and kidney forming γ-glutamyl diamino acids that may resonate *in vivo* at the same chemical shift as the labeled amino acid or endogenous compound (i.e., GSH) of interest. The Cori cycle represents the interaction between liver and muscle. The liver secretes glucose and the muscle forms lactate from glucose, which returns to the liver and is metabolized back to glucose or ATP. Additionally, GSH-S-conjugates are formed in the liver and are generally non-toxic until they are further metabolized in the kidney (Koob and Dekant, 1991).

Cell composition and intercellular communication also effects metabolite composition and normal cellular function (Mehendale et al., 1994). The liver by volume is composed of 80% hepatocytes, or parenchymal cells, bile duct cells, endothelial cells, and other non-hepatocytes (Arias et al., 1988). Gap junctions link the cytoplasm of one

cell with that of its adjacent neighbors, permitting molecules of less than 1,000 Dalton to flow between cells. Toxic agents may interfere with normal gap junctional intercellular communication affecting normal cell function (Mehendale et al., 1994). Therefore, cell composition and the effect of gap junctional intercellular communication can be investigated with cell models. Physico-chemical parameters, such as dose, temperature, and osmolarity can also change during the course of xenobiotic stress effecting xenobiotic metabolism and toxicity.

One problem of *in vivo* NMR animal studies of stress are the changes in T_1 and T_2. One of the first studies mentioning this problem was in the quantitation of lactate after ischemic insult (Chang et al., 1987b). Changes in T_1 and T_2 during the course of a NMR experiment results in differential saturation of peaks, causing apparent changes in metabolite levels. Comparison of metabolite peak areas from tissue extracts and *in vivo* spectra from control and stress experiment can distinguish the NMR relaxation effects from real toxicological effects, such as a decrease in GSH. Changes in saturation factors and metabolite levels can be determined, but changes in NMR-visibility caused by binding to macromolecules or compartation are still very difficult to determine.

Although these parameters inherent in the animal system may affect data interpretation, they are part of the xenobiotic stress in animals and thus very important in the complete scheme of the xenobiotic. Few *in vivo* NMR studies, particularly those using ^{31}P, account for these changes. Cell models can control for or at least account for these parameters, except NMR-visibility changes. Multinuclear *in vivo* NMR spectroscopy of animals, cells, and tissue extracts is the most powerful non-invasive technique available for monitoring xenobiotic stress, and if performed in conjunction the data is more useful for the determination of mechanism(s) of toxic action than if performed alone.

PART I: CELL MODELS

CHAPTER 2

Review of Available NMR-Compatible Cell Models

NMR studies of cell preparations permit the control of cell composition, and control contributions from immune and endocrine response, inter-organ transport, intercellular communication, and physico-chemical parameters not afforded in intact animals or perfused organ systems (for reviews see Egan, 1987; Gillies et al., 1986; Kaplan, 1992; Ruiz-Cabello and Cohen, 1993; Szwergold, 1992). However, the first NMR studies of cells did not control for physico-chemical parameters. Four categories of NMR-compatible mammalian cell perfusion systems have evolved since its inception in 1978: (1) suspension, (2) entrapment, (3) microcarrier and (4) membrane (Szwergold, 1992). The first spectroscopy of whole cells was a ^{31}P spectrum of erythrocytes, which were simply pelleted and placed in an NMR tube, and the spectrum consisted primarily of 2,3 diphosphoglycerate signals (Moon and Richards, 1973). Spectra from energized cells were first obtained from yeast suspensions (Salhany et al., 1975), and later from suspensions of *E. coli* (Ugurbil et al., 1978) and Ehrlich ascites tumour cells (Navon, 1977) These early suspension techniques relied on endogenous energy sources, wastes were not washed away, and oxygen was supplied by sparging or agitation, which is problematic for mammalian cells because it induces cell lysis and aggregation (Gillies et al., 1986).

The most widely applied technique developed thus far is the encapsulation technique (Szwergold, 1992) whereby cells are immobilized in threads of agarose (Foxall and Cohen, 1983) or alginate (Narayan et al., 1990). This method entails mixing a cell preparation with a material such as melted agarose and then allowing the polymer to

UCSF LIBRARY

solidify into threads or beads. Its wide use is due to its simplicity and the great cell density attainable. The drawbacks are that 1) cells are placed in a non-physiological environment and consequently do not grow within the bedding matrix, and 2) diffusion of nutrients and metabolic wastes are inhibited in the matrix (Gillies et al., 1986). Additionally, cells must undergo a hypoxic preparation period when they are isolated and then mixed with the viscous agarose matrix, a period of time that can last several hours.

Microcarrier beads were first introduced by Ugurbil et al. in 1981 (Ugurbil et al., 1981). In this system, which is applicable only to anchorage-dependent cells, cells are grown on the surface of small polymeric beads and placed in a NMR-compatible perfusion chamber for study. This system is considered to mimic normal metabolism of cultured cells because there is no cell preparation and cells are actively growing in a monolayer unlike the encapsulation technique (Szwergold, 1992). The problem is the high bead to cell volume. Additionally, cells grow in monolayer, a situation which does not commonly occur *in vivo*. However, for cultured cells, this may be a good comparison for monolayer cultures.

Membrane-type perfusion systems are considered to be the best for maintaining *in situ* metabolism since cultured cells can be monitored over a long period (up to months (Hrovat et al., 1985), they can be grown in three dimensions, and reach densities comparable to those found in tissues. In addition, these systems deliver nutrients similar to capillary beds found *in vivo* (Gillies et al., 1986). These systems separate the cells from the flowing perfusion solution by permeable membranes, allowing diffusion of nutrients and waste, but restraining the cells in the NMR probe (Ruiz-Cabello and Cohen, 1993).

A hollow-fiber bioreactor is also a membrane system that consists of a bundle of fibers running axially through a plastic housing capped at each end with epoxy. The cells grow on the outside of the fibers and nutrient media flows from a reservoir, through the fiber lumina, and back to the reservoir, perfusing the cells by diffusion. The hollow-fiber

bioreactor was first adapted for NMR spectroscopy in 1984 (Gonzalez-Mendez et al., 1982) and has subsequently been refined to enable cells cultured for many months to reach tissue densities (Gillies et al., 1994) Because the cells are separated from the media, nutrients reach the cells via diffusion or perfusion as opposed to the typical convection of nutrients. Therefore, this system has the lowest mass fluxes of all NMR-compatible methods (Gillies et al., 1986). Oxygen is always the limiting nutrient in these NMR-compatible cell models. Oxygen distribution was modeled in the hollow-fiber bioreactor. It was determined that cells become hypoxic if they are located more than 200 μm radially from the fibers and more than 2.5 cm distance from the inlet port (Gillies et al., 1986). Therefore, cells must be kept within 200 μm of the nutrient source in order to maintain a sufficient oxygen supply.

Relatively few NMR experiments using isolated cell preparations have been performed in comparison to those using cultured cells. The membrane-type of NMR-compatible bioreactor is ideal for isolated cell preparations because there is no preparation step that causes hypoxia, as with encapsulation, and tissue preparation would not be feasible with microcarrier beads which require attachment. This is probably why the first tissue preparations, kidney proximal tubules (Boulanger et al., 1985), used membrane-type NMR-compatible bioreactors. However, this bioreactor is made of dialysis membranes which are awkward, and the geometry of the apparatus does not allow the optimum distance between cells and the nutrient source (i.e., 200 μm). Therefore, there has been need for a better bioreactor design for cell preparations.

CHAPTER 3

Novel Application of Previously Developed NMR-Compatible Cell Models

INTRODUCTION

Recent ^{31}P studies of human prostatic cancer have revealed metabolite markers that may be useful to differentiate between benign and malignant tissues (Narayan et al., 1991) Interpretation of clinical ^{31}P NMR data of human prostatic cancer is complicated by a large number of variables encountered *in vivo*. These variables include tumor heterogeneity, immune and inter-organ responses, contamination from surrounding tissues and the inability to resolve and quantify resonance peaks (Narayan et al., 1991). NMR spectroscopy of PCA extracts of tumors can aid in the identification and quantification of metabolites observed *in vivo* (Corbett et al., 1987). Disadvantages of extraction studies especially applicable to human prostate cancer include rapid degradation of high energy phosphorus metabolites during freeze clamping at surgery and extraction, inability to kinetically monitor individuals, and the possibility of sample contamination from surrounding normal tissue during excision. Cell perfusion studies can eliminate many of the problems associated with *in situ* tumor and extraction studies. For example, viable cancer cells can be studied with superior spectral resolution and rapid kinetic timepoints, better tissue homogeneity, and more physiological control than can be obtained for *in situ* tumors. However, interpretation of perfusion studies requires strict control of experimental parameters, such as substrate availability and phase of growth, because these can have dramatic effects on metabolism, leading to aberrant conclusions.

The objective of this study was to determine the effect of phase of growth and varying glucose concentrations on ^{31}P metabolites of perfused DU 145 cells, a hormone-

resistant human prostate cancer cell line (Stone et al., 1978). The results of these studies were compared to the ^{31}P metabolite profiles observed using a surface coil and the same cell line grown in nude mice (xenografts), now defined as *in vivo*. These studies reveal that significant changes in ^{31}P metabolites of perfused cells occur with varying phase of growth and substrate glucose concentration. Determining experimental parameters for cell perfusion studies that best reflect the *in vivo* situation may be important for future comparisons between these two model systems.

MATERIALS AND METHODS

DU145 Cell Perfusion Studies: The DU 145 cell line at passage 48 was obtained from the American Type Culture Collection (Rockville, MD). Cells were grown in Falcon T-150 flasks at 37°C in an environment of 93% air and 7% CO_2. The cells were grown with Dulbecco's modified Eagle's medium (DMEM) supplemented with 10% fetal bovine calf serum, 25 mM glucose, 4 mM glutamine, 5 μg/ml transferrin and 100 unit/ml of penicillin and streptomycin. Depending on treatment, cells were grown to 100% or 50-75% confluency, harvested with PET solution (0.25% trypsin, 0.8% NaCl and 0.02% EDTA) and washed twice with phosphate buffered saline (PBS). Cells for low glucose treatment were passed 1:2 and grown in 5.5 mM glucose during the last passage and harvested at 50-75 % confluency.

Alginate beads (ca 3 mm) were made according to Narayan et al. (Narayan et al., 1990). All perfusion studies were conducted using $3x10^8$-10^9 cells encapsulated in a total volume of 7 ml of beads, and perfused with phosphate-free medium. Fully-relaxed ^{31}P spectra were obtained at 16 minute intervals for up to 12 hours in three groups of DU 145 cells; (1) grown in 25 mM glucose and harvested at 100% confluency (N=5), (2) grown in 25 mM glucose and harvested in log phase of growth (N=3), and (3) grown in 5 mM glucose and harvested in log phase of growth (N=3). The beads were placed into a

custom-built perfusion apparatus consisting of a 50 ml polycarbonate centrifuge tube fitted with teflon shims (mesh opening: 1 mm) used to position the cells reproducibly between experiments. A resealable septum with inserted inlet and outlet ports sealed the centrifuge tube. The perfusion apparatus was autoclaved before each experiment. The cells were perfused with oxygen-saturated phosphate free DMEM supplemented with 25 mM HEPES containing the glucose at the same concentration provided during growth. The cells were perfused at a rate of 8 ml/min using a variable speed drive Masterflex pump (Cole Parmer, Chicago, ILL.) and teflon tubing (0.042" x 0.006") which connected the sealed cells with the perfusate reservoir. The temperature was maintained at 35°C ± 0.5°C. The tube containing perfused cells was placed inside a custom-built NMR probe consisting of a 2.9 [o.d.] x 2.5 cm 3-turn solenoid connected to a balance-matched, double-tuned (^{1}H, ^{31}P) circuit (Chang et al., 1987a).

All spectroscopic experiments were performed using a Nalorac Cryogenic Corporation (NCC) Quest 4300 NMR imaging spectrometer connected to a horizontal, 22.5 cm usable bore, 4.7 Tesla Oxford magnet operating at the phosphorus resonance frequency of 81 MHz. The magnetic field homogeneity was optimized by shimming the water proton signal until a line width of 6 - 8 Hz was obtained. Fully relaxed ^{31}P spectra were obtained using a 1-pulse sequence from 80 transients with a 35 μs in-plane 45° flip angle, ±3125 Hz spectral width, 8192 data points and a pulse repetition time (TR) of 12 seconds yielding, a total acquisition time of 16 minutes. Spectra were processed with 4-8 Hz Gaussian apodization prior to Fourier transformation to improve signal-to-noise.

Nude Mouse Xenograft Studies: Cells were harvested, centrifuged, and the pellet containing cells ($5x10^6$ cells) were resuspended in a minimal volume of cell culture medium (1 ml). The cells were injected subcutaneously ($5x10^6$ cells) in the flanks of athymic male BALB/C "Nu/Nu" mice (age≈3 weeks) obtained from Simonson Laboratories Inc. (Gilroy, CA). Tumor volume, assuming an ellipsoid shape, was

calculated as V=(axbxc)π/6 where a, b and c are the three largest perpendicular diameters. *In vivo* ^{31}P NMR spectra were obtained from 0.9 ± 0.4 cc tumors (2-5 weeks after injection), using a 1 cm inner-diameter 2-turn surface coil connected to a balance-matched double-tuned (^{1}H, ^{31}P) circuit (Chang et al., 1987a) The coil was positioned on top of the tumor and a copper Faraday shield was placed around the tumor. The tumor was positioned at the isocenter of the magnet and shimmed until a water line width of <20 Hz was obtained. Partially saturated ^{31}P spectra were obtained with a 1-pulse sequence using 900 to 1,200 transients with a 6 - 10 µsec in-plane 90° flip angle, ±3125 Hz sweep width, 8192 data points, and a pulse TR of 3 seconds, yielding a total acquisition time of 45 - 60 min. Fully relaxed spectra (TR = 12 s) were used to estimate saturation factors (fully relaxed to saturated peak area) of the xenograft ^{31}P metabolites. Relative metabolite areas obtained *in vivo* were corrected using saturation factors in comparison with perfused cell results.

Data Analysis: The ^{31}P chemical shifts were recorded relative to PCr at -2.89 ppm (at pH 7.2) (Barany and Glonek, 1984) using α-NTP (-10.4 ppm) as an internal reference, because PCr levels were consistantly low and α-NTP has been previously shown to be insensitive to changes in pH (Shine et al., 1987). Identification was performed in our laboratory (Kurhanewicz et al., 1992) on a 300 MHz high-resolution NMR spectrometer by the addition of known compounds at various pH values to DU 145 xenograft perchloric acid extracts. Spectra were fit using a curve analysis-deconvolution program obtained from Nalorac Cryogenic Corp. This program permits analysis of a spectrum containing overlapping peaks and provides chemical shifts, widths, peak heights and areas of individual peaks. Parameters of computer-generated signals of Gaussian shape were adjusted until coincident with the experimental spectra. Relative metabolite concentrations are reported as ratios of metabolite areas relative to ß-NTP or as percentage of total NMR visible phosphorus and are expressed as mean ± standard error

of the mean (S.E.M.). Intracellular pH was determined using the chemical shift of inorganic phosphate (P_i) relative to PCr as previously described by Seo et al. (Seo et al., 1983):

$$pH = pK + \log[(\delta - \delta^{+})/(\delta - \delta^{0})]$$

where δ is the actual chemical shift of phosphate, δ^{+} is the concentration-weighted chemical shift of $H_2PO_4^-$, and δ^{0} is the concentration-weighted chemical shift of HPO_4^{2-}.

RESULTS AND DISCUSSION

Figure 1 shows a comparison between representative *in vivo* ^{31}P NMR spectra of a DU 145 xenograft (Fig. 1A) and perfused DU 145 cells (grown in a low glucose medium) in log phase(Fig. 1B). A comparison of Figure 1A and 1B demonstrates that the spectral resolution obtained in perfused cell studies is superior to that obtained *in vivo*. This resolution allowed the identification of the individual metabolites constituting the PME and PDE regions in the ^{31}P NMR spectrum of perfused DU 145 cells. A graphic comparison of the relative metabolite concentrations for DU 145 cells grown in nude mice (N=12) and perfused cells (5.5 mM glucose, log phase, N=3) is shown in Figure 2. Since time requirements necessitated the collection of partially saturated *in vivo* spectra, *in vivo* peak areas were corrected for differential metabolite saturation as described in the methods section. ^{31}P spectra of perfused DU 145 cells and *in vivo* nude mouse xenografts were similar with respect to their relative levels of PME, NTP and DPDE.

Similar to the ^{31}P spectra of other human tumors (Daly and Cohen, 1989), relatively high levels of PME and PDE were manifest in DU 145 perfused cell and xenograft spectra (Fig. 2). The phosphomonoester (PME) region was seen to be composed of approximately equal amounts of two resonances having chemical shifts

UCSF LIBRARY

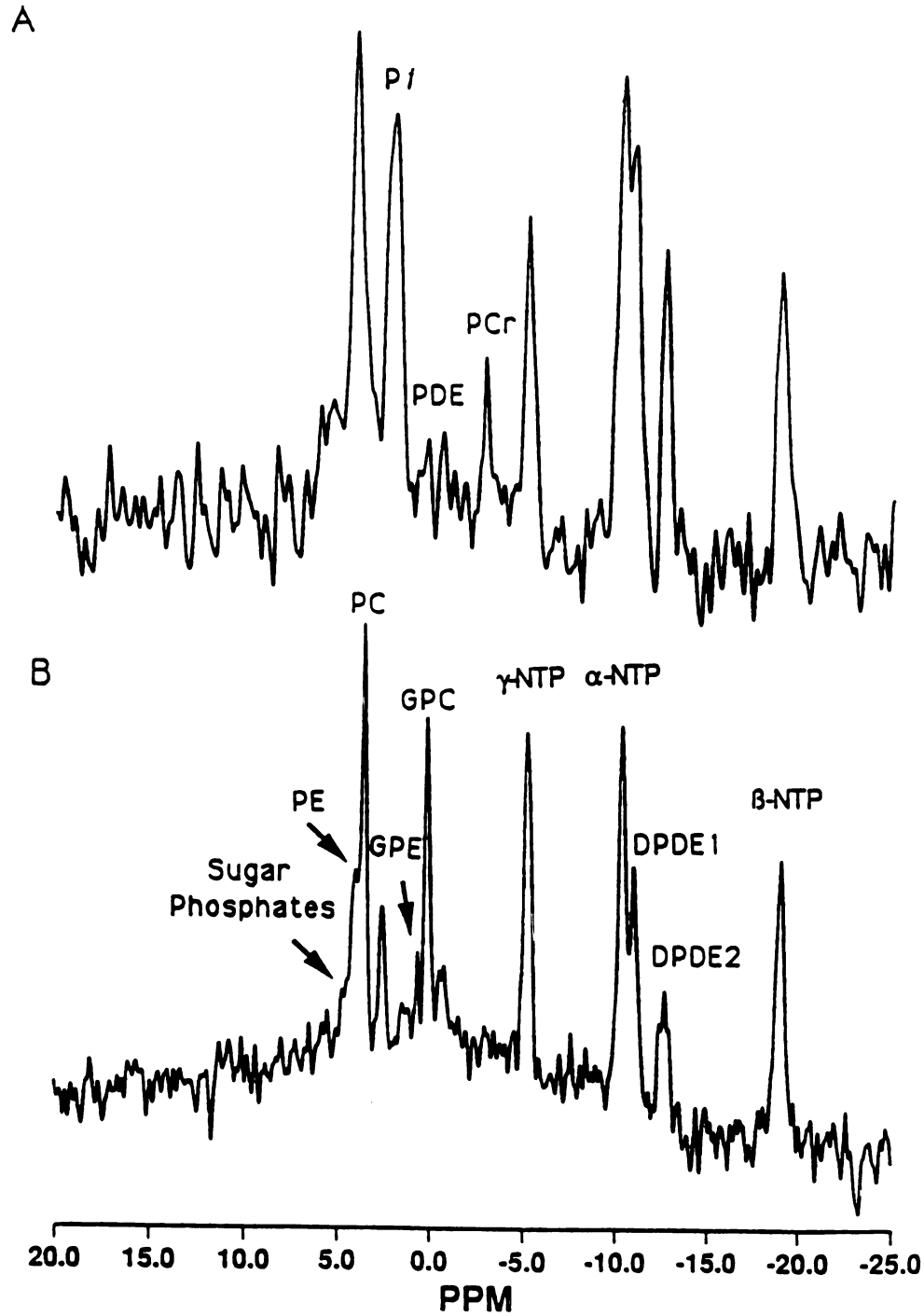

UCSF LIBRARY

Figure 1: Representative 81 MHz ^{31}P spectra of nude mouse xenograft of DU 145 (A) and perfused DU 145 cells grown in 5.5 mM glucose and harvested at log phase of growth (B). Large spectral peaks are attributed to PME (3.5-4.5 ppm), inorganic phosphate, P*i* (2.29 ppm), diphosphodiesters DPDE1 (-11.17 ppm) and DPDE2 (-13.14 ppm), and smaller peaks are due to phosphodiesters PDE1 (-0.6 to 1.5 ppm) and PCr (-2.89 ppm) relative to γ-, α- and β-ATP (-5.37, -10.47 and -19.14 ppm, respectively). Spectra were referenced to α-NTP at -10.4 ppm. See the Methods section for details on perfusion and spectroscopic procedures and Results and Discussion section for abbreviations.

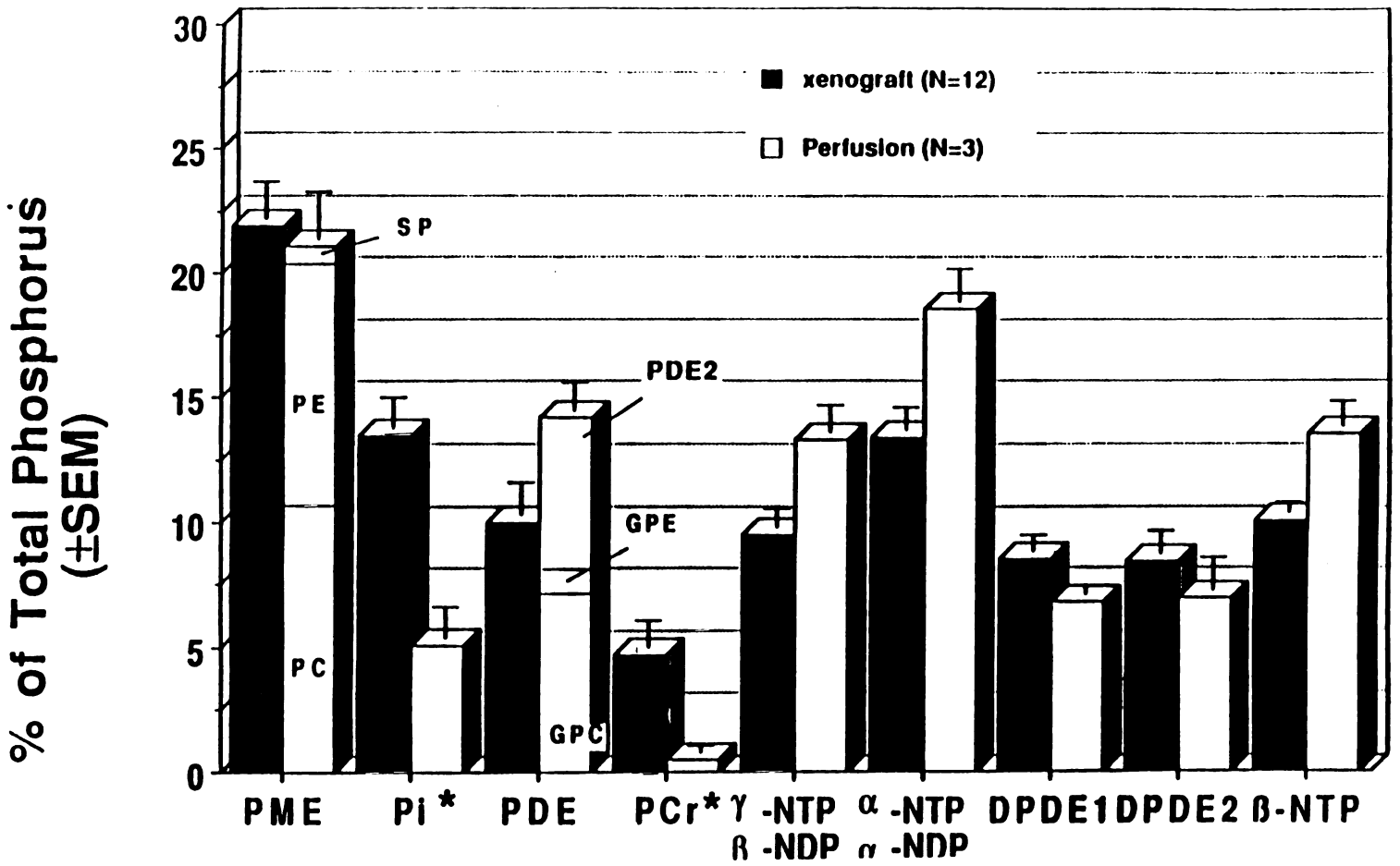

Figure 2: Bar graph comparing ^{31}P metabolites expressed as the percent of the total ^{31}P peak area. ^{31}P metabolites that are followed by "*" are significantly different using the Mann-Whitney U-test ($p<0.05$).

similar to phosphorylethanolamine (PE; 3.90 ppm) and phosphorylcholine (PC; 3.44 ppm). One of the major drawbacks of perfused cell studies is the inability to extract phosphate metabolites from alginate beads, probably due to their precipitation with Ca^{+2} or adsorption to the polysaccharide matrix. This made it impossible to directly identify perfused cell ^{31}P metabolites by analysis of the corresponding extract. However, studies performed in our laboratory on DU 145 xenograft extracts revealed that the PME resonance was also composed of equal amounts PE and PC (Kurhanewicz et al., 1992). PC and PE are intermediates in phospholipid metabolism (Daly and Cohen, 1989)and may have additional biochemical importance as neuromodulators (Bradler et al., 1991). A relatively smaller resonance was observed for sugar phosphates (SP, 4.49 ppm) in both DU 145 perfused cells and xenografts.

The phosphodiester (PDE) region of the spectrum consisted primarily of the phospholipid intermediates, glycerophosphocholine (GPC) at 0.05 ppm, with minor contributions from glycerophosphoethanolamine (GPE) at 0.69 ppm. The GPC resonance was consistently higher in perfused cell spectra compared to xenograft spectra, although the total PDE peak area was not found to be significantly different between the two systems. There was also a broad component (PDE2) in perfused cell spectra having noticeable fine structure resonating at -0.60 ppm. The PDE2 resonance needs further study for identification, but a similar resonance in cell and tissue extracts has been suggested to be due to phospholipids (Guidoni et al., 1987), RNA fragments (Askenasy et al., 1990; Guidoni et al., 1987), and saccharide phosphodiester (Barany and Glonek, 1984).

DU 145 perfused cells and xenografts consistently displayed high levels of diphosphodiesters (DPDE's). This is in contrast to that reported in ^{31}P NMR spectra of another human metastatic prostate tumor cell line, PC3 (Narayan et al., 1990). It has been recently shown that accumulation of DPDE phospholipid intermediates, CDP-choline and CDP-ethanolamine, do not occur in MDA-MB-231 human breast cancer

cells, yet these cells display high levels of PC and PE precursors (Daly et al., 1990). It is believed that formation of CDP-choline and CDP-ethanolamine via cytidylyltransferase enzymes is the rate-limiting step in phospholipid metabolism, and once formed, they are rapidly metabolized by phosphotransferases (Daly et al., 1990). CDP-choline is at concentrations of 0.006-0.3 mM in the cell (Pelech and Vance, 1984), well below detection limits of NMR, and therefore probably does not contribute to the DPDE signal in perfused DU 145 cells or *in vivo* DU 145 xenografts.

Several significant differences between the relative metabolite levels of perfused cells and xenografts were also observed (Fig. 2). Inorganic phosphate and PCr levels were found to be significantly ($p<0.05$) higher in DU 145 cells grown in nude mice, while the pH was lower (7.20 ± 0.06 versus 7.43 ± 0.07). Previous studies have shown that the absence of P*i* in the perfusion medium did not affect the concentration of intracellular phosphates (Neeman et al., 1987), or cell viability (Narayan et al., 1990). Alternatively, Evanochko et al. (Evanochko et al., 1984) have suggested that the higher P*i* and lower pH in nude mice xenografts relative to perfused cells reflects the tendency for xenografts to out-strip their blood supply and begin deriving their energy from anaerobic glycolysis. Increased P*i* may also be due to areas of secretory cysts which appear in nude mice xenografts of DU 145 cells (Kurhanewicz et al., 1992). Higher PCr levels in xenografts are most likely due to contamination from surrounding muscle. This explanation is supported by the heterogeneous appearance of the PCr resonance in *in vivo* DU 145 xenograft spectra indicating contributions from PCr in slightly different environments.

There was no significant change in metabolite ratios, pH, and signal-to-noise ratio noted in the 12-hour period that the cells were monitored. Similar metabolic stability was previously observed for three other mammalian cell lines encapsulated in alginate gels (Narayan et al., 1990). There were, however, a number of temporal changes in the steady state ^{31}P metabolite concentrations of perfused DU 145 cells. We found that the levels of PC and PE fluctuated, with one increasing as the other decreased, and these fluctuations

cycled every hour. Similarly, there were fluctuations in GPE and GPC levels, but these fluctuations were not as predictable. Fluctuations in these phospholipid intermediates could be due to phospholipid membrane turnover (Daly and Cohen, 1989); however, further studies are needed to confirm this hypothesis. PCr levels were quite variable from day to day and also showed small fluctuations during the 12-hour observation period. As previously reported, small differences in environmental factors such as alginate bead preparation, perfusion rate and temperature could account for the observed differences in PCr (Neeman and Degani, 1989). All other ^{31}P metabolites remained relatively constant during 12 hours of observation.

Figure 3 exhibits ^{31}P spectra that illustrate the effects of different phases of growth and glucose concentrations in the culture medium on the ^{31}P metabolite profile of DU 145 perfused cells. DPDE's are significantly higher with increased glucose concentration and confluency (Table 1). This could be due to differences in glucose availability and/or differences in glycolysis rate between experimental conditions. Increased DPDE levels have been observed in murine neuroblastoma clonal lines (N-18 and C-46) (Pettegrew et al., 1979) and human colon adenocarcinoma cells (HT-29) (Fantini et al., 1987) grown in high glucose medium at confluency. The DPDE resonances observed DU 145 nude mouse xenografts have been shown by HPLC and high resolution NMR in prior studies in our laboratory (Kurhanewicz et al., 1992) to consist mainly of uridine-5'-diphospho-N-acetylgalactosamine (UDP-NAcGal) and uridine-5'-diphospho-N-acetylglucosamine (UDP-NAcGlc). Similar results have been reported by Fantini et al. in HT-29 cells (Fantini et al., 1987). The accumulation of UDP-NAcGal and UDP-NAcGlc in HT-29 cells has been associated with the inability of these cells to differentiate (Galons et al., 1989; Wice et al., 1985). Furthermore, growth of HT-29 cells in sugar-free medium was found to induce enterocytic differentiation (Zweibaum et al., 1985). The mechanism by which the accumulation of UDP-NAcGlc and UDP-NAcGal is involved in the inability of cancer cells to differentiate is still obscure. Ogier

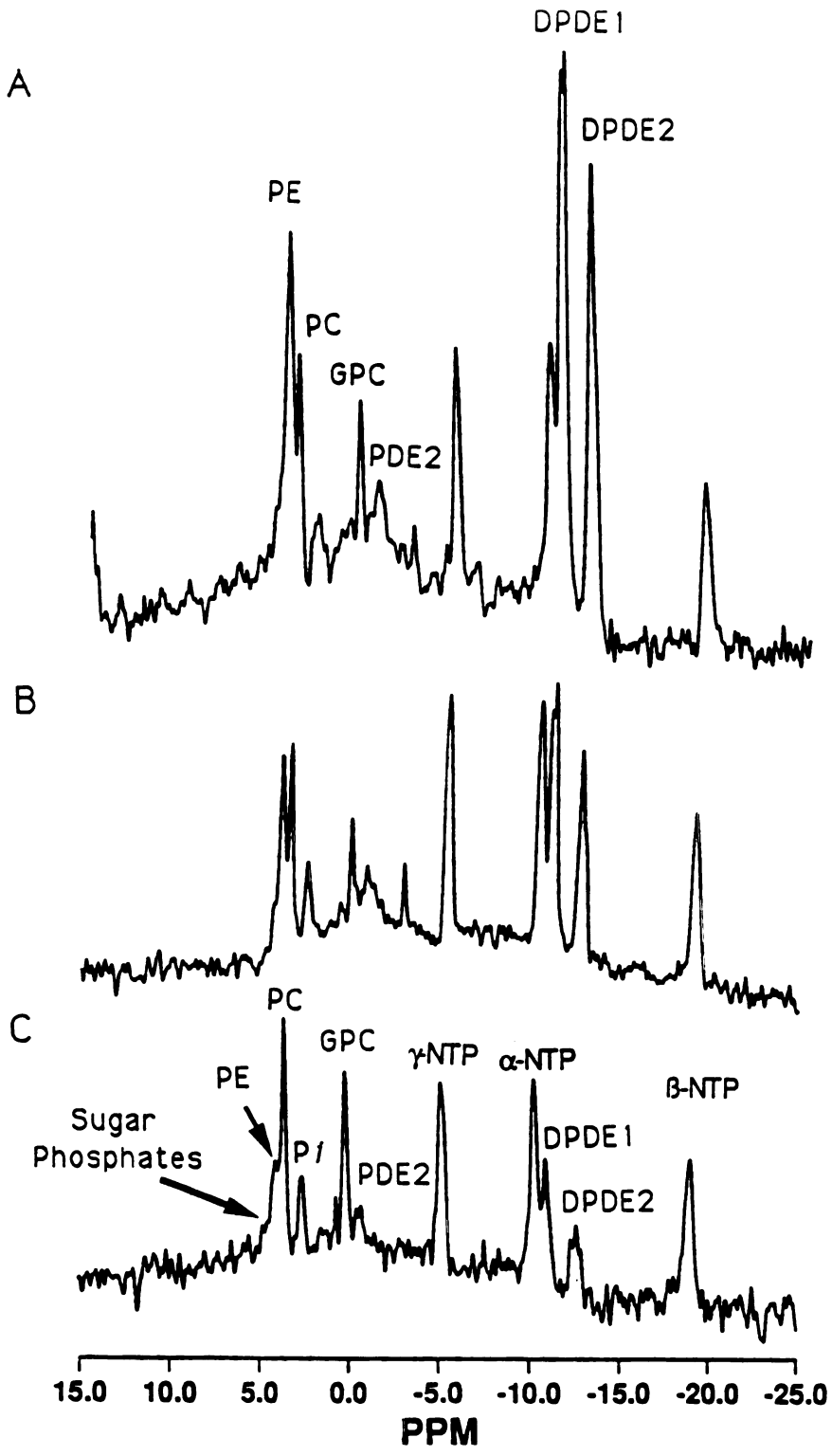

Figure 3: Representative 81 MHz ^{31}P NMR spectra of DU 145 cells grown in 25 mM glucose and harvested at confluency (A); 25 mM glucose and harvested at log phase (B); 5.5 mM glucose and harvested at log phase (C).

EXPERIMENTAL CONDITIONS			^{31}P METABOLITES/ß-NTP (x 100)					
#	Glucose (mM)	Growth Phase	DPDE1[a]	DPDE2	GPC	GPE	PC	PE
1	25	confluent	213 ± 41*	212 ± 42**	43 ± 4	12 ± 9	62 ± 10	44 ± 12
2	25	log	96 ± 17*	81 ± 10	35 ± 8*	8 ± 6	76 ± 4	76 ± 11
3	5.5	log	51 ± 4	50 ± 7	74 ± 15	17 ± 8	74 ± 5	73 ± 23

[a] Results are expressed as mean ± SEM of 3-5 separate experiments.
* Significantly different from 5.5 mM glucose, log phase ($p<0.05$) using the Mann-Whitney U-test.
** Significantly different from 25 & 5.5 mM glucose, log phase ($p<0.05$) using the Mann-Whitney U-test.

Table 1: Comparison of ^{31}P metabolite levels under three different experimental conditions: (1) 25 mM glucose and confluency (n=5); (2) 25 mM glucose and log phase (n=3); and (3) 5.5 mM glucose and log phase (n=3). ^{31}P metabolites were considered significantly different at $p<0.05$ using the Mann-Whitney U-test.

USDE LIBRARY

et al. (Ogier-Denis, 1988) have suggested that N-linked glycosylation is correlated with the state of enterocytic differentiation in HT-29 cells. Further studies are necessary to determine the relationship between DPDEs and differentiation in DU 145 cells.

This study has demonstrated that high resolution spectra of perfused human adenocarcinoma cells can be obtained in kinetically short periods of time (16 minutes). The ^{31}P metabolites of perfused DU 145 cells grown in low glucose medium and harvested at log phase growth were very similar to those growing in athymic nude mice. Additionally, we demonstrated that the stage of growth and glucose concentration affects DPDE levels in DU 145 perfused cells. Lower DPDE levels have been correlated with multi-drug resistant cells (Kaplan, 1990a; Kaplan, 1990b), and increased DPDE levels have been correlated with the degree of differentiation of tumor cells (Galons et al., 1989; Wice et al., 1985). Therefore, the determination of metabolic changes associated with experimental parameters, such as, substrate availability and growth phase, is important for interpretation of future therapeutic studies on these cells.

NMR spectroscopy studies of perfused cells can be a powerful tool for elucidating the biochemical mechanisms of differentiation and cancer chemotherapy because one can control immune, endocrine, inter-organ responses, and contamination from surrounding tissues associated with *in vivo* studies. However, cells do not grow in this encapsulation model and we do not know how the isolation and encapsulation process effects tumor cell biochemistry. Even though cultured tumor cells are extremely resilient, some of the more sensitive cells in the population, such as those in the midst of cell division, may have died, and oxygen has been shown to be limiting in encapsulation methods. Therefore, it is difficult to conclude that the cell population is representative and that physico-chemical parameters are controlled. However, the spectra are similar to those generated from *in vivo* xenograft under hypoxic conditions, and therefore, could mimic tumor biochemistry. Since normal tissues do not encounter hypoxic environments as tumor generally do, this model is certainly not optimum for normal tissue metabolism.

APPLICATION OF A NOVEL AIRLIFT BIOREACTOR

Introduction: An airlift bioreactor, illustrated in Figure 4, was used to test the feasibility of using a NMR-compatible cell suspension method for the study of anchorage-dependent cells, isolated intestinal cells. This design is a modification of a previously published NMR-compatible airlift bioreactor design used for high resolution NMR spectrometers (Santos and Turner, 1986). It circulates and aerates cells by bubbling a gas of desired composition through a small tube centered inside a larger tube. A convective current is formed inside the bioreactor that circulates cells. As the bubbles rise they expand, creating a suction at the bottom of the inner and bringing cells from the bottom of the outer tube to the top. The gas serves two functions: one to recirculate cells and the other is to aerate the medium.

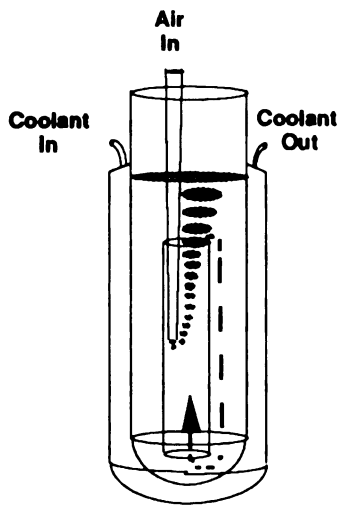

Figure 4:: Airlift bioreactor used for the *in vivo* ^{13}C NMR studies of isolated rat intestinal cells. The dashed arrows shows the direction of convective flow within the bioreactor chamber.

Intestinal cells are highly differentiated epithelial cells that line the gastrointestinal tract. They function to transport nutrients from the gastrointestinal lumen to the blood stream, and secrete mucous to aid in digestion. Studies of the small intestine have shown that glutamine primarily utilized in the fed state and ketone bodies in the

starved state (Fleming et al., 1990). We used a homebuilt NMR-compatible airlift bioreactor to monitor primary metabolism of 2-^{13}C-glucose by ^{13}C NMR spectroscopy. Intestinal cells are very difficult to maintain after isolation and are viable for only 3 hours, as determined by lactate dehydrogenase (LDH) activity in the surrounding media (Fleming et al., 1990).

Methods: Male Sprague-Dawley rats (Bantin and Kingman, Fremont, CA) weighing 235-280 g were maintained on nonpurified commercial rat diet (Ralston Purina, St. Louis, MO) and water on an *ad libitum* basis. On the day of experimentation, fed rats were anesthetized using pentobarbital, and killed by heart puncture. Jejunal cells were taken from a 20-cm length of intestine commencing 10 cm from the pylorus. Cecal cells were taken from the cecum, which was excised 1 cm proximal to the ileocecal valve and the cecocolonic junction. Colonic cells were taken from the large intestine, which was excised at the cecocolonic junction and at the distal end of the anal canal. All aspects of animal handling were approved by the Animal Care and Use Committee, University of California, Berkeley and San Francisco.

Generally, methodologies previously applied to the large intestine and described by others (Roediger and Truelove, 1979) were followed. All solutions were made with double-distilled and deionized water. All glassware that directly contacted cells was siliconized. Saline solutions were modified from Krebs-Henseleit physiological saline for most procedures. A bicarbonate-free buffer system was used for the final rinse of cells when preparing the incubation media for experiments in which oxygen utilization was quantified to avoid pH changes during incubation. Cells were removed using a combination of chemical (EDTA) and mechanical (stirring with plastic pipettes) techniques; care was taken to minimize cellular damage.

Viability of cells was tested using trypan blue, to which nonviable cells are permeable. Viability was calculated as the percentage of the total cell population that

excluded the trypan blue stain, using an American Optical hemocytometer (VWR Scientific, San Francisco, CA). No significant change in viability was noted during 60 min of incubation.

The airlift bioreactor is illustrated in Figure 4. After isolation intestinal cells were placed in the chamber of the bioreactor, silicone antifroth gel (Sigma Chem Co.) was rubbed around the mouth of the bioreactor to inhibit frothing caused by the albumin, and the bubble rate was set such that the bubble size nearly covered the mouth of the inner tube when it reached the top. Cells were placed in 20 mL of media monitored for 5 hours after introduction. The temperature of the medium was checked after the experiment.

Results and Discussion: The bioreactor shown in Figure 4 is modified from that used in the experiment by including a coolant chamber to maintain temperature changes caused by decoupling. Cells circulate in a convective fashion as shown in Figure 4. Figure 5A shows a ^{13}C spectrum 20 min after the addition of 2-^{13}C-glucose, illustrating the anapluerotic product, glutamine, formed from the TCA cycle. This product is thought to be the intestinal cells' energy source in the fed state represented in this experiment since glucose is present. Cells remained viable in this bioreactor for 2 hr as determined by LDH activity in the media. However, ^{13}C NMR spectra revealed that cell metabolism was relying on anaerobic glycolysis by 60 min as evidenced by the increase in lactate and alanine (Fig. 5B). Figure 5C is the ^{13}C spectrum after 2 hr post-glucose administration. A graph of the various metabolites found in the spectra of Figure 5 are shown in Figure 6. This graph illustrates that aerobic metabolism decreases 20 min after administration of glucose, and the anaerobic glycolytic products, lactate and alanine increase. This demonstrates that *in vivo* ^{13}C NMR provides a more sensitive technique to measure stress that conventional enzyme assay methods, which manifest only after cell death.

It is clear from these studies that the intestinal cells cannot be maintained in a viable condition. One explanation may be that the suspension technique for maintaining

UCSF LIBRARY

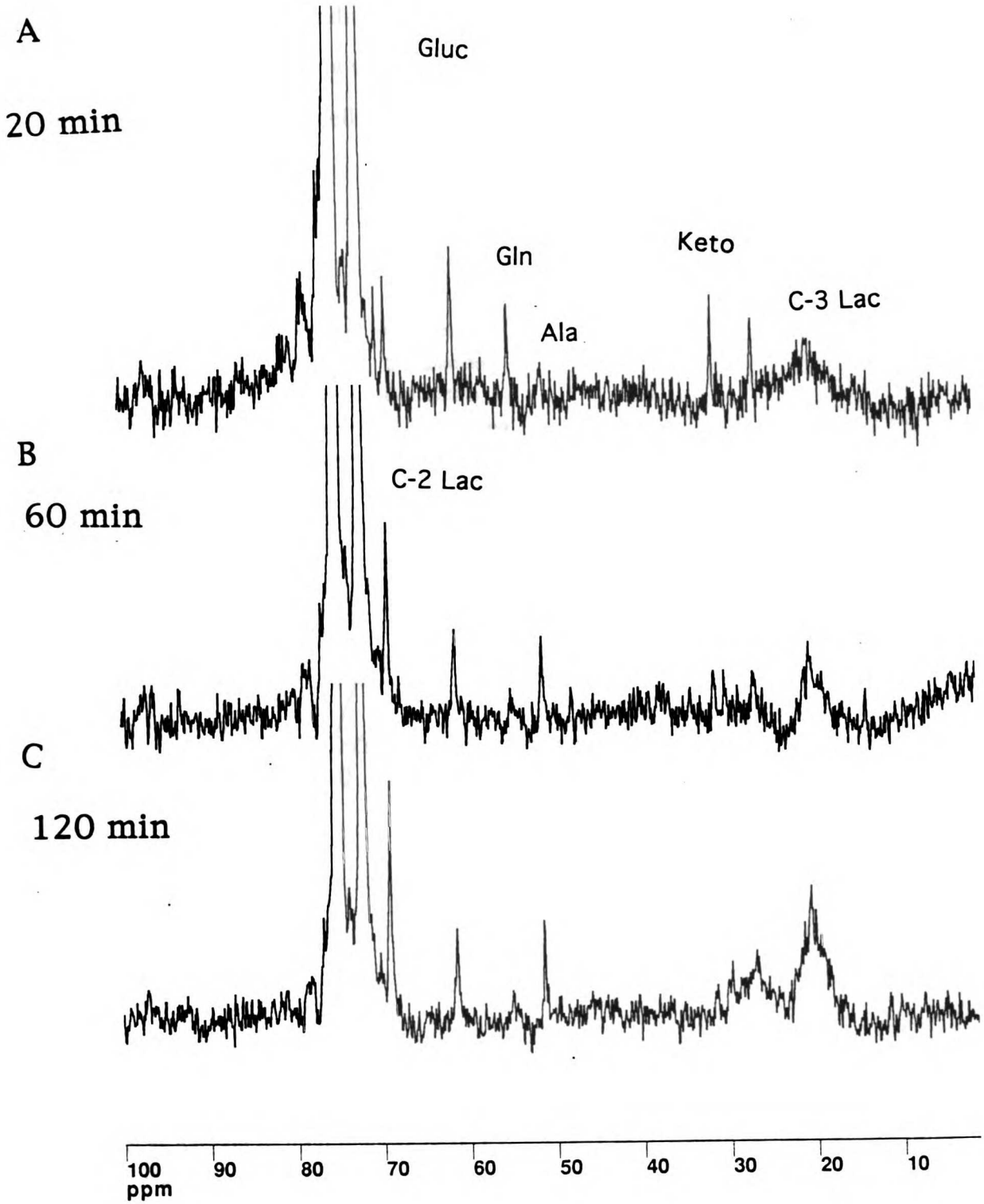

UCSF LIBRARY

Figure 5: *In vivo* ^{13}C NMR spectra of suspended rat intestinal cells at 20 (A), 60 (B), and 120 (C) min after administration of 2-^{13}C-glucose. One-pulse with decoupling during acquisition was used for A and B. SW=6666 Hz; TR=1 s; CB=4K; and acquisition=150 yielding a spectrum every 10 min. Abbreviations: Gluc, glucose; Gln, glutamine; Ala, alanine; Lac, lactate; Keto, α–ketoglutamate.

anchorage-dependent mammalian cells causes aggregation and lysis (Gillies et al., 1986). Intestinal cells are particularly sensitive mammalian cells and secrete enormous amounts of mucous which increases cell aggregation and viscosity, and further decreases oxygen diffusion to cells.

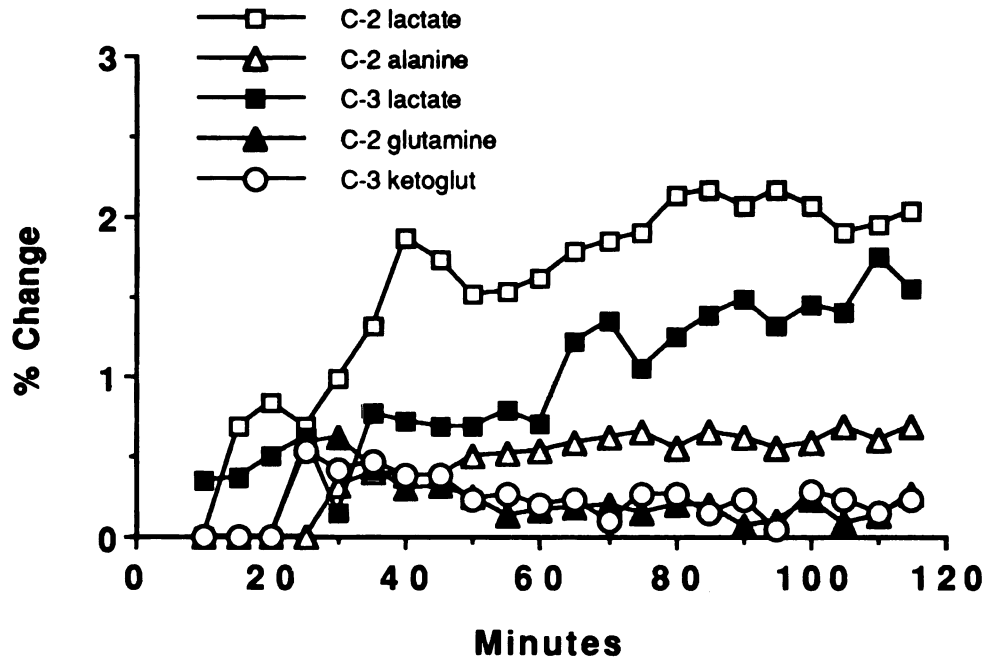

UCSF LIBRARY

Figure 6: A graph of the *in vivo* ^{13}C NMR spectra shown in Figure 5. Metabolites are expressed as percent of total glucose peak area. The ^{3}C-labeled compounds are define in the graph legend

Additionally, the temperature steadily increased during the course of this experiment (25°C to 38°C) due to the heat generated by proton decoupling (TR = 1.5 s), thus the T_1

increased for glucose which was used as an internal quantitative reference, biasing the slopes negatively for glucose and positively for metabolites. Our new water-jacketed design shown in Figure 4 will control the temperature cause by decoupling.

Conclusion: The airlift bioreactor equipped with a cooling system may work well for non-anchorage-dependent cells and parasites as others have found (Santos and Turner, 1986), but effects viability for anchorage-dependent cells as demonstrated for intestinal cells. The decrease in viability associated with suspension NMR-compatible bioreactors was found with kidney proximal tubule cells (Boulanger and Vinay, 1989) and is attributed to mechanical lysis of the cell membrane (Gillies et al., 1986). The encapsulation method is sufficient for short-term studies of cultured cells but, due to the non-physiological matrix and incomplete nutrient perfusion into the matrix, cannot maintain long-term cultures. Freshly isolated cells are more sensitive to the preparation conditions. The first membrane-type NMR-compatible cell perfusion system of isolated cell preparation was with renal proximal tubules and viability was maintained for at least 16 hr but not cellular function (Boulanger et al., 1985). A suspension/membrane hybid bioreactor was constructed that maintained cellular function, but there was significant mortality caused by cell lysis (Boulanger et al., 1988). Although we tested this bioreactor with one of the most sensitive anchorage-dependent cell types, we found viability and function was not maintained. We conclude that air lift bioreactors would be a very good tool for toxicological studies of non-anchorage-dependent cells (i.e., bacteria, unicellular plants) or parasites where mechanical agitation does not effect the viability of cells, and in fact is necessary. The hollow-fiber bioreactor has heterogeneous perfusion between the fiber bundle and housing making this bioreactor unfit for use with isolated cells preparations. Therefore, a better membrane-type NMR-compatible cell perfusion system is needed to permit sufficient perfusion of all cells axially and radially within the bioreactor.

UCSF LIBRARY

CHAPTER 4

Comparison of Two Novel NMR-Compatible Bioreactor Prototypes for Multinuclear NMR Spectroscopy and MRI of Perfused Isolated Rat Hepatocytes

UCSF LIBRARY

INTRODUCTION

An NMR investigation of cells permits the control of cell composition, immune and endocrine effects, inter-organ nutrient transport, and physico-chemical parameters not afforded in intact animal or perfused organ systems (for reviews see Egan, 1987; Gillies et al., 1986; Kaplan, 1992; Ruiz-Cabello and Cohen, 1993; Szwergold, 1992). Consequently, it is surprising that the fields of pharmacology and toxicology have not yet accepted this non-invasive technique (Kaplan, 1992). The present NMR techniques available for cell perfusion utilize suspension, entrapment, microcarriers, spheroids, and membranes (Szwergold, 1992). Cell suspension techniques have enjoyed the most diverse modifications, from bubbling the cell suspension (Navon, 1977) to an air-driven stirrer in combination with hyperbaric oxygenation (Balaban et al., 1981), to air-lift bioreactors (Lyngstad and Grasdalen, 1993; Santos and Turner, 1986). Studies have focused predominantly on cultured cells using entrapment and suspension techniques for short-term studies, and microcarriers such as beads or spheroids, and membrane techniques for long-term growth studies. Of these five cell perfusion techniques, the membrane-type NMR-compatible hollow-fiber bioreactors has permitted the longest duration of three-dimensional cell culture of many anchorage-dependent mammalian tissue-types (Hrovat et al., 1985;Gillies et al., 1991). Cultured cells attach and multiply within the fiber bundle of hollow-fiber bioreactors, but the majority of inoculated cells fall between the fiber bundle and the reactor housing. For long-term cultures this is not a

problem, but for short-term analysis of primary cells this results in a heterogeneously perfused cell mass, causing insufficient oxygenation - the primary limiting nutrient in cell perfusion systems (Gillies et al., 1991). Compared to cultured cells, few studies of isolated cell preparations have been reported.

Except for erythrocytes and lymphocytes, mammalian cells are anchorage-dependent, or need a suitable substrate in order to grow and exhibit normal biochemistry. Suspension and entrapment techniques have both been used for cell preparations, but cause cell lysis (Gillies et al., 1986) and selectively inhibit diffusion of nutrients or xenobiotics into the entrapment matrix (Farghali et al., 1992; Szwergold, 1992), respectively. The first NMR studies of tissue preparations using a membrane-type NMR-compatible bioreactor were in dialysis bags (Canioni et al., 1984) and in dialysis fibers of kidney proximal tubules (Bottomley, 1985). The bioreactor made of dialysis membranes was awkward, and does not achieve the optimum distance between cells and the nutrient source (i.e., 200 μm). The bioreactor made of dialysis fibers, where kidney proximal tubules reside inside the lumen of the fiber, did not maintain sufficient perfusion to maintain physiological function. The authors eventually developed a suspension-type bioreactor which maintained cell function but caused significant cell lysis after several hours (Ammann et al., 1989). A novel NMR-compatible membrane-type perfusion apparatus is needed to better control physico-chemical parameters while still maintaining a normal physiological environment which is essential when modeling *in situ* tissue for study of normal and stress biochemistry or development of artificial organs. The bioreactor needs a cell density that mimics *in vivo* conditions to maintain cell differentiation, sufficient perfusion to maintain cell function, and global cell density (the fraction of the NMR excitable volume filled with cells) to maximize NMR spectroscopic signal-to-noise. The goal of this study was to develop a cell model that can complement our animal model described in Part II, for use in xenobiotic studies. A membrane-type design for ultimate use with cell culture would permit reduction of animal use in

UCSF LIBRARY

toxicological research while simultaneously developing useful clinical artificial-liver technology.

Cell lines are usually dedifferentiated cells which are often derived from tumors. Primary cultures soon dedifferentiate; in particular, primary cultures of hepatocytes lose many of their metabolizing capabilities as soon as 12 hrs after isolation (Dunn et al., 1992; Lansford et al., 1989), due primarily to the still unknown aspects of extracellular matrix and cell-cell interactions (Dunn et al., 1992; Jauregui et al., 1986). There is strong political and ethical support to use cultured cells to replace animals and freshly isolated primary cells in order to reduce the massive number of animals used particularly in toxicological studies. Human cell lines are used as a model for studying hepatic effects of toxicants, such as Chang liver cells and HepG2. The Chang and HepG2 liver cells are derived from normal and hepatoma liver tissue, respectively, and depending on bioreactor design and serum composition, these cell lines are good models of normal hepatic metabolism (Hornhardt et al., 1994; Melkonian et al., 1994).

Normal hepatic function is generally defined in terms of enzyme activity, (i.e., P-450 or superoxide dismutase), protein synthetic activity (i.e., albumin secretion rate), primary metabolism (i.e., aerobic glycolysis or aerobic metabolism) and cell morphology (Shatford, 1992). *In vivo* NMR can non-invasively monitor primary metabolism as investigated by ^{31}P NMR, and can monitor enzyme kinetics by ^{13}C NMR permitting a comparison of normal function between cultured cells at various stages of growth and isolated primary cell preparations. Cultured cells generally depend more on anaerobic glycolysis, so ^{31}P NMR could be used to monitor phospholipid metabolism, diphosphodiester levels (an indicator of differentiation (Macdonald et al., 1993) bioenergetics, and pH. Using ^{13}C-labeled substrates, ^{13}C NMR can monitor *in vivo* enzyme activity, protein synthesis, anaerobic glycolysis activity, and other biochemical processes. This can be performed without disrupting the cell culture. Studies of isolated cells can be compared to *in vivo* animal studies in order to determine bioreactor efficacy

USF LIBRARY

in maintaining normal cell function. The primary flaw in present bioreactor designs is insufficient oxygen perfusion. Therefore, in this study we compared the *in vivo* ^{31}P NMR spectra of isolated rat hepatocytes to that of liver from intact rat as a determinant of the ability of a bioreactor to maintain normal function.

Isolated hepatocytes were the first isolated cell preparations to be monitored by NMR using the cell suspension technique (Cohen et al., 1978; Cohen et al., 1979). These studies were the first to demonstrate the pH difference between the mitochondria and cytosol using ^{31}P NMR (Cohen et al., 1978), and gluconeogenesis in hepatocytes using ^{13}C NMR (Cohen et al., 1979). Hepatocytes become hypoxic soon after entering suspension, and studies of hepatic 2-^{13}C-ethanol metabolism may have generated non-physiologically relevant data (Irving et al., 1985). Hepatocytes are very sensitive to environmental conditions, so a cell model has been difficult to develop, and thus many studies have used perfused liver (Cohen, 1991). Unlike the ideal cell model, perfused rat liver does not control for cell composition, intercellular communication, nor for physico-chemical parameters since perfusion rates are sometimes an order of magnitude greater than *in vivo* in order to deliver adequate oxygen. Elevated liver perfusion rates can increase extracellular pressure, generating regions of hypoxia, swelling, and affect normal cellular function. Encapsulation of hepatocytes in agarose threads (Farghali et al., 1992; Gasbarrini et al., 1992) was the first new technique used for isolated hepatocytes since Cohen et al., (1978) developed the cell-suspension method. Faraghala et al. (1992) monitored the effect of three toxicants on the *in vivo* ^{31}P NMR spectra over a period of 5 hrs. This technique was first developed by Foxall et al. (Foxall and Cohen, 1983) using cultured cells. It requires significant temperature changes and preparation prior to *in vivo* ^{31}P NMR analysis. PCA cell extraction is not possible, probably due to binding of endogenous phosphate metabolites to the encapsulation matrix (Macdonald et al., 1993). Additionally, ethanol diffusion into the agarose matrix may be inhibited, thus effecting dose-response curves (Farghali et al., 1992), and perhaps other xenobiotics will have a

USF LIBRARY

similar diffusion problem. Therefore, a better cell model is needed that eliminates the requirement for entrapment of cells in an artificial matrix which may effect physico-chemical parameters such as dose, and extended sample preparation prior to the *in vivo* ^{31}P NMR analysis. furthermore, a system that permits PCA cell extraction would be considerably advantageous.

Membrane-type NMR-compatible systems for isolated cells permits minimal preparation time prior to NMR analysis in conjunction with cell perfusion. One group (Boulanger et al., 1985) developed a membrane-type perfusion system for kidney proximal tubules. Proximal tubules from dog kidney were contained inside dialysis fibers while the extracapillary space was perfused at rates of 200 mL/min, permitting stable ^{31}P NMR spectra to be obtained for a period of 13 hrs. However, functional aspects of kidney proximal tubules were not observed due to lack of sufficient perfusion or stirring within the cell mass (Boulanger and Vinay, 1989). Eventually, this group developed a suspension-type bioreactor that was a combination of the technique of Balaban (1984) and dialysis fiber oxygenation to maintain kidney proximal tubule function, but it caused significant mortality due to mechanical lysis (Ammann et al., 1989).

There is presently no commercially available NMR-compatible bioreactor for cultured or isolated cells, which is surprising considering the extensive research performed in this area (Kaplan, 1992; Szwergold, 1992; Ruiz-Cabello and Cohen, 1993). Generally, researchers use encapsulation techniques because it is *ex situ* (i.e., trypsinize cells for short-term study) and thus quicker to perform experiments than *in situ* cell cultures (i.e., long-term cultures), materials are low-cost and commercially available, and it is an accepted method for short-term monitoring of cell metabolism (Szwergold, 1992). There is significant demand for a commercially available, NMR-compatible bioreactor which, if accepted, would standardize this field and permit direct comparison between various NMR studies of cells (Gillies et al., 1986). However, such a bioreactor would need to supply the cell mass by perfusion (e.g., movement of solutes from high to low

USF LIBRARY

pressure regions) rather than diffusion (e.g., movement of solutes by Brownian motion) if physiological function of cell isolates is to be maintained (Boulanger and Vinay, 1989).

Recently, a hollow-fiber bioreactor was adapted to serve as an artificial liver (Nyberg et al., 1992), but it has not been used for NMR studies. Central to the success of this bioartificial liver was development of a "functionally" three-compartment bioreactor made from a physically two-compartment hollow-fiber bioreactor (Shatford, 1992). This is accomplished by inoculating hepatocytes mixed with collagen inside a dialysis fiber. The collagen shrinks, permitting perfusion inside and outside of the dialysis fiber.

A commercially available bioreactor was also recently developed (Setec Inc, Livermore, CA). The design of this apparatus provides many advantages for potential application to NMR studies. It is called "tricentric™" because it is composed of coaxial fibers (a smaller fiber within a larger fiber) comprising the fiber pair, and contains three physically distinct compartments: (1) extra capillary compartment (ECC) - the space around the outside of the fiber pairs, (2) annular - the space between fibers, and (3) inter capillary compartment (ICC) - the space on the inside fibers. This design was first proposed by Robertson and Kim (Robertson and Kim, 1985) for growth of tetracycline-producing bacteria and used an inner silicone fiber coaxial to a macroporous polypropylene fiber. The tricentric™ bioreactor has been used only with anchorage-dependent cell cultures but not isolated primary cell (Jim Robinson, President, Setec Inc., personal communication). Custer (1988) has compared the hollow-fiber bioreactor and the tricentric™ bioreactor of a hybridoma cell-line, AB2-143.2, that produces an IgG2a antibody against benzene arsenate, and found superior antibody production per unit glucose with the tricentric™ bioreactor (a 4-fold increase). This can be attributed to the more efficient nutrient mass transfer to the entire cell culture by the tricentric™ bioreactor due to a better diffusion distance (e.g., the maximal distance of cells from the perfusion source), and perhaps perfusion of cell mass due to radial flow. For example, in hollow-fiber bioreactors used by Gillies (1993) but initially developed by Hrovat et al.

USF LIBRARY

(1985), fiber spacing is often not optimal and cells on the edge of the fiber bundle divert the majority of their resources to growth, whereas cells grown in the tricentric™ bioreactor use their resources for function, such as antibody synthesis in the case of hybridomas (Custer, 1988).

The tricentric™ bioreactor design is ideal for isolated rat hepatocytes because of its small volume and architecture which parallels the liver unit, ascinus. For example, the ascinus is composed of a triad with the portal vein, hepatic artery, and bile duct running perpendicular to the hepatic vein (Fig. 1A). The hepatic artery accounts for 20% of the blood flow and supplies nutrients, in particular oxygen; the portal vein accounts for 80% of blood flow and facilitates exposure to absorbed nutrients and toxins; and, the bile duct is the sewer link to the intestine (Campra and Reynolds, 1988). By volume the liver is composed of 80% hepatocytes (ca 25 μm diameter), or parenchymal cells, which perform metabolic functions specific to the liver, in particular - (1) the urea cycle (regulation of amino acids and excess ammonia), (2) lipid metabolism related to the massive intestinal absorption of lipids, (3) formation of bilirubin and bile acids for bile secretion (Arias et al., 1988). The triad is divided into three zones with the total distance of 500 mm across the three zones (Arias et al., 1988). Figure 1B illustrates the cross-section of a tricentric™ fiber pair used in this study. It is simply a smaller fiber inside a larger fiber. The maximum distance a cell is from oxygenated perfusate in the fiber pairs of prototype #1 and #2 is 500 or 200 μm, respectively, which is comparable to the dimensions of the liver ascinus. The success of the present non-NMR-compatible artificial-liver depends on a three-compartment design, attempting to mimic the *in situ* arterial/portal liver blood flow using a conventional two-compartment hollow fiber bioreactor. The tricentric™ design inherently resembles the *in situ* liver better than commercially-available hollow-fiber bioreactors.

Additionally, from an NMR standpoint, the tricentric™ is better as a cell model of the liver than the hollow-fiber bioreactor because of enhanced perfusion due to radial

UCSF LIBRARY

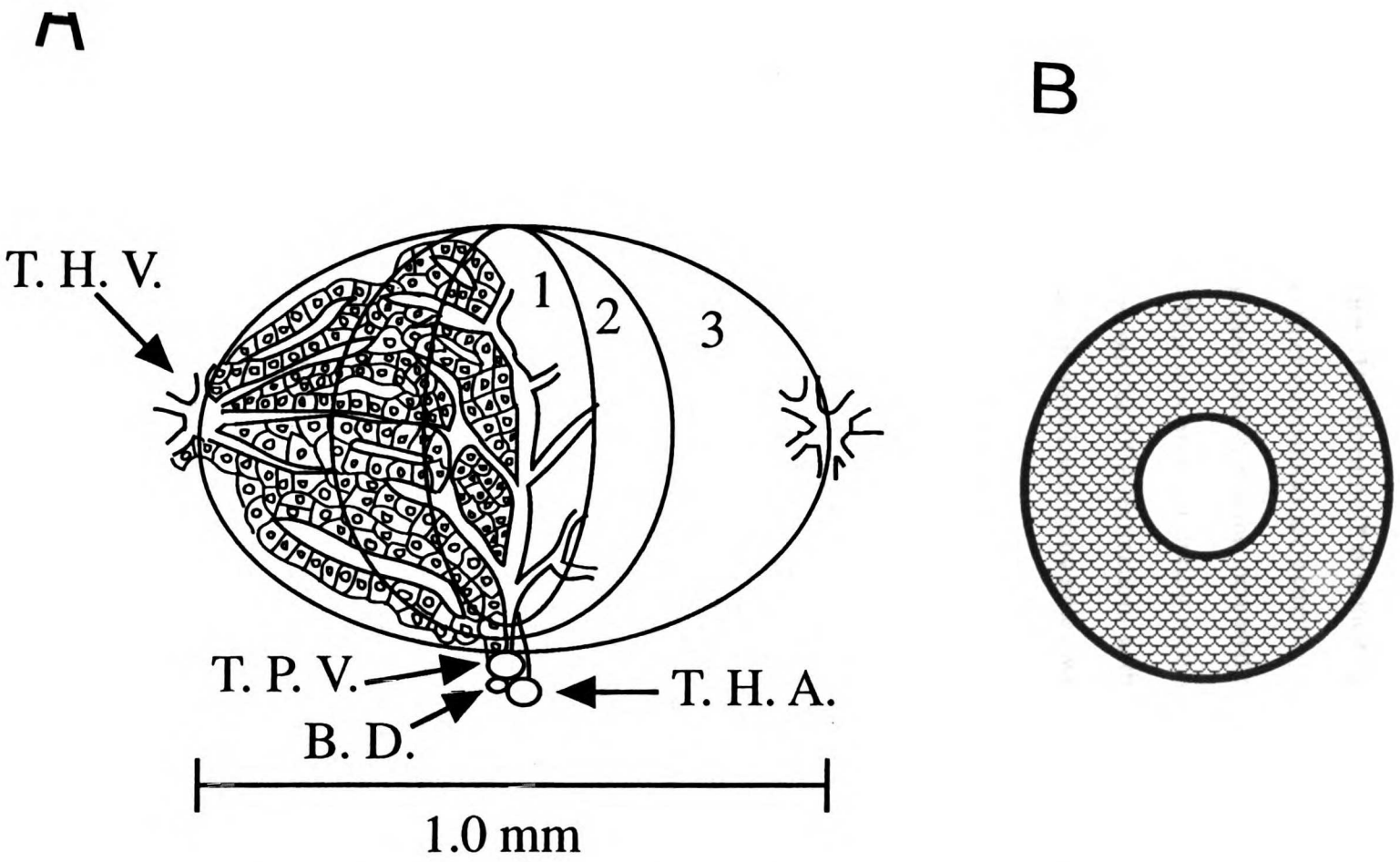

Figure 1: Drawing of a liver ascinus showing the three zones (A) and a cross section of a tricentric™ bioreactor fiber pair with the shaded area indicating where the cells reside, or the annular space (B). In prototypes #1 and #2, the o.d. of the inner fiber is 0.8 mm for both and the i.d. of the outer fiber is 1.8 mm and 1.2 mm, respectively. Abbreviations: T.H.A, terminal hepatic artery, which is perpendicular to the plane of the page; T.P.V., terminal portal vein; B.D., bile duct; T.H.V., terminal hepatic vein.

UCSF LIBRARY

flow from ICC to ECC (Custer, 1988). It also provides for easier extrication of cell mass, and is extremely resilience. The tricentric™ is made of polypropylene while the cellulose acetate fibers in hollow-fiber bioreactors are extremely fragile and even break at culture confluency with normal flow rates due to the increased resistance caused by the cell mass (Callies et al., 1993). This is a problem during recovery of cells, since attached cells cannot be readily forced out for PCA extraction, without bioreactor destruction. The tricentric™ bioreactor can be autoclaved many times, whereas the hollow-fiber bioreactor needs to be sterilized with ethylene oxide. One can destroy several hollow-fiber bioreactors before one acquires the art of inoculation. This fragility is common even during normal functioning (Callies et al., 1993) and precludes its use as an artificial-liver (Nyberg et al., 1992; Shatford, 1992). The hydrophobic nature of the tricentric™ membrane does not preclude use as an artificial liver since extracellular matrix components are coated on the fiber or within the fiber of present artificial-livers, and similar techniques can be used with the polypropylene tricentric™ bioreactor.

Therefore, we propose that the tricentric™ bioreactor would be ideal for perfusion of isolated rat hepatocytes because of (1) its small volume and similarity in dimension to the liver ascinus (Fig. 1), (2) uniform perfusion of cells, (3) rapid and easy extrication of cell mass without destruction of the bioreactor, (4) rapidity of preparation, (5) ability to se high resolution MRIs to check fiber integrity, cell distribution, and quality control. owever, some serious hurdles need to be overcome and questions needed to be swered in order to establish the suitability of this bioreactor for NMR studies. First, the reactor needs to be made NMR-compatible. Then tdetermine if there is outgassing in perfusate at high flow rates caused by the hydrophobic membrane/water interface. gassing can destroy NMR spectral resolution, and thus the Tricentric™ would not be ble for NMR studies. I used various flow rates to determine the effect of flow on R spectroscopic resolution. Finally, I needed to determine the feasibility of *in vivo* R spectroscopy of perfused isolated rat hepatocytes, since isolated cells are more

UCSF LIBRARY

sensitive to hypoxia that cell cultures, and would constitute the best comparison to an *in vivo* animal model - besides, we did not have convenient cell culture facilities. In short, the factors determining spectroscopic feasibility were cell viability, spectral resolution, and signal-to-noise (S/N) ratio. Cell viability is best ascertained by monitoring ATP and intracellular pH by *in vivo* ^{31}P NMR spectroscopy and is a function of the diffusion distance. Trypan blue exclusion by the cells is another indicator of cell membrane integrity and is commonly used in cell culture studies. The diffusion distance is the primary variable in controlling the physico-chemical parameters, and 200 μm, or 10 cell diameters, is the distance beyond which cells become hypoxic (Gillies et al., 1986). Isolated hepatocytes are better indicators of the effect of diffusion distance than cultured cells, since their biochemistry is not as dependent on anaerobic glycolysis. The S/N ratio is determined by the global density of the bioreactor, or the percent of bioreactor available for cells. This is smaller in the tricentric™ than the hollow-fiber bioreactor, since there are three compartments and the compartment containing cells is between two fibers rather than on the outside the entire bundle of fibers. Finally, in order to assure maximal global density, and more importantly mimic *in vivo* tissue, we needed to maintain cells at tissue densities, i.e., about 2 x 10^8 cells/mL (Gillies et al., 1991). This involved trying various inoculation procedures to fill the bioreactor maximally.

We compared the viability of hepatocytes in two prototype NMR-compatible tricentric™ bioreactors using an annular space filling factor (percent of total annular pace filled with cells [F_a]) of 1, and determining the temporal resolution for a omparable S/N. High resolution MRIs were taken to determine distribution of patocytes within fiber pairs, fiber pair integrity, flow dynamics, and quality control of reactor cleaning between experiments. Bioreactor prototype #1 is composed of a dle of 18 polypropylene coaxial fiber pairs - simply a smaller fiber (0.8 mm o.d.) de a larger fiber (1.8 mm i.d.), all housed in a larger tube (15 mm i.d.). Bioreactor totype #2 is similar to prototype #1 except it has 40 fiber pairs, the outer fiber has an

UCSF LIBRARY

i.d. of 1.2 mm with half the wall thickness, and thus the diffusion distance is 2.5-fold less, but the global densities are similar (ca 10%). We used minimal nutrient containing buffer solutions which are commonly used in short-term toxicology studies and isolated hepatocyte toxicology studies (Kassahun et al., 1994). High resolution MRIs were obtained to ascertain bioreactor integrity between experiments, cell distribution, fiber pair integrity, flow dynamics, and coil quality. The MRI would require sufficient pixel resolution, perhaps 50 μm (two hepatocyte diameters), and differences in the T_2-weighted MRIs between live and dead hepatocytes to obtain changes in cell viability within the cell mass.

METHODS

Materials: Perchloric acid [PCA ($HClO_4$)] KOH, $MgSO_4$, $CaCl_2$, Na_2HPO_4, KH_2PO_4, $NaHCO_3$, NaCl, KCL, HEPES, EDTA, albumin, mannitol, reduced and oxidized glutathione were obtained from Sigma Chem. Co. (St. Louis. Mo). Deuterium oxide (99.96%), dimethyl methylphosphonate (DMMP), and 3-(trimethylsilyl)propionic-2,2,3,3-d_4 acid (TSP) were purchased from Aldrich Chemical Co. (Milwaukee, WI). Collagenase B was purchased from Boerhinger Mannheim (Indianapolis, IN); entobarbital was purchased from Anthony Products, and 20% dextrose solution and line solution were purchased from Abbott Labs (Chicago, IL).

reactor: Prototype versions of the tricentric™ bioreactor were provided by Setec Inc. ermore, CA) and composed of polypropylene. Prototype #1 is the commercially lable 4 mL tricentric™ bioreactor and is 9 cm long (port to port), has 4 mL of cell me, is housed in a 15 mm i.d. and 25 mm o.d. polypropylene tube, and consists of 18 pairs. The inner fibers have a 0.8 mm o.d. (wall thickness, 100 μm), and the outer s have a 1.8 mm i.d. (wall thickness, 350 μm). This results in a diffusion distance of

USF LIBRARY

1000 and 500 μm assuming the inner fiber is skewed or perfectly centered, respectively. Prototype #2 is similar to prototype #1 except it has 40 fiber pairs. The inner fibers have a 0.8 mm o.d. (wall thickness, 100 μm), and the outer fibers have a 1.2 mm i.d. (wall thickness 200 μm). This results in a diffusion distance of 200 μm and 100 μm assuming the inner fiber is skewed or perfectly centered, respectively. The global densities are similar (ca 10%). Both prototypes were placed in the stand shown in Figure 2, and then inserted into the bioreactor loop illustrated in Figure 3.

NMR rf Probe and Bioreactor Loop: The NMR probe design illustrated in Figure 2 is composed of two Helmholtz coils (16 mm x 20 mm dia. or 16mm x 75 mm dia.) photo-etched by Dynaflex Inc. (San Jose, CA) onto flexible copper-coated composite (Pyralux™, Dupont, Towanda, PA), both wrapped around the bioreactor (16 mm dia.) orthogonally-oriented to each other, and insulated with polyethylene or polyester. The inner coil was double-tuned to 81 MHz (^{31}P) and 50 MHz (^{13}C) for solution studies (Chang et al., 1987a) or single-tuned to ^{31}P for cell studies (Murphy-Boesch and Koretsky, 1983), and the outer coil was single-tuned to 200 MHz (^{1}H). A plastic cradle was made to place the bioreactor reproducibly in the same position in the magnet, so comparisons of images and spectra could be made.

The bioreactor loop shown schematically in Figure 3 consists of a reservoir in-line to a peristaltic pump that moves media through a custom-built silicone tubing aeration device (STAD). The STAD is made of approximately 10 meters of silicone tubing (Dow [Midland, MI], Medical grade silicone tubing, 0.125 in o.d., 0.078 in i.d., or equivalent) wrapped around a rigid non-corrosive cage and supported in a container of water which permits gas exchange. The water is aerated with 100% O_2 and a common bicarbonate-based pH control device (shown schematically in Figure 3) is used to control the opening and closing of a solenoid sparging 100% CO_2. The pH control is based on formation of

USF LIBRARY

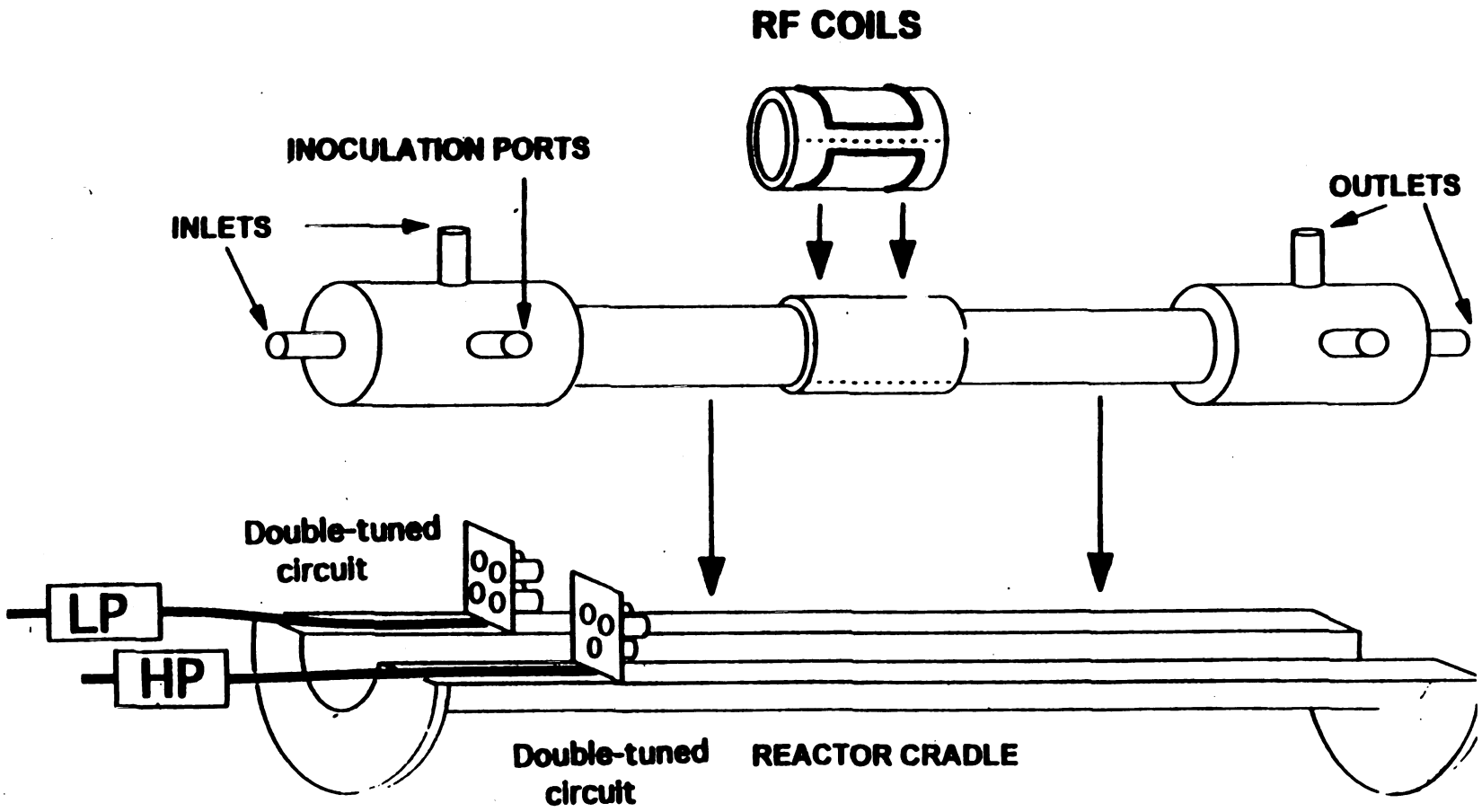

Figure 2: A schematic of the bioreactor, NMR coils, and plastic stand with circuits. Abbreviations: LP, low pass bandfilter; HP, high pass bandfilter.

UCSF LIBRARY

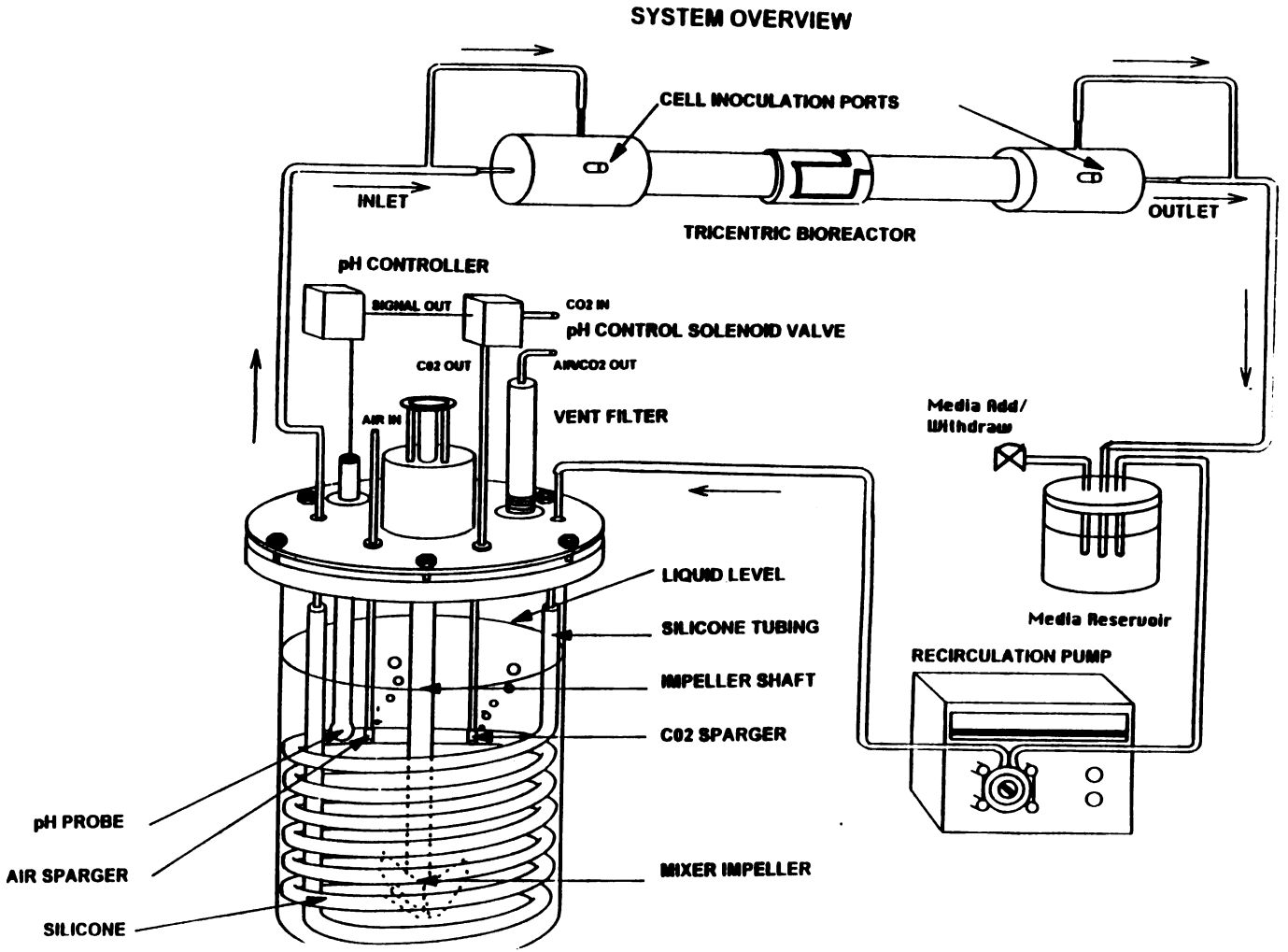

Figure 3: Schematic of the bioreactor loop.

UCSF LIBRARY

carbonic acid from CO_2 and H_2O, and then diffusion across the silastic tubing into the perfusate. The acid/base equilibrium follows: $H_2CO_3 \dashrightarrow HCO_3^- + H^+$ The pH controller was not necessary for the short-term studies performed and but is useful for long-term cell culture. Both the reservoir and STAD are temperature-controlled via water bath to 42°C, maintaining the bioreactor at 37°C. The media then flows from the STAD to the bioreactor and back to the reservoir.

Hepatocyte Protocol: Hepatocytes were prepared from female Sprague-Dawley rats (280-320 g) by the method of Moldéus et al. (Moldeus et al., 1978). In initial studies where only one rat liver was used, hepatocytes were split, one portion used for *in vivo* NMR studies and the other used for cell viability studies and PCA extraction. Four hepatocyte inoculation procedures were investigated for hepatocyte loading efficiency and viability (please refer to Fig. 2 for reference). In all four procedures a 20 ml plastic "inoculation" syringe contained the isolated hepatoctyes in K-H buffer at a concentration of ca 10^7 cells/ml. The luer tips of the "inoculation" syringe and a second 20 ml luer tip syringe containing 5 ml of K-H buffer were connected to separate lengths of #14 silastic tubing which in turn were connected to their own inoculation port (See Figure 2 for schematic). The length of tubing remained filled with K-H buffer by keeping the end of the tube above the inoculum head at all times. There are plastic clamps on short lengths of tubing attached to both ports permitting isolation of the annular compartment. In each inoculation procedure the hepatocytes flowed down the clear tubing into the annular compartment and the quantity of inoculum was visible through the tubing and syringe during the procedure.

The outlet and inlet ports are defined as the points where both the ICC and ECC connect via a plastic T connector. Therefore, perfusate enters both the ICC and ECC the inlet and exits through the outlet (see Fig. 3 for clarification). In all of the procedures the outlet was closed leaving only one path for flow: from annular space to the inlet. The

USF LIBRARY

following procedures were tested and will be represented in the text by their respective numbers: (#1) Inoculum was introduced via the inoculation port by reversing the pump and closing the outlet (see Figure 3). This causes the inoculum to be pulled by vacuum from the "inoculation" syringe to the annular compartment where the cells remain and the K-H buffer continues on to the ICC and ECC and out the inlet port, (2) Inoculum was pushed into the annular space with with "inoculation" syringes attached to both inoculation ports, flushed through one inoculation port and out through the other inoculation port into the syringe and then visa versa. The K-H buffer was then pushed through to the ICC or ECC leaving the cells in the annular space, (3) the same flushing of inoculum through the annular space as in inoculation #2, and then the pumps were reversed as in inoculation #1, but the ICC **inlet** was closed causing the inoculate to flow from the annular space to **inlet** ECC. The ICC was opened when inoculum flow slowed or stopped, (4) the annular space was voided to insure equal resistance across the total fiber pairs to evenly distribute cell radially from inoculation ports, and then inoculation #3 was followed.

For cell viability studies, hepatocytes ($6x10^6$ cells/mL) were incubated in Krebs-Heinseleit (K-H) buffer, in the presence and absence of P_i (1.2 mM) in order to assess the importance of P_i in maintaining viability. Aliquots (1 mL) were taken every hour and frozen (0°C) for subsequent assay of LDH (Worthington, 1993). Known amounts of the supernatent sample were mixed with pyruvate and NADH. LDH activity was determined by monitoring the rate of NADH disappearance at 340 nm using a Cary UV-vis spectrophotometer. LDH is expressed as a percent of the total LDH activity.

Animal Protocol: This is discussed in detail in the Methods section in Chapter 6. Briefly, female Sprague-Dawley rats (240-260 g) were anesthetized with pentobarbitaland maintained anesthetized throughout the experiment. An abdominal L-shaped incision was made, and a surface coil was inserted in the peritoneal cavity above the liver and held

USF LIBRARY

in place with sutures to the abdominal wall. The rats were placed in a home-built NMR probe and ^{31}P NMR spectra were obtained from the liver of living rat.

Solution Studies: The effect of media flow on the resolution of ^{1}H, ^{31}P, and ^{13}C spectra, and the quality of the images obtained by MRI was determined. Dulbecco's modified essential medium (DMEM) containing 25 mM glucose and 100 mM P_i was perfused through prototype #1 at flow rates of 0, 10, 20, 30, 40, 50, and 88 ml/min and ^{1}H, ^{31}P, and ^{13}C spectra and MRIs were obtained for each flow rate. To determine feasibility of ^{13}C metabolic studies, a series of experiments were performed with 150 mM glutathione in the annular space, which simulates 1.5 mM of 100% ^{13}C-labeled glutathione. This is a conservative concentration for the assessment of feasibility since normal hepatic glutathione concentrations are between 5-8 mM (Taniguchi et al., 1989). The hydrophobic fibers were air dried to prevent diffusion of glutathione into the ICC and ECC which contained DMEM. To test if the broad spectral component from the polypropylene and the signal from the medium could be eliminated, a spin echo sequence with decoupling (WALTZ16) during acquisition and delay period was performed at a flow rate of 20 ml/min. A ^{13}C NMR spectrum was obtained using a Hahn spin-echo sequence (interpulse spacing TE = 3.5 ms; optimized for G5 and G6 resonances). The spectrum was obtained from 1000 transients with a 40 μs (90°) flip angle, 4K data points, a sweep width of 10,000 Hz, and a pulse repetition time of 1 s, yielding a total acquisition time of 33 min. Prior to Fourier transformation, data were subjected to baseline correction and a Gaussian (12 or 7 Hz) apodization.

In Vivo NMR: *In vivo* ^{31}P NMR experiments of perfused hepatocytes and liver from intact rat were performed on a Nalorac Cryogenics Corp. 4400 Quest NMR imaging spectrometer with a 16 cm usable horizontal bore, 4.7 T Oxford magnet. ^{31}P NMR spectra were obtained using a 1-pulse sequence with decoupling (WALTZ16) on during

USF LIBRARY

acquisition, pulse repetition time of 1.5 s, 4K data points, and a sweep width of 3,800 Hz. This required 30 min and 8.8 min for spectral acquisition using a 45° and 70° flip angle for hepatocytes and intact liver, respectively. Hepatocytes were perfused at 20 mL/min with K-H buffer with or without 1.2 mM P_i depending on treatment, and monitored by ^{31}P NMR until 4.5 hr post-inoculation. ^{31}P spectra were subject to deconvolution difference to eliminate the broad component. The K-H buffer had 0.8 mM DMMP as an internal reference. The extracellular DMMP chemical shift was set to 41 ppm. DMMP was not added to the buffer in prototype #2 for fear of unknown toxicity (LD_{50}=2000 mg/kg gavage) even though DMMP has been found not to be significantly metabolized by the liver, and is commonly used in ^{31}P NMR spectroscopy studies of cell culture (Barry et al., 1993). For comparison of viability between experiments, the β-ATP peak area was compared to the total ^{31}P metabolite peak areas minus the DMMP peak area(s). The β-ATP/total ^{31}P peak area ratio from the first spectrum was set to 100%, for comparison with subsequent β-ATP peak areas. The intracellular pH was measured as the chemical shift difference between the P_i and α-ATP peaks. Peak areas were determined by curve-fitting with the program MacFID.

UCSF LIBRARY

^{1}H MRI: Transaxial T_1- and T_2- weighted MRIs of the bioreactor were obtained using an Oxford actively-shielded gradient coil with a 7.5 G/cm maximum gradient, TE = 24 and 80 ms, TR = 1 and 4 sec, respectively, and 1 acquisition, 16 mm field of view, 3 mm slice thickness, 256 x 256 data points and zero-filled in the y dimension. Each voxel was 62 x 62 μm x 3 mm. MRIs were taken with and without flow or hepatocytes. MRIs from the same slice were compared at the beginning and end of the experiment to monitor any visible changes. Hepatocytes were flushed from the bioreactor, and a ^{31}P spectrum and an MRI was obtained to measure the percent of ^{31}P metabolites and hepatocytes remaining, respectively. At the end of the experiment, the cells were recovered by forcing hepatocytes out via syringe. A sample for trypan blue analysis was obtained, and

then the majority of hepatocytes were submerged in liquid N_2 for lyophilization and subsequent PCA extraction. Quality control for complete removal of cell debris from the annular space was performed by obtaining an MRI after each rinse with 1N or 2N NaOH.

In Vitro NMR: ^{31}P and ^{1}H spectra of isolated rat hepatocyte extracts dissolved in deuterium oxide were obtained using a GE QE-300 spectrometer operating at a ^{1}H frequency of 300 MHz. ^{1}H spectra were obtained using a one-pulse sequence with a 10 sec interpulse delay, 16K complex points, and a spectral width of 3012 Hz. ^{31}P spectra were obtained using a one-pulse sequence with decoupling during acquisition and a 10 sec interpulse delay, 16K complex points and a spectral width of ±4000 Hz. ^{31}P compounds were identified by comparison of extract chemical shifts with those of known standards and literature values. ^{1}H spectra were referenced to TSP at 0 ppm, while ^{31}P spectra were referenced to the β-NTP peak at -7.5 ppm. All peak areas were fit using the program MacFID (Tecmag, Houston, TX).

UCSF LIBRARY

RESULTS

Figure 2 illustrates the bioreactor/coil unit and the plastic stand containing balance-matched single-tuned (Murphy-Boesch and Koretsky, 1983) and double-tuned (Chang et al., 1987a) NMR circuits. The entire assembly was placed in the magnet. The coils were photo-etched on Pyralux™ wrapped around the bioreactor and placed orthogonal to each other. They were autoclaved for four cycles while attached to the bioreactor without significant change in quality factor. The plastic stand served to position the bioreactor in the magnet so that shimming or determining a specific MRI region would be reproducible between and within experiments. The inside coil was initially double-tuned to $^{13}C/^{31}P$, but later it was single-tuned to enhance the S/N of the higher frequency ^{31}P (Chang et al., 1987a). A schematic of the bioreactor loop used for

NMR studies is illustrated in Figure 3. It shows that the peristaltic pump pushes perfusate through the STAD where the perfusate is oxygenated before reaching the bioreactor. The perfusate is returned to the reservoir; both the reservoir and GEM were kept in a water bath at 42°C maintaining a bioreactor temperature of 37 °C.

The primary peaks observed in ^{1}H and ^{31}P spectra of DMEM and 100 mM phosphate buffer were $^{1}H_2O$ and P_i, respectively, and these peaks were used to determine resolution and flow effects. At all flow rates two peaks were present for both $^{1}H_2O$ and P_i. One peak is attributed to the intercapillary and/or annular volume, and the other to the extracapillary space. The linewidth did not change with flow for ^{1}H or ^{31}P. For the ^{1}H spectra, the $^{1}H_2O$ linewidth was 8 Hz for the downfield and 14 Hz for the upfield peak, and the two peaks were 100 Hz apart. The P_i signals exhibited 1.9 Hz for the downfield and 2 Hz for the up field peak, and peaks were 4.5 Hz apart.

Figure 4 exhibits the ^{13}C spectrum of 150 mM glutathione using a one pulse sequence with proton decoupling in the vertical bore spectrometer at 75 MHz, and in the annular space of the bioreactor in the horizontal bore spectrometer at 50 MHz with DMEM flowing through the ICC and ECC at a rate of 40 mL/min (B). Figure 4C is a spectrum of the same glutathione (GSH) sample and flow rate as in figure 4B but using a spin echo sequence, illustrating the disappearance of the three broad polypropylene peaks centered at 35, 30 and 22 ppm emanating from the bioreactor, and little signal from media. For example, glucose concentration in DMEM is 25 mM, a sixth of the concentration of GSH, but resides in nearly five-fold the area [which is the ratio of ECC + ICC area to the annular area (where GSH resides)]. Therefore, glucose at this concentration should be represented by a peak comparable in height to that of GSH, but it is not visible.

Figure 5A and B are T_1 and T_2 -weighted transaxial MRIs of the prototype #1 and #2, respectively, with 20 ml/min flow rate. illustrating that T_2-weighted images give better resolution and less flow artifacts. The hypointense regions in the ECC are due to

USF LIBRARY

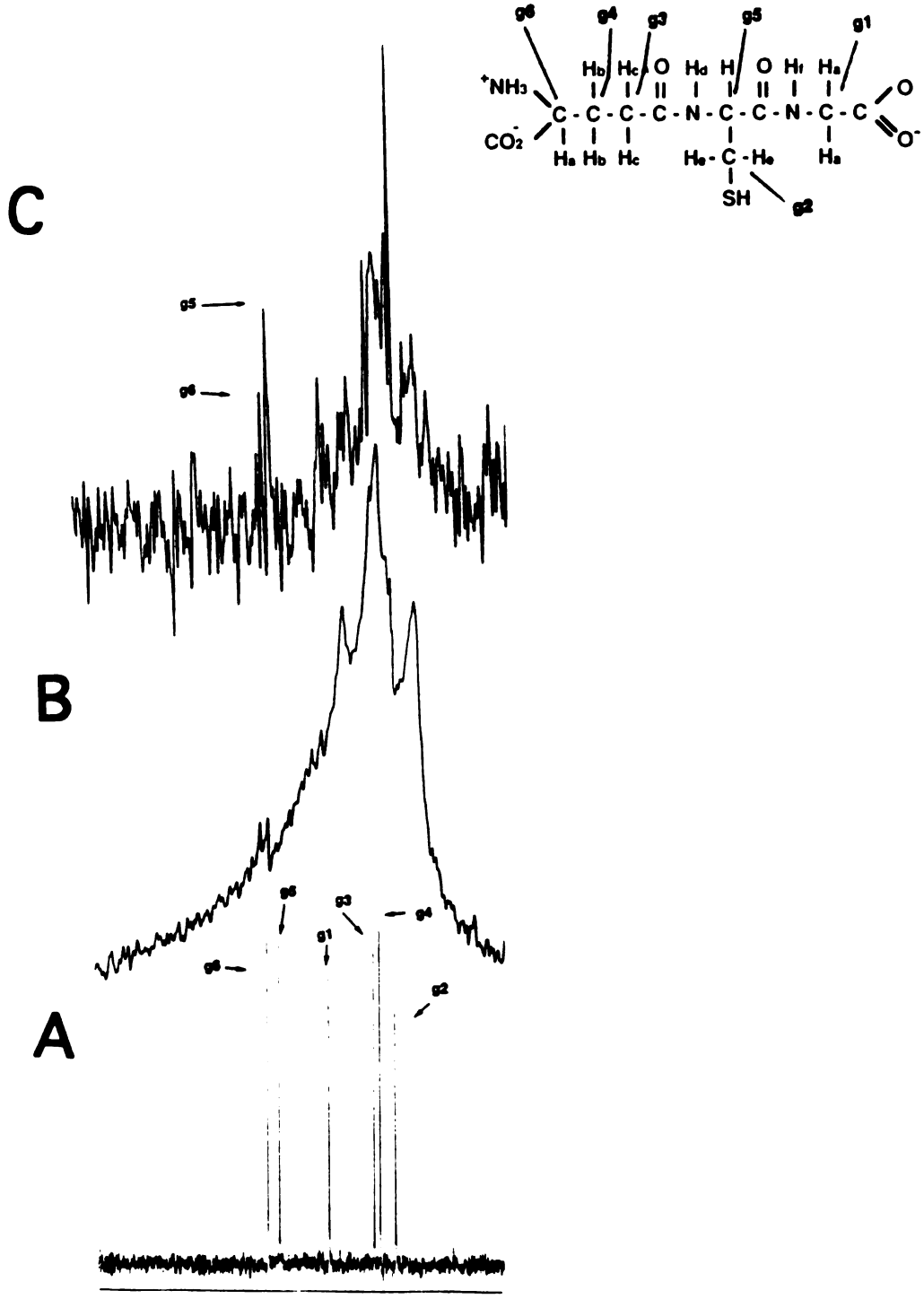

Figure 4: ^{13}C NMR spectra of 150 mM glutathione in the annular space of the bioreactor obtained with a one-pulse sequence on a QE300 NMR spectrometer (SW=10,000 Hz; CB=16K; TR=10 s) (A), and on the NCC 4.7T NMR spectrometer (B). Spectrum C was obtained with a spin echo sequence using an inter-pulse delay of 1.6 ms and demonstrating the reduction of the broad component emanating from the polypropylene material of the bioreactor. The specroscopic parameters for B and C are SW=8,000 Hz; CB=4K; TR=8 s. Note: inset shows the structure of glutathione and labeled carbons.

UCSF LIBRARY

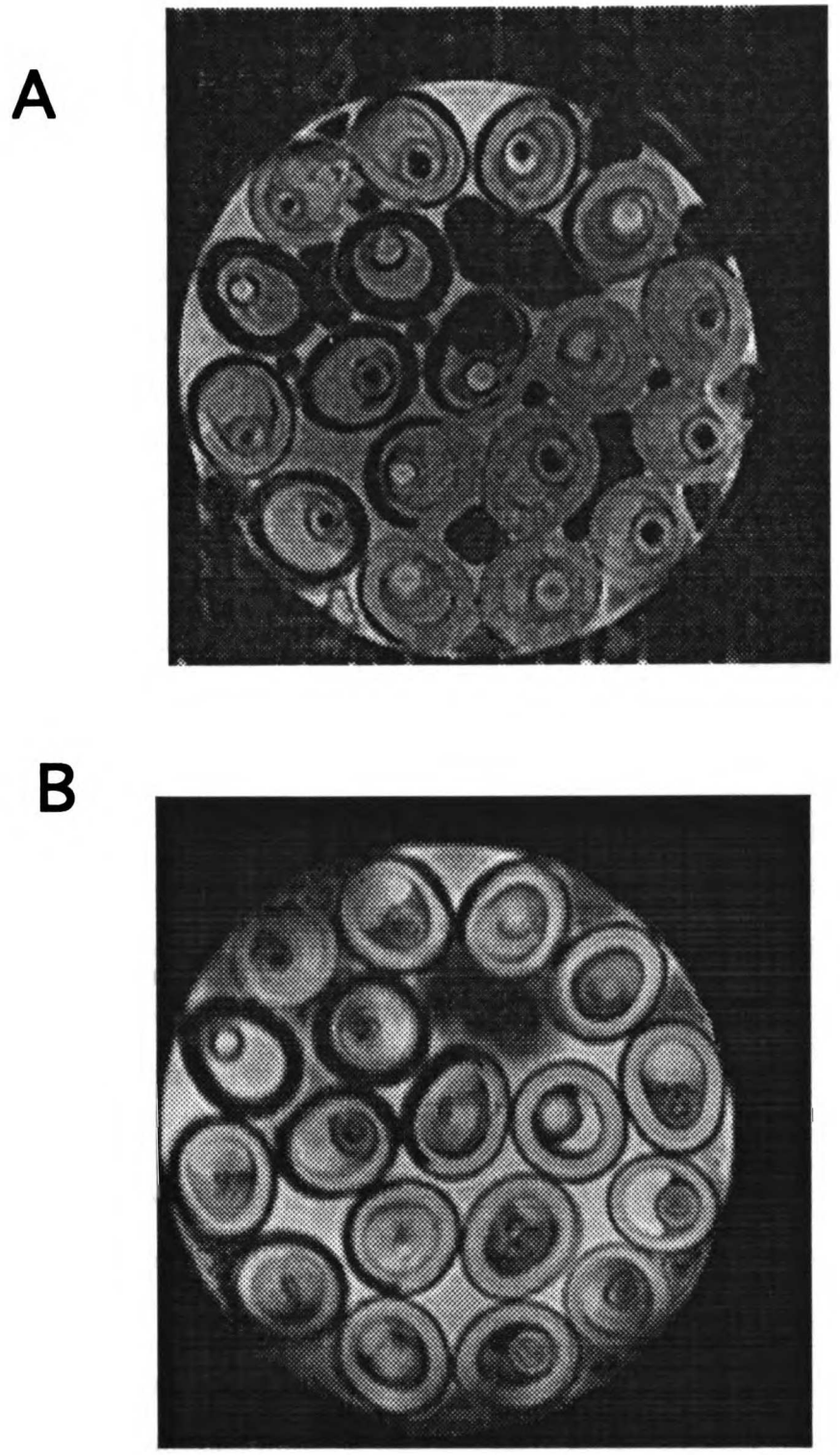

UCSF LIBRARY

Figure 5: A transaxial T_1 and T_2-weighted MRI of prototype #1. For both MRIs the flow rate was 20 mL/min and obtained the same day. Wetting the bioreactor with ethanol was incomplete, and these dry fibers appear hypointense. For A and B, respectively TE=24 ms and 80 ms; Tr=1 and 4 s; and FOV=16 mm, and one acquisition.

flow (i.e., bulk flow of ^1H_2O into and out of the pulsed region) and are not bubbles. There was an increase in fiber pair 'ghosts' associated with flow, and this was especially evident in the T_1-weighted MRIs. In fact, at a flow rate of 88 mL/min all of the fiber pairs in the T_1-weighted MRIs had highly shifted and smeared 'ghosts' that appeared as hyperintense rings on a background of hypointense ECC and ICC. One can distinguish the 18 fiber pairs in both MRIs, but the water signal emanating from the perfusate in the ICC and ECC is significantly more hypointense in the T_1-weighted MRI (Fig. 5A) than the T_2-weighted MRI, due to the severe flow effects. For example, the MRI in Figure 5A shows hypointensity in the ICC similar to the T_2-weighted MRI, but there is relatively more hypointensity in the middle of the ECC than at the perimeter. This indicates that perfusate flow rate is more rapid in the middle of the ECC.

Figure 6 demonstrates the various types of information obtained from a T_2 -weighted MRI. One can distinguish media flow, cell mass distribution, magnetic susceptibility, insufficient membrane wetting, bubbles, and coil inhomogeneity. Media flow appears hypointense in areas of high flow rate, such as the ICC. Cell mass appears as hypointense regions in the annular space and is more clearly demonstrated in Figure 7D and E. Magnetic susceptibility effects are demonstrated as dark rings around each fiber, clearly demonstrated in Figure 7D and E, and may be caused by the difference in magnetic susceptibility of the perfusate compared to the fiber material. Insufficient membrane wetting by ethanol is apparent in several of the fibers in the upper left of the MRI. To make the membrane permeable to water, it must first be completely rinsed with ethanol. During the ethanol wetting process the bioreactor was on its side, so the fibers on the top were never voided of air and not all fiber pairs were thoroughly rinsed with ethanol, and thus remained impermeable to water. Bubbles appear as dark areas with defined margins; an example is evident in the middle of the bioreactor in the ECC. Bubbles form in the ECC during inoculation procedure #1 probably due to cavitation or

UCSF LIBRARY

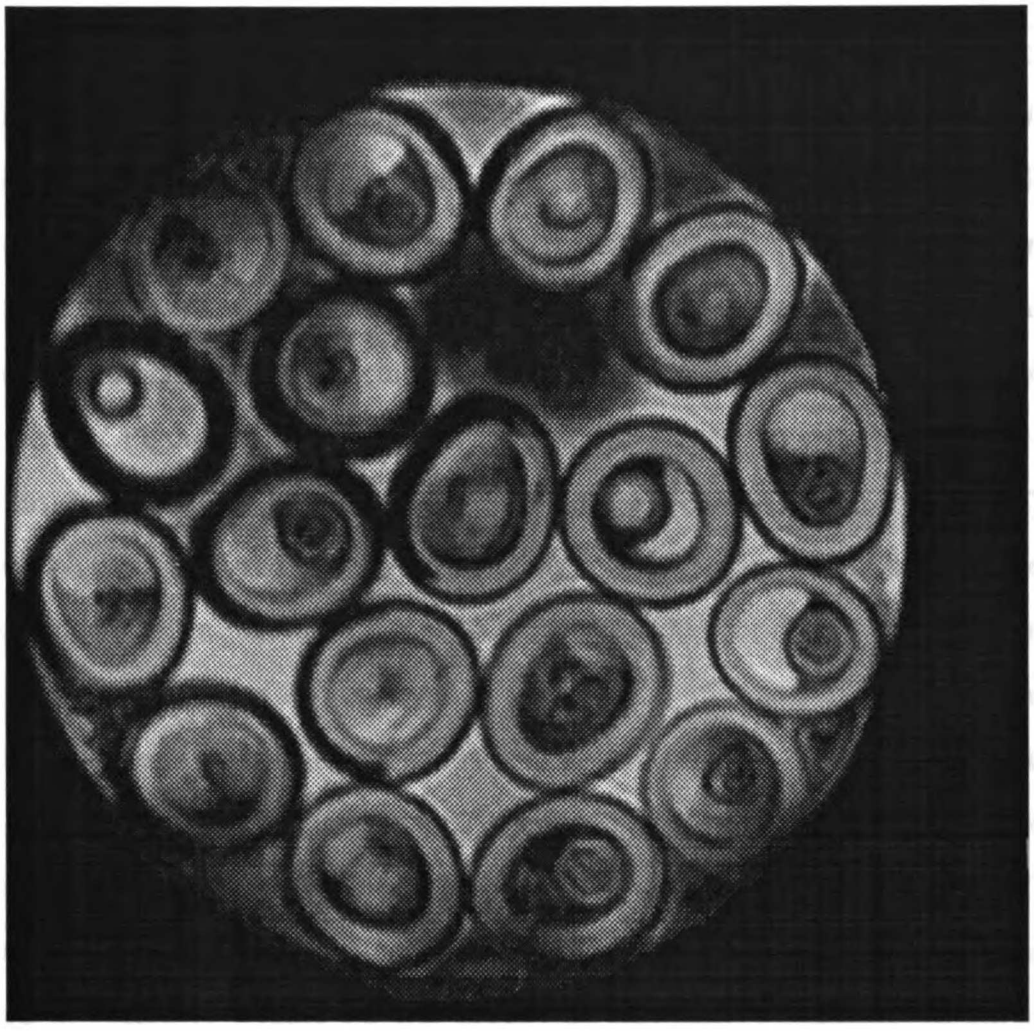

Figure 6: T_2 -weighted transaxial MRI of prototype #1 illustrating much information regarding flow dynamics, membrane wetting, cell mass distribution, coil homogeneity, and the 18 fiber pairs. The TE = 80 ms, TR = 4 s, NA=1.

outgassing from oxygen-saturated perfusate near the end of inoculation when fibers become clogged. After inoculation and the inoculation ports are closed and the ECC is reopened, one observes the bubbles exiting the ECC outlet when the flow rate is increased above 50 mL/min. Some coil inhomogeneity is barely observed as hypointense

UCSF LIBRARY

areas at the four corners of the MRI caused by magnetic flux or coil coupling near the four corner rungs of the Helmholtz coil.

Figure 7A through F are T_2-weighted transaxial MRIs that illustrate the cell distribution in prototype #1 within the 18 fiber pairs using inoculation procedure #1, which is simply to reverse the pumps and close off the outlet and open the inoculation ports, so media flows from the annular space to the ICC and ECC. The fibers that were not sufficiently wetted with ethanol have no cells in them because no water can flow through the membranes during inoculation and thus cells do not enter the annular space. Comparison of Figure 7A to 7B demonstrates that increased flow is associated with hypointensity and thus the ICC has a higher flow rate or velocity greater than the ECC. Additionally, there appeared to be greater loading of hepatocytes in the fiber pairs near the inoculation ports in Figure 7A and B on the lower and upper right of the MRIs than other fiber pairs. This was also observed in a subsequent MRI obtained from the same bioreactor with membranes that were completely wetted (Fig. 8A). Cells will follow the path of least resistance, during inoculation. The fiber pairs closest to the inoculation port are a shorter distance for the inoculated cells, and thus are a path of less resistance The distribution of cells within the fiber pairs is evident by close examination of data presented in Figure 7. Figure 7C was purged of cells from the annular space, and comparison of the enlargements of the white boxed regions in Figure 7A and C demonstrate that the majority of cells are concentrated around the inner fiber. This effect is similar to a clogged drain. Only 2 x 10^8 cells (or 5 10^7 cells/ml) were inoculated because perfusate did not continue to flow out of the inlet port while reversing the pumps even though there were still many hepatocytes left to inoculate. This is because the flow velocity of the inner fiber is greater than the outer fiber, so cells aggregate around the inner fiber and stop the flow by clogging the inner fiber pores. The cross-sectional area of the ICC is less than that of the ECC, so the interlumen vacuum is greater from the ICC due to the increased velocity of perfusate flowing through the ICC fibers.

UCSF LIBRARY

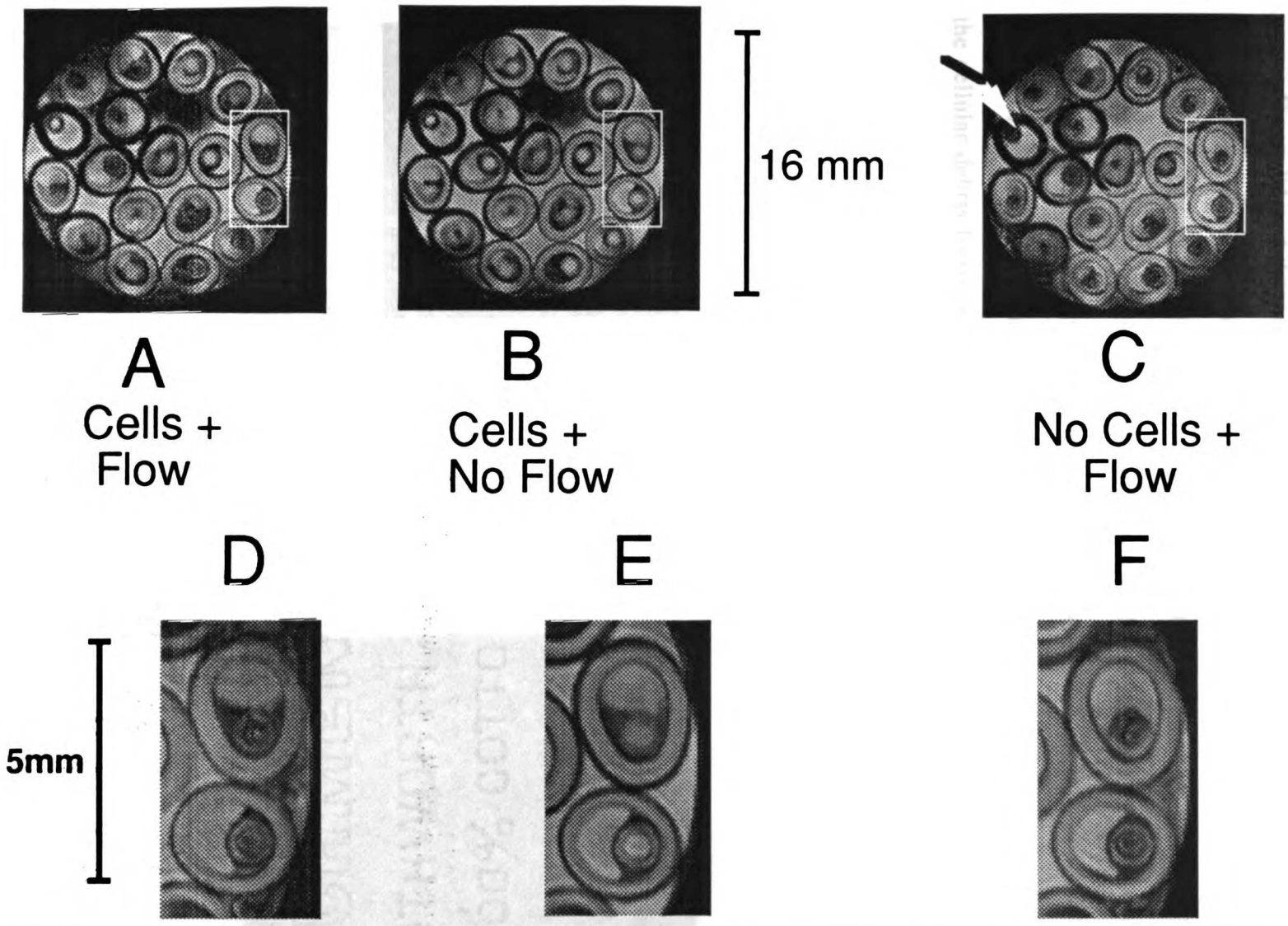

Figure 7: Transaxial T_2-weighted MRIs of the prototype #1 with and without flow and cels (A through C). D through F are enlargements of the white boxed regions in the above corresponding MRIs. TR=4s; TE=80ms; FOV=16mm, and one acquisition.

UCSF LIBRARY

Figure 8A and B are MRIs of prototype #1 (18 fiber-pairs) and #2 (40 fiber-pairs), respectively. This illustrates the larger outer fiber wall thickness and i.d. of prototype #1 resulting in an increased diffusion distance. The o.d. of the housing is 16 mm. Figure 8B was taken after one day of soaking the bioreactor in 1N NaOH to dissolve the cellular material and demonstrates that the annular space still was not clean in 5 fiber pairs. It required 1 hr perfusion at 2 mL/min and 24 hr of soaking in 2N NaOH to finally clean all the cellular debris from the annular space. This set of experiments demonstrates the utility of MRI for bioreactor quality control between experiments.

UWF LIBRARY

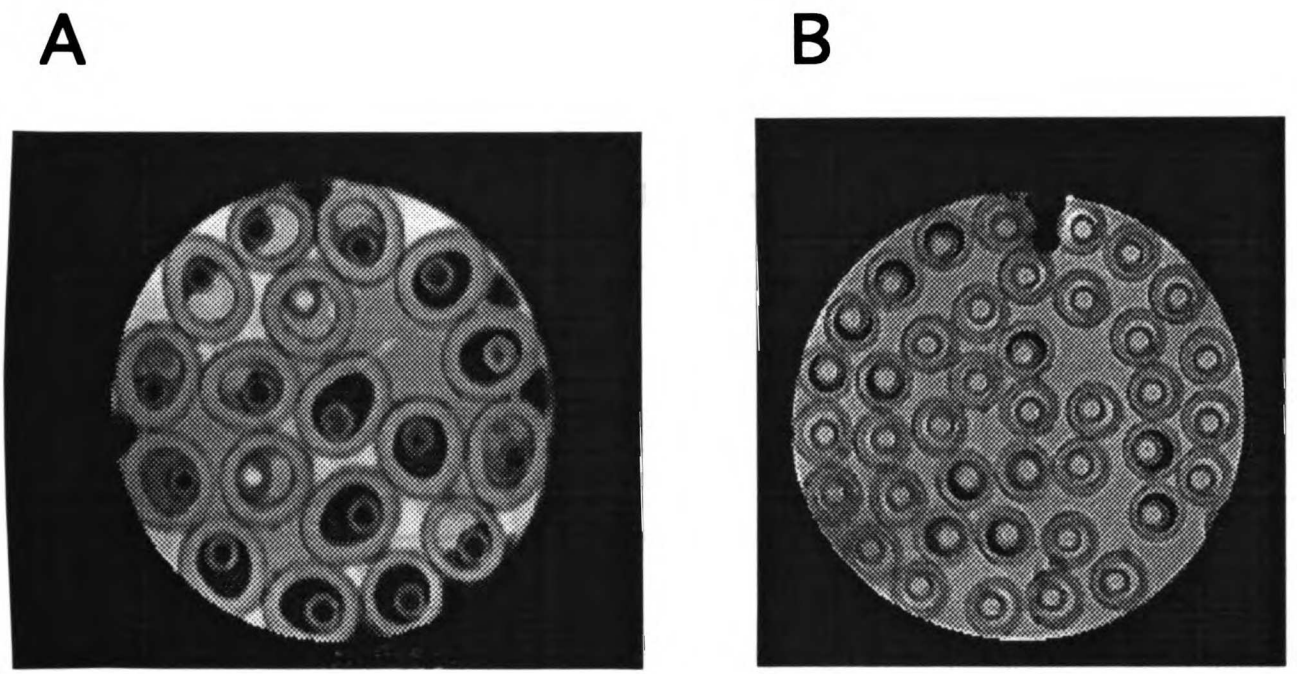

Figure 8: T_2-weighted transaxial images of prototype #1 (A) and #2 (B). The image of prototype #1 after inoculation procedure #2 and cells were flushed from the annular space, with little success. The hypointense regions in the annular space represent dead hepatocytes that required rinsing with 1N NaOH in order to dislodge. The image in B was taken after inoculation #4 and the hypointense regions in the annular space in 11 of the 40 fiber pairs were still evident even after rinsing with 1N NaOH and soaking for 24 hr (see text). TE = 80 ms; TR = 4 s; FOV = 16 mm; NA = 1. The inner housing diameter of both bioreactors is 15 mm.

Figure 9 is a graph of hepatocyte viability monitored via LDH activity and changes in ATP levels as determined by ^{31}P NMR, with and without 1.2 mM P_i in the K-H buffer. See Hepatocyte Protocol section for details of the experiment. The hepatocytes without P_i in the K-H began to lose viability, as determined by loss of membrane integrity and leakage of LDH, by the first timepoint (1 hr), whereas hepatocytes with P_i in

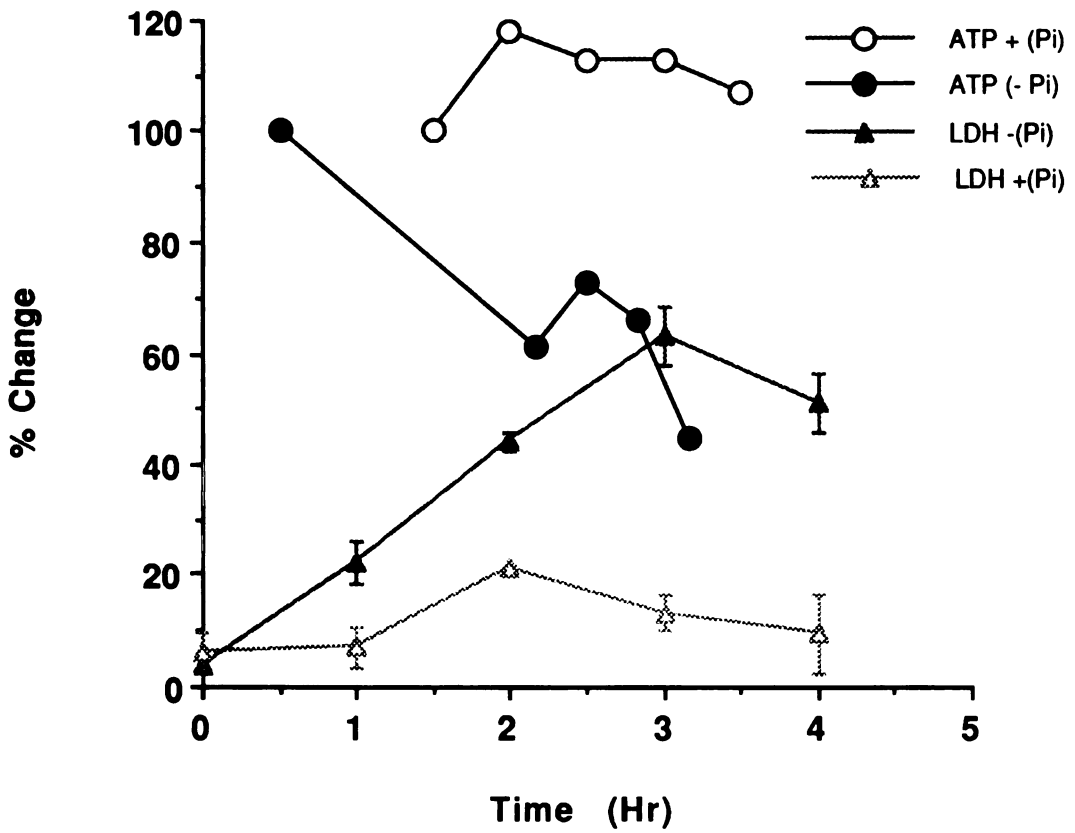

UUSF LIBRARY

Figure 9: The effect of P_i on hepatocyte viability. 1 mL of sample was taken every hour and frozen for LDH analysis by determining the disappearance of NADH using 340 nm UV-vis spectroscopy. 100% is referenced to the total LDH in a 1 mL sample if all the cells had died and released their LDH.

the K-H buffer appear to maintain membrane integrity over the entire period of sampling. However, as determined by the ^{31}P NMR of the β-ATP levels, a significant decrease was

parent by 2 hrs of perfusion whereas no decrease was observed with P_i -containing K-buffer. The β-ATP levels in cells incubated with P_i -containing K-H buffer appear to crease initially. This is probably due to recovery from the hypoxic insult incurred ring isolation, as demonstrated in the spectrum which shows very little β-ATP in the CA extract of hepatocytes just after isolation (Fig. 10B).

Figure 10A through D are ^{31}P spectra of a PCA extract of hepatocytes taken at the nd of the experiment (A), perfused in prototype #1 and inoculation procedure #1 (C), from a liver of intact rat (D), and a PCA extract from hepatocytes taken right after isolation but prior to inoculation (B). The extract represented in spectrum A reveals an ATP/ADP ratio of 3.1 which is within normal range (Schwenke et al., 1981) and identifies some of the resonances composing the PME, PDE and DPDE regions. The spectrum from the perfused hepatocytes arises from approximately 5 x 10^7 cells and took 38.5 min to acquire. The linewidth in the ^1H spectrum of water at half-height was 30 Hz. This spectrum in Figure 10C was taken from the same experiment as the MRIs shown in Figure 7 using inoculation procedure #1, and only 10% of the annular space was filled as determined by the difference in hypointensity in the annular space between Figure 7A and C. The viability before inoculation and after 5 hr of perfusion in the bioreactor was 80% as determined by trypan blue exclusion.

Using inoculation procedure #2 where hepatocytes were pushed into the annular space using a syringe and opening both the outlet and inlet, all cells died, probably due to implosion, although, >90% of the annular space was filled with hepatocytes. We returned to a modification of inoculation procedure #1, and developed inoculation procedure #3 by voiding the annular space and reversing the pump and restricting flow from the ICC inlet port, we observed a differential loading of fiber pairs that was greater closer to the inoculation ports. With inoculation procedure #3, we found that >90% of the annular space was filled as achieved by inoculation procedure #2. However, ATP

UCSF LIBRARY

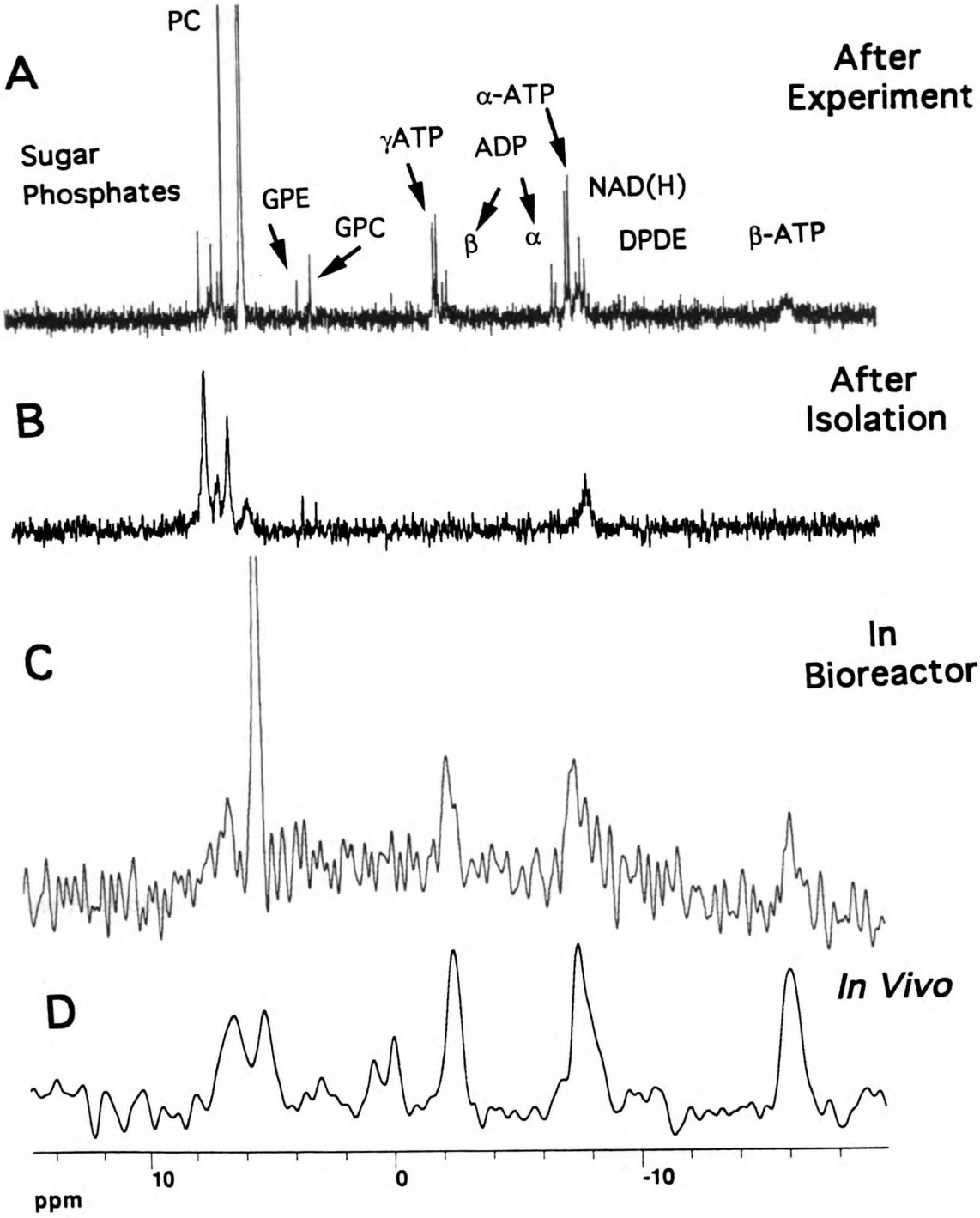

UVSF LIBRARY

Figure 10: ^{31}P NMR spectra of PCA extracts of hepatocytes perfused in prototype #1 for 4.5 hr (A), following the isolation procedure (B), the same hepatocytes used in A but during 2 to 2.5 hrs of perfusion in prototype #1 requiring 38.8 min to acquire (C), and liver *in vivo* (D). See Methods section for spectroscopic parameters.

was not observed and only NAD(H), PMEs and P_i (primarily from the media) were evident in the spectra.. In both inoculation procedures #2 and #3, there was 100% mortality as determined by trypan blue exclusion at the end of the experiment. The hepatocytes never recovered from inoculation procedures 1 through 3 when tissue densities of 2 x 10^8 cells/mL were attained. Figure 10 demonstrates that the perfused hepatocytes inoculated by procedure #1 (spectrum C) have a similar ^{31}P composition to that observed in rat liver *in situ* (spectrum D). The additional peaks in the *in vivo* ^{31}P spectrum of rat liver (spectrum D) is due to two peaks of phosphocreatine emanating from surrounding muscle tissue and are centered at 0 ppm. The large P_i peak in the ^{31}P spectrum of perfused hepatocyte is due 1.2 mM phosphate in the K-H perfusion buffer. Figure 10B demonstrates that after the two hour period required for isolation of hepatocytes, their metabolism is primarily anaerobic, resulting in no ATP and primarily sugar phosphates, NAD(H), and phosphomonoesters (PMEs).

Figure 11A and B are ^{31}P spectra of a PCA extract of hepatocytes that were taken at the end of the experiment (A) and perfused in prototype #2 which contains 40 fiber-pairs (B). The annular space was >90% filled with hepatocytes at tissue densities of 2 x 10^8 cells/mL. Inoculation procedure #4 was used to obtain this density. The PCA extract had an ATP/ADP ratio of 1.5, lower than that determined in the ^{31}P spectrum of the PCA extract shown in Figure 11A. Although the viability as assessed by trypan blue exclusion was not significantly different before inoculation (78%) and after recovery (76%), the ATP/ADP ratio indicates that the hepatocytes were stressed. It is probable that at tissue densities, which were not attainable in prototype #1 (Fig. 9), hepatocytes become hypoxic or need an organic nutrient to maintain viability. The spectrum shown in Figure 11B took 8.8 min to acquire and using the modified Helmholtz coil was obtained from approximately 6 x 10^8 cells, or 2 x 10^8 cells/mL. Comparison of ^{31}P spectra in Figure 11B to *in situ* rat liver shown in Figure 10D demonstrates a strong

UNF LIBRARY

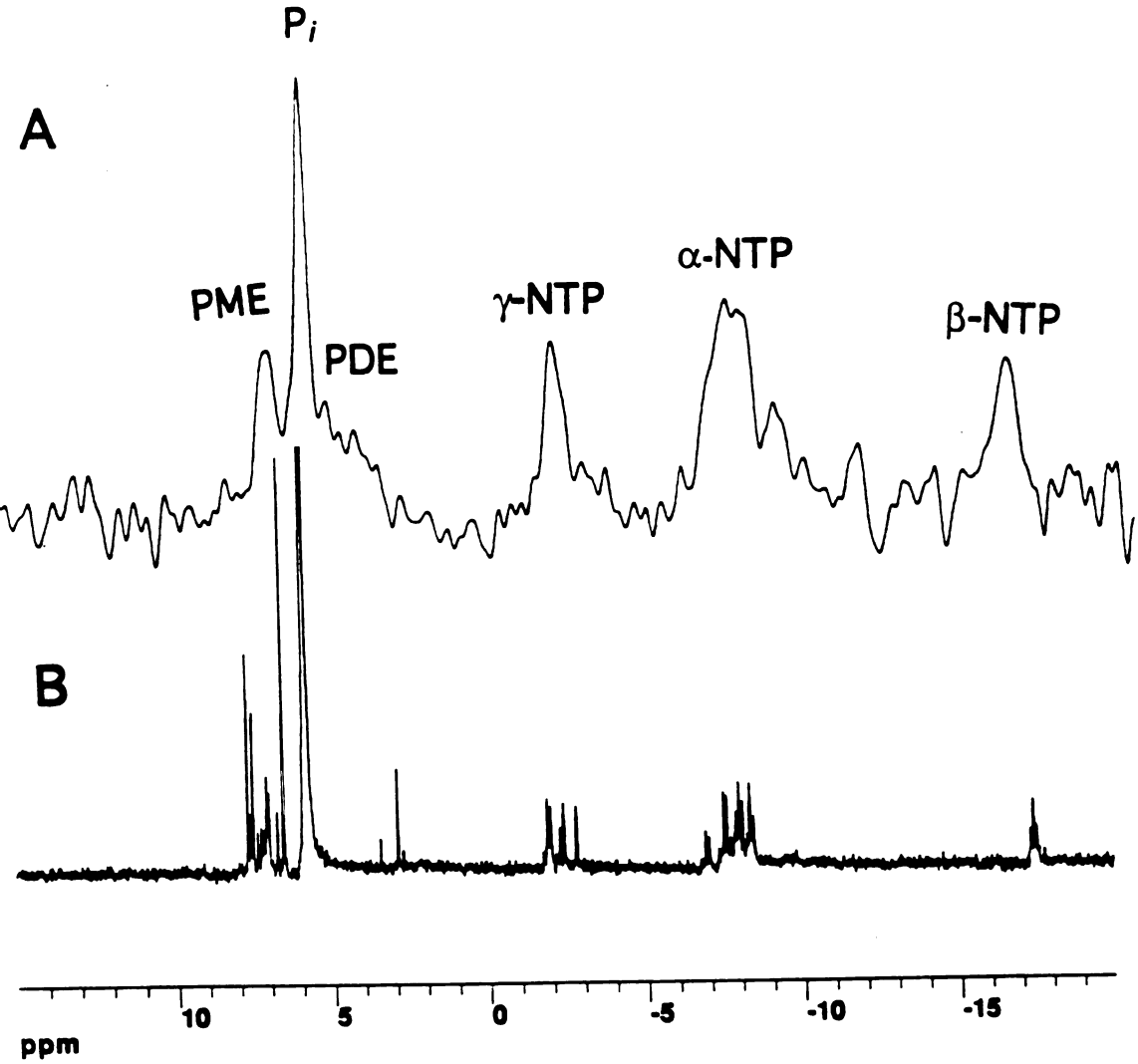

UUSF LIBRARY

Figure 11: ^{31}P NMR spectra of hepatocytes perfused in prototype #2 requiring 8.8 min to acquire (A), and the PCA extract taken after 5 hr of perfusion (B).

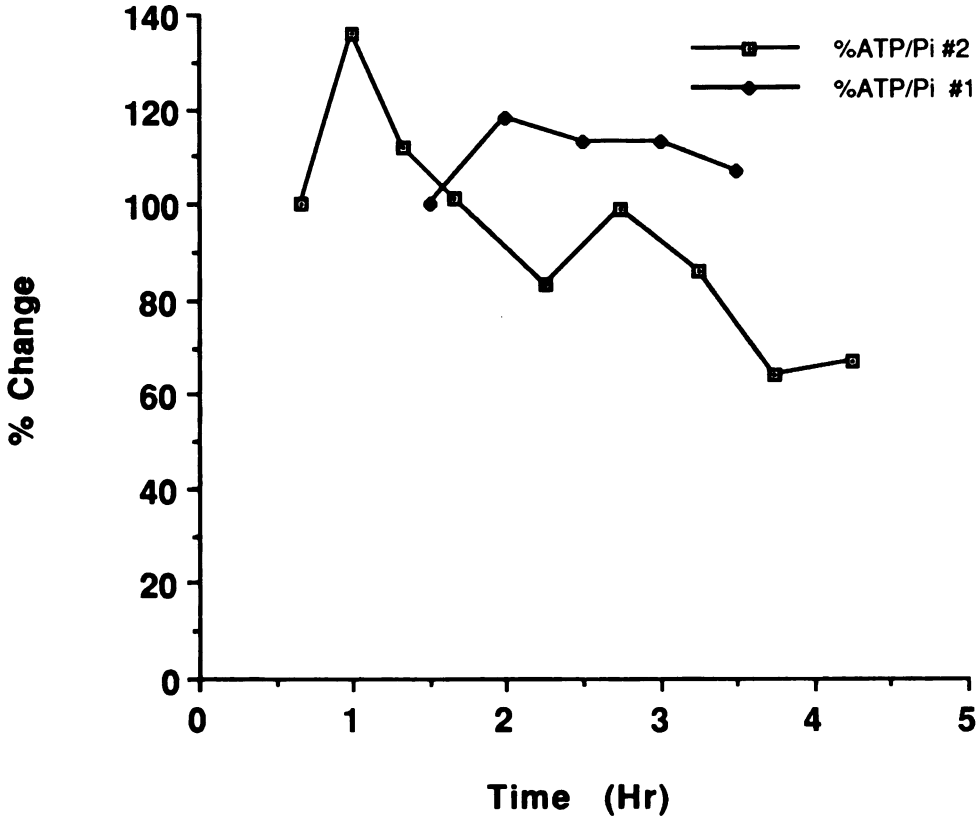

UUSF LIBRARY

Figure 12: β-ATP/P_i timecourse from isolated rat hepatocytes perfused in P_i -containing K-H buffer in prototypes #1 and #2 with a flow rate of 20 mL/min. The NMR parameters are the same for both experiments (TR=1.5 sec).

of phosphocreatine caused by muscle contamination in spectrum 10D, and of 1.2 mM P_i emanating from the K-H perfusion buffer in spectrum 11B.

Figure 12 is a comparison of β-ATP changes by hepatocytes in prototypes #1 and #2, demonstrating that both bioreactors maintained hepatocytes in a metabolically active state for up to 4.5 hours. However, prototype #2 was able to maintain hepatocyte viability at tissue densities (2 x 10^8 cells/mL) which were four-fold higher than prototype #1 (5 x 10^7 cells/mL). Therefore, prototype #1 appears to lack NMR-feasibility for monitoring isolated rat hepatocytes. In both bioreactors there appears to be an initial

recovery phase from isolation; however, in prototype # 2 this recovery is followed by a decrease in β-ATP 2 hr after post-inoculation.

DISCUSSION

We have built a NMR-compatible triple-tuned probe for a novel bioreactor design (Fig. 2) and a bioreactor loop (Fig. 3) capable of gas and pH control for dense cultures in horizontal or even vertical-bore NMR spectrometers. This NMR probe can be used for any bioreactor, even an artificial-bioreactor liver, to monitor normalcy. The multiple-tuned, flexible, radiofrequency (rf) dual-volume coil NMR probe permits simultaneous observation of many nuclei from *in vivo* or *in vitro* samples by NMR spectroscopy or imaging.

A combination of a flexible copper-coated composite sheet, such as Pyralux™, a double-tuned rf circuit, the photo-etch process, a non-magnetic holder, and coil insulation permitted the development of this autoclaveable NMR probe. The Helmholtz coils can be made using a computer-aided design (CAD) program, where the resulting Helmholtz template is used to photoetch the design onto the flexible copper-coated composite. If desired, multiple reproducible copies can be constructed. Once the two Helmholtz coils are in place, they are insulated by placing heat-shrink tubing around them, and coating with polyethylene or polyester making it autoclaveable. The dual-volume NMR probe can be tuned to detect up to four nuclei. One coil is tuned to the two higher frequencies while the other coil is tuned to the lower frequencies. This is the first time a quadruple-tuned NMR probe has been made from flexible printed-circuit sheet.

The advantages of the multiple-tuned flexible rf NMR probe are its diversity of applications to objects of any diameter or shape, with an increase in filling factor by attaching coils directly to the sample (such as a bioreactor, reaction vessel, limb, etc.) resulting in an increase in coil sensitivity, optimization of usable magnet bore volume

UUSF LIBRARY

(often limited in vertical-bore high-resolution magnets), and monitoring of up to four nuclei (e.g., ^{1}H, ^{19}F ^{31}P, ^{13}C) simultaneously. The combination of CAD and photo-etching has several advantages over presently-used copper foil. These Helmholtz coils can be made with higher precision and better reproducibility, they are easily mass produced, they have no variable distributed capacitance caused by solder joints, and the tighter binding reduces microphonics (Fukushima and Roeder, 1981).

Although double-sided flexible printed-circuit board, copper foil, solenoid and Helmholtz coil designs have previously been used to make NMR probes (Barker and Freeman, 1985), this is the first report of a dual-Helmholtz coil design enabling relatively inexpensive mass production via the photo-etch process and the flexible copper composite sheet, with an insulation process enabling autoclaveable coils without change in quality factor. Due to the relatively high melting point and insulation of the polyamide copper composite, Pyralux™, the present coils can resist high temperatures; however, any copper-composite would suffice. Thus, this coil design is superior for use with cell cultures where sterilization is essential.

The non-magnetic plastic holder, or stand, is shaped by a mill and lathe and could be designed for either a vertical- or horizontal-bore magnet. The stand enables reproducible placement of the bioreactor in the magnet permitting the comparison of MRIs and spectra. The bioreactor enables controlled temperature (±1°C), gas, and pH using recirculated media. Most cell culture media are formulated with a bicarbonate based buffering system. Therefore, we controlled pH by CO_2 sparging in the STAD (Fig. 3); however, this stringent pH control was not necessary for our short-term isolated rat hepatocyte experiments.

Flow studies of DMEM in the bioreactor revealed two spectral peaks for H_2O and P_i in ^{1}H and ^{31}P spectra, respectively, which may be attributed to bulk magnetic susceptibility (BMS) effects between the various compartments of the bioreactor. The linewidths and separation between the two peaks did not change with flow and appear to

UofF LIBRARY

be field sensitive because the peak separation is smaller for the ^{31}P spectrum. BMS effects on MRI have been misunderstood and underrepresented and depend, in part, on the orientation of bulk compartments with respect to the static magnetic field (B_0), paramagnetics in the solution of the compartments, and flow of solution through the compartments (Chu et al., 1990).

We demonstrate the feasibility of performing ^{13}C NMR spectroscopy using simple pulse sequences to eliminate the signal emanating from the bioreactor (Fig. 4A through C), however, the signal-to-noise ratio and the temporal resolution are not optimum. To monitor the kinetics of a ^{13}C-labeled compound will require either a ^{13}C pulse sequence to eliminate the broad component emanating from the bioreactor material (Fig. 4A) such as a spin-echo (Fig. 4B) or presaturation pulse since this signal dominates the ^{13}C spectrum, or a reverse detection pulse sequence, such as ^{1}H-observe ^{13}C-edit (POCE). Alternatively, direct detection of endogenous ^{1}H signal from the cell mass may be possible with gradient-enhanced (Mason et al., 1993) or diffusion-weighted spectroscopy (Van Zijl et al., 1991). However, work still remains to investigate these other pulse sequences.

Figure 5A and B demonstrate that T_2-weighted MRIs are superior to T_1-weighted MRIs in obtaining the best contrast between perfusate, bioreactor material and cell mass. The T_1-weighted MRIs revealed that the ECC and ICC become hypointense, and fiber pair 'ghosts' become more shifted and smeared in response to increased flow rate. Flow appears to be more rapid in the center than in the perimeter, especially in the area free from fiber pairs in prototype #1 (upper center right, Fig. 5A). The only published coronal MRI of a tricentric™ bioreactor is of prototype #2 (Custer, 1988). This study revealed that laminar flow increases in the ECC outlet and inlet in response to increased flow rate, and this laminar flow creates a greater perfusate velocity in the center of the ECC (Custer, 1988). Unfortunately, the flow rate through the bioreactor and MRI parameters were not given. The laminar flow appeared in the coronal MRI as a V-shaped hypointense region

UWSF LIBRARY

occurring at the inlet and outlet of the bioreactor. The hypointensity was attributed to fast moving nuclei that enter the image region without receiving an excitation pulse (Custer, 1988). There was no mention of fiber pair 'ghosts' in Custer's (1988) transaxial MRIs. We observed increased fiber pair 'ghosts' that shifted and smeared in response to increased flow rate. This could be due to magnetic susceptibility effects caused by the difference in magnetic environment between the fiber pairs and the flowing perfusate - the latter containing a BMS component. Why T_2-weighted MRIs are not as sensitive to flow as T_1-weighted MRIs is still unclear.

Various aspects of the tricentric™ bioreactor were characterized: (1) flow dynamics (2) cell inoculate distribution, (3) fiber integrity and wetting, (4) coil homogeneity, (5) inter-experimental quality control, and (6) percent recovery of cell mass for subsequent PCA extraction. These are demonstrated in the MRIs shown in Figures 6 and 7. The ability of our NCC 4.7T spectrometer to obtain 64 μm pixel resolution in the MRI was the reason MRI illustrates cell distribution. This pixel resolution is the maximum that our imaging gradient coil can obtain. A vertical-bore high-resolution NMR imaging spectrometer could achieve a pixel resolution as high as 0.1 μm (Johnson et al., 1993), permitting visualization of individual living cells. However, flow effects would be greatly accentuated and the present bioreactor would need to be miniaturized. This is the first study to use MRIs to characterize various aspects of NMR-compatible bioreactors. This is probably due to the fact that nearly all NMR studies of cells have been performed on high resolution NMR spectrometers.

^{31}P NMR spectroscopy revealed similar spectra between isolated hepatocytes perfused in the bioreactors and the *in vivo* liver (compare Figures 10C and 11A to 10D). Prototype #2 was able to maintain cell viability at tissue concentrations, but prototype #1 could not. This is probably due to the diffusion distance difference between the two bioreactors. For example, when prototype #1 maintained viability for over 4 hr in P_i-containing K-H buffer (Figs. 12 and 9) the cells were aggregated around the inner fiber

UUOF LIBRARY

where tissue densities were probably reached (Fig. 7D) yet, when completely packed with cells, prototype #1 was unable to maintain viability (Fig. 8A). The effective diffusion distance is 1,000 and 400 μm for bioreactors #1 and #2, respectively, when fully loaded with cells. It is the superior diffusion distance that Custer (1988) accounts for the superior antibody yield in the tricentric™ bioreactor compared to the hollow-fiber bioreactor. Custer (1988) used the prototype #2 design (i.e., inner fibers: 600 μm i.d., 800 μm o.d.; outer fibers: 1,200 μm i.d., 1,600 μm o.d.) for her studies, not prototype #1. Mass transfer models for both tricentric™ and hollow-fiber bioreactors have demonstrated Starling flow, or diffusion. The tricentric™ bioreactor has been proposed to have radial mass transfer, but this is difficult to directly show (Custer, 1988). Diffusion-weighted MRIs would be ideal to demonstrate that this exists in the tricentric™ bioreactor. The most generalized equation for modeling mass transfer in compartments of the bioreactor containing cells is (Gillies et al., 1986):

$$D_e d^2C_2/dr^2 + D_e/d \times dC_2/dr - R_2 = 0$$

where D_e is the effective diffusion coefficient for substrate within the cell compartment; C_2 is the concentration of substrate in the annular space; R_2 is the reaction rate for substrate in the cell; **d** is diffusion distance of the annular space; and **r** is half the diffusion distance of the annular space. From this equation it is apparent that decreasing the diffusion distance **d** will increase the mass transfer of nutrients to the cells. The MRI in Figure 7D shows that the cells were aggregated around the inner fiber, so the effective diffusion distance was less than, or at least similar to that of prototype #2. The complete mortality of hepatocytes in prototype #1 when completely filled with cells is probably due to its greater diffusion distance.

As evident in all of the MRIs obtained in this study, the inner fiber is not centered, but rather skewed to the side. Others have shown that cultured cells will center hollow

UVOF LIBRARY

fibers because the cells closest to the nutrient source will grow faster than the cells in more hypoxic regions. Custer (1988) observed from transaxial MRIs of prototype #2 that the majority of inner fibers were centered. This bioreactor contained an active cell culture occupying at least 25% of the annular space in prototype #2. It was not possible to clearly identify most of the inner fibers in Custer's two transaxial MRIs due to poor contrast and pixel resolution,. However, the majority of the inner fibers that are discernible do appear centered with respect to the outer fiber. In our study, the transaxial MRIs of tricentric™ bioreactors either fully packed with isolated rat hepatocytes or containing only perfusate revealed that the inner fiber is usually completely off-center, touching the inner wall of the outer fiber. Comparison of transaxial MRIs of prototype #2 obtained by Custer (1988) and in the present study, reveals that the inner fibers are off-center after cell inoculation and cell culture growth centers the inner fibers. At confluency, the inner fiber should be perfectly centered resulting in a two-fold decrease in the diffusion distance as compared to short-term NMR study of primary cells. Therefore, although prototype #1 was not successful in maintaining viability of isolated rat hepatocytes it may be successful with cell cultures.

Comparison of the ^{31}P spectra of isolated rat hepatocytes perfused in prototypes #1 (Figures 10C) and #2 (Figure 11A) demonstrate the ability to monitor bioenergetics with a temporal resolution of 38.5 and 8.8 min, respectively. Therefore, prototype #2 is feasible for ^{31}P NMR studies, but prototype #1 is not. In conjunction with trypan blue, LDH assay, and the β–NTP:total P_i ratio obtained by *in vivo* ^{31}P NMR, we maintained hepatocyte viability for up to 4 hrs perfusing with P_i K-H buffer. P_i-containing K-H buffer was necessary to maintain viability (Fig. 9). However, with the greater cell density obtained with prototype #2 (Fig. 11A), intracellular pH may be attainable if there is sufficient pH difference between cell buffer and P_i-. The apparent increase in β-ATP in both bioreactors is probably real due to recovery from the hypoxic stress imposed during isolation of rat hepatocytes. This increase is observed by comparing the ^{31}P spectra from

UWF LIBRARY

hepatocytes perfused in prototype #1 (Fig. 10C) and prototype #2 (Fig. 11A) to the spectrum of the PCA extract of hepatocytes taken just after isolation (Fig. 10B), which is composed of mainly sugar phosphates used in anaerobic glycolysis.

The graph of β-ATP levels in prototypes #1 and #2 shown in Figure 12 shows that hepatocytes became stressed by 2.5 hours of perfusion in prototype #2 as indicated by the decrease in β-ATP. This could be due to hypoxia. However, this is unlikely since the hepatocytes initially recovered from the hypoxic insult caused by isolation, and the diffusion distance of 200 μm is similar to that in liver *in situ* (Arias et al., 1988). Instead it is probably due to a lack of organic substrate such as glucose. The artificial liver developed in the hollow-fiber bioreactor (Shatford, 1992) is perfused with William's E perfusion media, which has a full complement of amino acids, glucose and proteins. Short-term toxicological studies of isolated rat hepatocytes are designed not for long-term culture of normal liver cells, but rather short-term (5 hr maximum) study of xenobiotic binding and metabolism studies. As evidenced from the ^{31}P spectrum of hepatocytes taken just after isolation, these cells are highly stressed, relying on anaerobic glycolysis to survive. We chose this minimal buffer, P_i-containing K-H to have direct significance to present toxicological studies. In other NMR studies of suspended hepatocytes (Cohen et al., 1978) and perfused hepatocytes (Farghali et al., 1992; Gasbarrini et al., 1992), 5.5 mM glucose was added to the K-H buffer. It is interesting that in the hepatocyte suspension study, the overall decrease in ATP levels was blamed on uncoupling of oxidative phosphorylation and not to hypoxia (Cohen et al., 1978). Therefore, future studies with prototype #2 should contain glucose in the K-H buffer in order to correlate results to our *in vivo* model.

In short, prototype #2 could be used with labeled ^{13}C compounds to monitor ^{13}C metabolites in the cells (Hrovat et al., 1985) and media (O'Leary et al., 1987) in dose-response studies, obtaining kinetics of endogenous compounds or xenobiotics in conjunction with indices of stress, (i.e., bioenergetics) using inter-leaved (Chang et al.,

UNIV LIBRARY

1987b) or sequential ^{13}C and ^{31}P NMR. Additionally, the bioreactor serves as a control of endocrine, immune, inter-organ cycling of nutrients, and physico-chemical parameters as compared to *in vivo* whole animal results. Magnetic resonance images with pixel resolution of 62 μm permits assessment of flow dynamics, fiber integrity, cell inoculum distribution, and quality control of the bioreactor. We found that insufficient fiber wetting appears hypointense in the T_2-weighted image, and it does not allow cells to enter the annular space because cell inoculate media needs to flow through the fibers leaving cells behind. Faster flow was associated with hypointensity in the MRIs, and the flow was faster in the ICC space than the ECC and annular spaces, and faster in the center of the ECC than the perimeter. This is predicted considering the cross section area is smaller in the ICC space, and the evidence of laminar flow in the ECC (Custer, 1988). Media flow or perfusion artifacts appeared above 20 and 50 mL/min for T_1-weighted images (TR=1s; TE=20ms) and T_2-weighted images (TR=4s; TE=80ms), respectively. Cell culture will need to be performed and high resolution MRIs obtained in order to determine if the inner fiber becomes centered due to differential cell growth. The hydrophobicity of the membrane is not a problem for spectral resolution and should not be a problem in culturing normal differentiated or dedifferentiated cells, since a biomatrix is necessary in any present bioreactor system, and the evolution of biomatrix coating of polystyrene petri dishes could serve as a guideline.

Future studies should be performed on normal acute metabolism using ^{13}C POCE and ^{31}P NMR to monitor metabolism of hepatocytes cultured in prototype #2. The culture medium should be adjusted, and biomatrices tested to maintain differentiated cells. In conjunction with the animal hepatic model described in Part II of this dissertation, this would serve to obtain the most complete database on xenobiotic toxicodynamics of any present combination of methods, and probably should have been carried out before this dissertation was submitted.

UMI LIBRARY

[illegible]

PART II: ANIMAL MODEL FOR XENOBIOTIC STRESS IN LIVER

CHAPTER 5

Review of Toxicological and *In Vivo* NMR Studies of Liver

UVDI LIBRARY

OVERVIEW

Since the mid-1970's, NMR spectroscopy has evolved into one of the most powerful techniques for non-invasive monitoring of biochemical concentration and flux, pH, enzyme kinetics, oxidation state, metal ion binding, compartmentation and molecular mobility (Gadian, 1989; James, 1975). *In vivo* NMR spectroscopy and MRI have been primarily used by the biomedical community. NMR studies of the liver have appeared in the literature from several groups (Cohen, 1991; Saini and Ferrucci, 1991). These studies have ranged from the investigation of normal biochemistry to biochemical consequences of toxicants. *In vivo* MRI and NMR spectroscopy are relatively new methods to the field of toxicology. Some recent toxicological studies have used ^{31}P NMR spectroscopy to follow the biochemical effects of CCl_4 (Hazle et al., 1991) and ethanol (Brauer and Ling, 1991), and attempts to determine the mechanism of toxic action of pentochlorophenol have been reported (Tjeerdema et al., 1991). However, it is difficult to make a clear determination of the biochemical mechanisms of toxicity based on *in vivo* ^{31}P NMR spectroscopy studies alone. Therefore, protocols using tissue extracts taken at the end of the experiment with subsequent *in vitro* analysis, and perfused cell studies have evolved. High resolution NMR analysis of tissue extracts permits quantification and identification of compounds containing NMR-observable nuclei and thus a significant amount of biochemical information.

Antioxidants may be the closest reality to Ponce De Leon's fountain of youth. Many prominent scientist believe the same, such as two-time Nobel Laureate Linus Pauling who consumed 10,000 g of Vitamin C daily. The antioxidant found nearly 4-fold in greater abundance than any other in the liver and the predominant in most other tissues is glutathione (GSH). GSH is a tripeptide (γ-L-glutamyl-L-cysteinyl-glycine) found in virtually all cells, and functions in metabolism, transport, immune response, and cellular protection (Dolphin et al., 1989; Tateishi and Sakamoto, 1983). It is the main endogenous antioxidant providing cellular protection either directly by transferring reducing power (H^+) to electrophilic agents, or indirectly by transferring to NADH or FADH to replenish reducing power to Vitamin E in the cell membrane or other antioxidants. Intracellular steady-state GSH concentrations depend on rate of synthesis, cell efflux, redox cycling of GSH, and conjugation of electrophilic compounds via glutathione S-tranferase (Dolphin et al., 1989; Reed, 1990b). Presently the primary means of non-invasive monitoring of GSH levels is by enzymatic or chemical analysis of blood plasma or radiotracer studies (Andersen, 1985; Chasseaud, 1988; Hayes et al., 1987). These studies suffer from the inability to directly monitor GSH in real time, correlate proximal and temporal GSH changes within the same individual, and correlate *in vivo* enzyme function with *in vitro* activity. All NMR studies performed to date that monitored GSH have used erythrocytes or cells immersed in D_2O for ^1H NMR (Rabenstein and Keire, 1989) or ^{13}C NMR spectroscopy (Gamcsik and Colvin, 1991). We have observed a large contribution from water and poor linewidths in ^1H MRS of rat liver *in vivo*. Therefore, we decided to pursue efforts in using ^{13}C NMR spectroscopy to monitor GSH *in vivo*.

The goal of this project was to develop an *in vivo* NMR animal model for non-invasive monitoring of early toxicological biomarkers of stress, such as GSH, bioenergetics, and intracellular pH in conjunction with NMR analysis of tissue extracts

UVOI LIBRARY

and body fluids containing excreted xenobiotics. This approach provides an extensive data base and novel application of NMR technology to the area of toxicology.

In order to test our animal model, we have proposed to examine the mechanism of toxic action of dibromoethane (DBE), an alkylating agent and carcinogen. It has been proposed that intracellular GSH protects against DBE toxicity (Warren et al., 1991). DBE is used extensively for fumigants, gasoline additives, solvents, and precursors of haloalkanes (Petersen and Guengerich, 1988), and is a common contaminant in groundwater (Barbash and Reinhard, 1989). The LD_{50} (gravage) of DBE is 117 mg/kg in female rats (NTP, 1982). DBE is a carcinogen and an acute toxin for the rat and other species (Macdonald, 1983). It is metabolized by direct conjugation with GSH and subsequent hydrolysis, or oxidized via cytochrome P-450 and subsequent conjugation with GSH. This bioactivation leads to toxic intermediates (Fig. 1) that bind DNA, glutathione, and protein thiols (Petersen and Guengerich, 1988). DBE was chosen for this study not only because of its environmental significance, but also because: (1) its metabolism and excretion have been extensively studied (Botti et al., 1989; Kitchin and Brown, 1986; van Bladeren et al., 1981; Warren et al., 1991); (2) metabolism of DBE is not extensive, it is bioactivated via GSH conjugation or P450 oxidation (Macdonald, 1983) (Fig. 1);

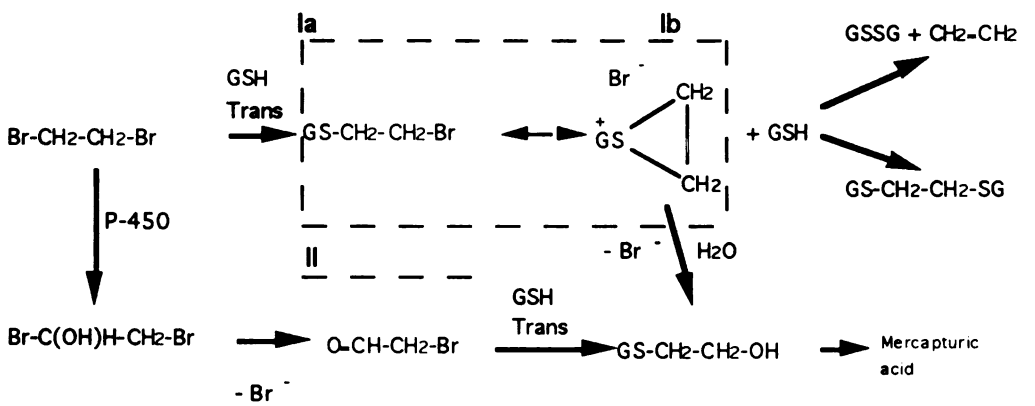

Figure 1: Major metabolic pathways for 1,2 dibromoethane (x=Br). Proposed reactive metabolites are framed except II (Ia, GSH conjugate; Ib, episulfonium ion, and II, bromoacetaldehyde).

(3) treatment of rats with DBE is not expected to cause substantial lipid peroxidation *in vivo* (Warren et al., 1991), which greatly simplifies data interpretation for accomplishing the objectives of this proposal. *In vivo* studies have shown that shortly after treatment with DBE there is a substantial reduction in GSH (Botti et al., 1989; van Bladeren et al., 1981; Warren et al., 1991)

In Vivo NMR Spectroscopy of Liver: Few toxicology studies have been performed using NMR spectroscopy. This technique is the only one presently available that could potentially monitor GSH, bioenergetics, and pH simultaneously using interleaved ^{13}C and ^{31}P NMR. *In vivo* ^{31}P NMR spectroscopy of the liver has been performed in mice, rat, rabbit, and humans since 1980. A review of this literature is given in Chapter 1. For the *in vivo* ^{31}P NMR spectrum of rat liver, individual metabolites cannot be resolved in the phosphomonoesters (PME), and phosphodiesters (PDE) regions of the *in vivo* spectrum due to spectroscopic imperfections and biochemical contaminants, such as iron. A high resolution ^{31}P NMR analysis of perchloric acid extracts of the rat liver permits one to identify the individual peaks contributing to the PME and PDE signals. Tissue can be obtained at the end of a ^{31}P MRS experiment and extracted for subsequent metabolite identification and quantification by NMR, chromatographic or other analytical method.

In vivo ^{13}C NMR studies of perfused liver and liver from intact animals have monitored natural abundance ^{13}C and ^{13}C-labeled compounds to determine metabolite composition, and metabolic processes, flux, regulation, and disease states (Cohen, 1991; Seelig and Burlina, 1992). Few *in vivo* ^{13}C NMR studies have been performed with the goal to determine toxicodynamics. Natural abundance ^{13}C studies have monitored metabolite composition, such as glycogen (Jue et al., 1989; Knuttel et al., 1991) and lipids (Canioni et al., 1983). Several biochemical processes have been investigated with ^{13}C-labeled compounds, such as: gluconeogenesis using ^{13}C-labeled glucose (Alger et al., 1981; Jehenson et al., 1992; Kunnecke and Seelig, 1991; Reo et al., 1984; Sillerud and

UVDI LIBRARY

[redacted]

Shulman, 1983; Stevens et al., 1982), alanine, and pyruvate (Stromski et al., 1986); β-oxidation and ketogenesis (Cerdan et al., 1988; Cross et al., 1984; Pahl-Wostl and Seelig, 1986; Pahl-Wostl and Seelig, 1987); the homonal effect on lipogenesis and flux through the TCA cycle (Cerdan et al., 1988; Cohen, 1983; Cross et al., 1984; Pahl-Wostl and Seelig, 1986; Pahl-Wostl and Seelig, 1987); and disease states such as diabetes (Cohen, 1987b; Cohen, 1987c) and cancer (Liu et al., 1991). One study administered 3-^{13}C-alanine and successfully labeled GSH in perfused rat liver, but it coresonated with a much larger peak from 4-^{13}C-glutamate. This is also the first *in vivo* ^{13}C NMR study to investigate the toxicodynamics of a toxicant, ethanol (Cohen, 1987a).

Recently, the first successful *in vivo* ^{13}C NMR toxicokinetic study to determine hepatic dose curves of intraperitoneally injected ^{13}C-labeled 2,2-dichloro-1-(2-chlorophenyl)-1-(4-chlorophenyl)-[3-^{13}C]-propane (DDP). DDP is an ideal xenobiotic for toxicokinetic study by *in vivo* NMR because the inherent problem of poor NMR sensitivity is overcompensated for by the its toxicological characteristics. DDP is slowly metabolized, it is a relatively nontoxicant, and it concentrates in the liver. This results in slow toxicokinetics, optimal signal in the organ of interest, and large doses can be administered due to its low toxicity. For example, maximal hepatic ^{13}C-DDP concentrations were reached until two days post-administration, and relatively high doses, 200 - 500 mg/kg, were administered. However, a high field NMR spectrometer (9.4 T) with a long acquisition time (1,024 transients) was still necessary to obtain suffient signal. Therefore, *in vivo* ^{13}C NMR is has proven very successful in monitoring the kinetics of ^{13}C-labeled endogenous compounds and ^{13}C-DDP, however, potent toxicants with rapid kinetics may be below the detection limit of ^{13}C. More sensitive NMR-observable nuclei, such as ^{3}H, are better.

The most powerful advance in ^{13}C NMR has been isotopomeric analysis which permits the determination of metabolic regulation and flux through various biochemical pathways such as TCA and the hexose monophosphate shunt (London, 1988a).

UVDI LIBRARY

RECEIVED

Isotopomeric analysis is the only technique available to biochemist for the investigation of metabolic flux and very effective in determining metabolic regulation. The combination of isotopomeric analysis and the low natural abundance of ^{13}C (1.1%) makes this the best NMR-observable nuclei for *in vivo* NMR investigation of toxic mechanism(s) of action. ^{13}C-labeled compounds can be enriched and selectively monitored similar to ^{14}C radiotracer studies. However, unlike ^{14}C radiotracer studies, *in vivo* ^{13}C NMR permits the non-invasive monitoring of ^{13}C-labeled compounds within the tissue of interest, while isotopomeric analysis of ^{13}C spectra permits identification and ^{13}C enrichment of the various carbon positions in labeled metabolites. Together, *in vivo* ^{13}C and ^{31}P NMR and isotopomeric analysis permit the non-invasive determination of toxicokinetics, mechanism(s) of xenobiotic biotransformation, and toxicodynamics.

UUI. LIBRARY

Stategies for Monitoring Glutathione in Rat Liver by *In Vivo* NMR Spectroscopy: All studies performed to date that monitored GSH have used erythrocytes or cells immersed in D_2O applying ^{1}H NMR (Rabenstein and Keire, 1989) and labeled glycine with ^{2}H or ^{13}C (York et al., 1987) or perfused with culture medium containing ^{13}C-labeled compounds for ^{13}C NMR spectroscopy (Gamcsik and Colvin, 1991). We have observed a large contribution of water and poor linewidth in ^{1}H NMR of rat liver *in vivo*, and substantial overlap of resonances in the region from 1-5 ppm. However, the amide resonances are between 8 and 10 ppm and could serve as a possible means to monitor GSH (Fig. 2A). These peaks are broad because of exchange with bulk water and relaxation due to the attached quadrupolar nucleus ^{14}N. Therefore, we explored the possibility of monitoring GSH in liver by decoupling the quadrupolar relaxation effect, relaxation of the second kind (James, 1975). Since ^{1}H has 64-fold greater sensitivity than ^{13}C for comparable nuclei, this would not require infusion of labeled compounds and could possibly be clinically useful. Figure 3 shows ^{1}H NMR spectra of pure formamide (structure given in above figure) with ^{14}N coupling and decoupling, demonstrating the

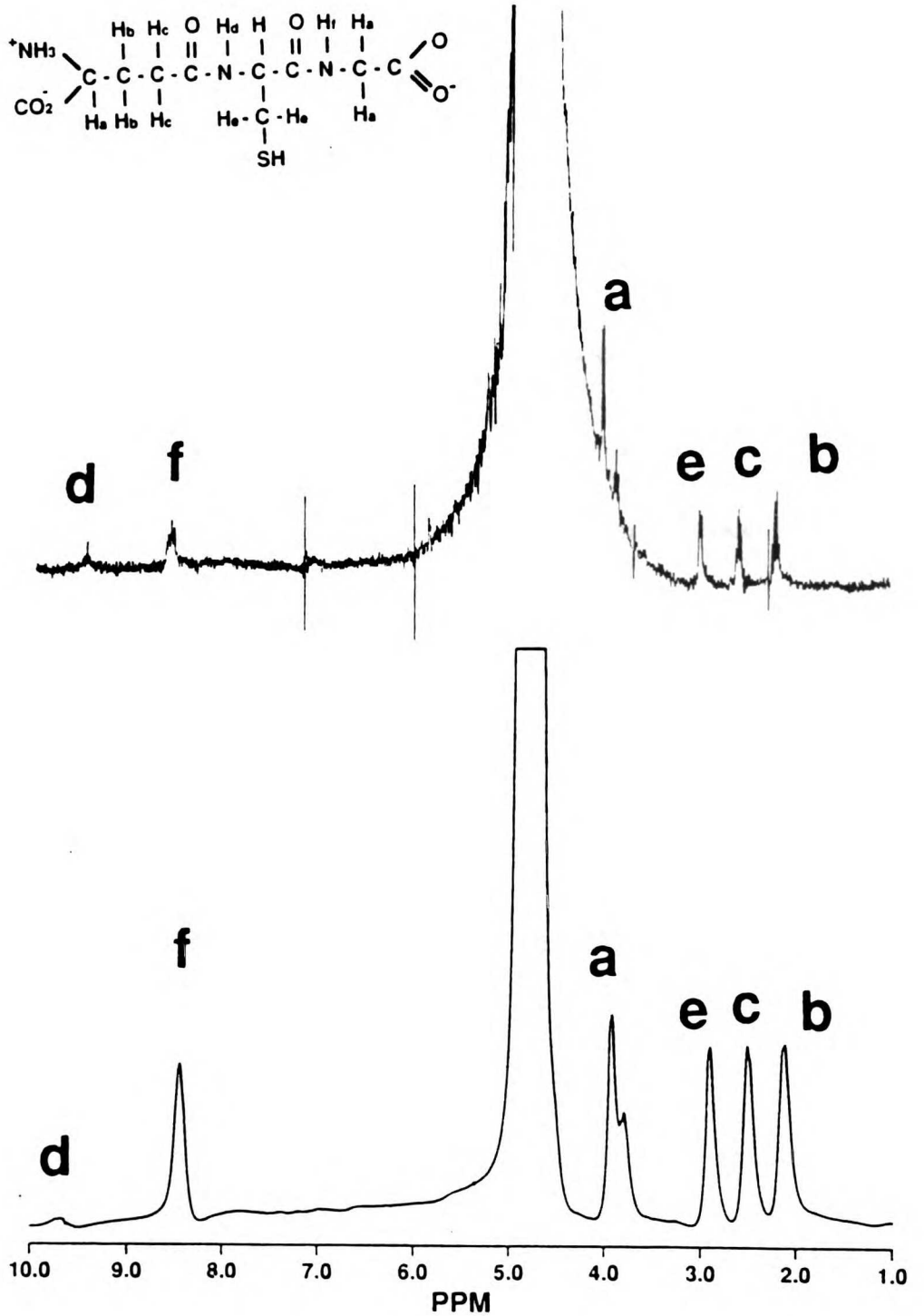

Figure 2: ^{1}H NMR spectra of GSH using 50 mM and 300 MHz high resolution QE300 spectrometer (A), and 300 mM and 200 MHz NCC 4400 Quest 4.7T spectrometer (B). Spectrum B is ^{14}N decoupled and was the same as the coupled spectrum obtaine on the NCC 4.7T spectrometer (not shown). The stucture of GSH is inset.

[redacted]

resolution enhancement of ^{14}N decoupling. Unfortunately, the broadening of the amide protons *in vivo* are apparently due primarily to exchange with water protons and, according to equations given for both of these relaxation effects (James, 1975) and known exchange rates for these amides of 100 ms (York et al., 1987), the spin-lattice (T_1) relaxation of the ^{14}N must be less than 100 ms since no effect was noticed with ^{14}N decoupling on physiologically relevant solutions of GSH.

Therefore, we decided to pursue ^{13}C NMR spectroscopy to monitor GSH *in vivo.* Chapter 6 describes our attempts to use 2-^{13}C-glycine infusion to monitor GSH in rat liver by *in vivo* NMR spectroscopy, and Chapter 7 describes our attempts to increase the in vivo GSH signal and an application of the animal model for studying the effects of DBE.

UUU LIBRARY

[illegible]

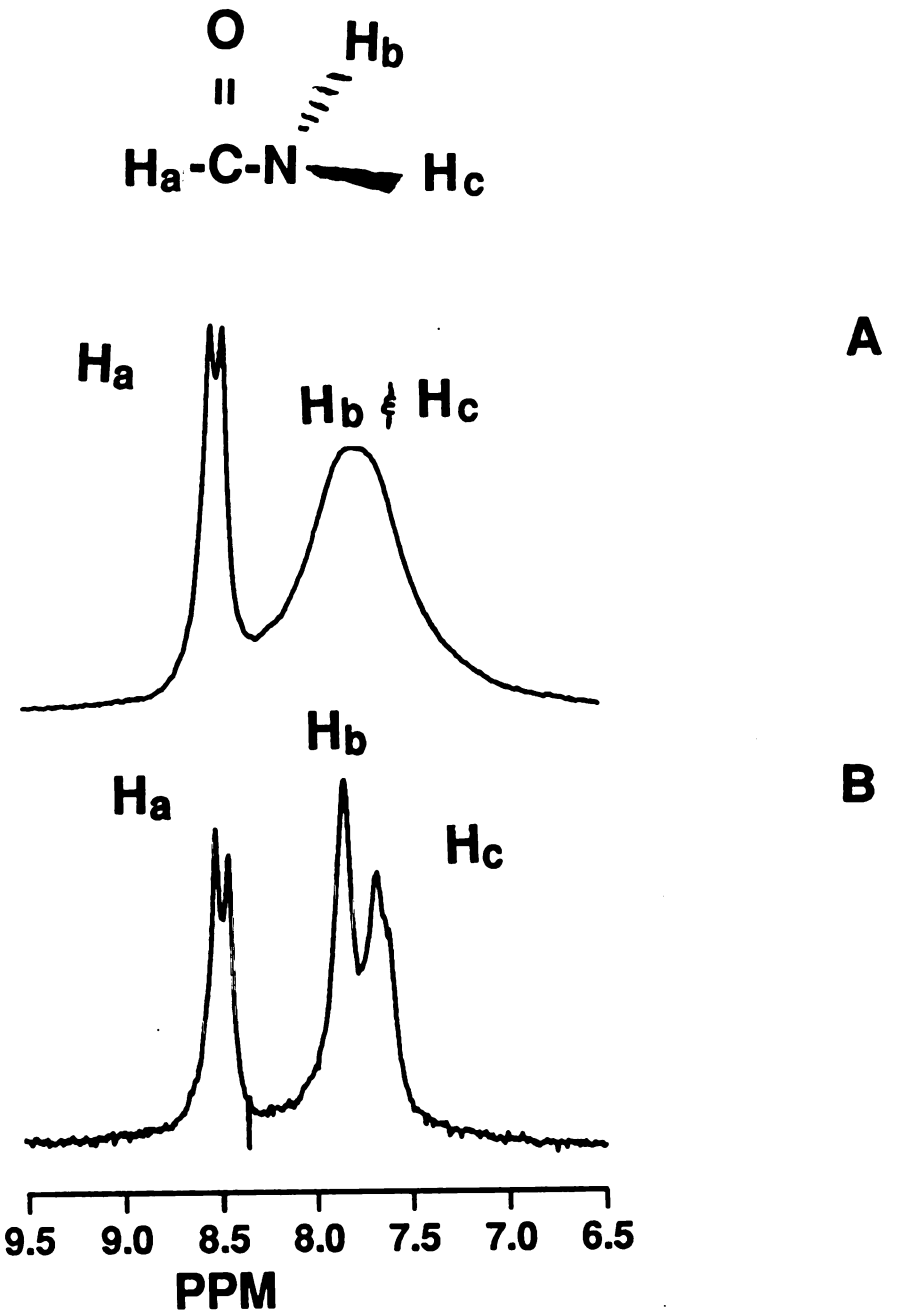

Figure 3: ^{1}H NMR spectra of ^{14}N coupled (A) and ^{14}N decoupled pure formamide (B). Performed at 23 °C, 200 MHz on a 23 cm usable horizontal bore magnet, using an 8-turn solenoid to decouple ^{14}N and a Helmholtz coil to observe ^{1}H.

CHAPTER 6

In Vivo Monitoring of Hepatic Glycine and High Energy Phosphorus Metabolism in Anesthetized Rat by ^{13}C and ^{31}P NMR

INTRODUCTION

Toxicology research has recently been under political and ethical pressure to reduce the number of animals used in acute and chronic studies. Presently the most accepted approach to this is to use quantitative structure analysis (QSAR) and toxicokinetics to predict the disposition, biotransformation, and distribution of toxicants and thus their potential risk (Krewski et al., 1994). This approach still needs at least one set of animal experiments to significantly assess the success of the QSAR prediction. This is a savings in animals usage by $\mathbf{x = nr - n}$, where **x** is the number of animals conserved per study, **r** is the number of time points taken per study and **n** is the number of animals used per time point. Using this method, some xenobiotic risk predictions can be as high as 75% or below 40% correct (Krewski et al., 1994). *In vivo* NMR also has the same equation for animal reduction, permits non-invasive monitoring of actual biochemical effects of xenobiotics, and even xenobiotic biotransformation directly in the tissue of interest. In conjunction with tissue extraction and body fluid analysis, one can determine NMR-observable nuclei and xenobiotic tissue distribution, disposition, biotransformation, and pharmacodynamics. We describe an *in vivo* NMR animal model that enables the non-invasive monitoring of glycine, high energy phosphate compounds, phosphomono and diesters kinetics and metabolism, intracellular pH, and with tissue extract and body fluid NMR analysis, we can determine effects on many biochemical processes and physiological function.

UVOL LIBRARY

As discussed in Chapter 4, we decided to employ *in vivo* ^{13}C NMR to monitor hepatic GSH in the rat. At the start of this study, I focused only on that biochemical reaction which would accomplish our goal of labeling GSH, i.e., that catalyzed by GSH synthetase, which combines glycine with γ-glucys. The *in vivo* and extract ^{13}C NMR spectra were not this simple; GSH did not appear as a peak isolated from any other glycine metabolite. It became apparent that I needed to understand all of the glycine metabolic pathways in order to interpret the data and hopefully manipulate the biochemistry to attain our objective of monitoring hepatic GSH *in vivo*. To quote Neuberger (1981) who was the first to study ^{15}N-glycine metabolism in humans, and which was later quoted in the glycine review by Jackson (1991) understanding the biological reactions of glycine is "a large slice of the biochemistry of metabolism." The present work determines the most complete disposition, biotransformation, and organ cycling of glycine of any one single study by use of *in vivo* NMR and high resolution NMR spectroscopic analysis of tissue extracts and body fluids.

Glycine was the first amino acid to be isolated from a protein (Neuberger, 1981) It is a glucogenic, non-essential, and sole non-chiral amino acid which participates in a variety of biochemical reactions, particularly in liver. Figure 1 depicts the fate of glycine absorbed from the blood by the liver (Devlin, 1986; Snell, 1983; Stryer, 1981). Glycine is transported into the hepatocyte by a Na^+-dependent transporter, *gly* (Moseley et al., 1988), and a glutathione-dependent transporter, γ-glutamyltranspeptidase, the latter forming γ-glugly (Meister, 1989) and, once inside the hepatocyte, glycine follows many biochemical pathways (Fig. 1). For example, it provides the C2 and C3 of serine (Snell, 1983) eight carbons and the four nitrogens of heme, the C4,5 and N-7 of purines (Stryer, 1981), C4 and N-5 of creatine (Devlin, 1986), and directly forms the glycine residue in GSH, xenobiotics conjugation, γ-glugly, and proteins. It can be metabolized to lactate and alanine via anaerobic glycolysis, to glucose or glycogen via gluconeogenesis, to fatty acids and phospholipids via lipogenesis, and to anaplerotic products of the tricarboxylic

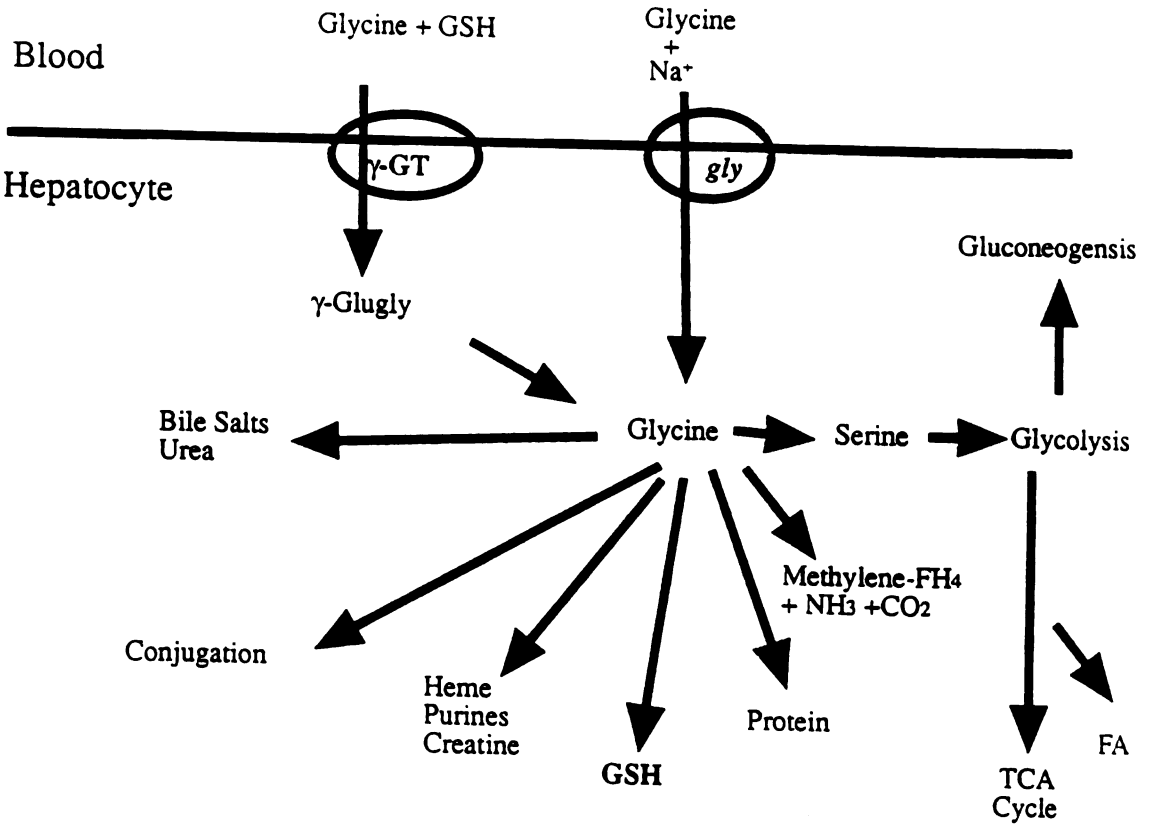

Figure 1: A diagram depicting the many metabolic pathways in which glycine is involved. Abbreviations: GSH, glutathione; GT, γ-glutamyl transpeptidase; FA, fatty acids; FH, tetrahydrofolate.

acid cycle (Jackson, 1991; Kornberg, 1966; Neuberger, 1981). Glycine is catabolized to CO_2 and ammonia with formation of methylene tetrahydrofolate by the mitochondrial glycine cleavage system or glycine dehydrogenase (Hampson et al., 1984; Jois et al., 1992). It forms bile salts and osmolytes (i.e., oxalate, betaine, choline), which are excreted (Devlin, 1986), and products from anaplerosis and the ureolysis (Harper, 1983; Stryer, 1981). The 'glycine cycle' occurs in the mitochondria and has been proposed to be a coupling of glycine dehydrogenase to serine methoxytransferase with the net reaction:

$$\textbf{2 Glycine + NAD}^{+} \text{ --> } \textbf{Serine + CO}_2 \textbf{ + NH}_4^{+} \textbf{ + NADH + H}^{+}$$

thus creating reducing equivalence for oxidative phosphorylation, and permitting serine to enter gluconeogenesis (Snell, 1983). This is supported by radiotracer studies that found equal labeling at C2/C3 with 2% glycine in the diet, but with 0.5% glycine in the diet, the radioactivity of the C3 was only 20% of the C2 of serine. The percent utilization of glycine by this reaction is greater in carnivores than in herbivores (Neuberger, 1981). We present results of hepatic glycine metabolism as it occurs in rat liver using *in vivo* ^{13}C NMR spectroscopy.

We have developed a triple-tuned NMR surface coil to determine the fate of glycine in rat liver. *In vivo* ^{13}C NMR spectroscopy of 2-^{13}C-glycine is ideal to non-invasively monitor antioxidant status (GSH) and metabolic processes because of its biochemical fate (Fig. 1) and its spectroscopic isolation from other major liver metabolites in the *in vivo* ^{13}C NMR spectrum. In particular, we were interested in GSH, a tripeptide (γ-L-glutamyl-L-cysteinyl-glycine), found in virtually all cells, exhibiting a key function in cellular metabolism, transport, immune response, and protection from chemical injury (Dolphin et al., 1989). GSH is maintained at high concentrations in rat liver, as high as 8 mM (Taniguchi et al., 1989), and therefore should become ^{13}C-labeled to a higher degree than other glycine metabolites. γ-glutamyl transpeptidase is expressed

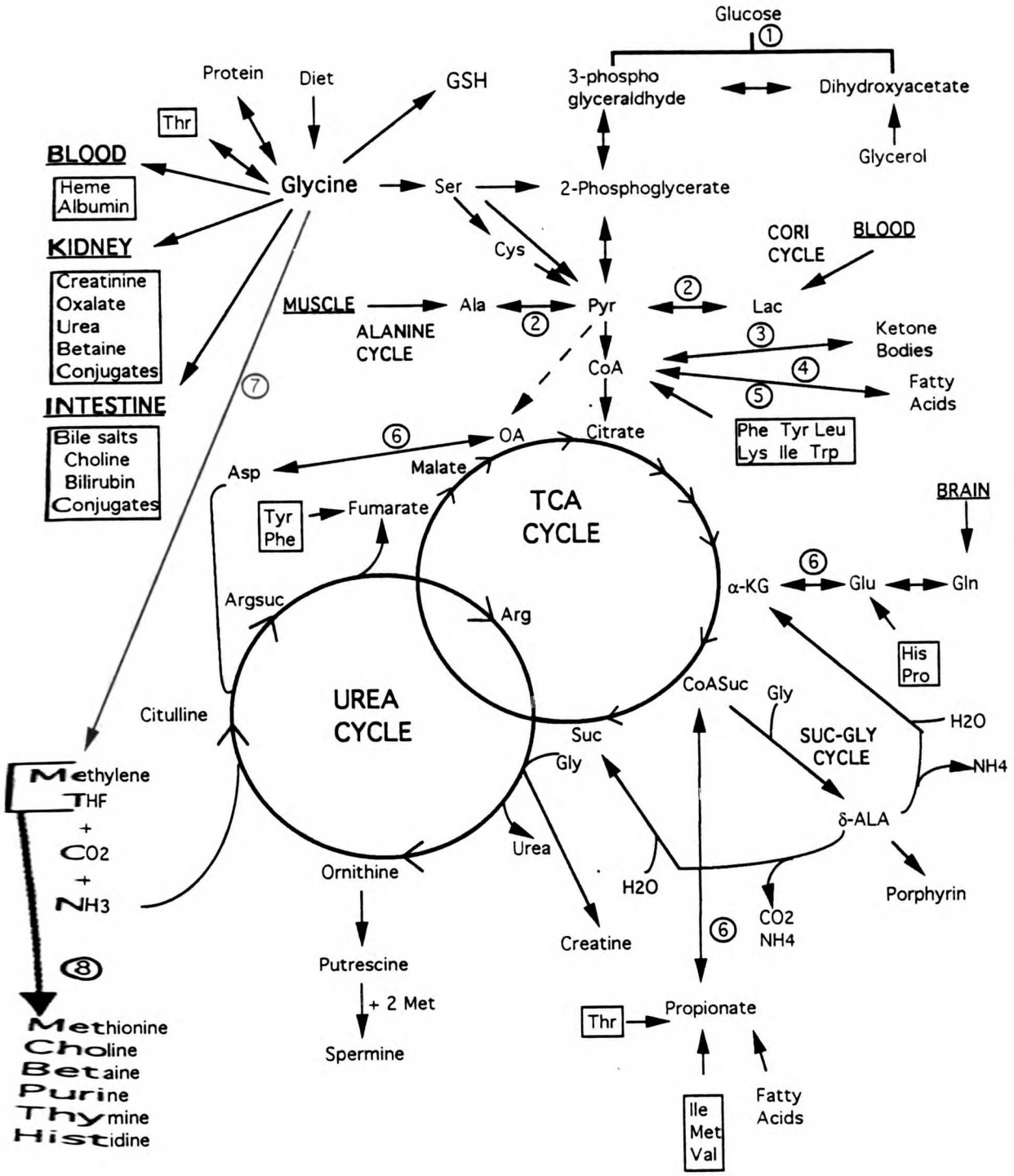

Figure 2: The many biochemical pathways, inter-organ cycles, and relation to other amino acids in which glycine participates. The following numbers represent the various biochemical processes: 1, gluconeogenesis; 2, anaerobic glycolysis; 3, ketogenesis; 4, lipogenesis; 5, lipolysis; 6, anapleurosis; 7, glycine cleavage involved in the glycine cycle; 8, methylation.

at high concentrations in rat liver canalicula (Inoue et al., 1983), and the intracellular concentration of γ-glugly would depend on glycine and GSH blood concentrations and γ-glutamylcyclotranspeptidase activity (Meister, 1989) In addition, biochemical and physiological processes can be monitored with 2-^{13}C-glycine. Figure 2 illustrates the relation of glycine to eleven biochemical processes, liver-organ metabolite cycles, and other amino acids.

Observation of NMR signals in intact liver, however, suffers from additional difficulties due to respiratory motion, magnetic susceptibility effects and shorter spin-spin relaxation (T_2) times from high concentrations of paramagnetic species, leading to low spectral resolution. There has been no report of *in vivo* NMR monitoring of *in situ* hepatic GSH or γ-glugly in any species. We describe here an animal model which employs a novel, surgically-implanted, triple-tuned, surface coil to monitor *in situ* glycine metabolism and kinetics using *in vivo* ^{13}C NMR following intravenous infusion of 2-^{13}C-glycine. Concomitantly, we monitor bioenergetics and intracellular pH by ^{31}P NMR. Analysis of tissue extracts by high resolution NMR permits determination of kinetics, NMR visibility, ^{13}C enrichment of metabolite pools, identification of metabolites containing ^{13}C or ^{31}P, and isotopomeric analysis for investigation of various biochemical processes (London, 1988a). Body fluid analysis permits investigation of kidney function and elimination kinetics of glycine conjugates.

MATERIALS AND METHODS

Chemicals: Glycine (99% $^{13}C_2$-labeled) was purchased from Isotec Inc. (Miamisburg, Ohio) pentobarbital from Anthony Products (Arcadia, California), 20% dextrose solution and saline solution from Abbott Labs (Chicago, Illinois). Mannitol, perchloric acid, KOH, choline, N-dimethylglycine, betaine, sarcosine, γ-glugly, cysgly, L-serine, 3-

phosphoglycerate, oxalate, L-cysteine, cystathionine, and 99.96% deuterium oxide were obtained from Sigma Chemical Co (St. Louis, Missouri).

NMR Probe Design: We constructed a coaxial, dual-slotted surface coil with a single- and double-tuned circuit. The coil was photo-etched onto UV-sensitive pc board [(Fan, 1989) and made rigid with epoxy and fiberglass. The outside coil (diameter 24 mm) was single-tuned to the ^{1}H frequency (200.11 MHz), the inside coil (diameter 13 mm) was connected to a balance-matched, double-tuned $^{13}C/^{31}P$ circuit (Chang et al., 1987a). After implantation in the abdominal cavity, the coil was bolted to a plastic stand via screw and wing nuts to insure reproducible placement in the isocenter of the magnet's field and to avoid coil movement (Fig. 3A). A glass sphere containing 40% dioxane was placed in the center of the surface coil as a reference.

Animal Protocol: All animal studies were approved by the UCSF Committee on Animal Research. Female Sprague-Dawley rats (240-260 g) were anesthetized with pentobarbital (50 mg/kg via intraperitoneal injection), and the femoral artery and vein were cannulated with PE-50 tubing for blood pressure and blood gas monitoring, as well as fluid and drug infusion. The rats were mechanically ventilated through a tracheal tube. An abdominal L-shaped incision was made, and the surface coil was inserted in the peritoneal cavity above the liver and held in place with sutures to the abdominal wall (Fig. 3B). The rats were placed on the cradle in a supine position. After obtaining baseline spectra, the rats received an intravenous infusion containing 4.4 mM/kg/hr 2-^{13}C-glycine, 10% glucose, 4% mannitol, and 7 mg/kg/hr pentobarbital at an infusion rate of 3 mL/hr for 4 hr. Blood samples were obtained every hr or as necessary, and plasma and blood were separated, centrifuged, and frozen in liquid N_2. Urine was collected through a transuretral catheter every 1-1.5 hours.

NCSE LIBRARY

After the experiment, the animals were quickly disconnected from the circuit, the coil extricated, and the liver excised and immediately submerged in liquid N_2 for subsequent extraction by perchloric acid (PCA). Less than 5 min passed between the time the last ^{13}C spectrum was completed to the time the liver was frozen in liquid N_2 with the actual dissection lasting less than 10 sec. PCA tissue extracts were prepared as described previously (Higashi et al., 1989), and titrated with KOH. The liver was powderized by morter and pestle under constant liquid N_2 conditions, weighed, and 0.6N (6%) PCA was added at a volume-to-weight ratio of 2:1. The mixture was then placed on ice in a centrifuge tube until thawed. The cell mass was pelleted by centrifugation at 15,000 rpm for 10 min. The supernatent was titrated to pH 7.40 and centrifuged (15,000 rpm for 10 min) to pellet the perchlorate salts. The supernatent was then frozen in liquid N_2 for lyophilization. The lyophilate was stored at 0°C. Tissue extracts, urine, blood, and plasma were lyophilized immediately after each experiment. Some plasma samples were deproteinized by titration to pH 4.0 and centrifugation. Samples were analyzed by high resolution NMR.

To evaluate the γ-glugly and GSH kinetics, a pulse-chase study was performed. Rats were given intraperitoneal injections of 4.4 mM/kg of 2-^{13}C-glycine and rats were placed in cages with water but no food. Rat livers were dissected at various times after the bolus injections, frozen and subjected to PCA extraction (see Animal Protocol section).

In Vivo Spectroscopic Studies: *In vivo* spectroscopic experiments were performed using a Nalorac Cryogenics Corporation Quest 4400 NMR imaging spectrometer (NCC, Martinez, CA) connected to a 4.7 Tesla horizontal bore (16 cm usable bore) Oxford magnet. The ^{1}H coil was used to optimize the static magnetic field homogeneity by shimming on the $^{1}H_2O$ proton resonance, using a 90° flip angle, until water linewidths in the range of 50-80 Hz were obtained. The in-plane 180° pulses for ^{1}H, ^{13}C, and ^{31}P were

calibrated using a microsphere containing 2 M 2-^{13}C-glycine. The in-plane 90° pulse was determined for ^{13}C using 40% dioxane at the beginning of each experiment. ^{13}C spectra were obtained at 50.3 MHz with decoupling of protons during acquisition and quadrature phase detection. Partially relaxed spectra were obtained from 144 single-pulse transients with a 70° flip angle, 2K data points, a sweep width of ±4500 Hz and a repetition time of 1 sec, yielding a total acquisition time of 9.6 min. The 90° pulse for ^{31}P was calculated from the ^{13}C pulse determined at the beginning of each experiment and using the difference 90° pulse length of standards. ^{31}P spectra were obtained at 81 MHz using a one-pulse sequence, with the same parameters as described above except the repetition time was 1.2 sec, yielding a total acquisition time of 8.8 min. Prior to Fourier transformation, time domain data were processed with a Lorentzian (-20 Hz) to Gaussian (20 Hz) or just Gaussian (18 Hz) transformation. ^{13}C and ^{31}P spectra were plotted and referenced to dioxane and α-NTP at 68.0 and -7.5 ppm, respectively. GSH and glycine were identified *in vivo* by determination of the CH coupling constant in a coupled spectrum. The elimination rate and half-life of glycine was determined by a first-order fit, using the program Cricket Graph, from the three individual experiments where the slope is equal to the elimination rate (k) and half-life is: $t_{1/2}$=0.693/k (Rowland and Tozer, 1989). The average k and $t_{1/2}$ values were determined from the three experiments.

In Vitro Spectroscopic Studies: NMR spectra of liver extracts dissolved in deuterium oxide, were obtained using GE QE-300 (^{13}C, ^{31}P) , and GN-500 (^{1}H) spectrometers operating at ^{1}H frequencies of 300 and 500 MHz, respectively. ^{1}H spectra were obtained to determine the fractional ^{13}C enrichment by difference spectroscopy using a modified sequence previously reported (Bendall and Dodrell, 1981), and as described in the Figure 8 legend. We used a second method to determine the fractional ^{13}C enrichment of glycine (Behar, 1986), which compares the coupled and uncoupled peak areas in the ^{1}H spectrum obtained with a one-pulse sequence. To account for NMR inaccuracies

associated with difference spectroscopy, we multiplied the fractional ^{13}C enrichment values by a correction coefficient - which was the ratio of the fractional ^{13}C enrichment value obtained from a one-pulse ^{1}H spectrum (Behar, 1986) to that obtained by difference spectroscopy (Bendall and dodrell, 1981). ^{13}C and ^{31}P spectra were obtained using a one-pulse sequence with decoupling during acquisition and a 10 sec interpulse delay, 16K complex points and a spectral width of ±10000 Hz (^{13}C) or ±4000 Hz (^{31}P). Natural linewidths are shown in Figures 4A, 7, 8, and 9. ^{13}C and ^{31}P compounds were identified by comparison of extract chemical shifts and CH coupling constants to those of known standards, literature values, and known glycine biochemical pathways. ^{13}C and ^{1}H spectra were referenced to 3-(trimethylsilyl)propionic-2,2,3,3-d4 acid at -2 and 0 ppm, respectively, while ^{31}P spectra were referenced to the α-NTP peak at -7.5 ppm. All peak areas were fitted using the program MacFID (Tecmag Inc. Houston, Texas).

RESULTS

To monitor glycine metabolism by *in vivo* ^{13}C NMR in rat liver we employed an implanted coaxial dual-slotted photo-etched triple-tuned NMR surface coil (Fig. 3B) bolted to a plastic stand (Fig. 3A), which greatly reduces coil motion and decreases shimming time by insuring reproducible placement of the coil. We used a one-pulse sequence with proton decoupling during acquisition only. Even though the ^{1}H coil was well-insulated with epoxy, sensitivity gain via the nuclear Overhauser effect with continuous proton irradiation was not attempted to avoid local heating of the liver (Bottomley and Roemer, 1992). The dioxane standard and glycine served to monitor decoupling throughout the experiment.

Figure 4A through C shows a portion of representative *in vivo* and *in vitro* (extract) ^{13}C NMR spectra of a rat liver. The *in vivo* ^{13}C spectra were obtained before (t=0) and 230 min after start of ^{13}C-glycine infusion (Figs. 4B and C, respectively). Both

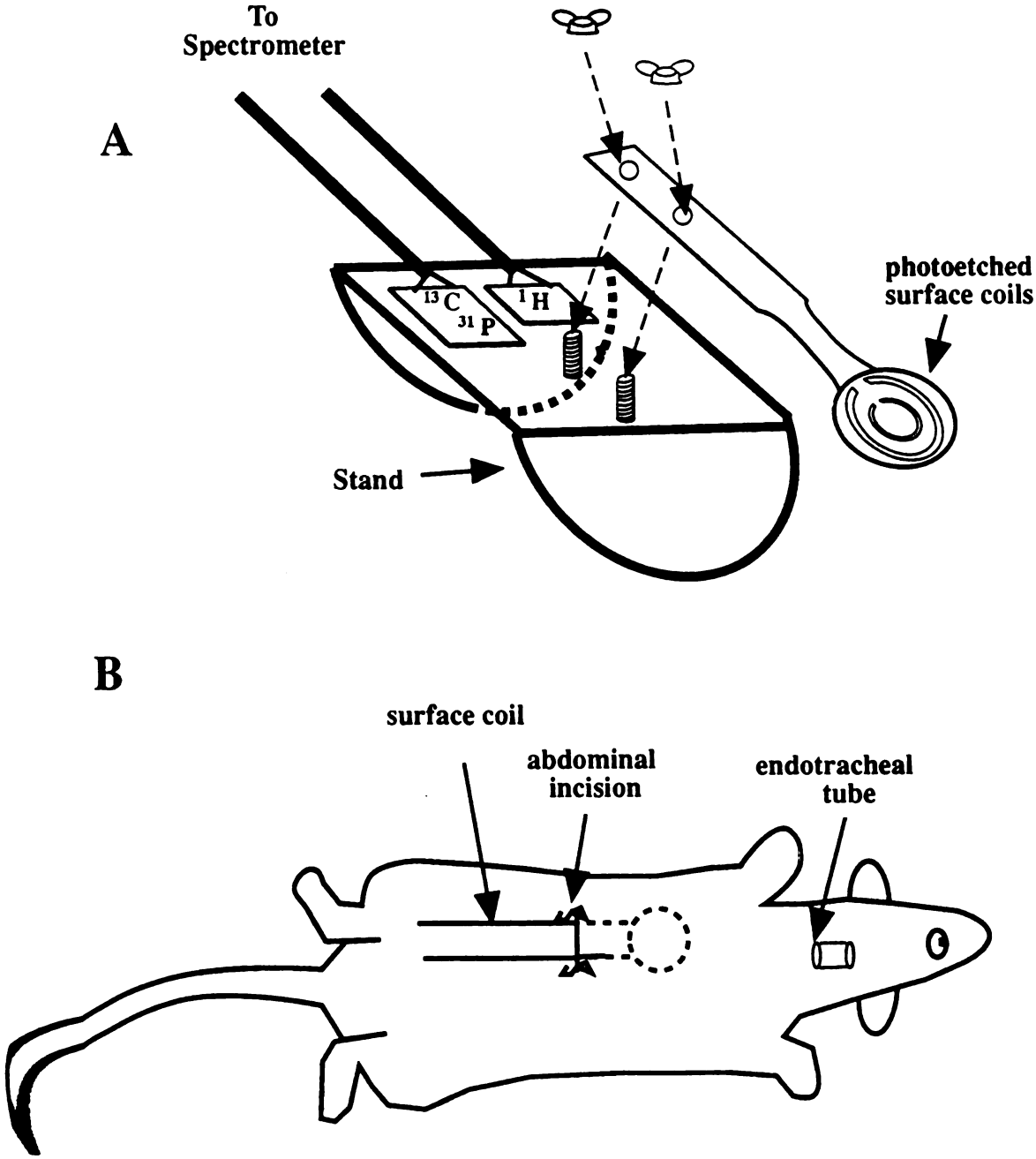

Figure 3: Schematic representation of (A) the coaxial dual-slotted photo-etched surface coil and plastic stand, and (B) the surface coil implant in a rat. After the surface coil is implanted in the rat (B), it is connected to the matching and tuning circuit on the stand, and the assembly is placed in a cradle which is then inserted into the magnet.

USF LIBRARY

were 9.6 min acquisitions with the external dioxane standard referenced at 68 ppm. Figure 4B shows the dioxane peak but no other peaks of interest. Besides dioxane, the largest peak after 230 min of infusion (Fig. 4C) is from glycine (42.4 ppm; J_{CH}=144.0 Hz), followed

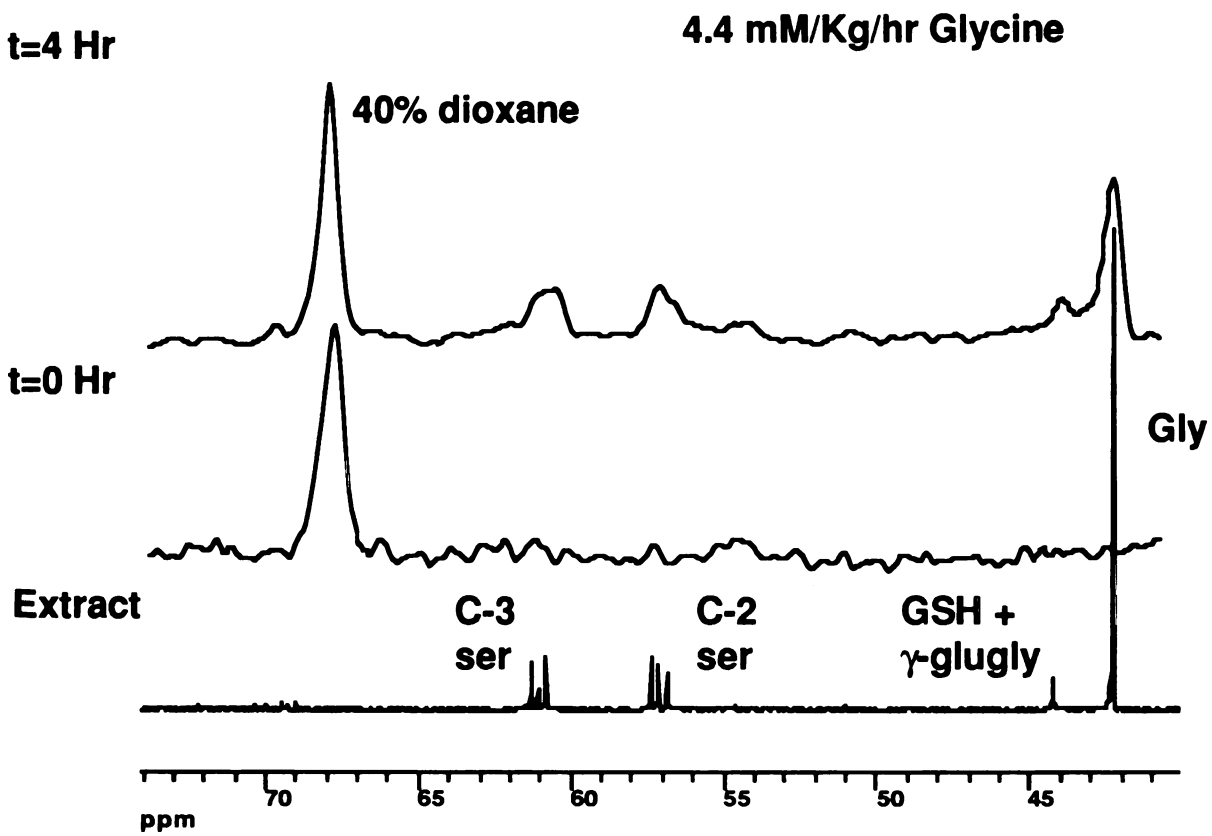

Figure 4: The central portion of a ^{13}C NMR spectra of rat liver extract (A), and *in vivo* spectra taken at baseline (B) and at 4 hr (230 min) (C), all from the same animal. The liver extract spectrum (A) is composed of 5,000 acquisitions with a repetition time of 11 sec, while the *in vivo* spectra (B and C) are composed of 144 acquisitions taking 9.6 min to acquire. Abbreviations for resonance assignments are as follows: C2 Ser, C2 serine; C3 Ser, C3 serine; GSH, glutathione; Gly, glycine.

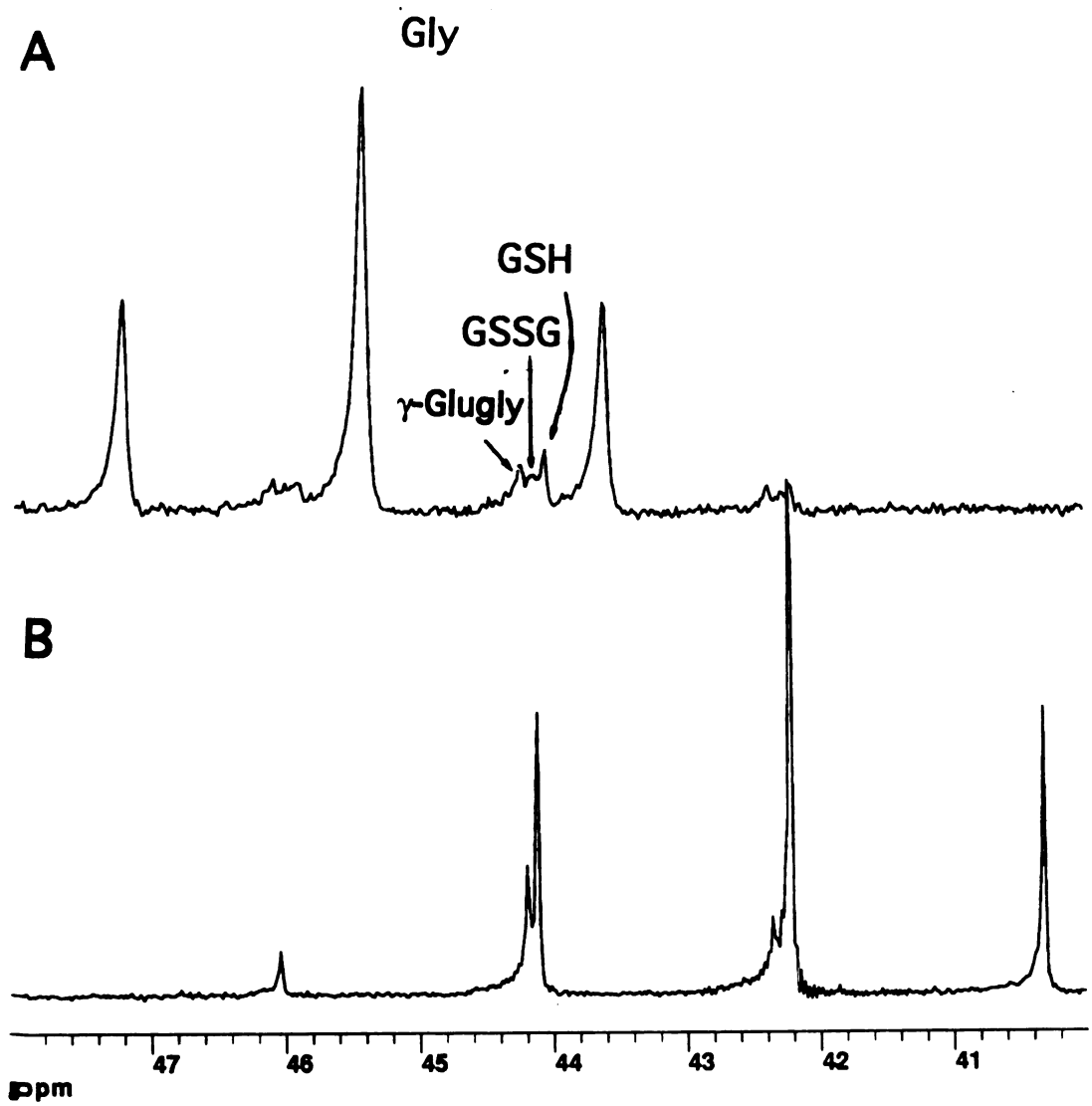

Figure 5: A portion of the ^{13}C spectrum of a liver extract taken at pH 3.00 (A) and 7.40 (B). GSSG is apparent as the broad unresolved peak in between the GSH and γ-glugly. The same parameters as in Figure 4 were used.

by GSH (44.2 ppm; J_{CH}=139.2 Hz), γ-glugly (44.2 ppm; J_{CH}=139.2 Hz) and C2 and C3 of serine (centered at 57.2 ppm, and 61.1 ppm, respectively). These as well as other peaks (vide infra) were identified by comparison to the ^{13}C spectrum of the PCA extract shown in Figure 4A and comparison to authentic standards. Figure 5 shows ^{13}C spectra obtained from a liver extract at pH 3.00 (5A) and 7.40 (5B), respectively, illustrating the

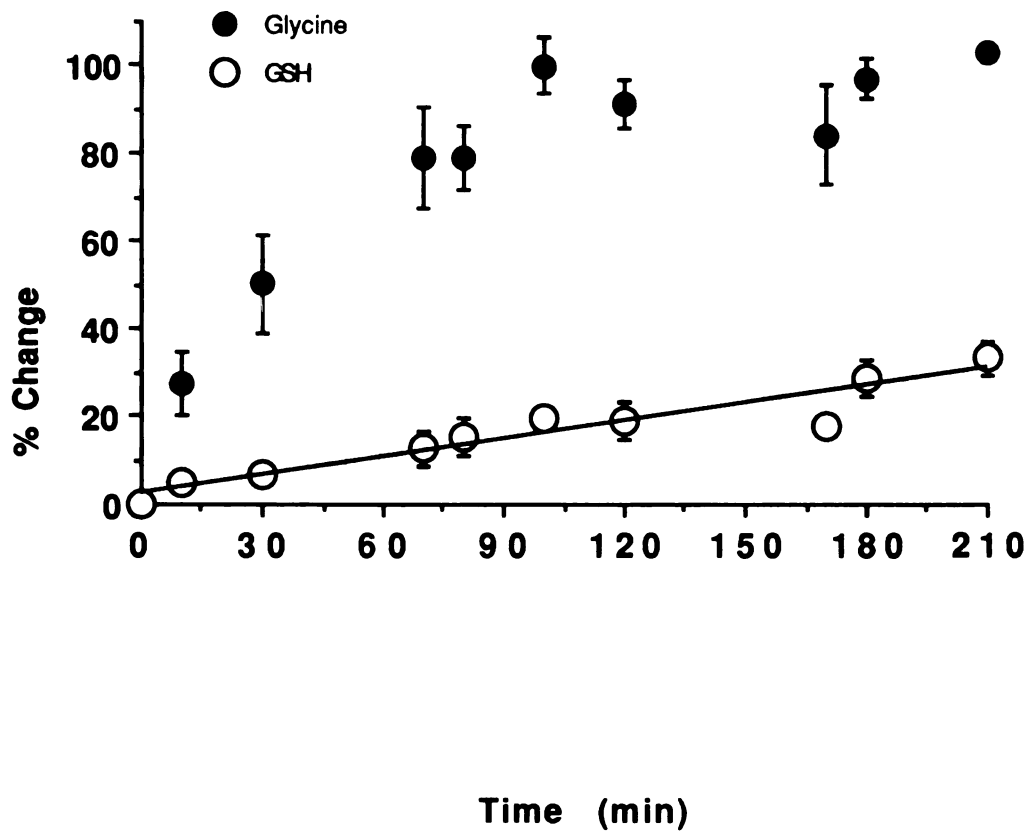

Figure 6: Kinetics of 2-^{13}C-glycine and ^{13}C-GSH in rat liver (n=3) over 210 min of 2-^{13}C-glycine intravenous infusion. Dioxane was referenced to 68.4 ppm. Glycine and GSH are expressed as a ratio of peak areas with respect to dioxane, and 100% was set to the average peak area from the last four glycine time-points within each experiment.

change in chemical shift of GSH and γ-glugly with pH. At physiological pH, GSH and γ-glugly coresonate at 44.2 ppm. GSSG formed during prolonged exposure to air at 25°C for NMR analyses at both pHs, as demonstrated by ^{1}H-observe ^{13}C-edit spectra.

Figure 6 shows the change of *in vivo* hepatic levels of GSH/γ-glugly and glycine after ^{13}C-glycine infusion. We believe that the GSH/γ-glugly signal emanates from liver tissue because no GSH/γ-glugly was detected in the ^{13}C spectrum of a 0.3 mL plasma sample with and without deproteinization obtained 2 hr after start of glycine infusion. Based on signal-to-noise in the ^{13}C spectra, this was 9.3-fold less than in liver extracts. Within each spectrum, the GSH and glycine peak areas were referenced to the dioxane peak area. The average from the last four glycine/dioxane ratios from three animals was set to 100% in Figure 6, and the GSH/dioxane and glycine/dioxane ratios were calibrated to these values. The glycine increases logarithmically (r=0.91), reaching a plateau after 100 min as shown in Figure 6, with a half-life of 24 ± 7 min and an elimination rate of 1.95 ± 0.72 hr^{-1}. The kinetic data were calculated from individual experiments, which consisted of three 9.8 min timepoints per hr for the duration of the study. Not all of the timepoints were the same between the three studies; therefore, the graph in Figure 6 is not representative of the actual number of timepoints obtained. Concomitantly, GSH/γ-glugly levels appear to increase linearly, and do not reach a plateau within the observation time, indicating that GSH formation is relatively slow compared to the cellular uptake of glycine. Depending on nutritional status and age, the turnover rate of GSH is in the range between 75-300 min^{-1} in rat liver (Taniguchi et al., 1989). The rate of γ-glugly formation resulting from glycine transport via γ-glutamyl transpeptidase has never been determined *in vivo*, but will depend on the blood GSH and glycine concentration (Meister, 1989). *In vitro* studies of γ-glutamyl transpeptidase show very rapid kinetics for uptake relative to GSH turnover. Figure 7 shows ^{13}C spectra of liver extracts from rats given a bolus of 4.4 mM/kg of 2-^{13}C-glycine taken 1, 2, 4 and 6 hours after injection. These spectra

NCSE LIBRARY

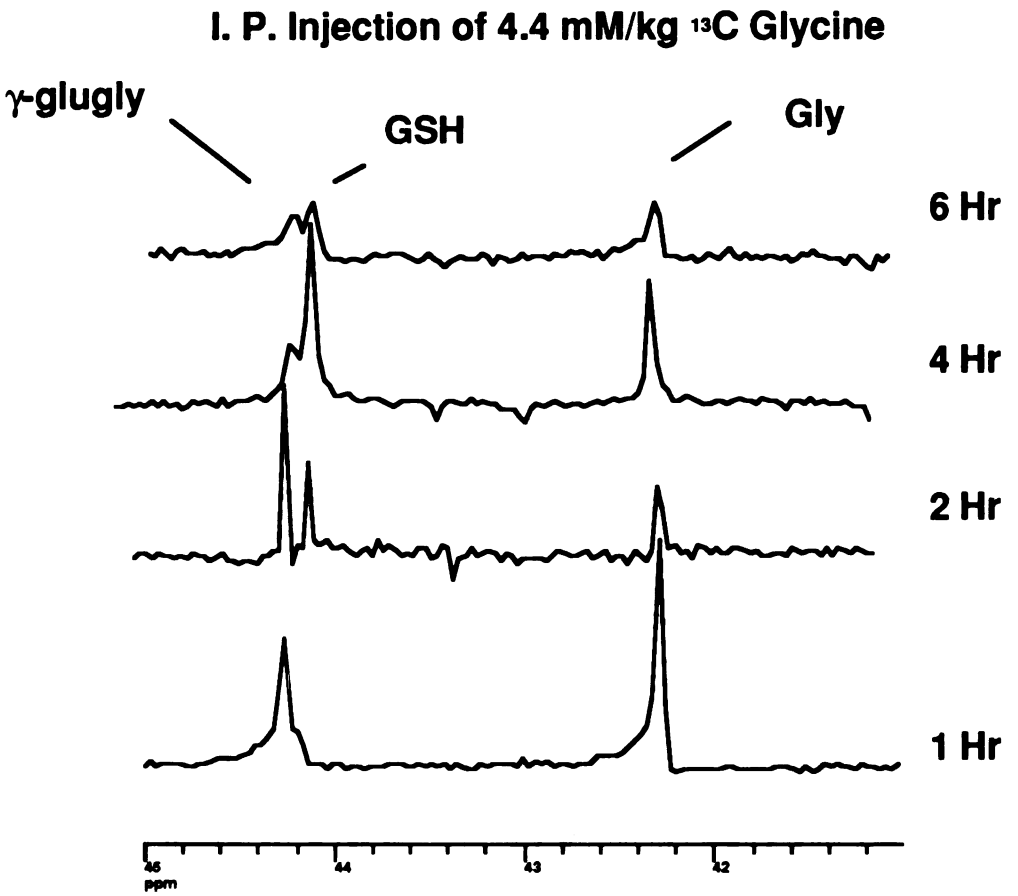

Figure 7: Liver extracts of rat given a 4.4 mM/kg i.p. injection of ^{13}C glycine dissected at 1, 2, 4 and 6 hours. A pH of 5.0 was obtained with a one-pulse sequence with decoupling during acquisition, TR = 11 s; SW = 10,000 Hz.

demonstrate that γ-glugly increases rapidly compared to GSH. The peak intensity is referenced to the β C3 of glucose which has been shown to remain unlabeled in liver extracts from glycine infusion studies. Therefore, the linear increase in the GSH/γ-glugly peak in Figure 6 is probably due to a rapid component created by γ-glugly formation, which shadows the glycine increase, and a slower GSH formation (Fig. 7).

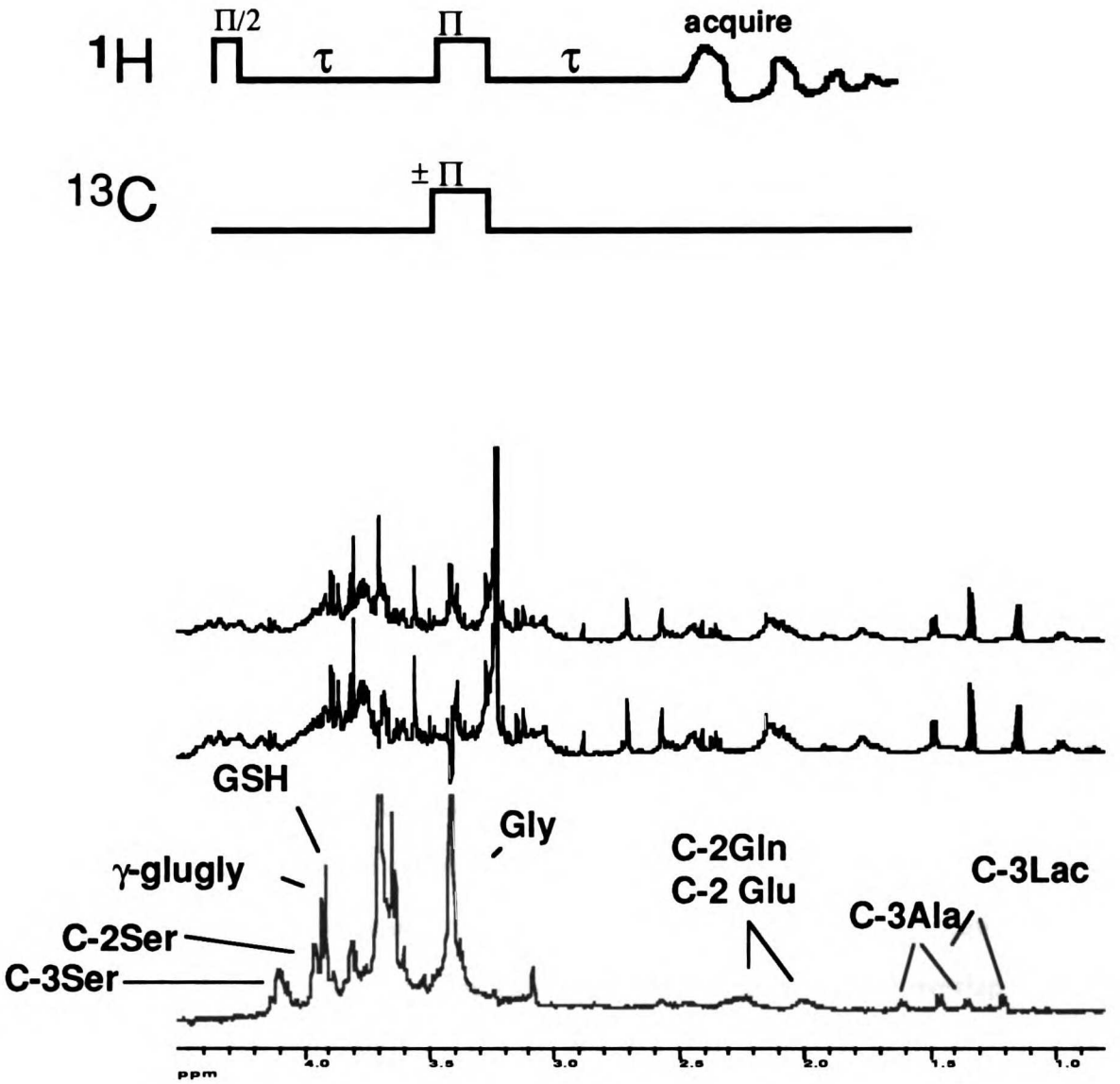

Figure 8: The {^{13}C}-^{1}H NMR pulse sequence (above) was used to obtain the difference spectrum (C). Π represents a 180 ° pulse. The ± for the Π [^{13}C] pulse signifies that the pulse is applied for alternate scans. The period, τ, was set equal to $2J^{-1}$ for the coupling constant of the C2 glycine of GSH. A portion of ^{1}H spectra from 4.2-3.9 ppm of rat liver extract with (A) and without (B) the Π [^{13}C] pulse, and the difference spectrum. The spectra are composed of 1000 acquisitions with a repetition time of 4 sec, sweep width of 3012 Hz, and 8K data points. The fractional ^{13}C enrichment was calculatedby dividing half the sum of the intensity of the [^{13}CH] stellite resonances in the coupled difference spectrum (C) by the sum of the intensities of the [^{12}CH] (A) and half the sum of the [^{13}CH] satellite resonances (C). The 2-[^{12}CH]glycine of GSH (3.77 ppm) is contaminated by other resonances (A), therefore, the 2-[^{12}CH]cysteine of GSH (2.97 ppm) was used in the fractional enrichment calculation of GSH.

^{1}H NMR spectroscopy of PCA liver extracts (Fig. 8A through C) permitted us to estimate the ^{13}C fractional enrichment in glycine and GSH to be 81 ± 3% and 76 ± 8% after 4 hr of ^{13}C-glycine infusion. Figure 8A and B are the ^{13}C-decoupled homo- and heteronuclear spin-echo ^{1}H spectra of liver extract, respectively, used to obtain the difference spectrum shown in Figure 8C. In Figure 8C, the C2 of glycine, GSH and γ-glugly are singlets centered at 3.578 ppm, 3.785 ppm, 3.814 ppm, respectively. Small amounts of GSSG were detected as an AB pattern due to the non-equivalence of the methylene protons (Rabenstein and Keire, 1989) centered at 3.778 and 3.747 ppm (J_{CH}=139.0 Hz), and this was formed due to sample oxidation caused by multiple NMR analyses. The C2 and C3 of serine appear as a doublet of doublets (J_{CH} = 144.0 and 146.5, respectively; J_{CC}= 36.6 Hz) of an ABX pattern for C2 ($J_{Hx\text{-}Hb}$ = 4.2 Hz; $J_{Hx\text{-}Hb}$ = 5.17 Hz) and C3 ($J_{Ha\text{-}Hb}$ = 4.2 Hz; $J_{Ha\text{-}Hb}$ = 4.2 Hz) and centered at 3.846 and 3.970 ppm, respectively. They do not appear sharply in Figure 8C due to long-range ^{1}H-^{13}C coupling from the ^{13}C dual-labeling of serine in conjunction with the ^{1}H-^{1}H couplings. We were unable to obtain fractional enrichment values for serine and γ-glugly because all the resonances in the one-pulse spectrum exhibit significant spectral peak overlap. Minor resonances are the multiplets of C3 of glu and gln, centered at 2.09 and 2.14, respectively, and two doublet of doublets: choline/betaine centered at 3.228 ppm (J_{CH}= 144.86 Hz, $J_{H\text{-}H}$= 3.35 Hz), and choline/betaine centered at 3.383 (J_{CH}= 143.4 Hz, $J_{H\text{-}H}$= 5.1 Hz). The C2 peaks of glutamate, glutamine, aspartate, alanine, and lactate were below detection levels or were contaminated with other peaks. Two unknown doublets of multiplets are centered at 2.42 ppm (ca J_{CH}= 103 Hz) and 2.38 ppm (ca J_{CH}= 143 Hz).

Saturation factors for *in vivo* GSH/γ-glugly and glycine ^{13}C signals observed three hours after initiation of 2-^{13}C-glycine infusion were 1.71 and 1.52, respectively (n=1). The peak area ratio of GSH+γ-glugly/glycine, after correction for saturation effects, was 0.3 *in vivo* (Fig. 4C) and 0.07 *in vitro* (Fig. 4A). Concentrations of metabolites other

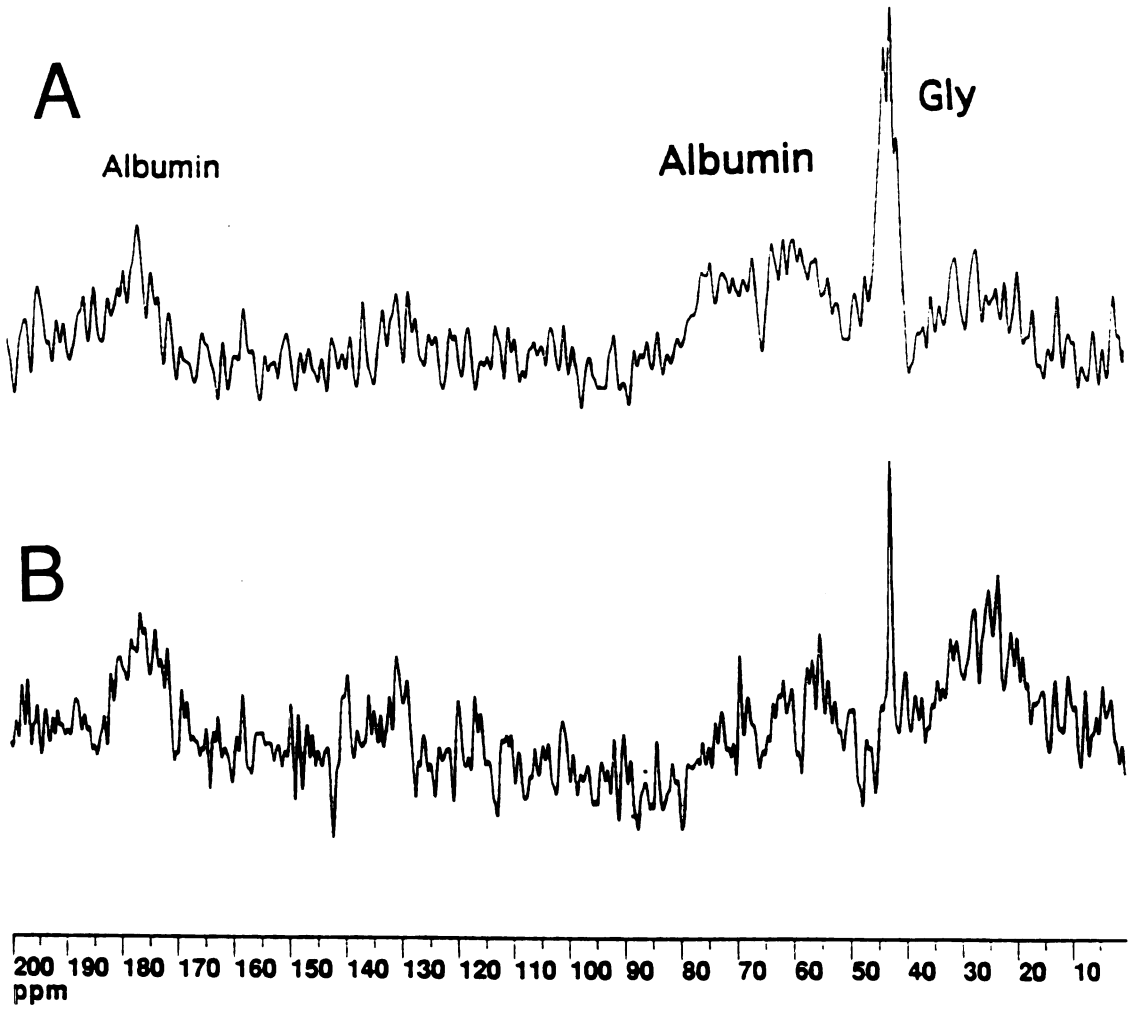

Figure 9: ^{13}C spectra of deproteinized plasma (A) and 0.3 ml of normal (B) taken 2 hrs after the start of 2-^{13}C-glycine from rat infusion. TR=11 s; SW=10,000. The broad components in both spectra are due to albumin. The top spectrum was not decoupled showing the glycine triplet. Each spectra is the result of 10,000 acquisitions. Spectra were referenced to TSP at -2 ppm.

than GSH and γ-glugly rapidly increased *in vivo* after administration of 2-^{13}C-glycine (Fig. 4A). Figure 9A and B are spectra of deproteinized and normal plasma samples, respectively. No GSH, γ-glugly, or serine was detected in either spectrum suggesting at least a 4-fold lower level of glycine/GSH+γ-glugly in plasma than in the tissue. Deproteinization evidently was not very effective at decreasing the broad component, as demonstrated by comparison of Figure 9A and B. In Figure 4A and C, the peaks centered at 57.2 and 61.1 ppm represent C2 and C3 of serine, respectively, at a ratio of 1:0.85 ± 0.05. This ratio was calculated using the total C2 and C3 peak area (i.e., single- and double-labeled) in the ^{1}H-decoupled ^{13}C spectrum shown in Figure 4.. The ^{1}H-coupled ^{13}C spectra of liver extracts revealed for the dual-labeled C2/C3 serine, a doublet of doublets for C2 (J_{CC}=36.6 Hz; J_{CH}=144.0 Hz), a triplet of doublets of doublets for C3 (J_{CC}=36.6 Hz; J_{CHa}=146.5 Hz; J_{CHc}= 4.9 Hz), and a doublet (J_{CH}=144.0 Hz) and triplet of doublets for C2 and C3 serine (J_{CH}=146.5 Hz; J_{CHc}= 4.9 Hz), respectively. The CC coupled peak areas (Fig. 4A) gave the relative labeling at the C2 and C3 positions (C2/C3-serine). Of the C2 and C3-labeled serine, 69 ± 3% and 67 ± 12% were doubly labeled, respectively. Interestingly, the extract also revealed similar ^{13}C-labeling patterns at both the C2 and C3 position in alanine (J_{CC}=34.2 Hz) and lactate (J_{CC}=36.6 Hz).

Minor labeling occurred throughout the ^{13}C spectrum. Figures 10, 11 and 12 are various portions of ^{13}C spectra taken from a control liver extract using the same infusion and animal protocol but without 2-^{13}C-glycine infusion. By comparing Figures 10 through 12, one can determine relative ^{13}C-labeling at various positions. Figure 10A illustrates C3-labeling of alanine, lactate, glutamate (27.9 ppm; J_{CC}=34.2 Hz), glutamine (27.1 ppm; J_{CC}=36.6 Hz), and four coupled unknown peaks with equal peak areas comprise two pairs of overlapping peaks: one pair is centered at 31.9 ppm and composed of two doubly-labeled ^{13}C resonances at 32.2 ppm (J_{CC}=39.1 Hz), and 31.7 ppm (J_{CC}=39.1 Hz); the other pair is centered at 12.7 ppm and composed of two doubly labeled ^{13}C resonances at 13.0 ppm (J_{CC}=36.6 Hz), and 12.5 ppm (J_{CC}=36.6 Hz). Two

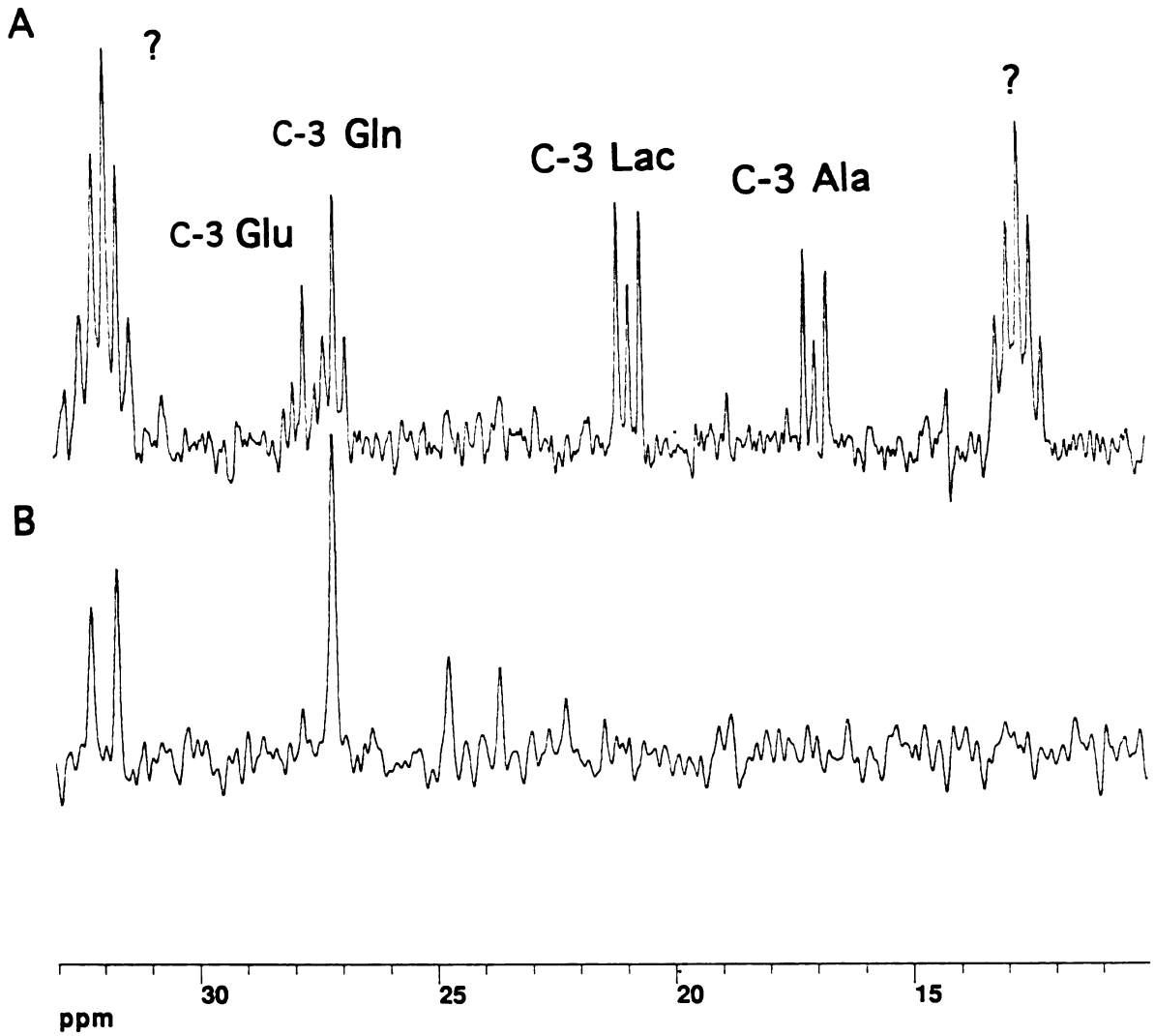

Figure 10: A portion (10-33 ppm) of the ^{13}C spectrum from the liver extract spectrum in Figure 4A is shown in (A), and a control rat liver extract obtained from a rat using the same protocol as in (A), but without 2-^{13}C-glycine infusion (B). This is enlarged approximately 4-fold from the spectrum in Figure 4A. Abbreviations: Ala, alanine; Lac, lactate; Gln, glutamine; Glu, glutamate.

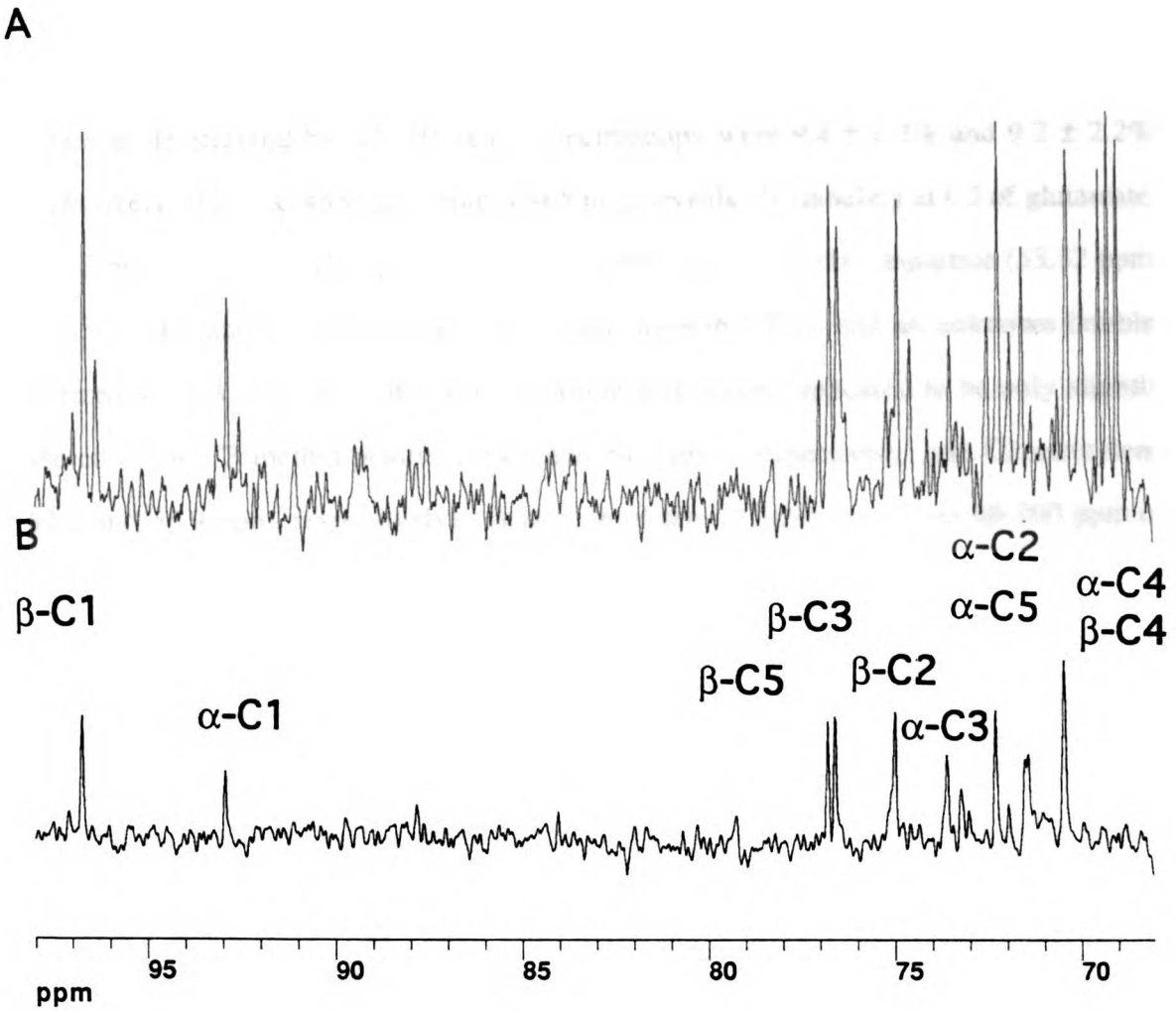

Figure 11: (A) A portion (68-98 ppm) of the ^{13}C spectrum from the liver extract of the animal whose *in vivo* spectrum is given in Figure 4A. (B) A control rat liver extract obtained from a rat using the same protocol as in (A), but without 2-^{13}C-glycine infusion. This is enlarged approximately 4-fold from the spectrum in Figure 4A. α and β refer to the C1 anomers of glucose.

methylene-methyl double labeled compounds would correspond to these chemical shifts, such as C2/C3 propionate (Sherry et al., 1985), however, the coupling constants are not similar. Better spectral resolution and signal is necessary to obtain more accurate coupling constants. A homonuclear COSY will be obtained to identify these connectivity of these unknown resonances. The fractional ^{13}C enrichments of the C3 of alanine and lactate as determined by ^{1}H difference spectroscopy were 9.4 ± 2.2% and 9.2 ± 2.2%, respectively. The ^{13}C spectrum from 32-65 ppm reveals ^{13}C-labeling at C2 of glutamate (55.13 ppm; J_{CC}=34.2 Hz), glutamine (54.87 ppm, J_{CC}=36.6 Hz), aspartate (53.32 ppm; J_{CC}=36.7 Hz) and C3 of aspartate (34.3 ppm; J_{CC}=36.5 Hz), and an unknown doublet centered at 39.4 ppm (J_{CC}=36.6 Hz). Choline and betaine appeared to be only slightly labeled at the C3 methyl position (54.6 and 54.9 ppm, respectively) and C2 methylene (67.2 and 56.9 ppm, respectively). A portion of the ^{13}C spectrum from 68-100 ppm of the ^{13}C-labeled and control study are shown in Figure 11A and B, respectively. Since serine is doubly-labeled, and if the triose isomerase reaction is at steady-state at the time of tissue dissection, then glucose should be equally labeled at the α- and β-C1,2,5 and 6 positions. The α- and β-C6 signals (61.4 ppm) are not shown, but C6 was labeled and was also contaminated by the serine C3 signal (61.1 ppm). In Figure 11B, the α- and β-C1 (96.7 and 92.8 ppm, respectively) both have satellite peaks due to the C2 of glucose with J_{CC}=46.4 Hz, respectively. Similarly, the α- and β-C2 (72.2 ppm, J_{CC}=47.6 Hz; 74.9 ppm, J_{CC}=47.4 Hz, respectively) and α- and β-C5 (72.2 ppm, J_{CC}=46.4 Hz; 76.6 ppm, J_{CC}=46.4 Hz, respectively). The α- and β-C3 at 73.5 and 76.4 ppm, respectively, and the α- and β-C4 centered at 70.4 ppm demonstrate that these positions are not ^{13}C-labeled, because they are singlets without any satellite peaks caused by ^{13}C-^{13}C coupling. The triplet at 69.9 ppm is from the C2 of lactate. Figure 12B is the final portion of the ^{13}C spectrum of ^{13}C-glycine infused liver extract. There is slight labeling in the purines at adenine C5 (119.3 ppm), bilirubin and/or protoporphyrin (161.1 and 163.5 ppm), and the C2 and C8 of adenine (142.0 and 142.7 ppm, respectively) and C2 of guanine (153.6

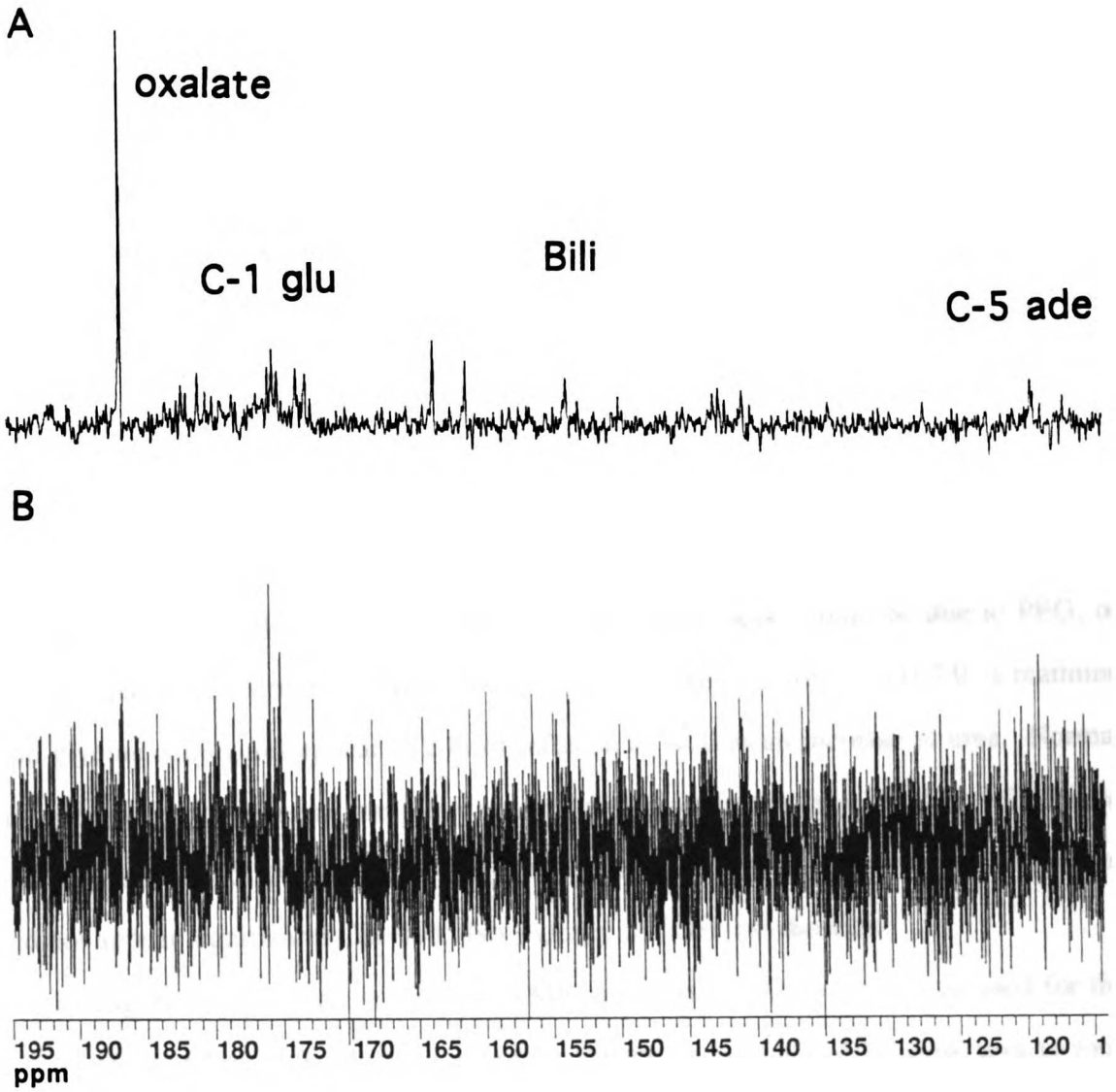

Figure 12: A portion (68-98 ppm) of the ^{13}C spectrum from the liver extract spectrum in Figure 4A is shown in (A), and a control rat liver extract obtained from a rat using the same protocol as in (A), but without 2-^{13}C-glycine infusion (B). This is enlarged approximately 4-fold from the spectrum in Figure 4A. Abbreviations: ade, adenine; Bili, bilirubin; glu, glutamate.

ppm). There are three ^{13}C signals in the vicinity of 175 ppm: one at 175.4 ppm due to C1 of glutamate (J_{C1-C2}=53.7 Hz), another unknown at 173.3 ppm (J_{CC}=52.5 Hz), and a very large singlet at 186.3 ppm that is probably a direct metabolite of 2-^{13}C-glycine such as oxalate, glyoxalate, or formate. EDTA added to the PCA to chelate Fe^{+2}, has a carboxylate resonance at 172.0 ppm but does not appear in these spectra.

Figure 13 shows ^{13}C spectra of urine taken at 0, 1, 2, and 4 hr, respectively, after the start of 2-^{13}C-glycine infusion from the same rat whose liver spectra are shown in Figures 4 and 8. The urine spectra reveals that glycine (42.3 ppm) is the major ^{13}C-labeled metabolite after 2 hours of glycine infusion. The anesthetic contains 40% polyethyleneglycol (PEG) which produces a doublet centered at 68.4ppm (J_{CH}=118.8 Hz). The control rat urine (t=0) shows that the three largest peaks after 3 hr are due to the infusion medium and not ^{13}C-label metabolites. These peaks could be due to PEG, or perhaps glyoxalate, which would be predominantly in the enol form at pH 7.0. Creatinine and glycine conjugates appear at 2 hr of infusion as well as an increase in urea. Normal and deproteinized plasma samples revealed that glycine was the primary ^{13}C-labeled compound detected. Albumin and smaller molecules were either below detection limit or did not appear significantly labeled. No γ-glugly or GSH was detected.

Figure 14 shows an *in vivo* ^{31}P NMR spectrum of the same liver as used for the experiments of Figure 3. In three experiments, the percent of β-NTP peak area to total phosphate signal was 19 ± 5% at baseline, and 17 ± 3% after 2.5 hours of ^{13}C-glycine infusion ($p \leq 0.05$), indicating that glycine did not significantly affect bioenergetics. Intracellular pH was measured at baseline, as well as 65 and 150 min after the start of glycine infusion; the intracellular pH (pH_i) was determined using the chemical shift of inorganic phosphate relative to α-NTP. The average pH_i was 7.34 ± 0.09 (n=9), with no significant change during the observation period. Two peaks of phosphocreatine appear in the ^{31}P spectrum in Figure 7, probably emanating from intestinal muscle and slightly ischemic incised peritoneal muscle. The contribution of signal from muscle tissue is

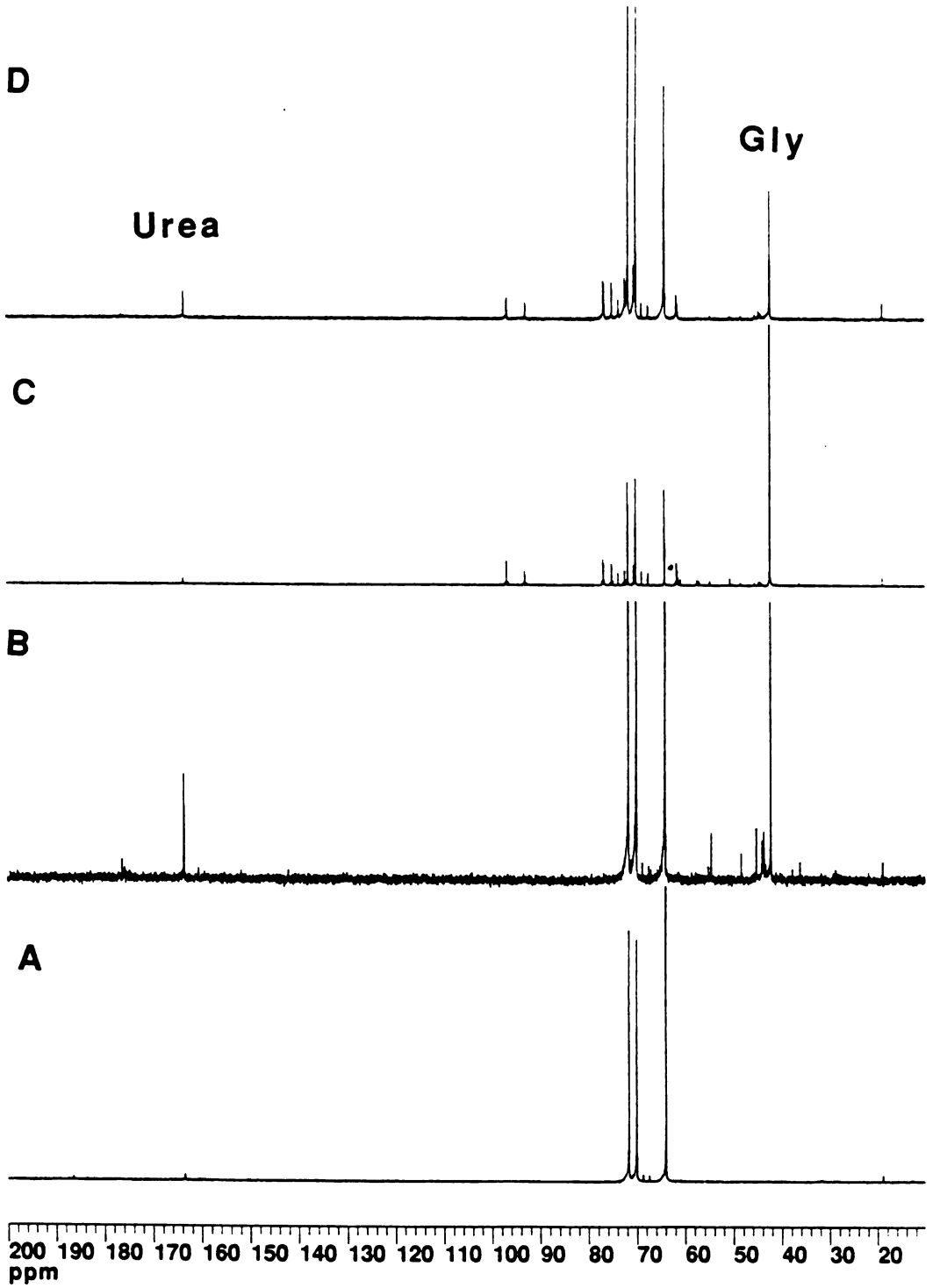

Figure 13: ^{31}C NMR spectra of urine taken from the control after 1 (A), 2 (B), 3 (C), and 4 (D) hours of ^{31}C-glycine infusion. TR=11 s; SW=10,000. Note that different scaling factors are utilized in the spectra.

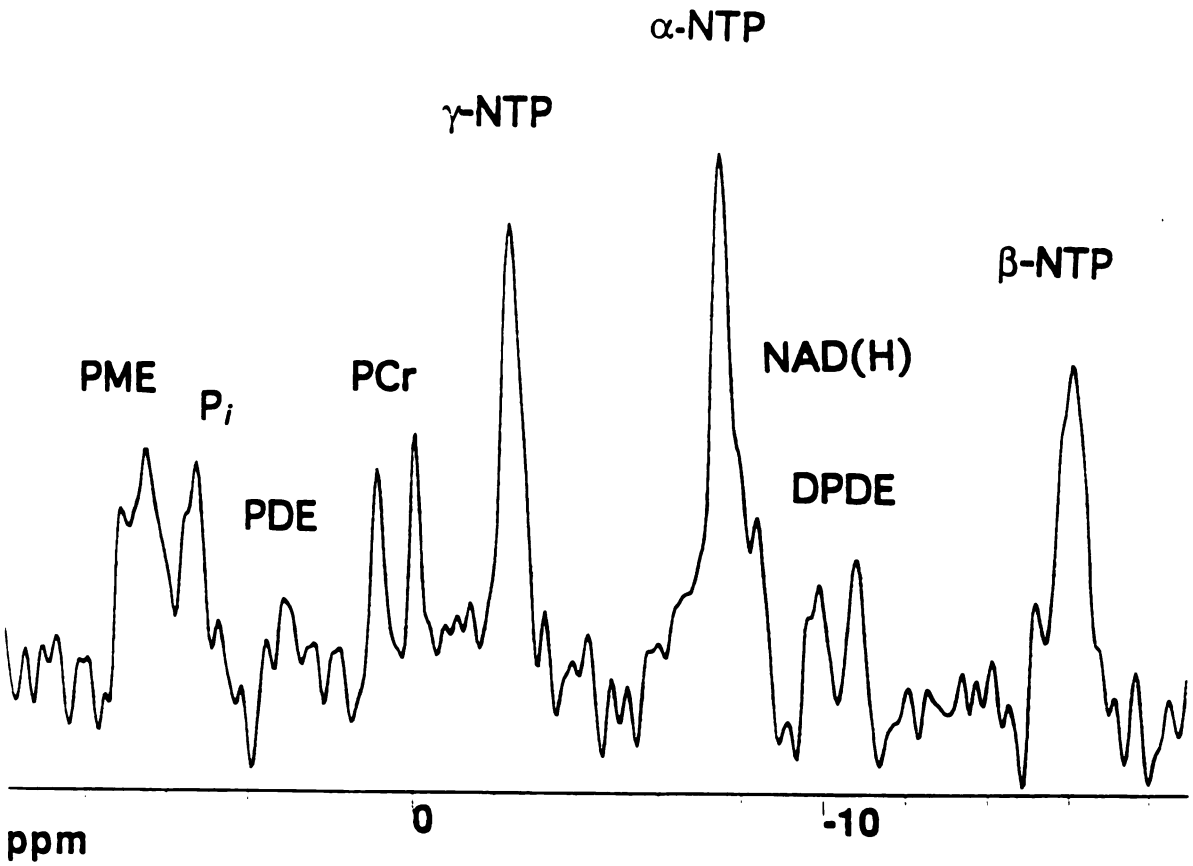

Figure 14: An *in vivo* ^{31}P NMR spectrum of rat liver 65-100 min after start of intravenous 2-^{13}C-glycine infusion. Abbreviations are as follows: PME, phosphomonoester; PDE phosphodiester; P_i, inorganic phosphate; NTP, nucleoside triphosphate; PCr, phosphocreatine; DPDE, iphosphodiesters; NAD(H), nicotinamide adenine diphosphate.

small, since the PCr/β-NTP ratio of 0.6 is much less than the normal muscle tissue of 6.2 (Gadian, 1989). If the PCr/β-NTP ratio was greater than 0.8, the pulse width would be reduced. If a reduced pulse width did not decrease the PCr/β-NTP ratio, it was concluded that the probe placement was incorrect and the ^{13}C data rendered non-interpretable.

DISCUSSION

^{15}N-glycine has been given to humans since 1940 (Ratner et al., 1940) to monitor the movement of ammonia and measure protein turnover. Disposition (elimination and tissue distribution), biotransformation, and toxicodynamics, (the biochemical effect of toxicants) has never been accomplished simultaneously and non-invasively for study of *in vivo* toxicology. Glycine is a good choice for the study of xenobiotic pharmacodynamics because it is involved in many primary metabolic processes and thus monitors a large number of biochemical processes, resulting in a broad database on which to prove toxicological or pharmacological hypotheses (Fig. 2). We developed an animal model for *in vivo* NMR that permits the concomitant monitoring of glycine, high energy phosphagens, phosphomono and diesters, intracellular pH, and some biochemical processes in rat liver and physiological function via body fluid collection. A critical factor in the success of this model was the development of a novel triple-tuned NMR surface probe. The probe provided well-resolved and decoupled ^{13}C and ^{31}P spectra of the liver. Due to the proximity of some of the resonances, in particular stemming from glycine and GSH/γ-glugly, it was imperative to obtain complete decoupling, good coil sensitivity, and narrow linewidth (usually 80 Hz at 4.7 T). The photo-etched coil in conjunction with the rigid assembly enabled the accomplishment of these criteria. Figure 3C exhibits a representative spectrum illustrating the decoupling, signal-to-noise ratio, and baseline resolution of glycine (42.3 ppm) and GSH/γ-glugly (44.2 ppm). Figure 15 shows all of the labeled glycine metabolites detected in tissue extracts and urine.

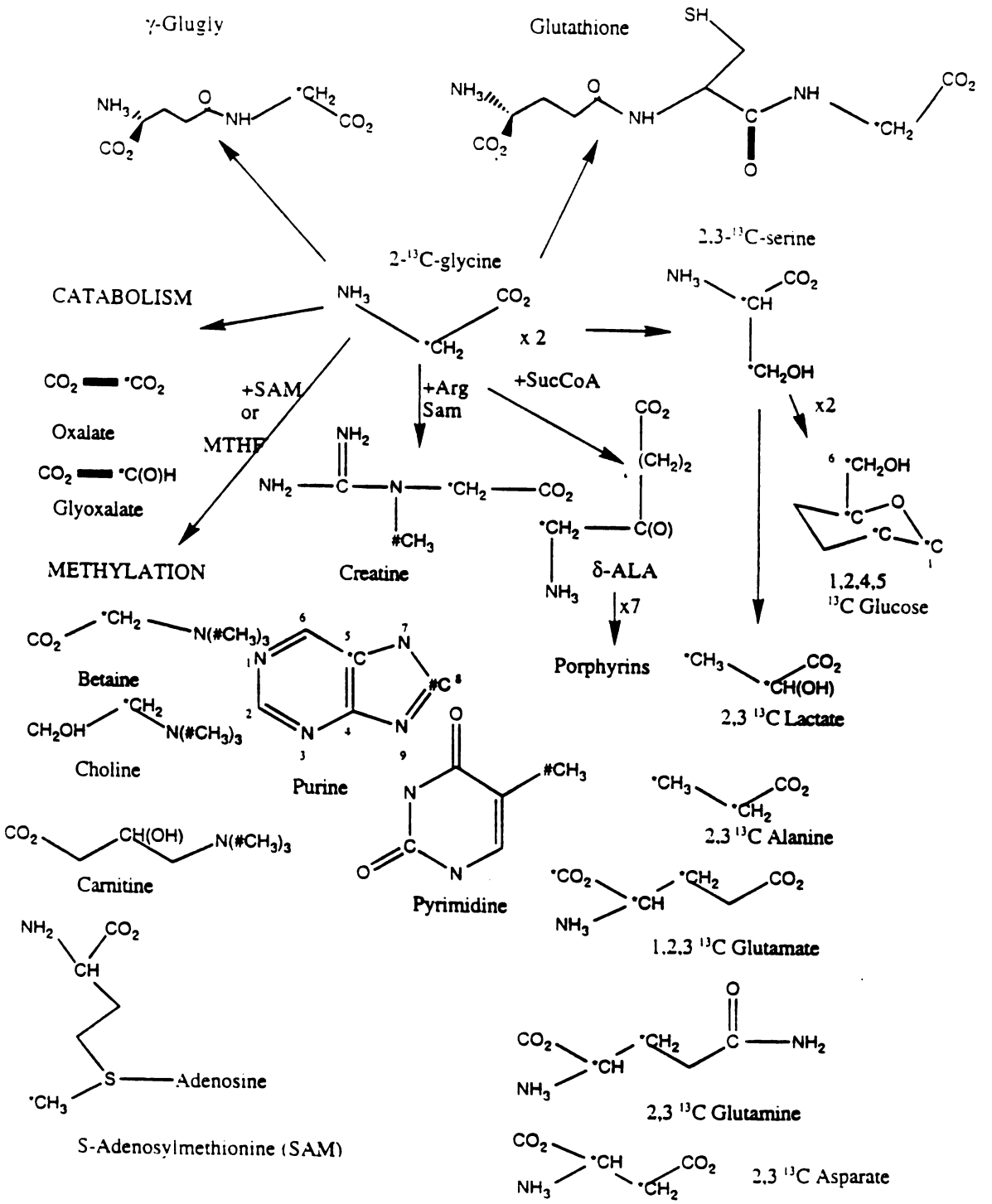

Figure 15: ^{13}C-labeled metabolites of 2-^{13}C-glycine found in tissue extracts and urine. The * represents direct labeling and # represents labeling via transmethylation.

Glycine Kinetics: The metabolic pathways of glycine observed by *in vivo* ^{13}C NMR during enrichment with ^{13}C-glycine are in accordance with those found in the literature (Devlin, 1986; Harper, 1983; Neuberger, 1981; Snell, 1983; Stryer, 1981). Hepatic glycine levels reached steady-state by ca 100 min after start of intravenous infusion of ^{13}C glycine and, with a half-life of 24 ± 7 min. The glycine turnover rate from the decay curve of an intravenous bolus of ^{15}N-glycine in rabbit showed diurnal, fasting and nutritional dependence and ranged from 1.79-6.03 hr^{-1} (Nissim and Lapidot, 1979). We found the elimination rate (k) of ^{13}C-glycine in the rat (Fig. 6) to be 1.95 ± 0.72 hr^{-1} by first-order fit of the increase in glycine peak area. This difference in k of rabbit and rat could be due to interspecies variation or to differences in pharmacokinetic data and in experimental conditions. Nissim and Lapidot (1979) determined k from the decay curve of glycine plasma concentration obtained from chronically implanted catheters in awake rabbits. We obtained k from the slope of the increase of tissue glycine concentration obtained from anesthetized rats with surgically implanted NMR coils. Glucagon secretion increases glycine turnover (K) (Nissim and Lapidot, 1984) in part by induction of serine dehydratase and serine-pyruvate aminotransferase (Snell, 1983). Surgery and handling of awake animals cause pancreatic secretion of glucagon in response to low blood glucose and adrenaline (Snell, 1983). We infused a 10% solution of glucose to inhibit glucagon secretion. However, *in vivo* ^{13}C NMR studies of glycogen metabolism have successfully used α-blockers to inhibit glucagon secretion (Alger et al., 1984) and this may be necessary to combat the effects of adrenaline in future studies. General anesthetics cause decreased blood pressure and blood flow to organs, such as liver, which would decrease K. A better calculation of K would be obtained in the present study if there were more data points which could be obtained during the decay curve, after the end of infusion. More importantly, as Nissim and Lapidot (1984) have shown, the biochemical status of the animal can effect glycine turnover four-fold.

Glutathione and γ-Glugly: During the course of ^{13}C-glycine infusion, major ^{13}C resonances arose at 44.2, 57.2, and 61.1 ppm. The peak at 44.2 ppm was of particular interest, since it represents GSH as reported in the literature (Rabenstein and Keire, 1989) and as compared to authentic standards. According to literature values, GSH can be maintained as high as 8 mM in rat liver, and thus is the primary pool for glycine (Meister, 1989). GSH has been monitored in red blood cells (Mason et al., 1993) and in perfused liver as an unresolved shoulder coresonating with it ^{13}C2-4 glutamate precursors (Cohen, 1987). The only reported attempt to monitor GSH in intact tissue was in the brain, and it was unsuccessful (Hanstock et al., 1991). The task to monitor GSH in the liver of whole animals is difficult compared to other tissues because of the short spin-spin relaxation times (T_2), respiratory motion, magnetic susceptibility effects and possibly macromolecular binding (Hanstock et al., 1991), which has precluded us and others (Hanstock et al., 1991; Mason et al., 1993; Rabenstein and Keire, 1989) from successfully monitoring this most abundant antioxidant using either *in vivo* ^{1}H NMR or natural-abundance ^{13}C NMR. Our PCA liver extract pulse-chase study revealed that the resonance at 44.2 ppm, which increased linearly during the observation period (Fig. 6), is a composite of GSH as well as γ-glugly, a metabolite of the membrane bound transporter γ-glutamyltranspeptidase. This is the first time γ-glugly has been monitored non-invasively in an animal model (Meister, 1989). The pulse-chase study (Fig. 7) revealed that the apparent linear increase in this peak *in vivo* results from two overlapping logarithmic curves. The γ-glugly production and elimination kinetics were rapid and essentially shadow the glycine, but GSH kinetics were slower. The levels of ^{13}C-labeled γ-glugly and GSH appear to be controlled by blood 2-^{13}C-glycine concentrations and the GSH turnover rate, respectively.

We found nearly a four-fold smaller peak area ratio of GSH+γ-glugly/glycine after correction for saturation effects *in vivo* compared to tissue extracts. An ischemia-induced

decrease in GSH concentration during excision of the liver is unlikely, since dissection required less than 10 sec and no oxidative product (GSSG) was detected in freshly prepared extracts. The difference could be due to difficulty in detection of glycine caused by binding to macromolecules, to blood flow effects, or to γ-glugly having a longer *in vivo* T_1 than GSH and thus increasing the measured saturation factor. Figure 7 demonstrates the more rapid kinetics of γ-glugly. Figure 7A -D illustrates the difference in γ-glugly/GSH peak area ratio at two different times after glycine administration, supporting the notion that a saturation factor will depend on the individual contribution of these two glycine metabolites. If their *in vivo* T_1 values are significantly different, then so will the saturation factor vary for the resonance at 44.2 ppm throughout the study. Investigation of *in vivo* and extract GSH and γ-glugly/gly ratios from rats infused with various doses of glycine would help elucidate NMR visibility since blood flow effects of glycine would vary, but macromolecular binding should remain relatively constant. Further studies are necessary to assess absolute quantities of glycine, GSH and other metabolites of interest in extracts and to determine the exact extent of NMR signal visibility *in vivo*.

The coresonance of GSH and γ-glugly may preclude the assessment of *in vivo* GSH kinetics unless one administers inhibitors of γ-glutamyltranspeptidase (γ-GT) or inducers of γ-glutamylcyclotransferase. Figure 16 illustrates points of control for eliminating γ-glugly accumulation either by inhibiting cell membrane-bound γ-GT or byinducing γ-glutamylcyclotransferase in the cytosol. Several naturally-occurring competitive inhibitors exist for γ-GT such as amino acids and dipeptides, as well as synthetic amino acid analogues such as acivicin (Meister, 1989). The most potent is acivicin which is commonly used in *in vivo* toxicology studies (Madhu et al., 1992) but is very non-selective in irreversibly inhibiting many other enzymes such as glutaminase. The administration of γ-glutamyl dipeptides provides a specific and nontoxic procedure for *in vivo* competitive inhibition of γ-GT (Anderson and Meiste, 1986), but they would

be metabolized by dipeptidases in the blood, need to be infused at higher concentrations than glycine, and are expensive. Cystine was a better substrate than any other amino acid for γ-GT (Thompson, 1975) and could be used as an competitive inhibitor of γ-GT while directly producing GSH and increasing intracellular cysteine levels, the biolimiting amino acid in GSH synthesis (Fig. 16). Inducers of γ-glutamylcyclotransferase would aid in

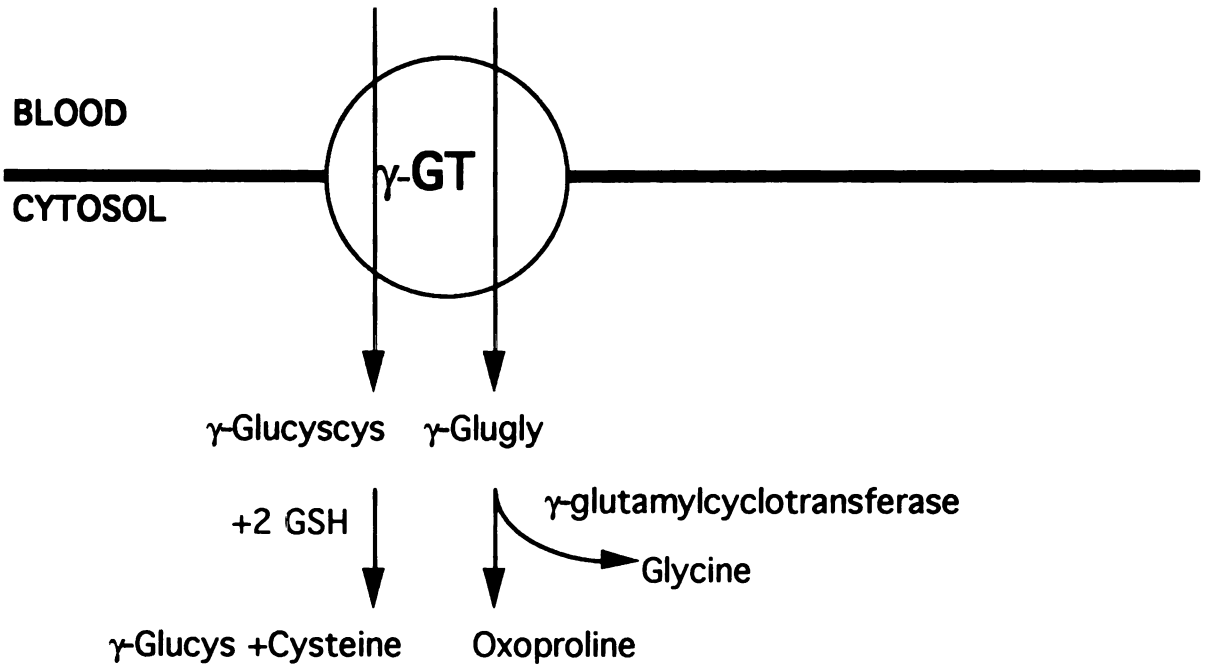

Figure 16: Points of control for decreasing γ-glugly accumulation. γ-glucys will be directly synthesized to GSH without any negative feedback control normally caused by GSH on γ-glutamylcysteinyl synthase.

decreasing γ-glugly accumulation, but little *in vivo* information is available for this enzyme (Meister, 1989).

Even with γ-glugly contamination, 2-^{13}C-glycine is the best candidate to isotopically enrich GSH at the dose employed, since (a) it is not toxic; (b) it is not biolimiting as is cysteine (Meister, 1989); (c) it is readily taken up by liver cells

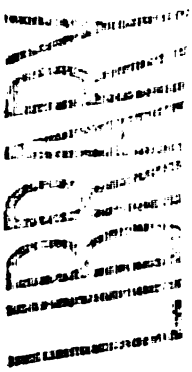

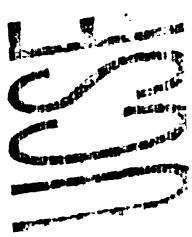

(Christensen and Handlogten, 1981); (d) it is not too expensive in quantities necessary to perform extended *in vivo* studies; and (e) unlike glutamate C2-C4 (Cohen, 1987c) and cysteine C2 and C3 resonances, there is a relatively large chemical shift difference between C2 glycine of the amino acid and the C2 glycine residue in GSH.

We are confident that the GSH, γ-glugly, and serine signals emanate from the liver and not from surrounding tissues, because the coil was placed on the liver, and the peritoneal muscle was kept away from the coil by a microsphere containing the external standard, dioxane. Although the liver is a well perfused organ containing 25-30 mL blood/100 g of liver (Campra and Reynolds, 1988), and significant amounts of 2,3 diphosphoglycerate, a biomarker of erythrocytes (Cohen, 1983), were detected in the ^{31}P NMR spectrum of the liver extract (data not shown), the average plasma/erythrocyte GSH concentration is a factor of thirty less than in liver (Taniguchi et al., 1989). Furthermore, neither GSH nor γ-glugly were detected in the ^{13}C spectrum of plasma (Fig. 9B). This small concentration of GSH and γ-glugly in the blood is below the detection limit of our NMR spectrometer. Low blood levels of GSH and γ-glugly are maintained by tight regulation via the kidney (Meister, 1989).

Serine: Figure 2 shows the major pathways that glycine takes in rats. In microorganisms, glycine is a major source of energy via the 'glyoxalate cycle', but mammals lack some enzymes making this a catabolic pathway with the formation of oxalate (Neuberger, 1981). In mammals, glycine is glucogenic by the 'glycine cycle': the net reaction is shown in the introduction. It is also directly linked to the TCA cycle and anaplerosis via the 'succinate-glycine cycle', where glycine binds arginine from the urea cycle to form δ-aminolevulinic acid (δ-ALA) which can reenter the TCA cycle at α-ketoglutarate or succinate, or continue to form porphyrin. Glycine regulates the urea cycle more than other amino acids because, as a byproduct of the 'glycine cycle', NH_4^+ is formed in the

mitochondria (Neuberger, 1981). This NH_4^+ enters the urea cycle as carbamoylphosphate and is excreted as urea in the urine (Fig. 2).

As predicted by the 'glycine cycle', we observed C2/C3 doubly-labeled serine. This reaction occurs in the mitochondria where glycine dehydrogenase and serine methoxytransferase are coupled, and where the cofactor (^5N,^{10}N-methylenetetrahydrofolate) is regenerated by the C2 carbon of glycine and forms the C3 of serine reforming tetrahydrofolate (THF). The near 1:1 ratio of C2/C3 -labeling indicates a tight coupling of serine methoxytransferase and glycine dehydrogenase, and that glycine at this concentration is significantly metabolized by this pathway *in vivo*. Serine labeled at C2 and C3 was also found in kidney proximal tubules [(Cowin et al., 1993) and yeast after 2-^{13}C-glycine was administered (Pasternack et al., 1992). The fact that we did not observe much methylated choline supports the theory that there are two THF pools, one mitochondrial and the other cytosolic. Glycine dehydrogenase is found only in the mitochondria, and therefore, ^{13}C-labeling of methylene-THF occurs in the mitochondria (Pasternack et al., 1994a). Methylene-THF cannot cross the mitochondrial membrane, and two pathways have been proposed by which this one-carbon unit could exit the mitochondria and enter the cytosolic THF pool and be incorporated into purines and choline: (1) as the C3 of serine from the 'glycine cycle', and (2) as formate (Pasternack et al., 1994a).

Choline is synthesized in a third compartment, the endoplasmic reticulum, by methylation of phosphatidylethanolamine derived from phosphatidylserine (Pasternack et al., 1994b) with the methyl group coming from S-adenosyl methionine (SAM). With excess methionine, choline and methylated products of glycine (sarcosine, dimethylglycine, betane, and carnitine) will form immediately after infusion via glycine N-methyl transferase (London, 1987). London and Gabel (London, 1988b) found that the predominant metabolic fate of excess methionine S-methyl is sarcosine. The sarcosine N-methyl then forms formate in the mitrochondria and, ultimately, the deuterons are

transferred to water. Based on localization of glycine methyltransferase (cytosolic) and sarcosine dehydrogenase (mitochondrial), they concluded that the glycine/sarcosine shuttle was responsible for transport of one-carbon units to the mitochondria. We found negligible choline labeling either at the N-methyl (transmethylation) or N-methylene (from glycine) indicating that very little choline synthesis occurred during the course of our experiment, which is unusual considering that liver is the primary source of choline for the entire body. We also found negligible N-methylated glycine products. However, significant transmethylation occurred when we infused 2-oxothiazolidine-4-carboxylate, a precursor to sulfur amino acids (data not shown; n=1). The purine C5 of adenine, which comes directly from the C2 of glycine, was not significantly labeled. In addition, C2 and C8 adenine positions derived from cytosolic methylene-THF were not significantly labeled. This suggests that at this physiologically high dose of glycine there is little flow of mitochondrial derived one-carbon units because of the tight coupling of mitochondrial glycine dehydrogenase and serine methoxytransferase forming the 'glycine cycle'. In cytosolic methylation requiring THF, such as in purine synthesis, there occurs as supported by ^{13}C-labeling; however, transmethylation requiring S-adenosyl methionine is inhibited due to the limited sulfur amino acid pool.

Minor Labeled Products: The C2/C3 double-labeling of serine creates a metabolic channel providing a unique and easy mode of identifying the contribution of serine to gluconeogenesis, anaerobic glycolysis, and anaplerosis. For example, glucose was 1,2,5,6 ^{13}C-labeled which would be expected if triose isomerase were at steady-state at the time of tissue extraction (Figs. 2 and 15). However, if there was an influx of glycerol (Fig. 1) derived from lipolysis, one would disturb the triose isomerase steady-state and expect a disproportional labeling of glucose, favoring the 1 and 2 carbons. Alanine and lactate were also doubly-labeled with similar fractional enrichment. One can use isotopomeric analysis (London, 1988a) in conjunction with the fractional enrichment to

investigate these biochemical processes under various conditions using the C2/C3 labeled serine as the reference. *In vivo* monitoring of gluconeogensis or anaerobic glycolysis using ^{13}C glycine infusion could be successful if glucagon secretion were inhibited or stress was imposed, respectively.

Isotopomeric analysis of anaplerotic products revealed labeling at C2 and C3 of aspartate, C2 and C3 of glutamine, and C1, C2, and C3 of glutamate. Cohen et al. (1987) found that the amount of pyruvate entering the TCA cycle from acetylCoA via pyruvate dehydrogenase (PD) compared to oxaloacetate via pyruvate carboxylase (PC) in normal-fed perfused rat liver was 1:1.2, and in 24-hr fasted rats was 1:7.7. The C2/C3 double labeling of aspartate, glutamine, and glutamate would occur from PC, and a C1/C2 or C4/C5 double labeling of equal proportions would occur for glutamine and glutamate if pyruvate entered via PD. Going from α-ketoglutarate to aspartate, there is loss of CO_2, which creates a pool of labeled C1 fumarate, from which C1 or C4 aspartate are equally labeled. Our results indicate that the majority of pyruvate enters via PC due primarily to C2 and C3 labeling of aspartate. If there were more signal, one could better observe some C1 and C4 labeling of aspartate. This is consistant with Cohen's (1987) findings that fasted rats derive much of the acetate entering the TCA cycle via lipolysis and, therefore, pyuruvate is shunted through PC to enter to the TCA cycle. Additionally, there is a demand for aspartate due to its use in the urea cycle caused by the increased NH_4^+ generated from the glycine cleavage system (Fig. 17). There is disproportional C1 labeling of glutamate, and much more total ^{13}C labeling of glutamine as demonstrated by comparison of C3 of glutamate and glutamine (Fig. 10). This could be explained by two pools of glutamine and the 'succinate-glycine cycle'. This hypothesis is supported by the marked increase in glutamine labeling as compared to glutamate, when in fact the increased NH_4^+ created by the glycine cleavage system (glycine dehydrogenase) increases the glutaminase activity and thus there should be less mitochondrial glutamine

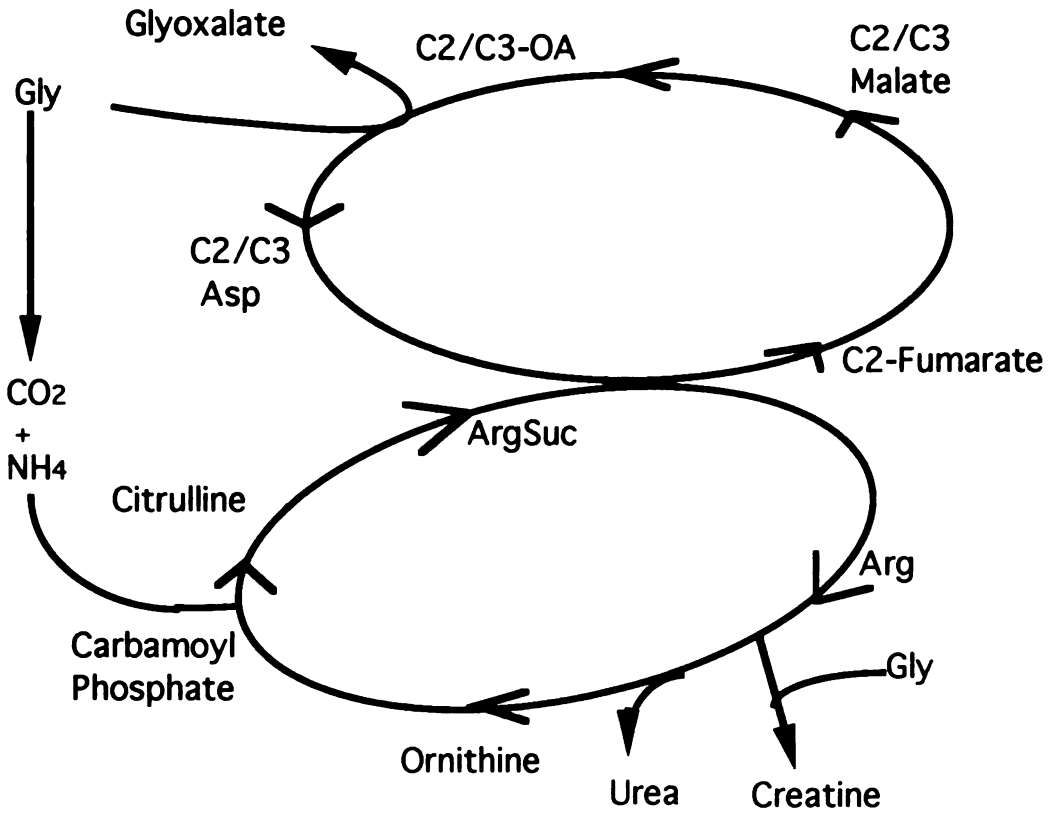

Figure 17: Aspartates role in the urea cycle and effect of glycine infusion.

(Neuberger, 1981). Figure 2 shows that glutamine is returned to the liver from the brain (Harper, 1983). Glycine is a neurotransmitter, and the 'glycine cycle' is active in the brain (Nyhan, 1981), but the urea cycle only occurs in the liver.

Figure 18 shows the two pools of glutamine, but the larger is cytosolic due to inter-organ transport to the liver from the brain and the increased glutaminase activity in the mitochondria caused by the glycine cleavage system. The increased glutaminase activity decreases glutamine levels in the mitochondria favoring formation of glutamate. The C1 of glutamate would be preferentially labeled from the C2 of glycine via δ-ALA and would accumulate because it would not form glutamine due to the increased glutaminase activity and the increased amino acid pool caused by glycine infusion. The

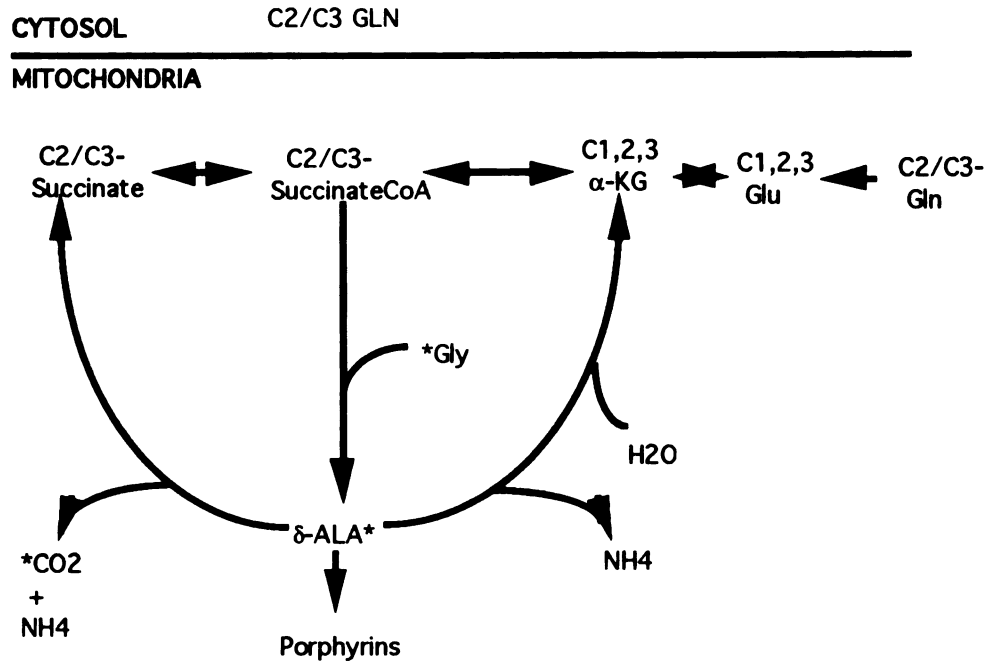

Figure 18: Schematic illustrating the two pools of glutamine.

increased amino acid pool would then increase transamination of α-ketoglutarate with the amine transferred from alanine or aspartate. *In vivo* ^{15}N NMR studies of ^{15}N-glycine in rat liver showed that glutamate was labeled within the first 20 min via transamination following alanine labeling (Grunder et al., 1992). Therefore, C1,2,3 glutamate could accumulate from anaplerosis with 2,3-^{13}C-labeled pyruvate entering primarily via PC and the 'succinate-glycine cycle', whereas the 2,3 glutamine originates from inter-organ transport, probably from the brain, and accumulates in the cytosol. I should mention that glutamate is linked to the urea cycle via ornithine δ-transaminase, but this enzyme has been demonstrated only in intestinal mucosa, not in liver (Devlin, 1986).

The urine and liver showed a resonance at 186 ppm which is probably oxalate a catabolic product of glycine (Fig. 2). The urine from the control rat had ^{13}C signals from three primary metabolites which are due to the infusion media: one from PEG (68.4 ppm), another possibly due to the enol form of glycoxate, and an unknown methylene carbon (Fig. 13). Glycine was the most abundant metabolite. Urea was unlabeled, but

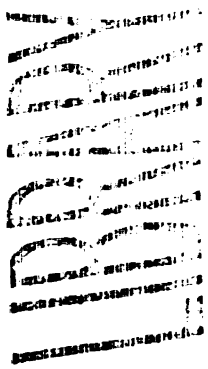

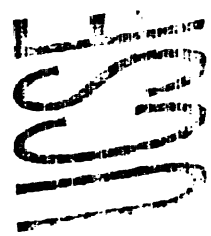

was higher in glycine-infused rats, and is formed from excess ammonia formed via glycine dehydrogenase. Creatinine, glycine conjugates, and oxalate are other metabolites that appear labeled. Urea increases as well.

Conclusions and Future Studies: Our findings are in agreement with well established metabolic pathways of glycine (Fig. 2) (Pasternack et al., 1992; Snell, 1983), but they are unique in the non-invasive observation of the *in vivo* enzyme stoichiometry of the serine methoxytransferase/glycine dehydrogenase complex in rat liver. Additionally, this is the first report of *in vivo* monitoring of γ-glugly and GSH in the liver of intact rat, and should prove to be a powerful model to study γ-GT activity and GSH levels. Future studies need to be performed to inhibit the accumulation of γ-glugly in order to monitor GSH kinetics *in vivo*. γ-GT is a high capacity nonspecific transporter (Meister, 1989), and one could reduce the glycine infusion concentration hoping to target the Na^+-dependent *gly* transporter (Fig. 1) which is more specific and/or inhibit γ-GT Unfortunately, as is common with very effective inhibitors, acivicin is very non-selective in its irreversible inhibition of γ-GT, and targets glutaminase as well as other enzymes. γ-glugly dipeptides are expensive and would be metabolized by dipeptidases in the blood, but may be the best *in vivo* choice, while not causing significant toxic side effects. However, cystine would provide an nice means of inhibiting γ-GT while increasing GSH levels (Fig. 16), because it forms cysteine and γ-glucys. GSH has a negative feedback on its biosynthesis by allosterically inhibiting γ-glutamycysteine synthase, the first enzyme in its synthesis, and therefore the intracellular formation of γ-glucys would bypass the inhibition and continue to increase GSH. Other studies to induce γ-glutamylcyclotransferase would also reduce the amount of γ-glugly, and in conjunction with the γ-GT inhibition studies may permit monitoring of GSH *in vivo* without contamination from γ-glugly.

The discovery of the doubly-labeled serine provides a unique means of separating direct glycine labeling pathways, and isotopomeric analysis of biochemical processes fed

by serine. The satellite peaks due to ^{13}C-^{13}C coupling permits the easy identification of serine-derived metabolites. Comparison of percent double-labeling of serine and subsequent metabolites permits a unique method to investigate biochemical processes (Cohen, 1987c) and compartmentation (Pasternack et al., 1994a). Choline and betaine labeling was found to be decreased as a result of the decreased sulfur amino acid pool. It would be interesting to test if inhibiting glucagon secretion via α-blockers would decrease the 1:1 stoichiometric C2:C3 serine labeling and enhance cytosolic methylation reactions in purines and choline. Glucagon induces serine entry into the TCA cycle by inducing serine dehydratase (Snell, 1983). Inhibition of this enzyme may result in less coupling of serine methoxytransferase and glycine dehydrogenase resulting in greater flow of 1-carbon-labeled units to the cytosol and thus increase purine and choline methylation and labeling. To test the hypothesis that the two pools of glutamine exists and the 'succinate-glycine cycle' are responsible for the 1,2,3 ^{13}C-labeled glutamate and 2,3 ^{13}C-labeled glutamine, we could infuse 1,2 ^{13}C-labeled glucose with cold glycine in order to increase the fractional enrichment of 2,3 ^{13}C-labeled pyruvate entering the TCA and thus increase our detection level.

The combined use of *in vivo* ^{13}C- and ^{31}P-NMR spectroscopy will be an ideal way for studying the effects of xenobiotics. With the addition of xenobiotic, the urine could then be used as a predictor of kidney function in this animal model. In this study we show the control urine and suggest it could be used, as has been shown before (Nicholson et al., 1988), to monitor kidney status and xenobiotic elimination. The development described here will permit the direct observation in intact animals of intracellular metabolic indicators highly susceptible to cell injury (GSH, ATP and pH) by a minimally invasive technique. However, more study is necessary to investigate if the GSH isolation from γ-glugly is possible, and if the urine sampling proves useful in determination of glycine conjugation and kidney function.

CHAPTER 7

The Effect Of Glycine Dose, 2-Oxothiazolidine-4-carboxylate, Cystine Dimethyl Ester, and Dibromoethane On Glycine Metabolism, Bioenergetics, and Intracellular pH By *In Vivo* ^{13}C and ^{31}P NMR

INTRODUCTION

In this chapter we examine the effect of glycine dose, 2-oxothiazolidine-4-carboxylate, cystine dimethyl ester, and dibromoethane on glycine metabolism, bioenergetics, and intracellular pH by *in vivo* ^{13}C and ^{31}P NMR. The goal of these studies was to monitor GSH *in vivo*, and then apply our animal model to toxicological theory. Specifically, our aim was to elucidate a generally accepted hypothesis for the mechanism of toxic action of bioactivated haloalkanes using dibromoethane (DBE) as a model toxicant (mechanism is shown in Chapter 5).

We first needed to decrease the γ-glugly contribution to the *in vivo* ^{13}C peak area composed of GSH and γ-glugly. We attempted to do this by decreasing the dose of glycine in anticipation that the 2-^{13}C-glycine would be transported by the more specific *gly* transporter. This should decrease intracellular γ-glugly levels since γ-glutamylcyclotransferase will not be saturated causing γ-glugly accumulation. Additionally, we infused cystine dimethylester (CDME) in order to generate cystine in the plasma (Ben-Nun et al., 1993). Cystine has 60% greater affinity for γ-glutamyltranspeptidase (γ-GT) than glycine (Thompson, 1975), and thus is a competitive inhibitor. It also increases GSH levels by increasing intracellular cysteine, the limiting amino acid in GSH synthesis, and by forming γ-glucys via γ-GT as shown in Figure 1. GSH has a negative feedback on its synthesis by allosteric inhibition of γ-glutamylcysteine synthase; therefore, γ-glucys, the product of this first enzymatic step in GSH synthesis, bypasses the inhibition. As a result, GSH should be artificially elevated. A prodrug of

cysteine, 2-oxothiazolidine-4-carboxylate (OTC), is metabolized by oxoprolinase, a cytosolic enzyme with the endogenous function to form glutamate from its cyclic form oxoproline (Meister, 1989). The OTC product is cysteine. OTC increases intracellular cysteine levels and, thus, increases intracellular GSH levels (Meister, 1989). The OTC transporter has not yet been identified. Figure 1, demonstrates that, although OTC should increase GSH by increasing intracellular cysteine bioavailability it is also a

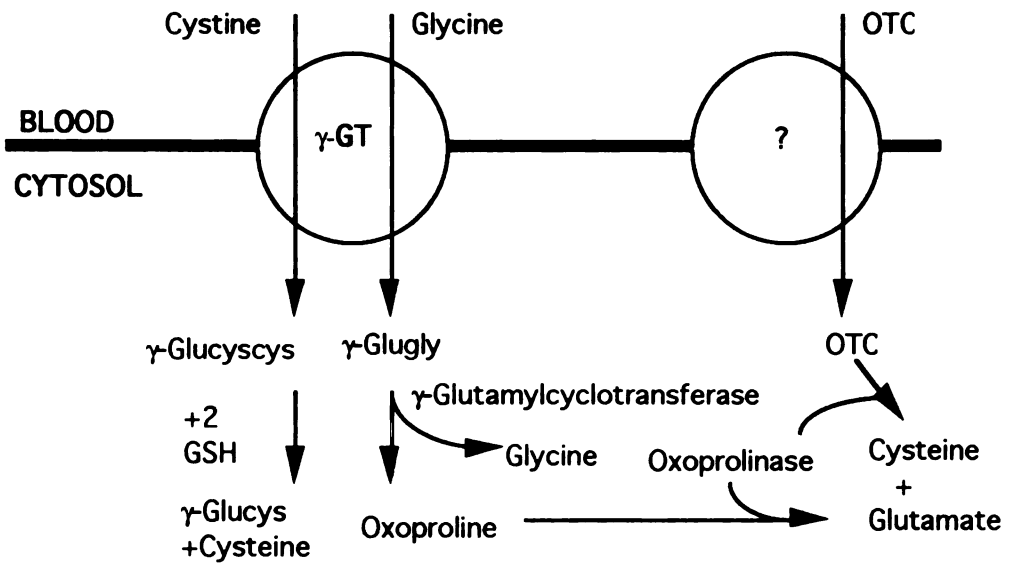

Figure 1: The mechanism of OTC, CDME, and glycine intracellular transport and formation of cysteine, γ-glucys, glutamate, and glycine.

competitive inhibitor of oxoprolinase and could exacerbate our problem of γ-glugly accumulation by causing oxoproline accumulation. If there was γ-glugly accumulation, we would have a direct *in vivo* method to identify this compound and monitor γ-GT kinetics.

In performing the glycine dose and CDME/OTC studies, we propose to simultaneously answer the two basic biochemistry questions posed from the studies performed in Chapter 6: (1) what is the effect of glycine dose on serine double-labeling, and (2) what is the effect of intracellular sulfur amino acid concentration on

transmethylation reactions. Radiotracer studies performed by Neuberger (1981) found that when 2% or 0.5% of the diet was glycine the double-label C3/C2 ratio for serine was 1 or 0.2, respectively. We will investigate this finding by comparing C3/C2 double-labeling of serine via *in vivo* ^{13}C NMR and with tissue extracts by comparing three intravenously infused 2-^{13}C-glycine doses: 4.4 mM (shown in Chapter 6), 1.6 mM, and 400 μm (per kg/hr).

In Chapter 6 we discovered that there was little evidence of transmethylation even after 4 hours of 4.4 mM/kg/hr of 2-^{13}C-glycine intravenous infusion; however, administration of OTC caused a significant increase in transmethylation products. Transmethylation reactions occur primarily in the cytosol via cofactors methylene tetrahydofolate (MTHF) and S-adenosylmethionine (SAM) (Pasternack et al., 1994a). The 'one-carbon' units generated by the glycine cleavage system are formed in the mitochondria and diffuse to the cytosol in the form of (1) the third carbon on serine and (2) in formate (Pasternack et al., 1994a). Once in the cytosol, serine can also form formate by serine methoxytransferase reacting in reverse. Formate will react with tetrahydrofolate (THF) forming methyleneTHF (MTHF) which can be transferred to ATP and onto homocysteine forming S-adenosylmethionine (SAM). Thus, there are two methylating compartments (mitochondrial and cytosolic) with transport mechanisms shuttling between the two compartments. Increased intracellular cysteine caused by OTC administration will increase methionine levels (Stryer, 1981), which should enhance capture of formate before it is catabolized to CO_2 (assuming sufficient THF levels), increasing SAM levels and thus ^{13}C-labeled methylated products. London and Gabel (London, 1988b) found that when methionine is in excess, the S-methyl of methionine forms catabolites of methylated glycine, such as betaine, sarcosine, and dimethylglycine via cytosolic glycine N-methyltransferase. They studied the sarcosine/glycine shuttle system which shuttles SAM 'one carbon' units from the cytosol to the mitochondria. The glycine cycle, which was very active with 4.4 mM/kg/hr of i.v. glycine infusion, is hypothesized to generate flow of 'one

UCSF LIBRARY

carbon' units from the mitochondria to the cytosol, a reverse of London's study (Pasternack et al., 1994a). Choline is formed in a third compartment, the endoplasmic reticulum, by methylation of phosphatidylethanolamine (PE) by SAM (Alberts et al., 1989), with PE coming from decarboxylated phosphatidylserine (Devlin, 1986). PCA-extractable glycerophosphocholine and phosphorylcholine are formed by phospholipase C and D, respectively (Gillies et al., 1994). Therefore, the effect of increased sulfur amino acids in conjunction with glycine infusion on ^{13}C-labeled metabolite composition will generate direct information on methylation compartmentation and whether sulfur amino acid bioavailability is a cause for the lack of transmethylation products found in the study described in Chapter 6.

The hypothesis of the mechanism of toxic action of DBE has been described in Chapter 5. The animal model, using 2-^{13}C-glycine infusion, can non-invasively test this hypothesis for the first time by determining the sequence of many biochemical events during the *in vivo* exposure. Tissue extract and body fluid analysis will give quantitative ^{13}C-label changes in metabolites. For example, by ^{13}C NMR we could potentially monitor changes in GSH, glycine, serine, anaerobic glycolysis, gluconeogenesis, lipogenesis, anaplerosis, phospholipid turnover, DNA/RNA synthesis, and protein synthesis. By *in vivo* ^{31}P NMR we can measure bioenergetics, intracellular pH, phospholipid and urea cycle [(carbamoyl phosphate (Cohen, 1987c)] intermediates. Therefore, the specific aims of this study were to optimize the animal model by decreasing the contribution of γ-glugly to the peak representing GSH *in vivo*, while simultaneously investigating some basic biochemistry questions posed in Chapter 6. Then, the effectiveness of the animal model for application to toxicodynamics will be tested using DBE, a model alkylating agent and carcinogen. Even if γ-glugly contamination of the GSH resonance is not successfully decreased, Chapter 6 revealed the broad range of biochemical participation of glycine, which could permit senedipitous discovery of glycine-derived biomarkers of DBE toxicity and lead to perhaps novel mechanism(s) of toxicity.

MATERIALS AND METHODS

Chemicals: The same chemicals as described in Chapter 6 were used, except EDTA was purchased from Sigma Chem Co., and Chelex-100 was purchased from (Sigma Chem. Co.).

NMR Probe Design: The same probe design described in Chapter 6 was used to obtain *in vivo* ^{13}C and ^{31}P NMR spectra.

Animal Protocol: The same surgical and physiological monitoring described in Chapter 6 was used these studies. Protocol #1 is described in Chapter 6 and consisted of an intravenous infusion containing 4.4 mM/kg 2-^{13}C-glycine, 10% glucose, 4% mannitol, and 7 mg/kg/hr pentobarbital at an infusion rate of 3 mL/hr for 4.5 hr. The other four protocols were the same as protocol #1 except: (2) 15 mM/kg were infused over 30 min at the beginning of the experiment, (3) 400 μM/kg/hr of 2-^{13}C -glycine and 100 μM/kg/hr of CDME were infused as a mixture, (4) 1.6 mM/kg/hr of glycine and 100 μm/kg/hr of CDME were infused as mixture. Protocol #5 was the same as protocol #4, except the rat was taken out of the magnet after 2.2 hr of glycine infusion and given an intraperiteoneal injection of DBE dissolved in sesame oil which corresponded to the i.p. LD_{50} (80 mM/kg) for DBE (NTP, 1982). The rat was placed back in the same spot in the magnet, and the *in vivo* ^{13}C and ^{31}P NMR spectra were followed for 1.5 hr. Blood samples were obtained every hr or as necessary, and plasma and red blood cells were separated and frozen in liquid N_2. Urine was collected through a transuretral catheter every 1-1.5 hours.

After the experiment, liver and the PCA extraction procedures described in Chapter 6 were followed. Some plasma samples were deproteinized by titration to pH 4.0 and centrifugation. Samples were dissolved in deuterium oxide with TSP and analyzed by high-resolution NMR.

Two sets of pulse-chase studies were performed to determine the effect of the aforementioned protocols #1 and #3 on the GSH/γ-glugly ^{13}C peak area ratio. Rats were injected intraperitoneally with either (1) 4.4 mM/kg glycine or (2) 0.4 mM/kg glycine plus 100 μM/kg of CDME dissolved in saline. They were placed in a cage without food, but with access to water and sacrificed at 1, 2, 4 and 6 hours. The livers were excised and frozen in liquid nitrogen and subjected to PCA extraction, lyophilization, and subsequent high-resolution analysis.

In Vivo Spectroscopic Studies: The *in vivo* spectroscopic conditions are described in Chapter 6.

In Vitro Spectroscopic Studies: The high resolution NMR analysis of tissue extracts and body fluids are described in Chapter 6. The only difference was that Chelex-100 was added to the sample dissolved in deuterium oxide to remove paramagnetic metal ions from the sample, and centrifuged prior to addition to the NMR tube.

RESULTS

We present the results from protocols #1-5, designed to elucidate the effects in rat liver metabolism of (1) 2-^{13}C-glycine dose, (2) intracellular cysteine bioavailability, and (3) DBE. For most protocols, we attained a statistically significant number of viable studies where the rat survived the experimental procedure (n_v=3). However, due to incorrect NMR probe placement (as determined by *in vivo* ^{31}P NMR), research and development modifications, and miscellaneous experimental flaws, we did not obtain the full compliment of interpretable *in vivo* data sets (n_d). In terms of presenting these data, tissue extract and body fluid data may be statistically significant, but the *in vivo* data are

preliminary. The experimental success of protocols 1 through 5 used to describe the three effects outlined above is as follows:

DOSE	PROTOCOL NO.	n_v	n_d
4.4 mM/kg/hr glycine	1	6	3
4.4 mM/kg/hr glycine + 15 mM/kg OTC	2	3	1
0.4 + 0.1 mM/kg/h glycine + CDME	3	1	1
1.6 + 0.1 mM/kg/hr glycine + CDME	4	3	1
1.6 + 0.1 mM/kg/hr glycine + CDME + 80 mg/kg DBE	5	1	1

Note: n_v=number of viable studies; n_d=number of interpretable data sets.

The Effect of Dose: Figure 2 illustrates portions of the *in vivo* ^{13}C NMR spectra of rat liver at three intravenous infusion doses of glycine - protocol #1 (spectrum A), #4 (spectrum C), and #3 (spectrum D). The rats in Figure 2C and D also received 100 μm/kg/hr CDME in the infusion elixir, adding an additional factor of increased intracellular cysteine levels. The effects of increased intracellular cysteine levels could be obtained by comparison to OTC, which are presented in the subsequent section, but CDME may have different effects from those exhibited by OTC and needs further elucidation. Each spectrum was composed of 140 acquisitions and required 9.8 min to obtain. The dose of 0.4 mM/kg/hr of 2-^{13}C-glycine was not sufficient to obtain acceptable signal-to-noise ratio in 9.8 min (Figure 2D). Figure 3 shows ^{13}C NMR spectra (acquired at 75 MHz) of PCA liver extracts obtained from the same rat livers (protocols 1through 4) shown in Figure 2. EDTA was added to the PCA solution and appears as three peaks in the ^{13}C spectrum (171.70, 59.18, 52.61 ppm at pH 5.00). Comparison of these *in vivo* and extract spectra from protocols #1, #3, and #4, in addition to liver extracts from i.p. pulse-chase studies comparing protocol #1 and #3, demonstrate four effects caused by decreasing the glycine dose: (1) increase in the GSH+γ-glugly/glycine peak area ratio, (2) no correlation in GSH/γ-glugly peak area ratio, (3) a

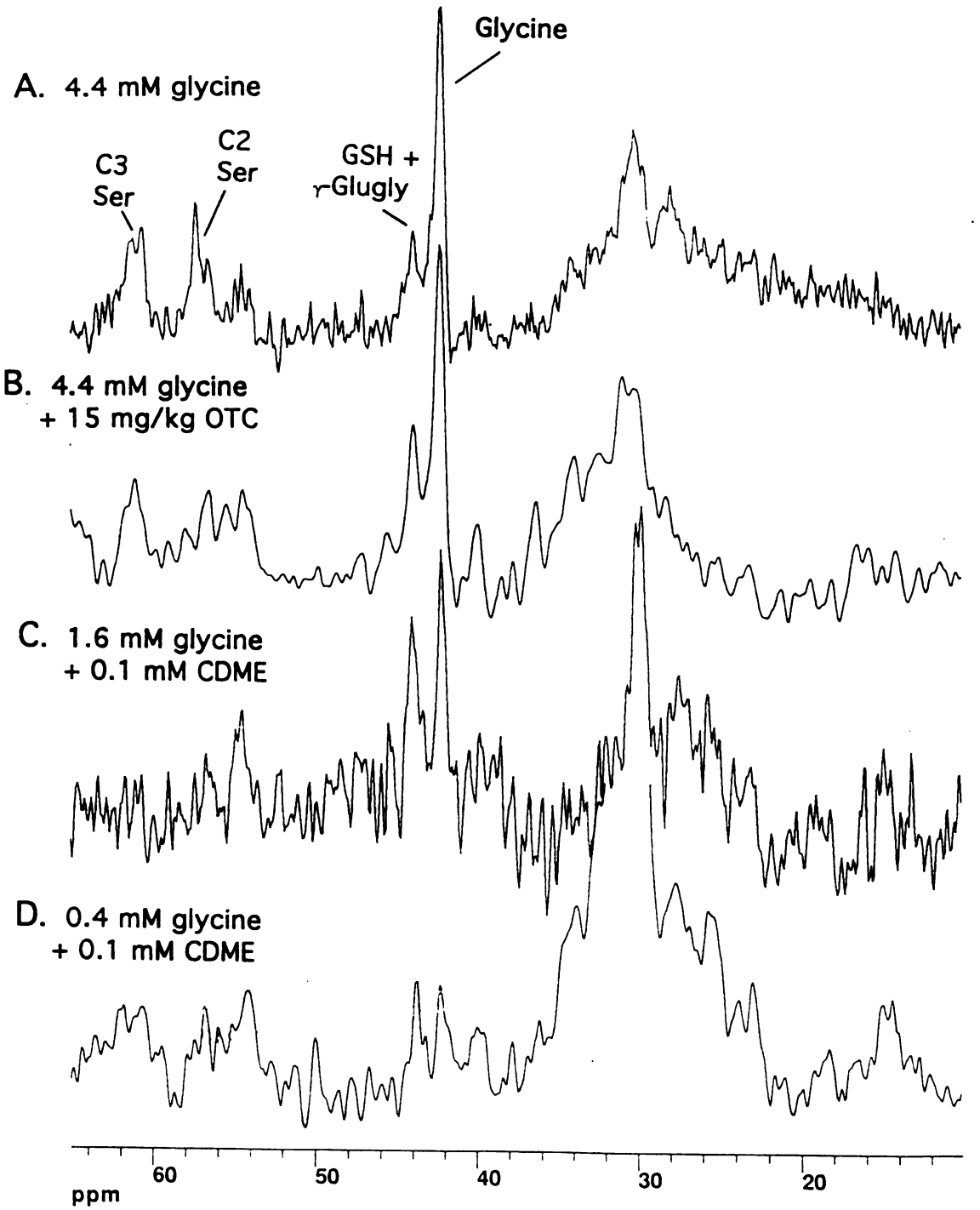

Figure 2: *In vivo* ^{13}C NMR spectra of the last spectrum obtained of rat liver using protocol #1 (A), #2 (B), #3 (D), and #4 (C). Spectra were obtained with a 70° in-plane flip angle, SW=4400 Hz; TR=1.2 s; and are the accumulation of 140 transients, except spectrum D which is a total of 420 transients.

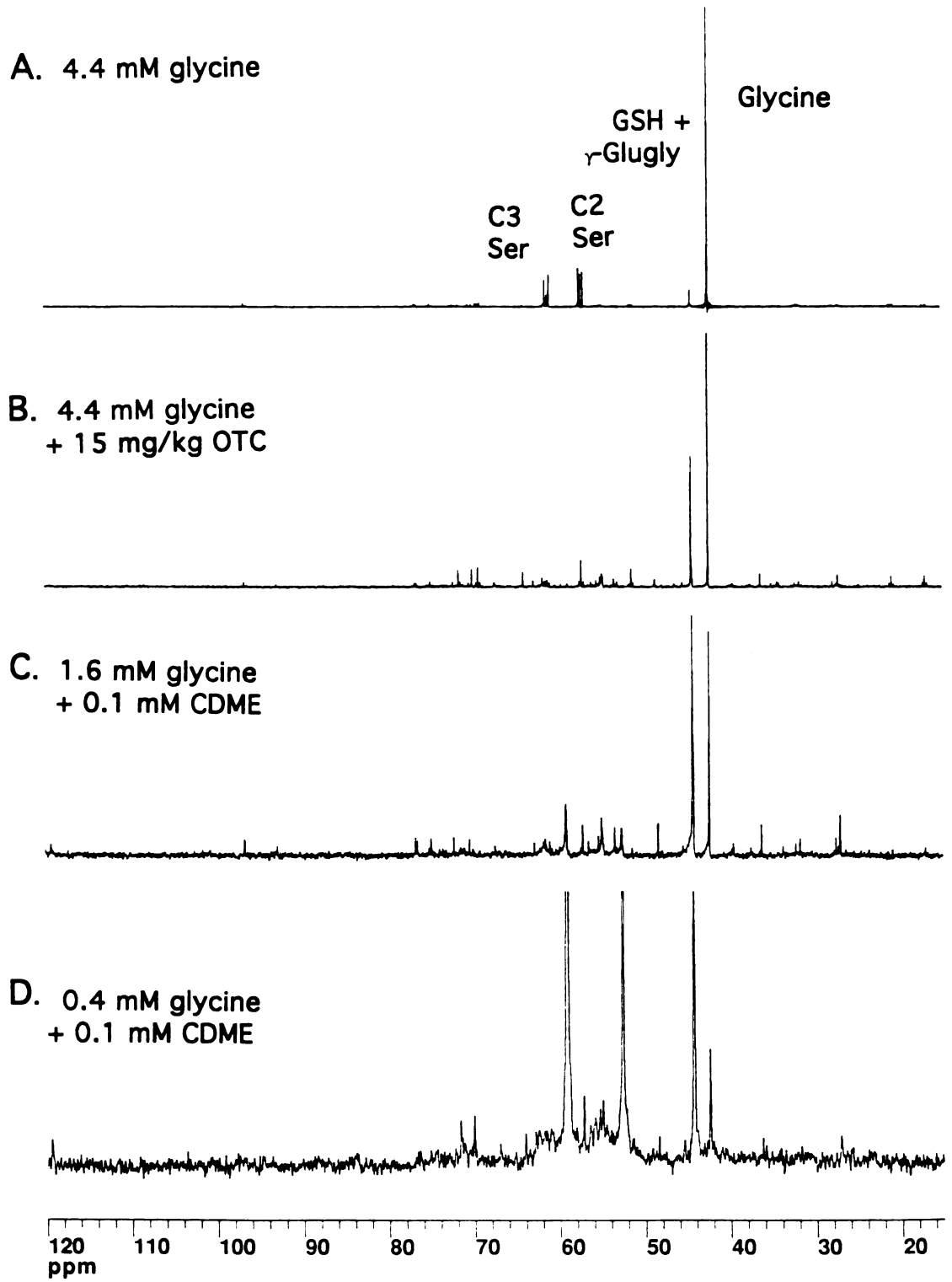

Figure 3: PCA extracts of the livers shown in Figure 2 with protocol #1 (A), #2 (B), #3 (D), and #4 (C). All spectra were obtained on a GE QE300 at 75 MHz with an interpulse delay of 10s, SW=10,000 Hz, data point=16K. The spectra are referenced to TSP at -2 ppm and the difference in signal-to-noise is primarily due to the amount of ^{13}C-label.

decrease in serine C3/C2 double labeling, (4) decreased utilization of glycine by gluconeogenesis, glycolysis and anapluerosis.

The increase in GSH+γ-glugly/glycine peak area ratio with decreased glycine dose is shown in Figure 4. Figure 4 is the timecourse of glycine and GSH+γ-glugly peak areas for protocol #1 and #4 obtained from *in vivo* ^{13}C NMR spectra. We arbitrarily set 100% equal to the last and the average of the last four glycine/dioxane peak area ratio(s) obtained for protocol #4, and #1, respectively (see Methods section, Chapter 6 for details.

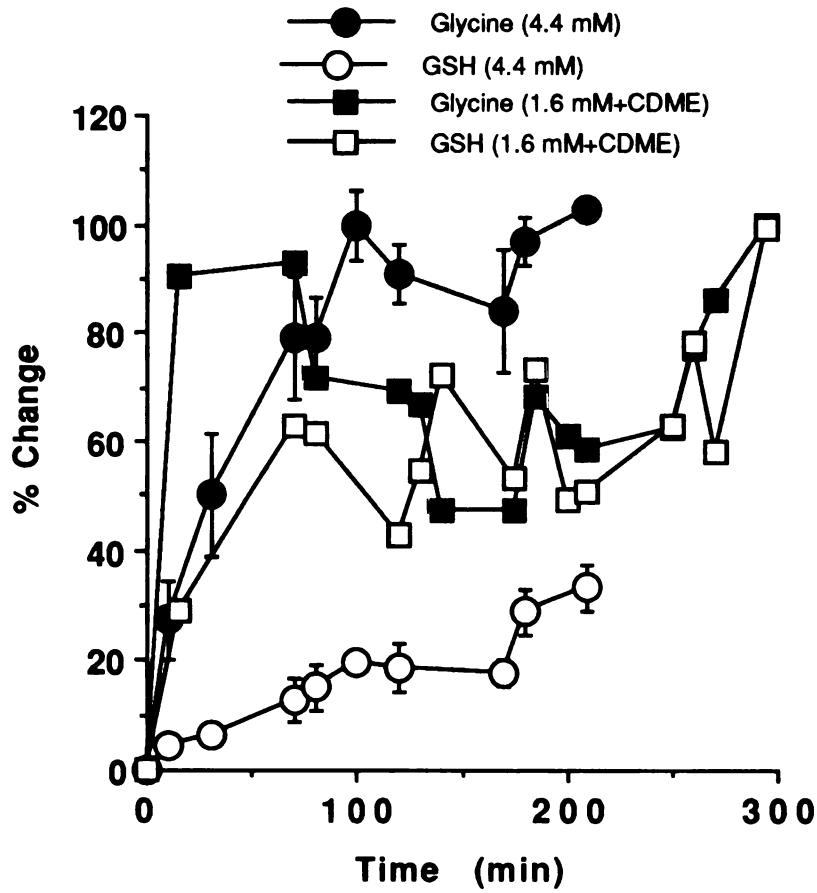

Figure 4: Kinetics of the two doses of 2-^{13}C-glycine on glycine, and GSH+γ-glugly kinetics in rat liver.

fTherefore, comparisons between protocols #1 and #4 cannot be made regarding absolute increases in the GSH+γ-glugly peak area. However, comparison of the signal-to-noise ratio of the GSH+γ-glugly peak obtained from protocol #1 and #4 (Fig. 3A and C, respectively) indicates the GSH+γ-glugly signal slightly increased with protocol #4, probably due to CDME. The GSH+γ-glugly/glycine peak ratios for the spectra in Figure 3 A, C, and D are 0.07, 1.95, and 3.97, respectively, supporting the notion that the GSH+γ-glugly/glycine ratio increases with decreased glycine dose. The GSH/γ-glugly peak area ratios obtained from the ^{13}C spectra of liver extracts shown in Figure 3 or protocols #1, #3, and #4 were 0.86 ± 0.2, 1.14, and 0.91, respectively, and did not correlate with increased glycine dose as they did in the rat liver extracts obtained from pulse-chase studies. For example, the GSH/γ-glugly peak area ratios from the pulse-chase studies with an i.p. bolus injection of 4.4 mM/kg 2-^{13}C-glycine were 0.87, 0.65, 1.30, and 1.56 at 1, 2, 4, and 6 hours, respectively. For 0.4 mM/kg + 0.1 mM/kg CDME, the ratios were 2.20, 1.34, and 3.00 at 1, 2, and 4 hours, respectively. This demonstrates that γ-glugly is more rapidly synthesized than GSH. These pulse-chase studies do not represent steady-state conditions as do the *in vivo* studies. The higher bolus dose of 2-^{13}C-glycine indicates that there is greater accumulation of γ-glugly and ^{13}C-labeling of the GSH pool as compared to the lower bolus dose, since at all timepoints the total ^{13}C label was greater. This is demonstrated by the significantly lower signal in the lower dose ^{13}C spectra (spectra not shown). Therefore, whether the increased GSH/γ-glugly ratio with decreased dose is due to the addition of CDME or faster clearance of γ-glugly by γ-glutamylcyclotransferase is unclear. It is clear, however, that γ-glugly has much more rapid kinetics causing the increased GSH/γ-glugly.

Figure 5 and 6 compare portions of the ^{13}C spectra of PCA liver extracts from protocols #1, #3, #4, (shown in Figure 3A, C, and D, respectively) and control. In spectrum 5B and C (protocol # 1 and #4, respectively), the largest natural-abundance peaks are due to excess EDTA (59.18 and 52.61 ppm) from the PCA solution. The most obvious difference is the decrease of C3/C2 (61.21 and 57.17 ppm, respectively), double-labeling of

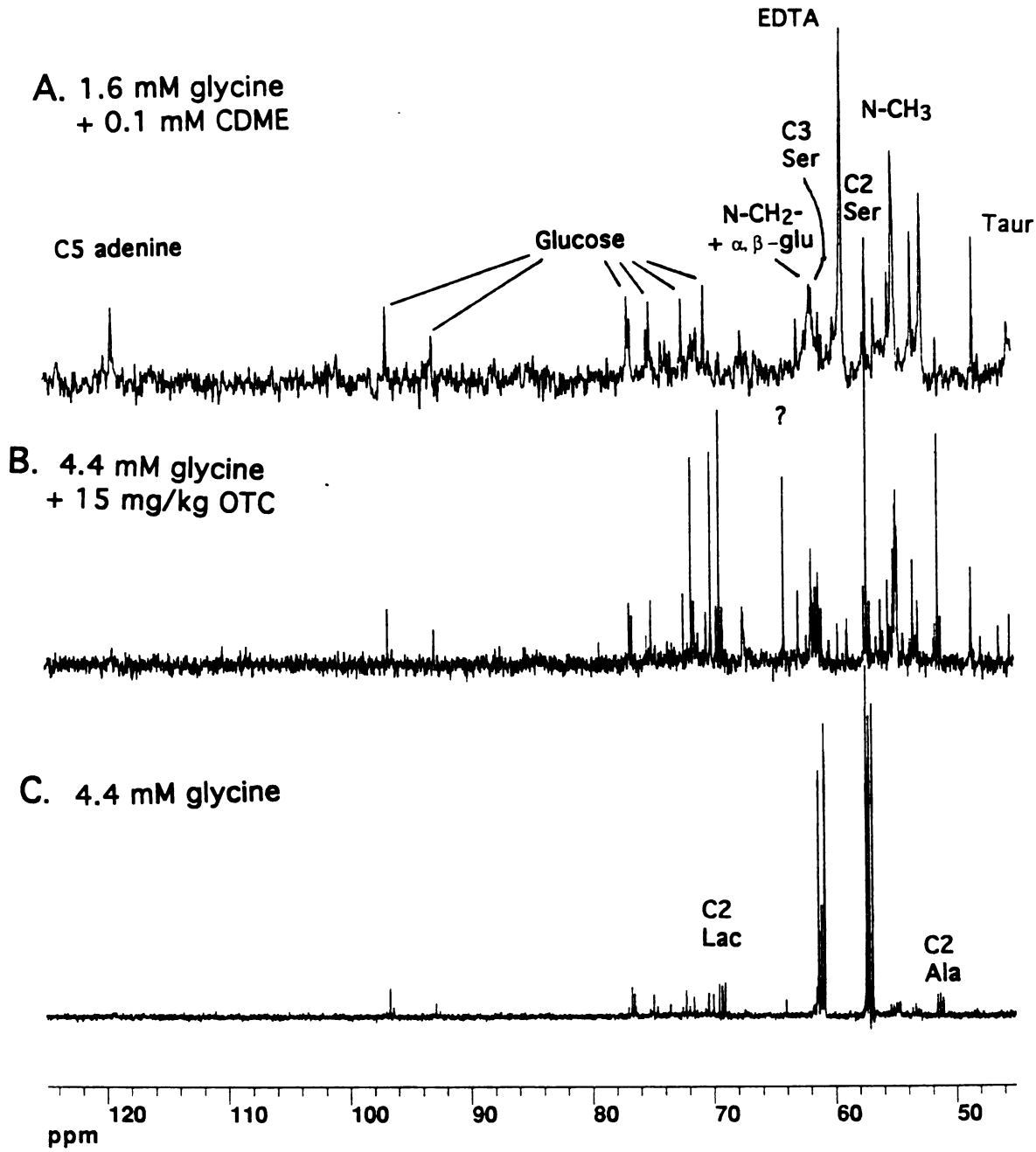

Figure 5: A portion of the of the ^{13}C NMR spectra (45-125 pmm) obtained from PCA extracts of the liver shown in Figure 3 with protocol #4 (A), #2 (B), and #1 (C). In spectrum A the two largest peaks are due to EDTA (59.2 and 52.6 ppm) from the PCA solution.

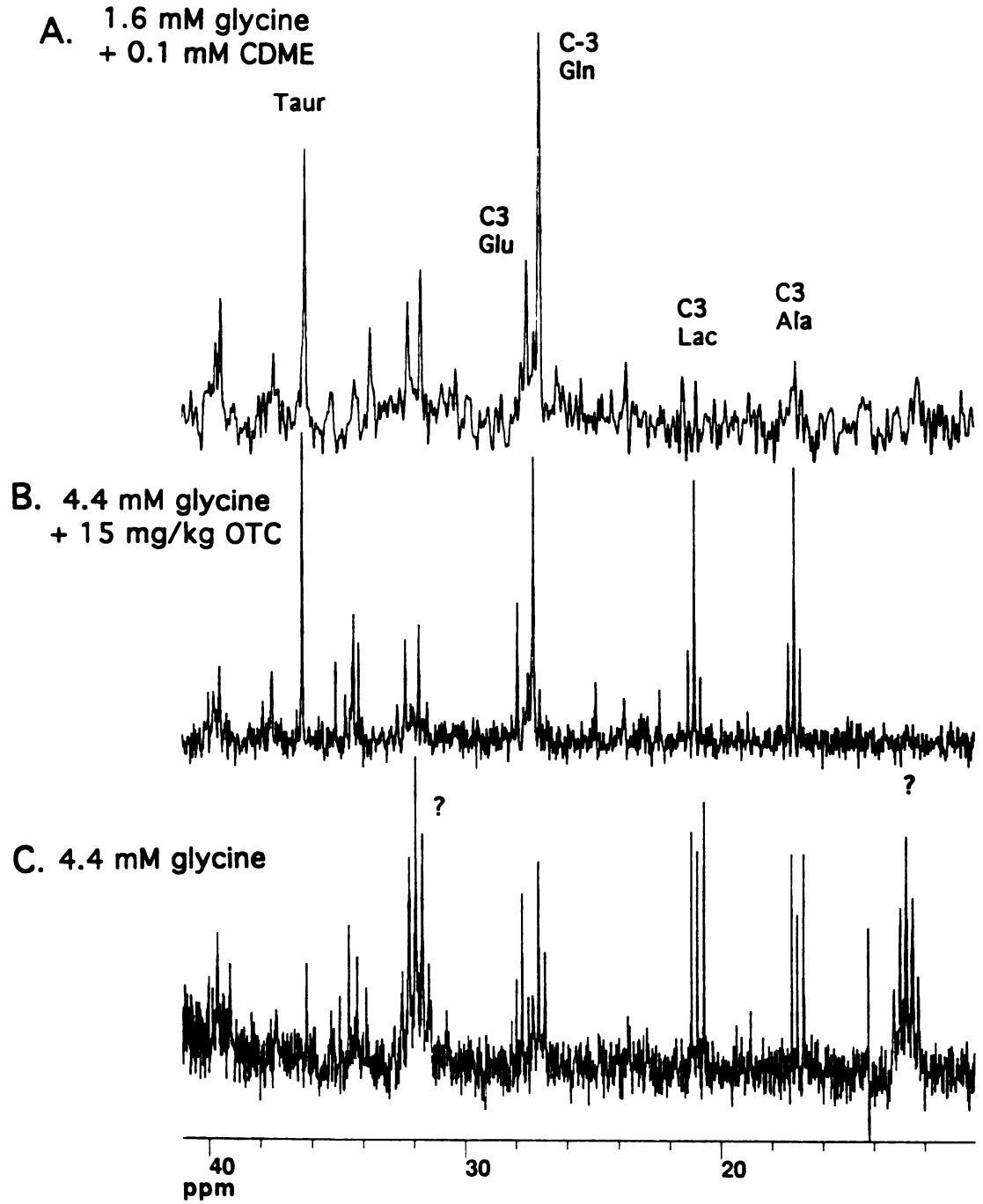

Figure 6: A portion of the of the ^{13}C NMR spectra (45-125 pmm) obtained from PCA extracts of the liver shown in Figure 3 with protocol #4 (A), #2 (B), and #1 (C).

serine with a ratio of 0.85 ± 0.05, and less than 0.1 for protocol #1 and #4, respectively. Comparison of the peak intensities for α-C2 and α-C5 glucose (72.2 ppm) to α, β-C4 glucose (70.4 ppm) reveals little difference in intensity, demonstrating that there is negligible ^{13}C labeling of glucose from 2-^{13}C-serine with the lower doses (protocols #3 and #4). The two methylene carbons from taurine (48.24 and 36.20 ppm at pH 5.00) appear in the ^{13}C spectrum from protocols #3 and #4, but not #1, and are probably due to the catabolism of CDME. The C2 of adenine [119.3 ppm at pH 5.00 (Fig. 5A)] is also significantly labeled by the addition of CDME to the infusion media.

The Effect of Increased Intracellular Cysteine: Figure 2 demonstrates the effect of intracellular cysteine bioavailability on the GSH+γ-glugly/glycine peak area ratio by comparison of the last *in vivo* ^{13}C NMR spectrum obtained using protocols #1 (spectrum A) and #2 (spectrum B). Comparison of the glycine and GSH levels for protocols #1 and #2 are shown in Figure 7 (protocol #2 was reference the same as protocol #4 in Figure 4). Figure 3 shows ^{13}C NMR spectra (acquired at 75 MHz) of PCA liver extracts obtained from protocol #1 (spectrum A) and #2 (spectrum B). The GSH+γ-glugly/glycine peak area ratios for spectrum 3A and 3B are 0.07 and 0.53, respectively. The addition of 15 mg/kg OTC (protocol #2) resulted in a 7.6-fold increase in the GSH+γ-glugly/glycine ratio. The GSH/γ-glugly ratio composing the peak centered at 44.2 ppm in Figures 3A and 3B is 0.56 and 0.25, respectively. Therefore, 15 mM/kg OTC caused an apparent accumulation of γ-glugly, but increased GSH levels nearly 3.3-fold since the GSH+γ-glugly/glycine and the GSH/γ-glugly peak area ratios are 7.6-fold greater and 2-fold less, respectively.

Figure 8 compares portions of the ^{13}C spectra of PCA liver extracts from protocols #1 and #2, and intravenously infused OTC (20 mM/kg/hr for 2 hr). There is a decrease of C3/C2 (at 61.21 and 57.17 ppm, respectively) double-labeling of serine with a ratio of 0.85 ± 0.05 and 0.14 for protocols #1 and #2, respectively. Comparison of the peak intensities

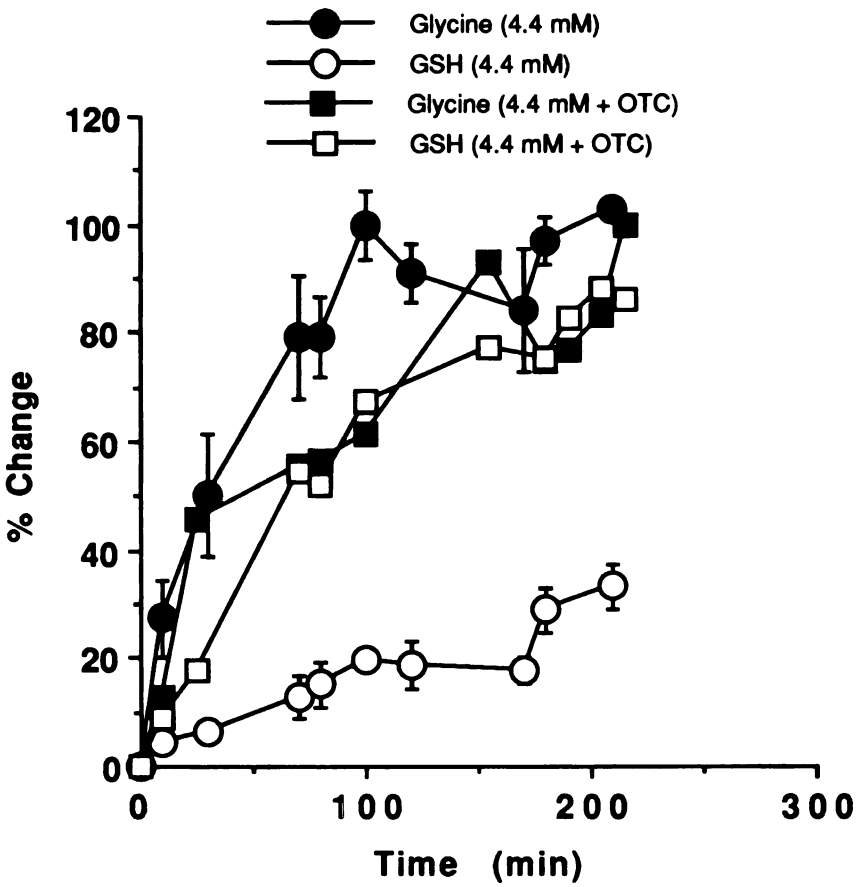

Figure 7: The effect of OTC on glycine and GSH+γ-glugly peak areas in the *in vivo* ^{13}C spectra.

for α-C2 and α-C5 glucose (72.2 ppm) to α β-C4 glucose (70.4 ppm) reveals a significant difference in intensity demonstrating that there is significant ^{13}C labeling of glucose from 2-^{13}C-serine. The two methylene carbon signals from taurine (48.2 and 36.2 ppm at pH5.00) appear in the ^{13}C spectrum from protocol #4 but not #1 and are probably due to the catabolism of OTC. With OTC infusion (spectrum C), taurine is the second largest peak (48 and 36 ppm) with OTC (59 and 34 ppm) being the largest. GSH was also increased with OTC infusion (spectrum 8C) as compared to control spectra (spectra not shown). Methylation products exhibited slightly increased ^{13}C-labeling with protocol #2 at

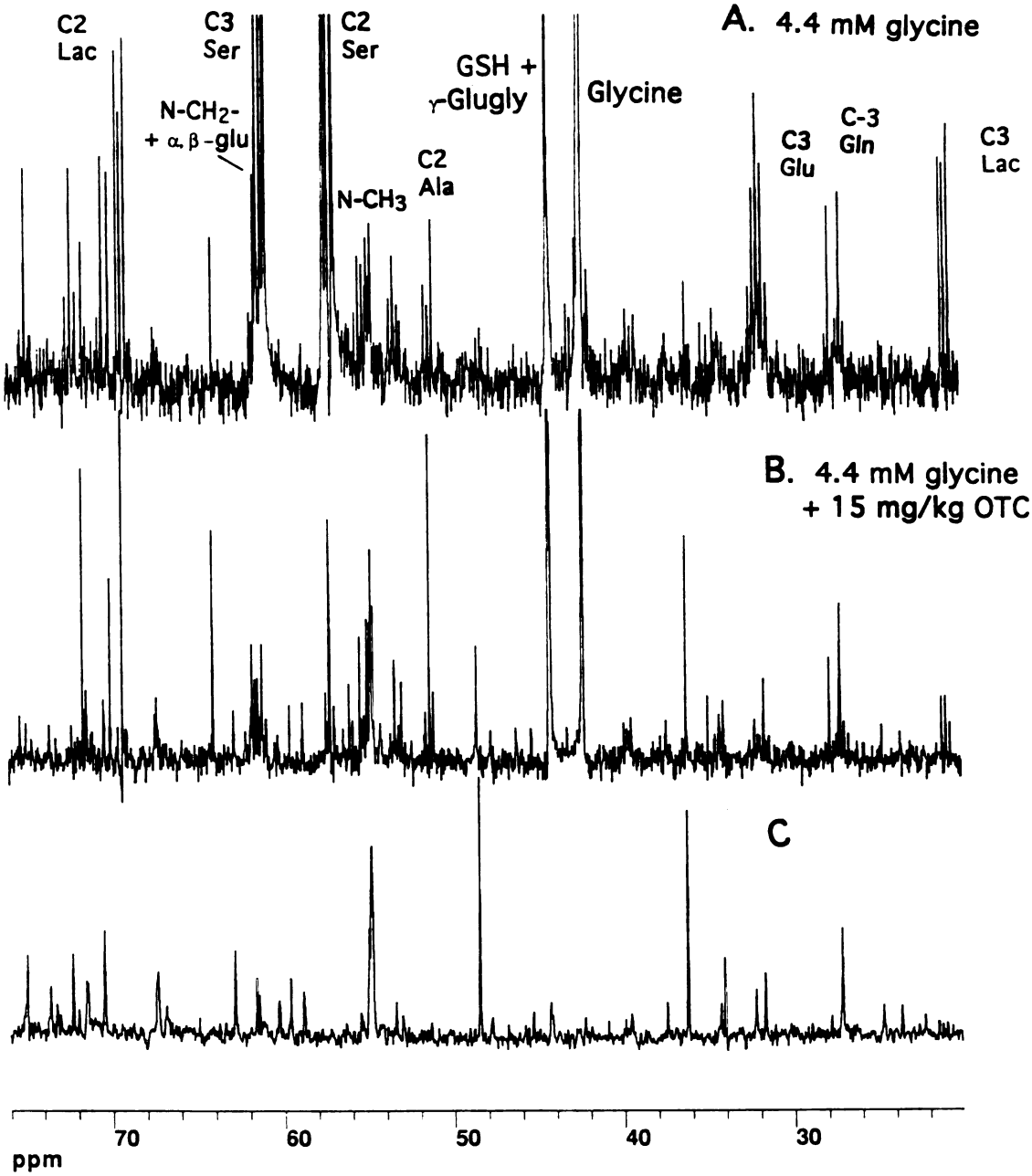

Figure 8: A portion of the of the ^{13}C NMR spectra (45-125 pmm) obtained from PCA extracts of the liver shown in Figure 3 with protocol #1 (A), #2 (B), and control rat given i.v. infusion of 20 mM/kg/hr OTC for 2 hr and without 2-^{13}C-glycine (C).

betaine (54.9 ppm) and choline (54.4 ppm) as compared to protocol #1 and OTC infusion. More ^{13}C-label appears in lactate and alanine in protocol #2 than #1. Double-labeling appears in C2 and C3 of lactate (69.3 and 21.0 ppm), alanine (51.4 and 17.0 ppm), glutamine (55.0 and 27.0 ppm), glutamate (55.5 and 27.9 ppm), and aspartate (53.1 and 37.5 ppm) and reflects similar relative labeling as C2 and C3 serine (scale is 4 times greater in Figure 6). The C5 of adenine [119.3 ppm at pH 5.00 (Fig. 5A)] was not significantly labeled by the OTC addtition.

The Effect of Dibromoethane: Figure 9 shows portions of the *in vivo* and liver extract ^{13}C spectra during the course of an experiment using protocol #5 and demonstrates the effect of 80 mg/kg DBE on glycine and the GSH+γ-glugly levels. As compared to the ^{13}C spectrum obtained just before DBE administration (spectrum B) and the dioxane external standard (not included in the spectra shown in Figure 9), the glycine and GSH peaks decrease, C2 of serine increases, and a broad component appears centered at 44 and 55 ppm (spectrum C). The timecourse of glycine and GSH levels for protocol #5 is shown in Figure 10. Both glycine and GSH decrease by the second timepoint obtained 60 min following i.p. injection of DBE (i.e., t=190 min). GSH steadily decreases, but glycine appears to have a homeostatic increase followed by a steady decrease. The GSH+γ-glugly/gly and GSH/γ-glugly ratios in the liver extracts are 1.95 and 0.91 for protocol #4 (Figure 2C), respectively, and 1.0 and 0.85 for protocol #5 (Fig. 9D), respectively. The liver extract revealed dramatic *de novo* protein, purine synthesis, and a yet unidentified resonance. Figure 11 shows the complete ^{13}C spectra from the last *in vivo* spectrum obtained (spectrum A) and the corresponding extract (spectrum B). When the extract was prepared for high-resolution NMR analysis and titrated from pH 7.4 to 5.0, there was a brownish precipitate which dissolved when the pH was increased again to 7.0. The ^{13}C spectrum of the precipitate is shown in Figure 11C. The three broad components ranging from 39-47 ppm, 51-64 ppm, and 68-79 ppm may emanate from protein fragments that

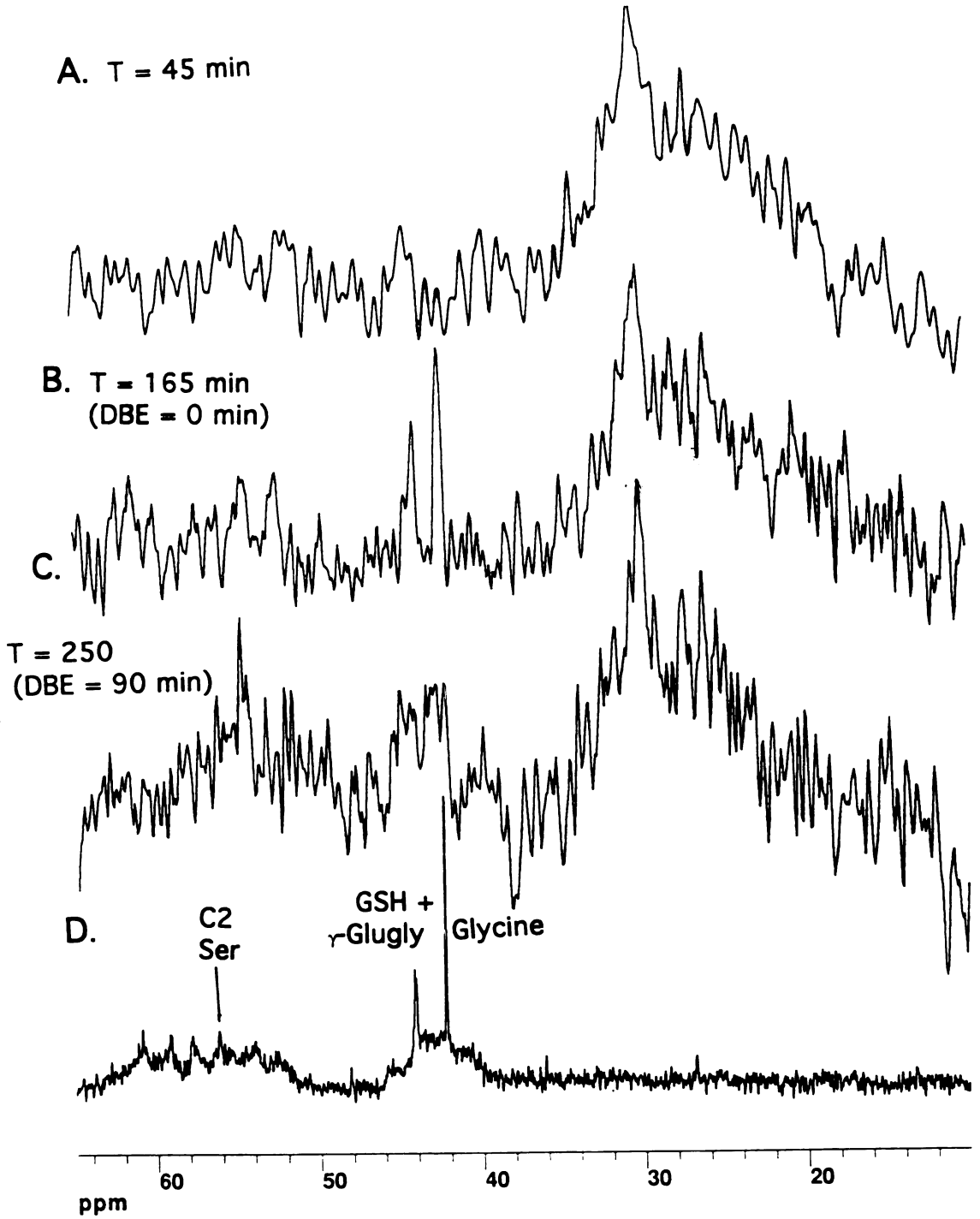

Figure 9: The *in vivo* ^{13}C timecourse (A through C) showing the effect of DBE on the spectra with the extract (D). 80 mg/kg of DBE was injected intraperitoneally in sesame seed oil at time 130 min after start of 2-^{13}C-glycine infusion. The ^{13}C spectra were obtained with a with a 70° in-plane flip angle, SW=4400 Hz TR = 1.2 s; and are the accumulation of 140 transients, requiring 9.8 min each to acquire.

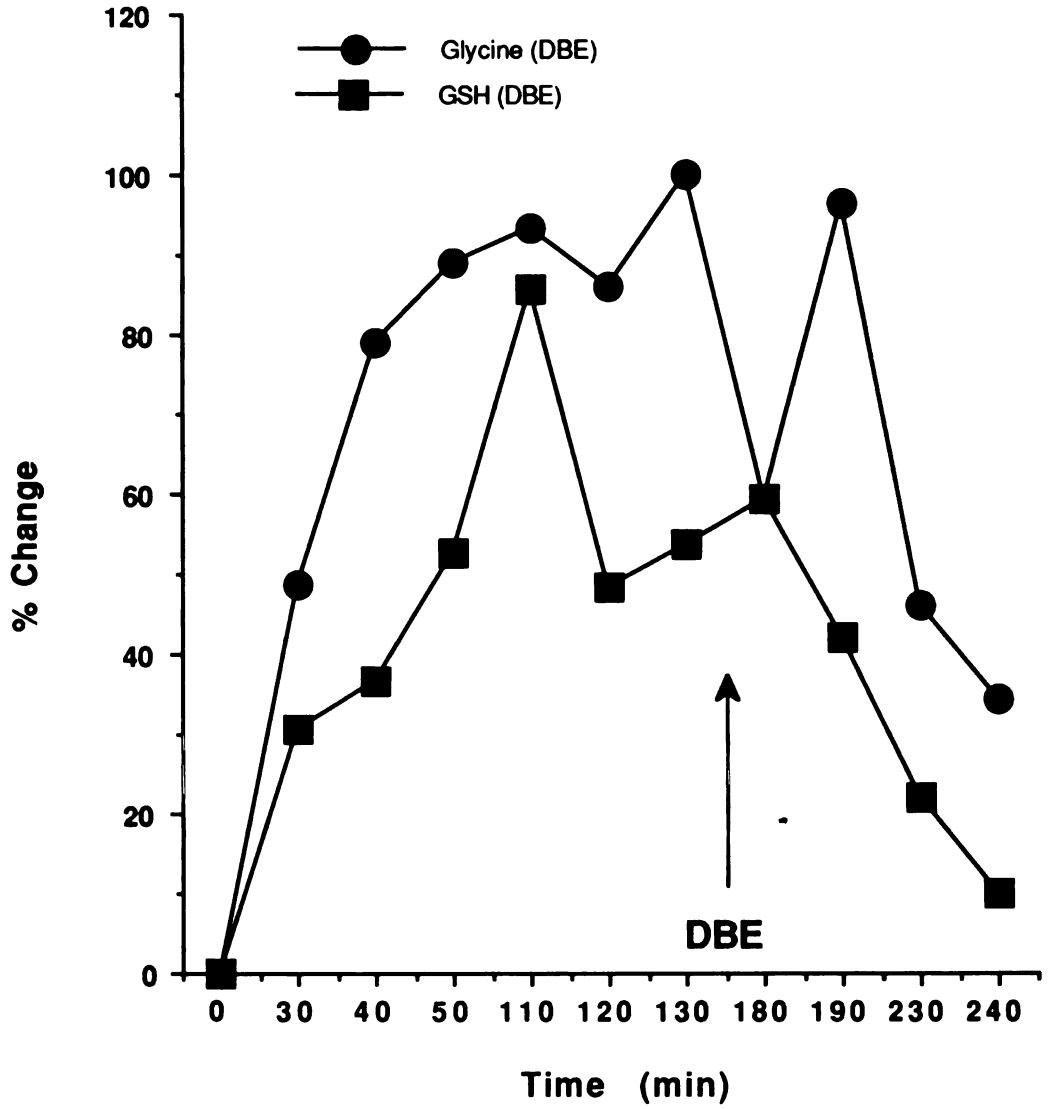

Figure 10: The effect of DBE on glycine and GSH+GSH+γ-glugly peak areas in the *in vivo* ^{13}C spectra. 80 mg/kg of DBE was injected intraperitoneally at t = 130.

bhave incorporated C2-labeled amino acids because large proteins are extracted with PCA. For example, collagen is composed of 33% glycine, and perhaps collagen fragments that were in the process of being synthesized may be partially responsible for the broad component ranging from 39-47 ppm. A peak resonating at 119.3 ppm significantly increased, indicating *de novo* purine synthesis. Based on literature values, this peak is

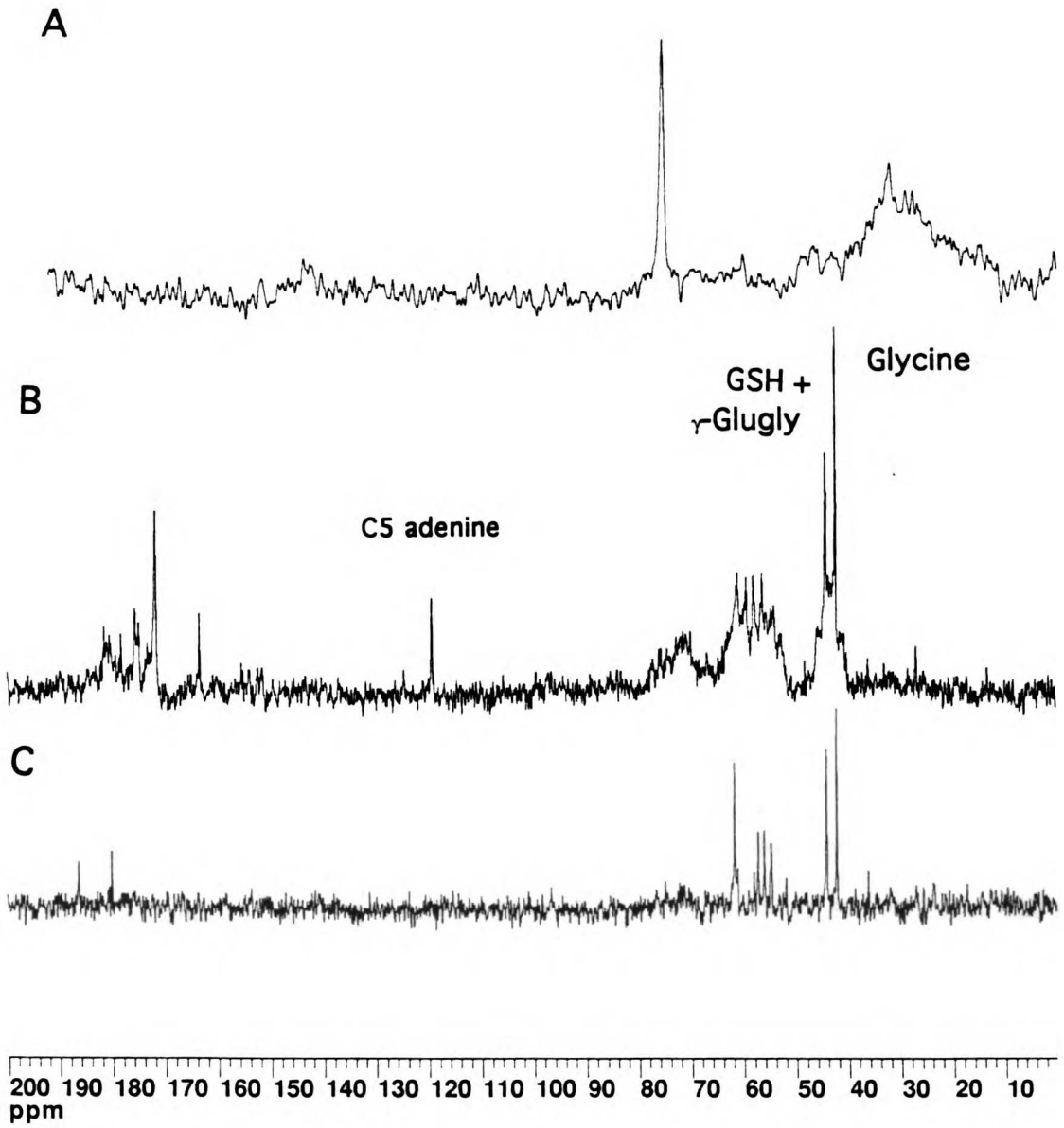

Figure 11: The *in vivo* ^{13}C spectra taken of the liver prior to dissection (A), of the liver extract (B), and of the precipitate that formed when the PCE extract was titrated from pH 7.4 to 5.0 (C). The effect of DBE on the ^{13}C spectrum revealed three broad components centered at 42, 58, and 72 ppm. All spectra were obtained on a GE QE300 at 75 MHz with an interpulse delay of 10 s; SW=10,000 Hz; data point = 16K; and the spectra are referenced to TSP at -2 ppm.

tentatively identified as C5 of adenine. The precipitate (spectrum C) revealed glycine (42.3 ppm), GSH + γ-glugly (44.2), methyl of betaine and choline (56.9 and 56.4 ppm, respectively), C2 of glutamine (55.0 ppm), C2 of glutamate (55.5 ppm), an unknown resonating at 56.2 ppm tentatively identified as C2 of cysteine, C2 of serine (57.3 ppm), and an unknown at 61.2 ppm, 61.8 ppm, 180.2 ppm, and 186.5 ppm. No anaerobic products, such as lactate or alanine, were observed.

Figure 12 shows ^{13}C spectra of the kidney PCA extract dissected after dissecting the liver from the rat subjected to protocol #4 (spectrum C), urine from 3-4 hr after the start of 2-^{13}C-glycine infusion with protocol #4 (spectrum B), and urine from 0-1.5 hr DBE injection from protocol #5 (spectrum A). The primary difference between the kidney (spectrum C) and urine from protocol #4 (spectrum B), besides the peak emanating from EDTA (52.6 ppm), is a peak at 45.1 ppm. The only differences between the urine from protocols #4 and #5 are multiplet peaks at 12.7 ppm and 31.9 ppm, possibly from the same unknown coupound discovered in the liver extracts with protocol #1 described in Chapter 6.

Figure 13 and 14 are the *in vivo* ^{31}P NMR spectra from rat liver subjected to protocol #4 and #5, respectively. For protocol #4 the intracellular pH and β-NTP/Total P_i ratio is 7.41 and 16.58, 7.41 and 16.49, and 7.41 and 11.69 at 40, 160, and 220 min, respectively, after start of infusion and obtained from the *in vivo* ^{31}P spectra shown in Figure 12. For protocol #5 the intracellular pH and β-NTP/total P_i ratio is 7.40 and 20.6, 7.42 and 20.3, 7.38 and 18.2, 7.40 and 6.90 and 17.41 at 45, 165 (DBE; t = 0), 225 (DBE; t=60 min), 250 (DBE; t = 90 min), respectively, after start of infusion and obtained from the *in vivo* ^{31}P spectra shown in Figure 13. There are two P_i peaks after 90 min from injection with DBE, but more control studies with protocol #4 need to be performed for a better comparison of bioenergetics which appear to deteriorate at 220 min of infusion.

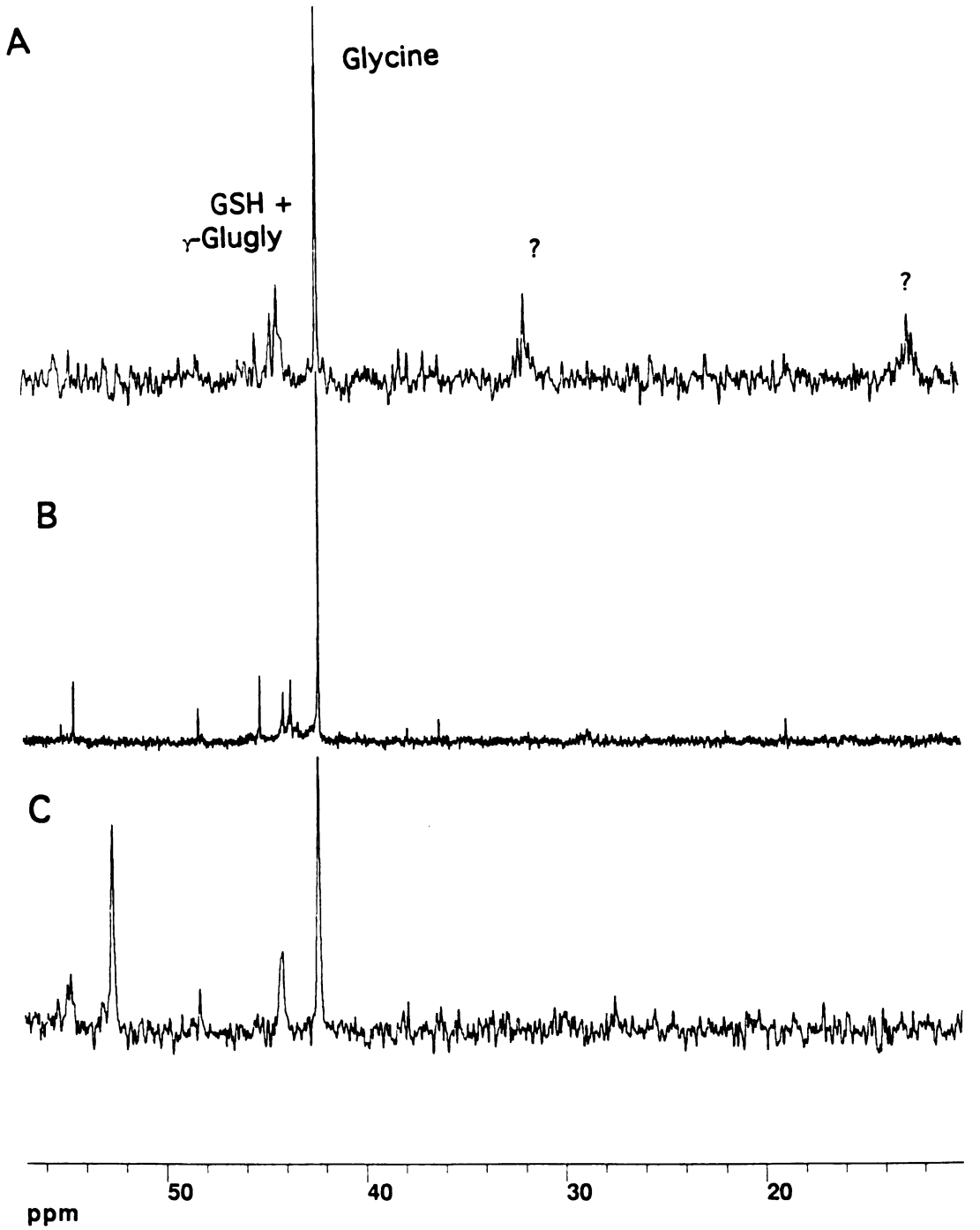

Figure 12: The urine obtained from 3-4.5 hr of glycine infusion for protocol #5 (A) and # 4 (B), and the PCA extract of the kidney from the *in vivo* experiment shown in Figure 2 with protocol #4 (C). The peak at 52.6 in spectrum C is due to EDTA from the PCA solution. All spectra were obtained on a GE QE300 at 75 MHz with an interpulse delay of 10 s; SW=10,000 Hz; data point=16K; and the spectra are referenced to TSP at -2 ppm.

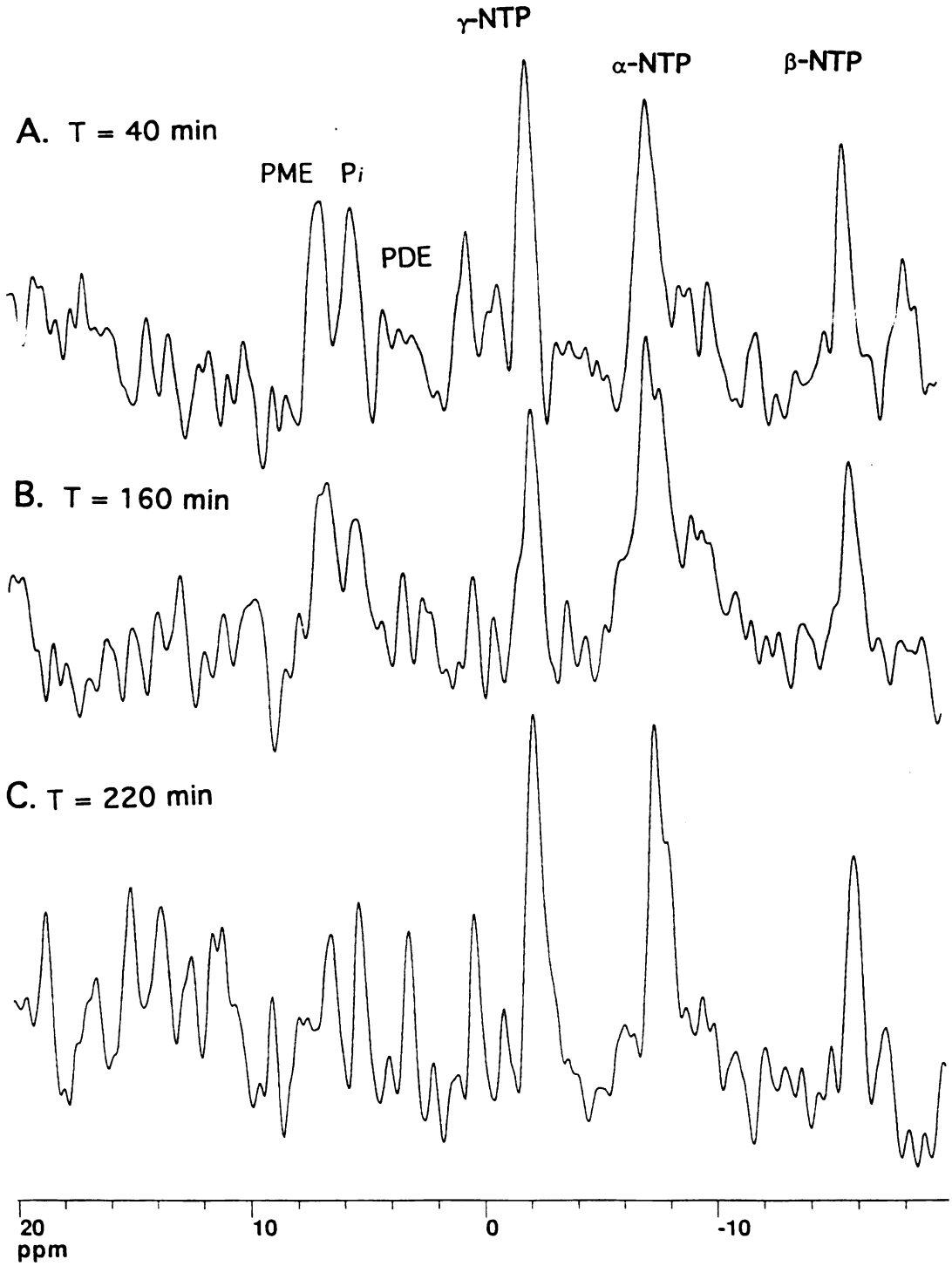

Figure 13: The *in vivo* ^{31}P spectra of rat liver administered protocol # 4. The spectra were obtained with a one-pulse sequence, and interpulse delay of 1.4 s; SW= ±4400 Hz, data points=2048, and a total of 360 transients or 26.4 min.

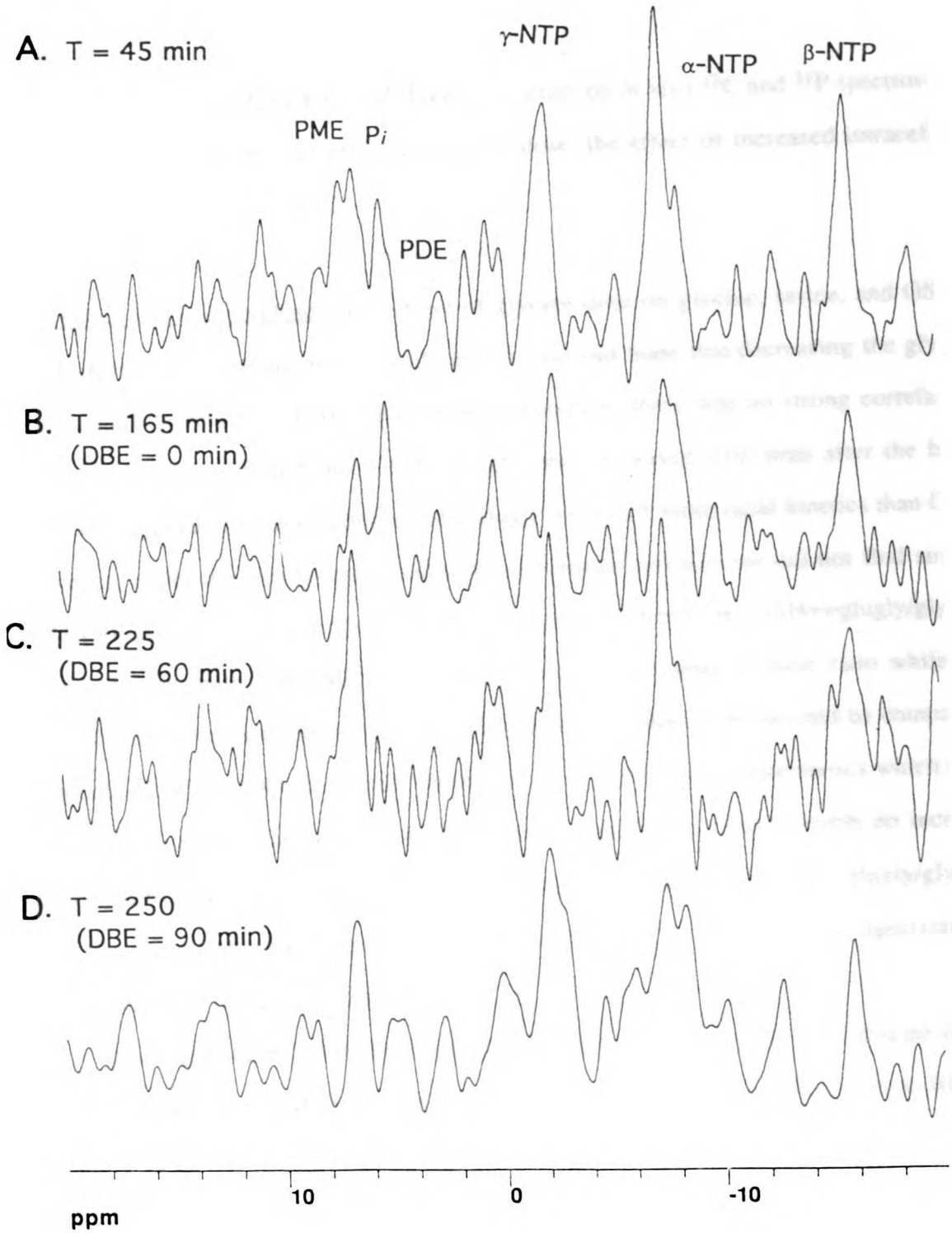

Figure 14: The *in vivo* ^{31}P spectra of rat liver administered protocol # 5. Spectra A through C were obtained with a one-pulse sequence, and interpulse delay of 1.4 s; SW= ±4400 Hz; data points=2048, and a total of 360 transients or 26.4 min. Spectrum D was obtained from 120 transients and required 8.8 min.

DISCUSSION

We investigated the effect of three parameters on *in vivo* ^{13}C and ^{31}P spectroscopy using our animal model: the effect of glycine dose, the effect of increased intracellular cysteine, and the effect of DBE.

The Effect of Glycine Dose: The effect of glycine dose on glycine, serine, and GSH/γ-glugly metabolites (ratios) were significant. It was our hope that decreasing the glycine dose would decrease the GSH/γ-glugly ratio; however, there was no strong correlation. Pulse-chase studies found that GSH/γ-glugly ratio increased with time after the bolus injection supporting earlier findings that γ-glugly has much more rapid kinetics than GSH. However, under the steady-state conditions of constant infusion we did not find similar GSH/γ-glugly ratios. There was a strong correlation between the GSH+γ-glugly/glycine ratio and dose, with 1.6 mM/kg/hr resulting in the best signal-to-noise ratio while not swamping the liver with glycine signal. The effect of CDME as determined by comparing protocols #1, #3, and #4 is unclear. However, based on the OTC experiments which used similar glycine doses as protocol #1, increased intracellular cysteine levels do increase intracellular GSH levels. Therefore, CDME may have increased the GSH+γ-glugly/glycine ratio, the extent of which remains to be determined, but it should not be significant in comparison with the glycine signal.

Nueberger (1981) found using radiolabels that when the percent of glycine in the diet is 0.5% as compared to 2%, the C2/C3 serine double labeling only occurs at 20% as compared to 100%. We found a similar result with glycine dose, with 85 ± 5% versus 10% for protocol #4. There was also negligible ^{13}C-labeling in glucose, as well as the C2 of amino acids and glycolytic end products, lactate and alanine. This may be due to the fact that we supplement our infusion media with 10% glucose, so the rats do not need to use

glycine as a supplemental energy source at the low doses. Alternatively, it could be due to the added effect of CDME, which was included in protocols #3 and #4 but not #1.

We added CDME because we wanted to elevate GSH levels artificially (Fig. 1), while inhibiting γ-GT. Thompson and Meister (1975) found that cystine competes for γ-GT 60% better than does glycine, but it is nearly insoluble in water, and we used the methylester of cystine (CDME). CDME diffuses across the cell membrane and is stored in lysosomes in the kidney, but a significant amount forms cystine in the plasma via esterases and cystine concentrations were nearly 9-fold greater than controls (Ben-Nun et al., 1993) CDME causes cystinosis and decreases oxygen consumption of renal tubules probably by inhibiting Na^+K^+ ATPase which is tightly coupled to oxidative phosphorylation in the kidney (Foreman and Benson, 1990). For liver it is unclear whether CDME will have the same effect as in the kidney, but we used a CDME dose that was a fourth of the dose causing cystinosis (Ben-Nun et al., 1993) In addition, glycine is cytoprotectant and reverses the effects of CDME-induced cystinosis (Sakarcan et al., 1992). For *in vivo* ^{13}C NMR, it is necessary to use a glycine dose 16-fold greater than the CDME dose (i.e., protocol #4). The glycine/CDME dose difference in conjunction with the fact that only a portion of CDME forms cystine in plasma, makes it ineffective as a competitive inhibitor of γ-GT. However, CDME may be effective at increasing GSH levels

The Effect of Intracellular Sulfur Amino Acids: We gave a bolus of 15 mM/kg of OTC one hour prior to the surgery to observe the effect of increasing intracellular cysteine levels on the GSH/γ-glugly ratio. We found that OTC decreased the GSH/γ-glugly ratio by half, but increased the GSH+γ-glugly/glycine ratio by 7.6-fold, thus increasing ^{13}C-labeled GSH levels nearly 3.3-fold as compared to no OTC. As mentioned in the introduction, OTC could cause the accumulation of γ-glugly if oxoproline accumulates which can inhibit γ-glutamylcyclotransferase which metabolizes γ-glugly to glycine and oxoproline (Meister et al., 1985). The overall increase in GSH is in agreement with other researchers (Goyal et

al., 1988) who also investigated DBE toxicity, and is due to the increased bioavailability of cysteine. However, OTC also appears to cause γ-glugly accumulation, and thus was not helpful to our goal of decreasing the γ-glugly contamination of the GSH peak *in vivo*.

OTC decreased the double labeling of serine to 14% as compared to 85 ± 5% with no OTC. It is possible that OTC directly or indirectly inhibits mitochondrial metabolism of glycine and/or enhances glycine formation of 2-^{13}C-serine in the cytosol where serine methoxytransferase also occurs but glycine dehydrogenase does not. There was an increase in betaine and choline methyls (54.8 and 54.6 ppm, respectively) with protocol #2 in rats infused with 20 mM/kg/hr, and these compounds had the largest peak in the spectrum (spectrum 8C). There was also an increase in -CH_2-N of betaine and choline (67.4 and 67.8 ppm, respectively) in the control OTC experiment with a methylene to methyl peak area ratio of ca 1:3, reflecting the number of carbons in betaine and choline. A similar ratio was also obtained in protocol #2. Therefore, there was little ^{13}C-labeling of methylated glycine products but perhaps this was different earlier in the infusion. There was a significant natural-abundance taurine level in the liver from the degradation of OTC. The exact mechanism by which OTC inhibited serine double-labeling is still unclear.

The OTC did not affect the amount of glycine entering gluconeogensis, just the ^{13}C-labeling pattern, and seemed to increase anaerobic glycolytic endproduct, C2 lactate (69.3 ppm) and C2 alanine (51.3 ppm). OTC requires ATP to form cysteine via oxoprolinase, and to be catabolized to taurine, and perhaps this caused a greater energy demand on the liver, thus increasing anaerobic glycolysis. There was an increase in labeling of an unknown compound resonating at 64.1 ppm.

The Effect of Dibromoethane: DBE had a dramatic effect on the *in vivo* ^{13}C spectra. Both glycine and GSH peak areas decreased with similar magnitude creating little change in the GSH+γ-glugly/glycine ratio which was 1.0 prior to and 0.85 after 90 min of intraperitoneal injection of DBE. Therefore, the GSH+γ-glugly/glycine ratio was not an effective

biomarker of DBE. It is hypothesized that once GSH levels reach 30% of normal, alkylating agents will attack important electrophilic sites on proteins and hinder normal functioning of the cell (Amdur et al., 1991). The cell will begin to swell as it loses its ability to control osmolarity, pH will decrease due to anaerobic glycolyis since mitochondria become damaged, and the cell loses homeostatic control of Ca^{+2}. Ultimately, the cell's bioenergetics reach a critical low, phospholipids break down and the cell lysis (Amdur et al., 1991). It has been hypothesized that DBE causes cell death by directly depleting mitochondrial GSH, alkylation of proteins leading to loss of Ca^{+2} homeostatic control (Botti et al., 1989; Warren et al., 1991). The exact sequence of these events has never been monitored *in vivo* directly in the tissue and non-invasively. In our experiment, GSH levels had just decreased below 30% on the last timepoint obtained, and we just started to observe a decrease in pH. There was no change in bioenergetics as compared with controls and as monitored by *in vivo* ^{31}P NMR. It was surprising that the decrease in glycine was as abrupt as the GSH.

There are three possiblities for the decrease of glycine *in vivo*: (1) the glycine peak broadened due to release of iron from intracellular storage sites, which is necessary to induce lipid peroxidation (Halliwell and Gitteridge, 1986) (2) it was conjugated with some unknown metabolite of DBE and perhaps excreted in the urine; and (3) it was used in metabolism or production of glycine products, such as proteins and phopholipids. The PCA liver extract effectively answered these questions since there was extensive *de novo* synthesis of purines (adenine, 119.3 ppm), broad resonances centered at 42, 57, and 72 ppm possibly emanating from partially synthesized proteins, C2 serine (57.3 ppm), an unknown tentatively assigned to C2 cysteine (56.2 ppm), C2 glutamate (55.5 ppm) and C2 glutamine (55.0), methyls of betaine and choline (54.8 and 54.4 ppm, respectively), and unknowns at 61.2 ppm (perhaps glycerophosphocholine), 61.8 ppm (possibly C1, C3 glycerol), 180.2 ppm, and 186.5 ppm.

DBE follows two paths to form toxic intermediate (see Fig. 1, Chapter 5), by oxidation via cytochrome P450 and GSH conjugation via GSH-S-transferase (Anders et al., 1988; Koob and Dekant, 1991). It is interesting that over 20% of extractable protein in the liver is GSH-S-transferase (Hayes et al., 1987). *In vivo* studies using tetradeutero-1,2-dibromoethane demonstrated that approximately 20% was excreted as 5-(2-hydroxyethyl-N-acetyl-L-cysteine in urine (van Bladeren et al., 1981), therefore the ratio of oxidative versus conjugative biotransformation in DBE metabolism has been calculated as 4:1 (Koob and Dekant, 1991). It is hypothesized, although it has never directly demonstrated, that the reactive species are episulfonium ion and bromoacetaldehyde, which are formed after GSH conjugation and by P450 oxidation, respectively (see Fig. 1, Chapter 5) (Koob and Dekant, 1991). The sulfur mustard (i.e., episulfonium ion) binds preferentially to DNA, whereas bromoacetaldehyde binds preferentially to proteins (Anders et al., 1988). Support for the *in vivo* episulfonium ions from DBE is provided by animal studies where S-[2-(N^7-guanyl)ethyl-glutathione is the major DNA-adduct comprising over 90% of all DNA-adducts (Kim et al., 1990). Additionally, DBE was not mutagenic to GSH-deficient bacteria (Anders et al., 1988). DBE also forms adducts with RNA. An *in vivo* study with rats determined dose-response of DBE and monitored DNA damage, biochemical changes (GSH, cytochrome P450, ornithine decarboxylase), and liver damage (Kitchin and Brown, 1986). They found that with an oral dose of 56 mg/kg (we administered 80 mg/kg, i.p. - the LD_{50}) there was nearly a three-fold increase in ornithine decarboxylase activity and marked DNA damage with a dose as low as 5.6 mg/kg, measured at 4 and 21 hrs. However, two hours after the 56 mg/kg dose there was no significant decrease in hepatic GSH. They concluded that DBE is a much more potent carcinogen than previously thought. Therefore, at the i.p. dose used in this study and for the period monitored, we should observe extensive GSH depletion, protein alkylation, and DNA-adduct formation

Induction of protein synthesis has been shown to occur with DBE toxicity (Anders et al., 1988). Few studies have monitored the initiation events of DBE toxicity. There is

still a void in the literature regarding the biochemical changes in these initial stages of hepatocarcinogenesis, because there has been no comprehensive study that can monitor GSH, bioenergetics, intracellular pH, lipid and protein metabolism, and redox state of the cell. Most of these studies monitored kinetic biomarkers of toxicity with timepoints covering the stages of hepatocarcinogenesis from the end of initiation to the beginning of promotion. Initiation and promotion have opposite effects on biomarkers of carcinogenicity, such as GSH and GSH-S-transferases, causing some conflicting reports in the literature. For example, for most carcinogens during initiation GSH is decreased permitting DNA damage and during promotion GSH and GSH-S-transferases increase. Therefore, it is possible that we have observed an induction of many proteins, one of which is probably GSH-S-transferase, and the time scale for this induction is much more rapid than *in vitro* studies have shown presently in the literature (Hayes et al., 1987; Koob and Dekant, 1991). In conjunction with *de novo* protein synthesis, there was also purine synthesis, which could be used for translation and transcription or to renew adenine supplies. *De novo* purine synthesis is supported by the fact that only the C5 is significantly ^{13}C-labeled. If this resonance represented ATP catabolism, for example, other resonances would have equal peak intensities. Additionally, this resonance does not appear in control liver extracts.

Our results indicate that the first sequence of toxic events for DBE toxicity is a decrease in GSH as the literature would predict (Reed, 1990b; Warren et al., 1991)]. However, there is a marked increase in amino acid utilization for *de novo* synthesis of proteins, purines, and some unknown metabolites. We also found that two pools of pH: one perhaps in the centrilobular section or zone 1 of the liver where the dose of DBE would be higher, and one in zone 3. Bioenergetics did not change within 90 min of DBE injection. Aditionally, there were no anaerobic endproducts accumulated. These results indicate that our animal model would be ideal for monitoring early phases of initiation and mechanisms of carcinogenesis.

CHAPTER 8

Conclusions

Novel NMR-compatible cell and animal models were developed that, in conjunction with tissue extract and body fluid analysis, can be used to determine mechanism(s) of toxic action. The animal model permits the non-invasive monitoring of potentially twelve biochemical processes, generating an enormous database composed of the many complex organismal interactions. The cell model was created to deconvolute the complex interactions of the animal data by controlling cell composition, endocrine and immune responses, intercellular communication, and physico-chemical and inter-organ parameters. For example, our animal studies discovered that during the initiation phase of DBE-induced hepatocarcinogenesis there is an enormous induction of protein synthesis. The cell model could maintain a relatively differentiated hepatocyte culture and could collect large quantities of excreted ^{13}C-labeled products during the entire course of DBE-induced hepatocarcinogenesis, unlike the animal models. This could be a novel method of determining the structure-function of unknown molecules induced by a stress. The ^{13}C label can be used to detect, identify, and purify the excreted products, and bioassays could be developed to determine their function. Using both models in conjunction ,rather than separately, is a stronger, more effective analytical tool to evaluate mechanism(s) of toxic action and pathologies.

Glycine metabolism in rat liver was determined. Intravenous infusion of 4.4 mM/kg/hr 2-^{13}C-glycine generated *in vivo* ^{13}C NMR spectra with a temporal resolution of 9.8 min. The three 13C-labeled resonances detected were: (1) glycine, which increased logarithmically then plateaued in 100 min with a half-life of 24 ± 7 min (2) GSH, which corresonated with γ-glugly; and (3) doubly-labeled C2/C3 serine. The double labeling of serine is glycine dose dependent. Since glycine must pass through

serine to enter glycolysis, the double-labeling of serine creates a reference point from which one can elucidate aspects of cell biology, such as compartmentation. In the tissue extracts we obtained information regarding gluconeogenesis, anapluerosis, methylation, purine and protein synthesis, bioenergetics, intracellular pH, and phospholipid and urea metabolism.

^{31}P NMR of the novel NMR-compatible tricentric™ bioreactor prototypes revealed that diffusion distance is a critical factor for cell viability. Cells did not remain viable at tissue densities in prototype #1 but did in prototype #2. This is because the diffusion distance for prototype #1 and #2 are 100 and 40 μm, respectively. At tissue densities the global density of both bioreactors (ca 10%) were NMR feasible with a sufficient signal-to-noise ratio in the ^{31}P spectra with an 8 min temporal resolution. For isolated rat hepatocytes, prototype #2 should be used with an organic substrate for energy, such as 5.5 mM glucose, in order to maintain viability for a longer period of time. For cell culture, prototype #2 would be ideal, but prototype #1 may also work, since the culture should center the inner fiber, and therefore decrease diffusion distances by half. The tricentric ™ design should be developed as an artificial liver because the architecture and dimensions match that of liver.

The best NMR-compatible bioreactor for toxicology studies of anchorage dependent cells is the tricentric™. The suspension bioreactor should be best for non-anchorage-dependent cells. Cell encapsulation techniques have unknown effects on the perfusion of xenobiotics through the encapsulation matrix, and thus may give erroneous results for dose-response studies.

FUTURE STUDIES

1. At least our more successful animal studies need to be performed with intravenous infusion of 1.6 mM/kg/hr glycine + 0.1 mM/kg/hr CDME with and without 80 mg/kg

DBE injected after 130 min of glycine + CDME infusion, to obtain a significant number of datasets for comparison. The broad components probably emanate from protein fragments, such as collagen and GSH-S-transferase, but they need to be identified. The experiment needs to be extended by two hours in order to obtain significant ^{31}P changes in bioenergetics and phospholipid and urea metabolism.

2. At least two more animal studies need to be performed with 4.4 mM/kg/hr glycine infusion and bolus injection of 15 mg/kg OTC, to obtain a significant number of datasets for comparison with controls (4.4 mM/kg/hr). OTC increases GSH 3.3-fold but decrease the GSH/γ-glugly ratio *in vivo*, so it exacerbates the contamination of the *in vivo* GSH peak by γ-glugly. This apparent accumulation of γ-glugly may be due to the competitive inhibition of oxoprolinase by OTC, thus,causing an accumulation of oxoproline - the product of γ-glugly degradation. OTC decreased serine double-labeling perhaps by causing cytosolic synthesis of serine from 2-^{13}C-glycine via serine methoxytransferase.

3. The effect of 0.1 mM/kg/hr CDME infusion needs to be determined. At least three control studies using 1.6 mM/kg/hr 2-^{13}C-glycine as the control need to be performed. This glycine dose was determined to be optimum because it had sufficient NMR signal-to-noise obtained in 9.8 min yet had a minimal impact on liver biochemistry, as indicated by single-labeled serine. The signal-to-noise ratio of the GSH+γ-glugly peak was between 1.6 mM/kg/hr 2-^{13}C-glycine + 0.1 mM/kg/hr CDME and 4.4 mM/kg/hr 2-^{13}C-glycine. Therefore, increasing dose did not significantly increase GSH + γ-glugly signal-to-noise ratio which was our goal.

4. A NMR pulse sequence, such as proton-observe-carbon-edit, needs to be optimized with the bioreactor in order to obtain ^{13}C NMR data for comparing to the animal

model. Once accomplished, the DBE study needs to be performed with isolated rat hepatocytes. It may be better to use fairly well-differentiated cell cultures to obtain enough ^{13}C-labeled products of DBE-induced toxicity from the perfusate to identify them. Additionally, the control 2-^{13}C-glycine studies need to be performed to determine if the disproportional C3 glutamine label is being produced in inter-organ or intracellular compartments.

5. Cinical applications of the cell model need to be pursued with the goal of developing an artificial liver for clinical use as well as research. One could optimize the tricentric™ design for an artificial liver using cell culture techniques and various compounds, or other NMR-observable nuclei, to determine degree of differentiation. Comparison of ^{13}C-labeled (or other NMR-observable nuclei) metabolites between the cell and animal model can serve as a means to determine the degree of cell differentiation.

CONCLUDING REMARKS

The animal and cell models, when used in conjunction, are far more powerful than used separately. Although this has been the goal since the beginning of *in vivo* NMR spectroscopy, there has been no NMR-compatible cell model to adequately successfully mimic the *in vivo* system to study "normal" biochemistry. The animal model contains data on many complex interactions (e.g., immune, endocrine, cell-cell, physico-chemical, and inter-organ), and present *in vivo* NMR studies rely only on animal data. NMR-compatible cell models have been fraught with problems of mimicking the *in vivo* system mainly due to the inability to control physico-chemical parameters. This has created a preception that *in vivo* NMR data from animal models are too complex to interpret, while cell models do not represent the *in vivo* system. We hope to change this perception by

developing our multinuclear NMR cell and animal models, with the ability to monitor any biochemical process or substrate of interest *in vivo* and in a controlled environment. This could be major contribution to the methodology of *in vivo* NMR spectroscopy.

In vivo NMR has not been accepted into the mainstream of toxicology. Presently, toxicology studies monitor (1) substrate by radiotracer methods, employing enzymatic, chromatographic, spectroscopic, or electrophoretic analysis of tissue extracts or body fluids, (2) biochemical changes by molecular biology techniques, and (3) tissue damage by histology. These radiotracer and biochemical procedures are optimized to monitor only those metabolites or enzymes of interest. *In vivo* NMR permits non-invasive analysis of a multitude of *in vivo* events. For the determination of the mechanism(s) of toxic action of xenobiotics, toxicologist presently seem to monitor only specific events of interest, whereas *in vivo* NMR permits a non-invasive "complete view" of the toxic event. Serendipitous discovery, such as the rapid massive increase in glycine consumption that we discovered with DBE toxicity, can be further investigated with the cell model to determine *in vivo* factors controlling production and composition of glycine products. The cell model can be used to produce the DBE-induced glycine products for structure-function analysis. In conjunction, the cell and animal model could be a useful contribution to toxicology, greatly increasing the rate and accuracy of determining toxic mechanism(s) of action, and discovery of stress-related proteins and growth factors.

REFERENCES

Ackerman JJH, Grove TH, Wong G G, Gadian DG, and Radda GK (1980) Mapping of metabolites in whole animals by ^{31}P NMR using surface coils. Nature *283*:167-170.

Alberts B, Bray D, Lewis J, Raff M, Roberts K, and Watson JD (1989) Molecular Biology of the Cell. New York: Garland Pub. Inc.

Alger JR, Behar KL, Rothman DL, and Shulman RG (1984) Natural-abundance ^{13}C NMR Measurent of hepatic glycogen in the living rabbit. J. Magn. Reson. *56*:334-337.

Alger JR, Behar KL, Gillies RJ, Shulman RG, Gordon R E, Shaw D, and Hanley PE (1981) In vivo carbon-13 nuclear magnetic resonance studies of mammels. Science *214*:660-662.

Alison MR, and Sarraf CE (1994) Liver cell death: patterns and mechanisms. Gut *35*:577-581.

Amdur MO, Doull J, and Klaassen CD (1991) Casarett and Doull's Toxicology : The Basic Science of Poisons. New York: Pergamon Press.

Ammann H, Boulanger Y, Legault P, and Vinay P (1989) An incubation system for the NMR study of kidney tubules. Magn. Reson. Med. *12*:339-347.

Anders MW, Lash L, Dekant W, Elfarra AA, and Dohn DR (1988) Biosynthesis and biotransformation of glutathione-S-conjugates to toxic metabolites. CRC Crit. Rev. Tox. *18*:31-341.

Andersen M (1985) Determination of glutathione disulfide in biological samples. Meth. Enzym. *113*:548-555.

Anderson ME, and Meiste RA (1986) Inhibition of gamma-glutamyltranspeptidase and induction of glutathionuria by gamma-glutamyl amino acids. Proc. Natl. Acad. Sci *83*:5029-5032.

Arias IM, Jakoby WB, Popper H, Schachter D, and Shafritz DA (1988) The Liver: Biology and Pathobiology, Second Edition. New York: Raven Press, Ltd.

Askenasy N, Kushnir T, and Navon G (1990) Differences in metabolite content between intact pancreases and their perchloric acid extracts. A 2D $^{1}H/^{31}P$ correlation NMR study. nmr Biomed. *3*:220-226.

Balaban RS, Gadian DG, Radda GK, and Wong GG (1981) An NMR probe for the study of aerobic suspensions of cells and organelles. Anal. Biochem. *116*:450-455.

Barany M, and Glonek T (1984) Identification of diseased states by phosphorus-31 NMR. In DG Gorenstein (ed.): Phosphorus-31 NMR, Principles and Applications. London: Academic Press, pp. 519.

Barbash JE, and Reinhard M (1989) Abiotic dehalogenation of 1,2 dibromoethane and 1,2 dichloroethane in aqueous solution containing hydrogen sulfide. Environ. Sci Tech. *23*:1349-1357.

Barger G (1931) Ergot and Ergotism. London: Gurney and Jackson.

Barker P, and Freeman R (1985) Pulsed field gradients in NMR. An alternative to phase cycling. J. Magn. Reson. *64*:334-338.

Barry JA, McGovern KA, Lien Y-HH, Ashmore B, and Gillies RJ (1993) Dimethyl methylphosphonate (DMMP): A ^{31}P nuclear magnetic resonance spectroscopic probe of intracellular volume in mammalian cell culture. Biochem. *32*:4665-4670.

Behar D (1986) Detection of metabolites in rabbit brain by ^{13}C NMR spectroscopy following administration of [1-^{13}C]glucose. Magn. Reson. Med. *3*:911-920.

Ben-Nun A, Bashan N, Potashnik R, Cohen-Luria R, Moran A (1993) Cystine loading induces Fanconi's syndrome in rats: in vivo and vesicle studies.. Am. J. Phys. *265*:F839-844.

Botti B, Ceccarelli D, Tomasi A, Vannini V, Muscatello U, and Masini A (1989) Biochemical mechanism of GSH depletion induced by 1,2-dibromoethane in isolated rat liver mitochondria. Evidence of a GSH conjugation process. Biochim. Biophys. Acta. *992*:327-332.

Bottomley PA Redington, R.W., Edelstein, W.A., and Schenck, J.F. (1985) Estimating radiofrequency power deposition in body NMR imaging. Magn. Reson. Med. *2*:336-349.

Bottomley PA, and Roemer PB (1992) Homogeneous tissue model estimates of RF power deposition in human NMR studies. Local elevations predicted in surface coil decoupling. Ann. N. Y. Acad. Sci. *649*:144-159.

Boulanger Y, Pascale L, Tejedor A, Vinay P, and Theriault Y (1988) Biochemical characterization and osmolytes in papillary collecting ducts from a dog kidneys. Can. J. Physiol. Pharmacol. *66*:1282-1290.

Boulanger Y, and Vinay P (1989) Nuclear magnetic resonance monitoring of sodium in biological tissues. Can. J. Physiol. Pharmacol. *67*:820-828.

Boulanger Y, Vinay P, Phan Viet MT, Guardo R, and Desroches M (1985) An improved perfusion system for NMR study of living cells. Magn. Reson. Med. *2*:495-500.

Bradler JE, Barrionuevo G, Panchalingam K, McKeag D, and Pettegrew JW (1991) Actions of phosphomonoesters on CA1 hippocampal neurons as revealed by a combined electrophysiological and nuclear magnetic resonance study. Synapse *9*:7-13.

Brauer M, and Ling M (1991) The effects of chronic ethanol consumption on the intact rat liver studied by in vivo ^{31}P NMR spectroscopy. Magn. Reson. Med. *20*:100-112.

Callies R, Jackson ME, and Brindle KM (1993) Studies of cellular distribution within a hollow-fibre bioreactor using localised and diffusion-weighted NMR spectroscopy. 12th ann. mtng. Soc. Magn. Resn. Med. :626.

Campra JL, and Reynolds TB (1988) The hepatic circulation. In Arias IM, Jakoby, W. B., Popper, H. (eds.): The Liver: Biology and Pathology. Second Edition. New York, N.Y.: Raven Press, Ltd., pp. 911-947.

Canioni P, Alger JR, and Shulman RG (1983) Natural abundance carbon-13 nuclear magnetic resonance spectroscopy of liver and adipose tissue of the living rat. Biochem. *22*:4974-4980.

Canioni P, Alger JR, and Shulman RG (1984) Natural abundance carbon-13 nuclear magnetic resonance spectroscopy of liver and adipose tissue of the living rat. Biochem. *22*:4974-4980.

Cerdan S, Kunnecke B, Dolle A, and Seelig J (1988) In situ metabolism of 1ω medium chain dicarboxylix acids in the liver of intact rats as detected by ^{13}C and ^{1}H NMR. J. Biol. Chem. *263*:11664-11674.

Chang L-H, Chew WM, Weinstein PR, and James TL (1987a) A balanced-matched double-tuned probe for in vivo ^{1}H and ^{31}P NMR. J. Magn. Reson. *72*:168-172.

Chang L-H, Pereira BM, Weinstein PR, Keniry MA, Murphy-Boesch J, Litt L, and James TL (1987b) Comparison of lactate concentration determinations in ischemic and hypoxic rat brains by in vivo and in vitro ^{1}H NMR spectroscopy. Magn. Reson. Med. *4*:575-581.

Chasseaud LF (1988) Determination of thioethers as biochemical markers for monitoring exposure to potential toxicants. In H Sies and B Ketterer (eds.): Glutathione Conjugation: Mechanisms and Biological Significance. New York: Academic Press, pp. 391-413.

Christensen HN, and Handlogten ME (1981) Role of system *gly* in glycine transport in monolayer cultures of liver cells. Biochem. Biophys. Res. Comm. *98*:102-107.

Chu SCK, Xu Y, Balschi JA, and Springer CS (1990) Bulk magnetic suscptibility shifts in NMR studies of compartmentalized samples: use of paramagnetic reagents. Magn. Reson. Med. *13:*239-262.

Cohen S (1987a) ^{13}C NMR study of effects of fasting and diabetes on the metabolism of pyruvate in the tricarboxylic acid cycle and of the utilization of pyruvate and ethanol in lipogenesis in perfused rat liver. Biochem. *26:*581-589.

Cohen S (1987b) Effects of insulin on perfused liver from streptozotocin-diabetic and untreated rats: ^{13}C NMR assay of pyruvate kinase flux. Biochem. *26:*573-580.

Cohen S, (1991) Applications of nuclear magnetic resonance spectroscopy in experimental models and man. In H Popper and Schaffner, F eds.: Progress in Liver Desease. New York: Academic Press.

Cohen SM (1983) Simultaneous ^{13}C and ^{31}P NMR studies of perfused rat liver. J. Biol. Chem. *258:*14294-14308.

Cohen SM (1987) Physiological NMR spectroscopy: from isolated cells to man. New York: Annals of the New York Academy of Sciences.

Cohen SM (1987c) ^{13}C and ^{31}P NMR study of gluconeogenesis: utilization of ^{13}C-labeled substrates by perfused liver from streptozotocin-diabetic and untreated rats. Biochem *26:*563-572.

Cohen SM, Ogawa S, Rottenberg H, Glynn P, Yamane T, Brown TR, and Shulman RG (1978) ^{31}P nuclear magnetic resonance studies of isolated rat liver cells. Nature *273:*554-556.

Cohen SM, Ogawa S, and Shulman RG (1979) ^{13}C NMR studies of gluconeogenesis in rat liver cells: utilization of labeled glycerol by cells from euthyroid and hyperthyroid rats. Proc. Natl. Acad. Sci. USA *76:*1603-1607.

Corbett JT, Nunnally RL, Giovanella BC, and Antich PP (1987) Characterization of the ^{31}P magnetic resonance spectrum from human melanoma tumors implanted in nude mice. Can Res *47:*5065-5069.

Cowin GJ, Willgoss DA, Bartley J, and Endre ZH (1993) ^{13}C NMR study of glycine metabolism in rat renal proximal tubules. 12th ann. mtng. Soc. Magn. Reson. Med. :208.

Cross TA, Pahl C, Oberhansli R, Aue WP, Keller U, and Seelig J (1984) Ketogenesis in the living rat followed by ^{13}C NMR spectroscopy. Biochem. *23*:6398-6402.

Cunningham D, Malloy C, and Radda GK (1986) Effects of fasting and acute ethanol administration on the energy state of the in vivo liver as measured by ^{31}P NMR spectroscopy. Biochim. Biophys. Acta *885*:12-22.

Custer LM (1988) Physiological Studies of Hybridoma Cultivation in Hollow Fiber Bioractors. Ph.D. Dissertation, University of California, Berkeley.

Daly PF, and Cohen JS (1989) Magnetic resonance spectroscopy of tumors and potential in vivo clinical applications: a review. Can Res *49*:770-779.

Daly PF, Zugmaier G, Sandler D, Carpen M, Myers CE, and Cohen JS (1990) Regulation of the cytidine phospholipid pathways in human cancer cells and effects of 1-beta-D-arabinofuranosylcytosine: a non-invasive ^{31}P nuclear magnetic resonance study. Can. Res. *50*:552-7.

Desmoulin F, Cozzone PJ, and Canioni P (1987) ^{31}P NMR study of phosphorylated metabolites, compartmentation, intracellular pH, and phosphorylation state during normoxia and hypoxia, and ethanol perfusion in perfused rat liver. Eur. J. Biochem. *162*:151-159.

Devlin TM (1986) Textbook of Biochemistry with Clinical Correlations. New York: John Wiley & Sons.

Dolphin D, Poulson R, and Avramovic O (1989) Glutathione: Chemical, Biochemical, and Medical Aspects. Part A. New York: John Wiley and Sons.

Dunn JCY, Tompkins RG, and Yarmush ML (1992) Hepatocytes in collagen sandwich: evidence for transcriptional and translational regulation. J. Cell Biol. *116*:1043-1053.

Egan WM (1987) The use of perfusion systems for nyclear magnetic resonance studies of cells. In RK Gupta (ed.): NMR Spectroscopy of Cells and Organisms. Baton Rouge: CRC Press, pp. 135-162.

Eisenberg RM, and Lerner LS (1981) Physics: Foundations and Applications. New York: McGraw-Hill, Inc.

Eriksson O, Pollesello P, and Saris N-EL (1994) Effect of phenylephedrine on the compartmentation of inorganic phosphate in perfused rat liver during gluconeogenesis and urea synthesis: a ^{31}P-nmr spectroscopic study. Biochem. J. *298:*17-21.

Evanochko WT, Sakai TT, NG TC, Krishna NR, Kim HD, Zeidler RB, Ghanta VK, Brockman RW, Schiffer LM, Braunshweiger PG, and Glickson JD (1984) NMR study of in vivo RIF-1 tumors analysis of perchloric acid extracts and identification of ^{1}H, ^{31}P, and ^{13}C Resonances. Biochim. Biophys. Acta *805:*104-116.

Fan TW-M R.M. Higashi (1989) Reproducible nuclear magnetic resonance surface coil fabrication by combining computer-aided design and a photoresisit process. Anal. Chem. *61:*636-638.

Fantini J, Galons J-P, Marvaldi J, Cozzone PJ, and Canioni P (1987) Growth of a human colonic adenocarcinoma cell line (HT 29) on microcarrier beads: metabolic studies by 31-phosphorus nuclear magnetic resonance spectroscopy. Int. J. Can. *39:*255-260.

Farghali H, Rossaro L, Gavaler JS, Van Thiel DH, Dowd SR, Williams DS, and Ho C (1992) ^{31}P-NMR spectroscopy of perifused rat hepatocytes immobilized in agarose threads: application of chemical-induced hepatotoxicity. Biochim. Biophys. Acta *1139:*105-114.

Fleming SE, Choi SY, and Fitch MD (1990) Absorption of short-chain fatty acids from the rat cecum in vivo. J. Nutr. *121:*1787-1797.

Foreman JW, and Benson LL (1990) Effect of cystine loading on substrate oxidation by rat renal tubules. Ped. Neph. *4:*236-239.

Foxall DL, and Cohen JS (1983) NMR studies of perfused cells. J. Magn. Reson. *52*:346-349.

Fukushima E, and Roeder SBW (1981) Experimental Pulse NMR: A Nuts and Bolts Approach. Reading, Massachusetts: Addison-Wesley Publishing Company, Inc.

Gadian DG (1989) Nuclear Magnetic Resonance and Its Application to Living Systems. Oxford, England: Clarendon Press.

Galons JP, Fantini J, Vion DJ, Cozzone PJ, and Canioni P (1989) Metabolic changes in undifferentiated and differentiated human colon adenocarcinoma cells studied by multinuclear magnetic resonance spectroscopy. Biochimie *71*:949-61.

Gamcsik MP, and Colvin M (1991) ^{13}C NMR studies of glutathione metabolism in drug-sensitive and resistant MCF-7 human mammary adenocarcinoma cells. 10th Annual Meeting of the Society of Magnetic Resonance of Medicine, abstr. :p 597.

Gasbarrini A, Borle AB, Farghali H, Francavilla A, and Van Thiel D (1992) Fructose protects rat hepatocytes from anoxic injury: effect on intracellular ATP, $Ca^{2+}i$, $Mg^{2+}i$, $Na^{+}i$, and pH*i*. J. Biol. Chem. *267*:7545-7552.

Gillies RJ, Alger JR, Den Hollander JA, and Shulman RJ (1982) Intracellular pH measurements by NMR: methods and results. In R Nuccitelli and DW Deamer (eds.): Intracellular pH: Its Measurement, Regulation , and Utilization in Cellular Function. New York: Liss Pub. Co., pp. 79-104.

Gillies RJ, Barry JA, and Ross BD (1994) In vitro and in vivo ^{13}C and ^{31}P NMR analyses of phosphocholine metabolism in rat glioma cells. Magn. Reson. Med. *32*:310-318.

Gillies RJ, Chresand TJ, Drury DD, and Dale BE (1986) Design and application of bioreactors for analyses of mammalian cells by NMR. Rev. Magn. Reson. Med. *1*:155-179.

Gillies RJ, Galons J-P, McGovern KA, Scherer PG, Lien Y-H, Job C, Ratcliff R, Chapa F, Cerdan S, and Dale BE (1993) Design and application of NMR-compatible

bioreactor circuits for extended perfusion of high-density mammalian cell culture. nmr Biomed. *6*:95-104.

Gillies RJ, Scherer PG, Raghunand N, Okerlund LS, Martinez-Zaguilan R, Hesterberg L, and Dale BE (1991) Iteration of hybridoma growth and productivity in hollow fiber bioreactors using ^{31}P NMR. Magn. Reson. Med. *18*:181-192.

Gonzalez-Mendez R, Wemmer D, Hahn G, Wade-Jardetzky W, and Jardetzky O (1982) Continuous-flow NMR culture system for mammalian cells. Biochimi. Biophys. Acta *720*:274-280.

Goyal R, Tardif R, and Brodeur J (1988) Influence of a cysteine prodrug, L-2-oxothiazolidine-4-carboxylic acid, on the urinary elimination of mercapturic acids of ethylene oxide, dibromoethane, and acrylonitrile: a dose-effect study. Can. J. Physiol. Parmacol. *67*:207-212.

Grunder W, Krumbiegel P, and Gersonde K (1992) ^{15}N NMR of glycine metabolism in liver, muscle and kidney using a new pulsed Overhauser technique (POE). Isotopenpraxis *28*:81-84.

Guidoni L, Mariutti G, Rampelli GM, Rosi A, and Viti V (1987) Mobile phospholipid signals in NMR spectra of cultured human adenocarcinoma cells. Magn Reson. Med. *5*:578-585.

Halliwell B, and Gitteridge JMC (1986) Oxygen free radicals and iron in relation to biology and medicine: Some problems and concepts. Arch. Biochem. Biophy. *246*:501-514.

Hampson RK, Taylor MK, and Olson MS (1984) Regulation of the glycine cleavage system in the isolated Perfused rat liver. J Biol. Chem. *259*:1180-1185.

Hanstock DL, Brown K, and Boisvert DP (1991) Feasibility of in vivo glutathione measurement in brain and tumor tissue by 3D-ISIS localised NMR spectroscopy - a comparison with in vitro studies. Abstracts, 10^{th} Ann. Mtng. of the Soc. of Magn. Reson. Med. *2*:598.

Harper HA (1983) Harper's Review of Biochemistry. Los Altos: Lange Med. Pub.

Hayes PC, Portmann B, Aldis PM, Williams R, and Hayes JD (1987) Glutathione-S-transferase and carcinogenesis. In TJ Mantle, CB Pickett and JD Hayes (eds.): Glutathione S-Transferase and Carcinogensesis. London: Taylor and Francis, pp. 175-187.

Hazle JD, Narayan PA, and Kurdle WA (1989) In vivo proton NMR studies of normal rat liver. J. Magn. Reson. *83:*595-600.

Hazle JD, Narayana PA, and Dunsford HA (1991) In vivo NMR, biochemical, and histologic evaluation of alcohol-induced fatty liver in rat and a comparison with CCl_4 hepatotoxicity. Magn. Reson. Med. *19:*124-135.

Helzberg JH, Brown MS, and Smith I (1987) Metabolic states of the rat liver with ethanol: comparison of in vivo ^{31}P NMR. Hepatol. *7:*83-88.

Higashi RM, Fan. TW-M, and Macdonald JM (1989) Monitoring of metabolic responses of intact *Haliotis*, abalones, under salinity stress by ^{31}P surface probe localized NMR. J. Exp. Zool. *249:*350-356.

Hodgson E, and Guthrie FE (1984) Introduction to Biochemical Toxicology. New York: Elsevier Pub. Co.

Hornhardt S, Jenke HS, and Michel G (1994) Polychlorinated biphenyls modulate protooncogene expression in Chang liver cells. Febs Lett. *339:*185-188.

Hoult DI, Busby S, Gadian DG, Radda GK, Richards RE, and Seeley PJ (1974) Observation of tissue metabolites using ^{31}P nuclear magnetic resonance. Nature *252:*285-287.

Hoult DI, and Richards RE (1976) The signal-to-noise ratio of the nuclear magnetic resonance experiment. J. Magn. Reson. *24:*71-85.

Hrovat MI, Wade CG, and Hawkes SP (1985) A space-efficient assembly for NMR experiments on anchorage-dependent cells. J. Magn. Reson. *61:*409-417.

Iles RA, Griffiths JR, Stevens AN, Gadian DG, and Porteous R (1980) Effects of fructose on the energy metabolism and acid-base status of the perfused starved-rat liver. Biochem. J. *192:*191-202.

Inoue M, Kinne R, Tran T, Biempica L, and Arias IM (1983) Rat liver canalicular membrane vesicles: isolation and topological characterization. J. Biol. Chem. *258:*5183-5188.

Irving MG, Simpson SJ, Brooks WM, Holmes RS, and Doddrell DM (1985) Application of the reverse dept polarization-transfer pulse sequence to monitor in vitro and in vivo metabolism of ^{13}C-ethanol by ^{1}H-NMRspectroscopy. Int. J. Biochem *17:*471-478.

Jackson AA (1991) The glycine story. Eur. J. Clin. Nutr. *45:*59-65.

James TL (1975) Nuclear Magnetic Resonance in Biochemistry. New York, N.Y.: Academic Press, Inc.

Jauregui HO, McMillan PN, Driscoll J, and Naik S (1986) Attachment and long term survival of adult rat hepatocytes in primary monolayer cultures: comparison of different substrata and tissue culture media formulations. In Vitro Cell. Dev. Biol. *22:*13-22.

Jehenson P, Canioni P, Hantraye P, and Syrota A (1992) Carbon-13 NMR study of glycogen metabolism in the baboon liver in vivo. Biochem. Biophy. Res. Com. *182:*900-905.

Johnson GA, Benveniste H, Black RD, Hedlund LW, Maronpot RR, and Smith BR (1993) Histology by magnetic resonance microscopy. Magn. Reson. Quart. *9:*1-30.

Jois M, Ewart HS, and Brosnan JT (1992) Regulation of glycine catabolism in rat liver mitochondria. Biochem. J. *283:*435-439.

Jue T, Arias-Mendoza F, Gonnella NC, Shulman GI, and Shulman RG (1985) A ^{1}H NMR technique for observing metabolite signal in the spectrum of perfused liver. Proc. Natl. Acad. Sci. *82:*5246-5249.

Jue T, Rothman DL, Hanstock CC, Hughes E, and Shulman RG (1987) 31-P NMR spectra of humanlLiver and kidney using surface coil ISIS. 6th Ann. Mtng Soc. Magn. Reson. Med. *2:*607.

Jue T, Rothman DL, Tavitian BA, and Shulman RG (1989) Natural-abundance ^{13}C NMR study of glycogen repletion in human liver and muscle. J. Biol. Chem. *86:*1439-1442.

Kaplan O van Zijl, C.M., and Cohen, J.S. (1990a) Information from combined ^{1}H and ^{31}P NMR studies of cell extracts: differences in metabolism between drug-sensitive and drug-resistant MCF-7 human breast cancer cells. Biochem. Biophys. Res. Comm. *169:*383-390.

Kaplan O Navon, G., Lyon, R.C., Faustino, P.J., Straka, E.J., and Cohen, J.S. (1990b) Effects of 2-deoxyglucose on drug-sensitive and drug resistang human breast cancer cells: toxicity and magnetic resonance spectroscopy studies of metabolism. Can. Res. *50:*544-551.

Kaplan O Van Zijl, P. C. M, Cohen. J.S. (1992) NMR studies of metabolism of cells and perfused organs: NMR Basic Principles and Progress, pp. 4-52.

Kassahun K, Hu P, Grillo MP, Davis MR, Jin L, and Baillie TA (1994) Metabolic activation of unsaturated derivatives of valproic acid. identification of novel glutathione adducts formed through coenzymeA-dependent and -independent processes. Chem-Biol. Inter. *90:*253-275.

Kim D-H, Humphreys WG, and Guengerich FP (1990) Characterization of *S*-[2-(N^1-adenyl)ethyl]glutathione as an adduct formed in RNA and DNA from 1,2-dibromoethane. Chem. Res. Toxicol. *3:*587-594.

Kitchin KT, and Brown JL (1986) 1,2-dibromoethane causes rat hepatic DNA damage at low doses. Biochem. Biophys. Res.. Comm.. *141:*723-727.

Knuttel A, Kimmich R, and Spohn K-H (1991) Motion-insensitive volume-selective pulse sequences for direct and proton-detected ^{13}C spectroscopy: detection of glycogen in the human liver in vivo. Magn. Reson. Med. *17:*470-482.

Koob M, and Dekant W (1991) Bioactivation of xenobiotics by formation of toxic glutathione conjugates. Chem.-Biol. Interact. *77:*107-136.

Koretsky AP, Wang S, Murphy-Boesch J, Klein MP, James TL, and Weiner MW (1983) ^{31}P NMR spectroscopy of rat organs, in situ, using chronically implanted radiofrequency coils. Proc Natl Acad Sci USA *80:*7491-7495.

Kornberg HL (1966) Anaplerotic sequences and thier role in metabolism. Meth. Enzym. *40:*1-31.

Krewski D, Withey JR, Ku LF, and Andersen ME (1994) Applications of physiologic pharmacokinetic modeling in carcinogenic risk assessment. Environ. Heal. Persp. *11:*37-50.

Kunnecke B, and Seelig J (1991) Glycogen metabolism as detected by in vivo and in vitro ^{13}C-NMR spectroscopy using [1,2- ^{13}C]glucose as substrate. Biochim. Biophys. Acta *1095:*103-113.

Kurhanewicz J, Dahiya R, Macdonald JM, Jajodia P, Chang L-H, James TL, and Narayan P (1992) Phosporus metabolite characterization of human prostatic adenocarcinoma in a nude model mouse model by ^{31}P magnetic resonance spectroscopy and high pressure liquid chromatography. nmr Biomed. *5:*185-192.

Lansford RE, Carey KD, Estlack LE, Smith GC, and Hay LE (1989) Analysis of plasma protein and lipoprotein synthesis in long-term primary cultures of baboon hepatocytes maintained in serum-free medium. In Vitro Cell. Dev. Biol. *25:*174-182.

Liu KJM, Kleps R, Henderson T, and Nyhus L (1991) ^{13}C NMR Study of hepatic pyruvate carboxylase activity in tumor rats. Biochem. Biophys. Res. Com. *179:*366-371.

London RE S.A. Gabel, and A. Funk (1987) Metabolism of excess methionine in the liver of intact rat: an in vivo ^{2}H NMR study. Biochem. *26:*7166-7172.

London RE (1988a) ^{13}C labeling in studies of metabolic regulation. Prog. NMR Spectr. *20:*337-383.

London REaSAG (1988b) A deuterium surface coil NMR study of the metabolism of D-methionine in the liver of the anesthetized rat. Biochem. *27:*7864-7869.

Lyngstad M, and Grasdalen H (1993) A new NMR airlift bioreactor used in ^{31}P-NMR studies of itaconic acid producing *Aspergillus terreus*. J. Biochem. Biophys Meth. *27:*105-116.

Macdonald JM, Kurhanewicz J, Dahiya R, Espanol MT, Chang L-H, Goldberg B, James TL, and Narayan P (1993) Effect of glucose and confluency on phosphorus metabolites of perfused human prostatic adenocarcinoma cells as determined by ^{31}P MRS. Magn. Reson. Med. *29:*244-248.

Macdonald TL (1983) Chemical mechanisms of halocarbon metabolism. CRC Crit. Rev. Toxicol. *11:*85-120.

Madhu C, Gregus Z, Cheng CC, and Klaassen CD (1992) Identification of the mixed disulfide of glutathione and cysteinylglycine in bile: dependence on gamma-glutamyl transferase and responsiveness to oxidative stress. J. Pharm. Exper. Therap. *262:*896-900.

Malloy C, Cunningham C, and Radda Gk (1986) The metabolic state of the rat liver in vivo measured by ^{31}P NMR spectroscopy. Biochim Biophys. Acta. *885:*1-11.

Mason R, Cha GH, Gorrie GH, Babcock EE, and Antich PP. (1993) Glutathione in whole blood: a novel determination using double quantum coherence transfer proton NMR spectroscopy. Febs Lett. *318:*30-34.

Masson S, Desmoulin F, Sciaky M, and Cozzone PJ (1992) The effects of ethanol concentration on glycero-3-phosphophate accumulation in the perfused rat liver. Eur. J. Biochem. *205:*187-194.

Masson S, and Quistoff B (1992) The ^{31}P NMR visibility of ATP in perfused rat liver remains about 90%, unaffected by changes of metabolic state. Biochem *31:*7488-7493.

Mehendale HM, Roth RA, Gandolfi AJ, Klaunig JE, Lemasters JJ, and Curtis LR (1994) Novel mechanisms in chemically induced hepatotoxicity. FASEB J. *8:*1285-1295.

Meister (1989) Metabolism and function of glutathione. In D Dolphin R. Poulson, O. Avramovic (eds.): Glutathione: Chemical, Biochemical, and Medical Aspects. New York, NY: John Wiley & Sons, pp. 930.

Meister A, Anderson ME, and Hwang O (1985) Intracellular cysteine and glutathione delivery systems. Symposium on conditionally essential nutrients in medicine, pp. 138-151.

Melkonian aD, Gaylor JDS, Cousins RB, and Grant MH (1994) Culture of a differentiated liver cell line, HepG2, in serum with application to a bioartificial liver: effect of supplementation of serum with amino acids. Art. Organs *18:*611-617.

Menon DK, Harris M, Sargentoni J, Taylor-Robinson SD, Cox IJ, and Morgan MY (1995) In vivo hepatic ^{31}P magnetic resonance spectroscopy in chronic alcohol abusers. Gastroent. *108:*776-778.

Merlke H, Wei HR, Garwood M, and Ugurbil K (1992) B_1-insensitive heteronuclear adiabatic polarization transfer for signal enhancement. J. Magn. Reson. *99:*480-494.

Moldeus P, Hogberg J, and Orrenius S (1978) Isolation and use of liver cells. Meth. Enzym. *52:*60-71.

Monk TJ, and Lau SS (1988) Reactive intermediates and their toxicological significance. Toxicol. *52:*1-53.

Moon RB, and Richards JG (1973) Determination of Intracellular pH by 31-P magnetic resonance. *248:*7276-7278.

Morikawa S, Inubushi T, Kitoh K, Kido C, and Nozaki M (1992) Chemical assessment of phospholipid and phosphoenergetic metabolites in regenerating rat liver measured by in vivo and in vitro ^{31}P-NMR. Biochim. Biophys. Acta *1117*:251-257.

Moseley RH, Ballatori N, and Murphy SM (1988) Na^+-glycine cotransport in canalicular liver plasma membrane vesicles. Am. J. Physiol. *193*:G253-259.

Muller H.J, Lanen, D, DeCock Buning tj, Van De Vyver, FL, Alderweireldt, FC, Domisse, R, Spanoghe M, Mulder GJ and Lugtenburg J (1992) Noninvasive in vivo ^{13}C-NMR spectroscopy in the rat to study the pharmacokinetics of ^{13}C-labeled xenobiotics. Drug Metab. Disp. *20*:507-509.

Murphy EJ, Brindle KM, Rorison CJ, Dixon RM, Rajagopalan B, and Radda GK (1992) Changes in phosphatidylethanolamine metabolism in regenerating rat liver as measured by ^{31}P-NMR. Biochim. Biophys. Acta :27-34.

Murphy-Boesch J, and Koretsky AP (1983) An in vivo NMR probe circuit for improved sensitivity. J. Magn. Reson. *54*:526-532.

Narayan KS, Moress EA, Chatham JC, and Barker PB (1990) ^{31}P NMR of mammalian cells encapsulated in alginate gels utilizing a new phosphate-free perfusion medium. nmr Biomed. *3*:23-6.

Narayan P, Jajodia P, Kurhanewicz J, Thomas A, Macdonald JM, Hubesch B, Hedgecock M, Anderson CM, James TL, Tanagho EA, and Weiner M (1991) Characterization of Prostate Cancer, Benign Prostatic Hyperplasia and Normal Prostates using Transrectal ^{31}P MRS; A Preliminary Report. J Urol .

Navon G Ogawa, S., Shulman, R.G., and Yamane, T. (1977) High-resolution ^{31}P nuclear magnetic resonance studies of metabolism in aerobic *Escherichia coli* cells. Proc. Natl. Acad. Sci. USA *74*:888-891.

Neeman M, and Degani H (1989) Metabolic studies of estrogen- and tamoxifen-treated human breast cancer cells by nuclear magnetic resonance spectroscopy. Can. Res. *49*:589-94.

Neeman M, Rushkin E, Kaye AM, and Degani H (1987) ^{31}P-NMR studies of phosphate transfer rates in T47D human breast cancer cells. Biochim. Biophys .Acta *930:*179-92.

Neuberger A (1981) The metabolism of glycine and serine. In A Neuberger (ed.): Comprehensive Biochemistry: Amino Acid Metabolism and Sulphur Metabolism. New York: Elsevier Scientific Pub. Co., pp. 258-304.

Nicholson JK, Walshe JA, and Wilson ID (1988) Application of high resolution ^{1}H-NMR spectroscopy to the detection of penicillamine and its metabolites in human urine. Drug Met. drug Inter. *6:*439-436.

Nissim I, and Lapidot A (1979) Plasma amino acid turnover rates and pools in rabbits: in vivo studies using stable isotopes. Am J Physiol *237*E418-427.

Nissim I, and Lapidot A (1984) The roles of insulin and glucagon in the regulation of amino acid turnover rate and pool size: *in vivo* study with [^{15}N]glycine and gas chromatography-mass spectrometry. Biochemical Medicine *31:*185-200.

NTP (1982) National Toxicology Program: Carcinogenesis Bioassay of 1,2 Dibromoethane in F344 Rats and B6C3F Mice: U.S. Department of Health and Human Services, National Institutes of Health.

Nyberg SL, Shatford RA, Peshwa MV, White JG, Cerra FB, and Hu WS (1992) Evaluation of a hepatocyte-entrapment hollow fiber bioreactor: A potential bioartificial liver. Biotech. Bioeng. *41:*194-203.

Nyhan WL (1981) Inheritable abnormalities of amino acid metabolism. In A Nueberger (ed.): Comprehensive Biochemistry: Amino Acid Metabolism and Sulphur Metabolism. New York: Elsevier Scientific Pub. Co., pp. 305-481.

O'Leary DJ, Hawkes SP, and Wade CG (1987) Indirect monitoring of carbon-13 metabolism with NMR: analysis of perfusate with a closed-loop flow system. Magn. Reson. Med. *5:*572-577.

Ogier-Denis E Codogno, P., Chantret, I., and Trugnan, G. (1988) The processing of asparagine-linked oligosaccharides in HT-29 cells is a function of their state of enterocytic differentiation. J Biol. Chem. *263*:6031-6037.

Okuda M, Muneyuki M, Nakashima K, Sogabe T, and Miura I (1987) In vivo ^{31}P-NMR studies on energy metabolism in and catecholamine effect on rat liver during hypovolemic shock. Biochem. Inter. *15*:1089-1095.

Pahl-Wostl C, and Seelig J (1986) Metabolic pathways for ketone body production. ^{13}C NMR spectroscopy of rat liver in vivo using ^{13}C-multilabeled fatty acids. Biochem. *25*:6799-6807.

Pahl-Wostl C, and Seelig J (1987) Ketogenesis in the living rat followed by ^{13}C-NMR spectroscopy. Infusion of [1,3-^{13}C]octanoate. Biol. Chem. Hoppe-Seyler *368*:205-214.

Pasternack LB, Laude DAJ, and Appling DR (1994a) ^{13}C NMR analysis of intercompartmental flow of one-carbon units into choline and purines in *Saccharomyces cerevisiae*. Biochem. *33*:74-82.

Pasternack LB, Laude DAJ, and Appling DR (1994b) Whole-cell detection by ^{13}C NMR of metabolic flux through the C_1-tetrahydrofolate synthase/serine hydroxymethyltransferase enzyme system and effect of antifolate exposure in *Saccharomyces cerevisiae*. Biochem. *33*:7166-7173.

Pasternack LB, Laude Jr. DA, and Appling DR (1992) ^{13}C NMR detection of folate-mediated serine and glycine synthesis in vivo in Saccharomyces cerevisiae. Biochem. *31*:8713-8719.

Pelech SL, and Vance DE (1984) Regulation of phosphatidylcholine biosynthesis. Bichim. Biophys. Acta *779*:217-251.

Petersen La, and Guengerich FP (1988) Comparison of 1,2 dibromoethane and relationships between glutathione-S-transferase and cytochrome P450. In H Sies and

For reference

Not to be taken from the room.

6435294

3 1378 00643 5294